The Fate of Magnetic Monopoles in the Early Universe

Maximilian Bachmaier

München 2026

The Fate of Magnetic Monopoles in the Early Universe

Maximilian Bachmaier

Dissertation
an der Fakultät für Physik
der Ludwig-Maximilians-Universität
München

vorgelegt von
Maximilian Bachmaier
geboren in Freising

München, den 21. April 2026

Erstgutachter: Prof. Dr. Gia Dvali
Zweitgutachter: Dr. Lasha Berezhiani
Tag der mündlichen Prüfung: 2. Juni 2026

Zusammenfassung

Diese Dissertation untersucht die Eigenschaften und kosmologischen Konsequenzen von topologischen Defekten. Der Fokus liegt auf magnetischen Monopolen und ihrer Rolle im frühen Universum. Der erste Teil dieser Arbeit dient als Einführung in topologische Defekte. Einige Eigenschaften von Domain Walls, Vortices und Strings sowie magnetischen Monopolen werden diskutiert. Dies beinhaltet auch ihr Verhalten in Soliton–Antisoliton-Kollisionen sowie ihre Eigenschaften in der Dynamik von mehreren Solitonen gleicher Ladung. Der aktuelle Forschungsstand zur Dynamik von topologischen Defekten ist präsentiert und neue Ergebnisse werden diskutiert. Neue Resultate beinhalten das Mehrfach-Rückprallverhalten in Vortex–Anti-Vortex-Kollisionen, den Einfluss von Modenanregungen auf die Moduli-Raum-Dynamik von Vortices und die ersten komplett feldtheoretischen Simulationen von Kollisionen von magnetischen Monopolen gleicher Ladung.

Der zweite Teil dieser Dissertation thematisiert die Rolle von magnetischen Monopolen im frühen Universum. Es wird angenommen, dass das Standardmodell von einer großen vereinheitlichten Theorie abstammt, welche die drei fundamentalen Kräfte der Teilchenphysik, die elektromagnetische, die schwache und die starke Wechselwirkung, vereint. Allerdings sagen solche vereinheitlichten Theorien in der Regel einen Überfluss von magnetischen Monopolen voraus. Diese Arbeit fokussiert sich auf zwei mögliche Lösungen für dieses kosmologische Problem der magnetischen Monopole, welche auf Interaktionen zwischen verschiedenen unterschiedlichen Typen von topologischen Defekten basieren. Diese erste Lösung beschreibt die Auslöschung von magnetischen Monopolen durch die Kollision mit Domain Walls. Durch diesen Prozess kann die Anzahl an Monopolen auf ein Level reduziert werden, das konsistent mit Beobachtungen ist. Die zweite Lösung ist, dass der magnetische Fluss von den Monopolen in magnetischen Flussröhren konzentriert (confined) werden kann. Dadurch verbinden sich magnetische Monopole durch kosmische Strings, welche diese zusammenziehen, bis sie kollidieren und sich auslöschen. Es werden numerische Simulationen zu beiden Mechanismen präsentiert, und deren kosmologische Konsequenzen werden in dieser Dissertation diskutiert.

Zu guter Letzt wird eine Modifikation des Confinement-Mechanismus, der sogenannte “Slingshot-Effekt”, präsentiert. Er beschreibt Monopole, welche mit einer Wand kollidieren, welche die Coulomb-Phase von einer Confinement-Phase trennt. Sobald ein Monopol die Confinement-Phase betritt, erzeugt dieses einen kosmische String, welche es mit der Wand verbindet. Die numerischen Ergebnisse zur Dynamik des Slingshot-Mechanismus werden präsentiert. Zudem werden Anwendungen in anderen Feldern wie QCD-Confinement oder D-Branen-Physik diskutiert. Außerdem kann der im frühen Universum relevante Slingshot-Effekt beobachtbare Signale in Form von Gravitationswellen, primordialen schwarzen Löchern und dunkler Materie erzeugen. Diese Arbeit bietet erste Abschätzungen für die Grenzwerte dieser Beobachtungsgrößen.

Abstract

This thesis investigates the properties and cosmological implications of topological defects, with a specific focus on magnetic monopoles and their role in the early Universe.

The first part of this thesis serves as an introduction to topological defects and reviews several features of domain walls, vortices and strings, as well as magnetic monopoles. This also includes their behaviour in soliton–anti-soliton collisions, as well as their characteristics in the dynamics of multiple solitons of the same charge. The current status of research on the dynamics of topological defects is presented, and new results are discussed. The new findings include multi-bouncing behaviour in vortex–anti-vortex collisions, the influence of mode excitations on the moduli space motion of vortices, and the first fully field-theoretic simulations of collisions of magnetic monopoles with the same charge.

The second part of this thesis addresses the role of magnetic monopoles in the early Universe. It is assumed that the Standard Model originates from a Grand Unified Theory, which unifies the three fundamental forces of particle physics: the electromagnetic, weak, and strong interactions. However, such unification scenarios generically predict an overabundance of magnetic monopoles. This thesis focuses on two possible solutions to this cosmological magnetic monopole problem that are based on interactions between different types of topological defects. The first is the erasure of magnetic monopoles through collisions with domain walls. Through this process, the number of monopoles may be reduced to a level that is consistent with observations. The second solution involves confining the magnetic flux of monopoles into magnetic flux tubes. In this way, monopoles become connected by cosmic strings, which pull them together until they collide and annihilate. Numerical simulations of both mechanisms are presented, and their cosmological implications are discussed in this thesis.

Last but not least, a modification of the magnetic monopole confinement mechanism, the so-called "slingshot effect", is presented. It describes monopoles colliding with a wall that separates the Coulomb phase from a confining phase. When the monopole enters the confining phase, it stretches a cosmic string connecting it to the wall. The numerical results on the dynamics of this slingshot mechanism are presented, and applications in other fields, such as QCD confinement or D-brane physics, are discussed. Moreover, the slingshot effect, which is relevant in the early Universe, could leave observable imprints such as gravitational radiation, primordial black holes, and dark matter. This thesis provides first estimates of the bounds on these observables.

Table of Contents

Acknowledgements

This thesis is the end of an important chapter in my life. Its completion is not solely my own achievement. It was made possible by the support and encouragement of remarkable people around me. The output of my work is the result of their invaluable support.

First, I want to thank my PhD advisor Gia Dvali. Thank you very much for giving me the amazing opportunity to work with you and your group. You taught me so much about theoretical particle physics and cosmology. Your huge amount of knowledge and goal-directed approach to tackling physics problems showed me what research truly means.

Many thanks to Juan Sebastián Valbuena-Bermúdez and Michael Zantedeschi. I would like to thank you not only for the collaboration on several projects, but also for being outstanding teachers over the past four years. The amount of physics we covered, as well as the many conversations beyond physics, were pretty invaluable.

I want to thank Andrzej Wereszczynski. The two publications we wrote together represent only a small part of all that for which I have to be thankful to you. I am deeply grateful for the incredible amount of time and effort you invested in supporting me in my physics career. Thank you very much for everything you have done for me.

I would like to thank my collaborators Alberto Alonso Izquierdo and Josef Seitz. Thank you very much for the work we did together. I truly enjoyed learning from you.

Moreover, thanks to all my colleagues at LMU and MPP, including our entire group: Ana Alexandre, Philipp Bakauov, Lasha Berezhiani, Davide Chiego, Giordano Cintia, Giacomo Contri, Manuel Ettengruber, Anna Jankowsky, Oleg Kaikov, Georgios Karananas, Lucy Komisel, Emmanouil Koutsangelas, Florian Kühnel, Otari Sakhelashvili, Juan Sebastián Valbuena-Bermúdez, Anja Wachowitz, Sebastian Zell, Tongxuan Zhang, as well as several colleagues beyond our group: Christian Biello, Johannes Diehl, Rhorry Gauld, Ulrich Haisch, Prisco Lo Chiatto, Georg Raffelt. Many of you were not only colleagues but became very good friends. I truly enjoyed our collaborations, as well as the many lunches, coffee breaks, and discussions we shared.

I would like to thank three group members in particular. Giacomo Contri, I cannot imagine the past years without you as my office mate. Although we have not written a publication together (so far), you have indirectly contributed to many of mine. You have been one of my most important teachers and friends. The many hours we spent discussing (not only physics) were truly among the highlights of my time. Thank you from the bottom of my heart for always being there for me over the past years.

Lasha Berezhiani, you truly hold our group together and are always available when needed. I often turned to you for advice on a wide variety of topics. To me, you have been a mentor, someone I could rely on whenever I faced challenges, whether simple or complex. Thank you very much for your great help and support.

Davide Chiego, what began as a supervisor–student relationship during your master project evolved into a truly wonderful collaboration. I always enjoy our discussions, and I

sincerely hope we will continue working together for a long time. Furthermore, thank you very much for carefully reviewing many equations in this thesis.

I would like to thank two more people who, despite not having collaborated with them so far, have played an important role during my PhD. Nick Manton, thank you very much for the many insightful discussions we have had and for hosting me in Cambridge. You also introduced me to the solitons community, which was one of the most important influences during my PhD and finally one of the key reasons I am able to remain in academia.

Jose Juan Blanco-Pillado, I would like to thank you very much for hosting me in Bilbao. It was truly a wonderful time. Our discussions were incredibly valuable, and I learned a great amount from you. I am looking very much forward to our future collaborative work in the coming years. Thank you for offering me such an excellent postdoctoral position.

Without naming individuals explicitly, I would also like to thank all those who hosted me during my many travels. These physics visits were a significant part of my PhD experience. The numerous discussions I had with people at these institutions greatly influenced how I shaped many parts of this thesis. I am grateful for the engaging seminars and for the warm hospitality I received everywhere I went.

I would like to thank Davide Chiego, Deniz Ali Duru, and Luc Malinowski for the opportunity to supervise your master theses, and Danial Jalaeiansamani for the opportunity to supervise your bachelor thesis. It was a pleasure working with all of you.

Furthermore, I would like to thank Frank Steffen and Giulia Zanderighi for the outstanding organization of the IMPRS program. The many events, including the colloquia and the young scientist workshops at Ringberg Castle, provided an excellent platform for me to engage in both scientific and social exchange with my fellow PhD students.

Many thanks go out to Lasha Berezhiani, Davide Chiego, Giacomo Contri, Gia Dvali, Lucy Komisel, and Andrzej Wereszczynski for proofreading and helping to improve several parts of this thesis.

I would like to thank my reference letter writers Lasha Berezhiani, Jose Juan Blanco-Pillado, Gia Dvali, Nick Manton, and Andrzej Wereszczynski, who made it possible for me to successfully complete the postdoctoral application period.

All the people mentioned so far are connected to my work. However, it is equally important to acknowledge the huge support I have received from people beyond the academic community. I would like to thank the amazing team of the Wallace Bar, with whom I am already working for many years. I am also very grateful to the friends I met during my physics studies, as well as to all the other friends in my life. You all support me in everything that I am doing and you provide me plenty moments where I can relax and recharge. Each of you holds a special place in my heart.

I would like to thank my family – my parents and their partners, my siblings and their partners, and my parents-in-law. You have been my lifelong supporters, accompanying me every step of the way and encouraging me in all that I do. Thank you for always being there for me.

Above all, I want to thank my wife Vroni. Your love, patience, and belief in me are a constant source of strength and motivation. I am deeply grateful to have you by my side on this journey. I love you.

Publications

The basis of this thesis is the work I carried out during my doctoral studies at the Ludwig-Maximilians-Universität München (LMU) and at the Max-Planck-Institut für Physik (MPP). The thesis is based on the following publications:

1. M. Bachmaier, G. Dvali, and J. S. Valbuena-Bermúdez, *Radiation emission during the erasure of magnetic monopoles*, Phys. Rev. D **108**, 103501 (2023), arXiv:2306.12958 [hep-th].
2. M. Bachmaier, G. Dvali, J. S. Valbuena-Bermúdez, and M. Zantedeschi, *Confinement slingshot and gravitational waves*, Phys. Rev. D **110**, 016001 (2024), arXiv:2309.14195 [hep-ph].
3. M. Bachmaier, G. Dvali, J. Seitz, and J. S. Valbuena-Bermúdez, *Simulations of magnetic monopole collisions*, Phys. Rev. D **111**, 075014 (2025), arXiv:2502.01756 [hep-th].
4. M. Bachmaier and A. Wereszczynski, *Resonance phenomena in vortex-antivortex collisions*, Phys. Lett. B **875**, 140324 (2026), arXiv:2510.17964 [hep-th].
5. A. Alonso Izquierdo, M. Bachmaier, and A. Wereszczynski, *From BPS geodesics to mode-driven dynamics in the scattering of multiple BPS vortices*, arXiv:2603.04495 [hep-th] (2026).
6. M. Bachmaier, G. Dvali, J. S. Valbuena-Bermudez, and M. Zantedeschi, *Cosmological Implications of the Slingshot Effect: Gravitational Waves, Primordial Black Holes and Dark Matter*, arXiv:2603.18512 [hep-ph] (2026).

All authors of the papers share first authorship. The author lists are ordered alphabetically, as is standard in the field of high-energy physics. The following publication is mentioned in the conclusions of this thesis but is not discussed in detail:

7. M. Bachmaier, G. Dvali, and J. S. Valbuena-Bermúdez, *Witten Effect in* 3*-Form Description of* θ*-vacua*, arXiv:2510.05237 [hep-th] (2025).

Conventions and Units

Throughout the thesis, natural units are used. This means, the speed of light c, the Planck constant $\hbar$, and the vacuum permittivity ε_0 are set to 1. In addition, we set the Boltzmann constant k_{B} to 1. If not otherwise stated, the Planck mass M_{P} is never set to one and is always kept explicit.

We denote space-time coordinates by x^μ, where x^0 corresponds to the time coordinate and x^i, with $i \in 1, \ldots, d$, denote the spatial coordinates in d space dimensions. Greek indices run from 0 to d, while Latin indices run from 1 to d. To avoid confusion between spatial indices and the group indices of the symmetry group $SU(2)$, we use i, j, k, … for spatial vector components and a, b, c, … for group indices. For the Minkowski metric $\eta_{\mu\nu}$, we take the mostly-minus signature. Throughout the thesis, we follow the Einstein summation convention, meaning that $A_\mu B^\mu = \sum_{\mu,\nu} A^\mu B^\nu \eta_{\mu\nu}$ and $A_i B_i = \sum_i A_i B_i$.

The Levi-Civita tensor with Greek indices follows the conventions $\varepsilon_{0123} = +1$, $\varepsilon_{012} = +1$, and $\varepsilon_{01} = +1$ in $3+1$, $2+1$, and $1+1$ spacetime dimensions, respectively. For the Levi-Civita symbols with Latin indices we use the conventions $\varepsilon_{123} = +1$ and $\varepsilon_{12} = +1$.

The $SU(2)$ generators are normalised according to $\mathrm{Tr}\big(T^a T^b\big) = \delta_{ab}/2$, where δ_{ab} denotes the Kronecker delta. In $SU(2)$, the generators satisfy the commutation relation $[T^a, T^b] = i\varepsilon_{abc} T^c$.

Bold symbols such as $\boldsymbol{A}$ always denote a spatial vector $\vec{A}$. A hat, $\hat{\boldsymbol{A}}$, indicates that the vector is normalised to length one. We use a similar notation for the adjoint scalar fields ϕ^a, where the normalised field is given by $\hat{\phi}^a = \phi^a/\sqrt{\phi^b\phi^b}$. The dot $\dot{f}(t)$ denotes the time derivative of $f(t)$, while the prime $f'(x)$ denotes the spatial derivative of $f(x)$. Finally, we sometimes use the notation $\supset$ in equations to indicate that only a subset of terms is shown. This means that, if an expression contains several terms, some are omitted because they are not relevant for the discussion. For example, one may write $L = f_1 + f_2 + f_3 \supset f_1$.

Finally, we introduce some terminology that is typically used in a different context. A major part of this thesis deals with an $SU(2)$ gauge theory that is spontaneously broken to $U(1)$ via an adjoint scalar field ϕ^a. This leads to two massive gauge bosons and one massless gauge boson. Due to the analogy with the Standard Model, we will refer to the massive gauge bosons as W-bosons and to the massless gauge boson as the photon. Accordingly, when we speak of electric and magnetic fields, we mean those associated with the massless gauge boson in the $SU(2)$ theory. The massive scalar field that remains after symmetry breaking will be referred to as the Higgs boson (and similarly for the massive scalar degree of freedom in the Abelian-Higgs model). For the spontaneously broken phase, we will also use the term Higgsed phase. Furthermore, unless stated otherwise, we use the term confinement not in the sense of QCD confinement, but in the context of magnetic field confinement. This means, confinement describes the effect that magnetic fields become concentrated (confined) in flux tubes, in analogy to the confinement of the colour-electric field in QCD flux tubes.

In this thesis, we use the following abbreviations:

BPS	Bogomol'nyi–Prasad–Sommerfield
VEV	Vacuum Expectation Value
DW	Domain Wall
SM	Standard Model
QCD	Quantum Chromodynamics
GUT	Grand Unified Theory
PBH	Primordial Black Hole
KK	Kaluza–Klein
GW	Gravitational Wave

Chapter 1

Introduction

Magnetic monopoles play a central role in theoretical physics. Paul Dirac set up the foundations for magnetic monopole research in the year 1931 [1]. He introduced the magnetic monopole as a singularity of the vector field, the Dirac string, which can be considered as an infinitely long solenoid ending on the monopole. Since this string should not be measurable, he had to introduce the quantization condition, $Q_e = nQ_m/2\pi$, where n is an integer, and Q_e and Q_m are the electric and magnetic charge, respectively. This condition means that the existence of magnetic monopoles would explain why electric charge is quantized. Because of its singularity, the Dirac monopole has infinite energy and is thus in its original form not physical, but nevertheless, until today, serves as a very good prototype.

The UV completion for a magnetic monopole was found in 1974 by 't Hooft and Polyakov [2, 3] who, independently from each other, wrote down a magnetic monopole ansatz in theories where the $SU(N)$ gauge symmetry is spontaneously broken by a scalar field, transforming in the adjoint representation. In their model, the magnetic monopole is a topological defect that is stable due to its topological charge. After this discovery, two communities became particularly interested in magnetic monopoles. On the one hand, because of the 't Hooft-Polyakov monopole's non-trivial topological structure, people started working on multi-monopole configurations and their moduli space structure. On the other hand, because of its applications in high-energy physics, people started thinking about the consequences of magnetic monopoles in cosmology and particle physics.

Besides magnetic interactions, 't Hooft–Polyakov magnetic monopoles also possess a non-trivial scalar structure that gives rise to scalar attraction. Usually, these scalar interactions are exponentially suppressed. However, in the special Bogomol'nyi–Prasad–Sommerfield (BPS) limit, where the Higgs boson mass vanishes, the scalar interactions become long-range and can compete with the magnetic force. In this limit, Manton demonstrated that the scalar and magnetic forces exactly cancel for two equally charged monopoles [4]. This remarkable observation motivated the study of higher-charged magnetic monopoles, which were indeed found and shown to have non-trivial topological structures [5, 6, 7]. Manton later proposed that monopole dynamics could be understood as geodesic motion on the moduli space [8]. This idea finally led to the work of Atiyah and Hitchin, who constructed the moduli space of two monopoles [9, 10]. Building on their results, many mathematicians and physicists worked out several different monopole scattering processes. Now, about 40 years later, advances in computational power and numerical techniques allow us to simulate these scattering scenarios.

A major part of this thesis (Chapter 3) is devoted to numerical simulations of the dynamics of topological defects. One long-term goal is to achieve a more detailed understanding of magnetic monopole collisions. However, due to their non-Abelian structure the numerical simulation of magnetic monopoles turns out to be highly non-trivial, as will be shown throughout the thesis. For this reason, Chapter 3 first discusses the collisions of lower-dimensional topological defects, such as domain walls and Nielsen–Olesen vortices [11], before presenting the most recent results on the simulations of monopole collisions currently available [12]. These simulations not only support the robustness of the moduli space approximation, but also provide explicit confirmation of predicted scattering phenomena, such as the famous right-angle scattering of two magnetic monopoles predicted by Atiyah and Hitchin [9].

As mentioned before, another important direction in magnetic monopole research is their role in high-energy physics. Magnetic monopoles naturally arise in theories where a non-Abelian gauge group undergoes spontaneous symmetry breaking to a subgroup containing a $U(1)$ factor[1]. Prominent examples for theories that contain such spontaneous symmetry breakings are provided by Grand Unified Theories (GUTs), in which the strong, weak, and electromagnetic interactions are unified within a single gauge group. For instance, the Standard Model (SM) group $SU(3) \times SU(2) \times U(1)$ can be embedded into the gauge group $SU(5)$, which is the minimal possibility for grand unification [13]. Since today's Universe is well-described by the SM, a phase transition from the unified phase down to the SM phase is required. During such a transition, magnetic monopoles are produced through the Kibble mechanism [14]. Zeldovich and Khlopov in 1978 [15], as well as Preskill in 1979 [16], estimated the abundance of monopoles generated in this process and found that they would dominate the energy density of the Universe, which is in contradiction with observations. This inconsistency is now known as the *magnetic monopole problem*.

This overabundance of magnetic monopoles in the Universe was, besides the horizon and flatness problems, one of the original motivations for Guth in 1980 to propose the idea of cosmic inflation [17]. During inflation the Universe expands so rapidly that the monopole density can be decreased to a level consistent with current observations. However, this mechanism only solves the monopole problem if the monopoles were produced before inflation. If instead inflation occurred before magnetic monopole production, the problem would remain, and alternative solutions are required.

Around the same time, Langacker and Pi [18] proposed the possibility of an intermediate stage in the evolution of the Universe during which the electromagnetic $U(1)$ symmetry is temporarily broken. At a certain critical temperature, a phase transition in which the $U(1)$ symmetry breaks may take place, leading to the formation of cosmic strings that connect monopoles to anti-monopoles. These strings pull the monopole–anti-monopole

---

[1] More generally, the requirement is that the second homotopy group of the vacuum manifold $\mathcal{M}$ is non-trivial, $\pi_2(\mathcal{M}) \neq 1$, as we will discuss in Appendix B.

pairs together until they collide and annihilate.

This solution is particularly appealing because it may be tested through future gravitational wave experiments. When cosmic strings pull monopoles toward anti-monopoles, the resulting strong acceleration leads to the emission of gravitational waves. First estimates of this radiation, within a point-like approximation, were carried out in [19]. In Chapter 4, we review these estimates and confirm them using numerical simulations. In this thesis we also investigate a slight modification of the original idea by Langacker and Pi. Specifically, we focus on magnetic monopoles connecting by strings during first-order phase transitions. When a nucleating bubble collides with a single monopole, the monopole stretches a string inside the bubble. We named this process the *confinement slingshot effect*. As the bubble continues to expand, the monopole attached to the string is accelerated, leading to the emission of gravitational waves in a manner analogous to the radiation from monopole–anti-monopole pairs connected by strings. The slingshot mechanism, together with several of its implications, is discussed in detail in Chapter 5, which is based on the two papers [20, 21]. In particular, we present numerical simulations of both single and multiple slingshots, and use the resulting data to calculate the amplitude and frequency spectrum of the corresponding gravitational radiation. Furthermore, applications of the slingshot effect in other theories, such as QCD and string theory, are discussed.

A third solution to the magnetic monopole problem was suggested by Dvali, Melfo, and Senjanovic in 1995 [22], who presented an example in which the symmetry remains non-restored even at very high temperatures. In this case, the grand unified phase would never have been realized in the early Universe, and thus no phase transition in which monopoles are produced would have taken place.

The last solution to the monopole problem that we will discuss in detail in this thesis is the erasure of magnetic monopoles through domain walls. In 1997, Dvali, Liu, and Vachaspati argued [23] that in a grand unified phase transition, in addition to magnetic monopoles, domain walls can also appear. These domain walls have the property that within their cores, subgroups of the grand unified symmetry group can be restored. As a consequence, if the subgroup from which the monopole originates is restored inside the wall, the monopole can no longer be resolved there and unwinds when it collides with such a wall.

The origin of the magnetic monopole problem, along with the various proposed solutions, will be discussed in detail in Chapter 4.

This thesis is intended to emphasize the importance of magnetic monopoles, and other topological defects, in theoretical physics. The work is organized along two closely connected research directions. The first part is devoted to the dynamics of topological defects, with particular focus on the classical scattering of point-like defects. The second part investigates the role of magnetic monopoles in high-energy physics. If monopoles were produced during cosmological phase transitions, their subsequent evolution would have had strong implications for cosmology. Research in both directions is essential in getting a full understanding of *The Fate of Magnetic Monopoles in the Early Universe*.

Chapter 2

Introduction to Topological Defects

This thesis is about topological defects, their properties, and their role in high-energy physics. Topological defects are classical solutions in field theory that are stable due to a conserved topological charge. They form a subclass of solitons, which are classical field configurations not necessarily stabilized by topological arguments. In this thesis, we will focus in particular on domain walls, vortices and strings, and magnetic monopoles. This chapter aims to introduce these types of defects and discusses their main features.

The material presented in this chapter is standard and can be found in the literature. It is based on and adapted from the textbooks [24, 25, 26, 27, 28, 29].

2.1 Domain Walls

In this section, the simplest type of topological defect is introduced, the domain wall, also called a kink. It appears in theories with a discrete vacuum manifold. The vacuum manifold, $\mathcal{M}$, is defined as the set of field configurations that minimizes the energy of the system. The most minimal theory in which domain walls can arise is a $1+1$-dimensional theory with a real scalar field $\phi(t,x)$ and a Lagrangian density of the form

$$\mathcal{L} = \frac{1}{2}\partial_\mu\phi\,\partial^\mu\phi - V(\phi)\,. \tag{2.1}$$

For the moment, the potential is kept arbitrary, with the only condition that it gives rise to a discrete vacuum manifold, $\mathcal{M}$. All elements of the vacuum manifold are degenerate in energy, and thus any choice $\phi \in \mathcal{M}$ is equally preferred. It is possible that, at different points in space, the field ϕ chooses different values of $\mathcal{M}$. For example, in the Universe, when two regions are causally disconnected and initially do not transfer any information to one another, the scalar field in one region is not influenced by the other region in the choice of the vacuum value. This application to the Universe will be discussed in more detail later in this section, when phase transitions are addressed. The choice of two different values at two different points in space implies that there has to exist a continuous function, the domain wall, interpolating between these two domains.

2.1.1 ϕ^4 Domain Walls

For a prototype example of domain walls, let us consider the potential

$$V(\phi) = \frac{\lambda}{4}(\phi^2 - v^2)^2\,, \tag{2.2}$$

where λ and v are constants of energy dimension two and zero, respectively. The vacuum manifold is given by the two scalar field values $\phi = \pm v$ that minimize the potential. Consequently, a domain wall solution must interpolate between $\phi(x \to -\infty) = \mp v$ and $\phi(x \to \infty) = \pm v$. Imposing these boundary conditions, one can find an analytic (static) solution to the field equations of the model. The static field equation is

$$\frac{\mathrm{d}^2\phi}{\mathrm{d}x^2} = \frac{\partial V(\phi)}{\partial \phi}\,. \tag{2.3}$$

Multiplying this equation by $\mathrm{d}\phi/\mathrm{d}x$ and applying the product rule, one obtains, after integration, the Bogomol'nyi equation [30]

$$\frac{\mathrm{d}\phi}{\mathrm{d}x} = \pm\sqrt{2V(\phi)}\,, \tag{2.4}$$

where the integration constant has been set to zero, since both $\mathrm{d}\phi/\mathrm{d}x$ and the potential vanish asymptotically.

This equation has the trivial constant solutions $\phi = \pm v$. In addition, it possesses two non-trivial domain wall solutions,

$$\phi_{\mathrm{DW}}(x) = \pm v \tanh\left(\frac{m_h}{2}(x - x_0)\right)\,, \tag{2.5}$$

where $m_h = \sqrt{2\lambda}\, v$ is the Higgs boson mass of the theory and x_0 is the position of the domain wall centre. These two solutions are shown in Figure 2.1.

Using the Bogomol'nyi equation (2.4), the static energy density of the domain wall can be written as

$$\varepsilon(x) = 2V(\phi_{\mathrm{DW}}(x)) = \frac{m_h^2 v^2}{4}\left(\tanh^2\left(\frac{m_h}{2}(x - x_0)\right) - 1\right)^2\,, \tag{2.6}$$

which illustrated in Figure 2.1. Integrating over the full space yields the total mass of the domain wall,

$$m_{\mathrm{DW}} = \int_{-\infty}^{\infty} \mathrm{d}x\; 2V(\phi_{\mathrm{DW}}(x)) = \int_{-v}^{v} \mathrm{d}\phi\; \sqrt{2V(\phi_{\mathrm{DW}})} = \frac{2}{3} m_h v^2\,. \tag{2.7}$$

2.1.2 Topological Charge

Topological defects, such as the domain wall derived in the previous section, are characterized by a non-trivial topological structure that is connected to a conserved topological

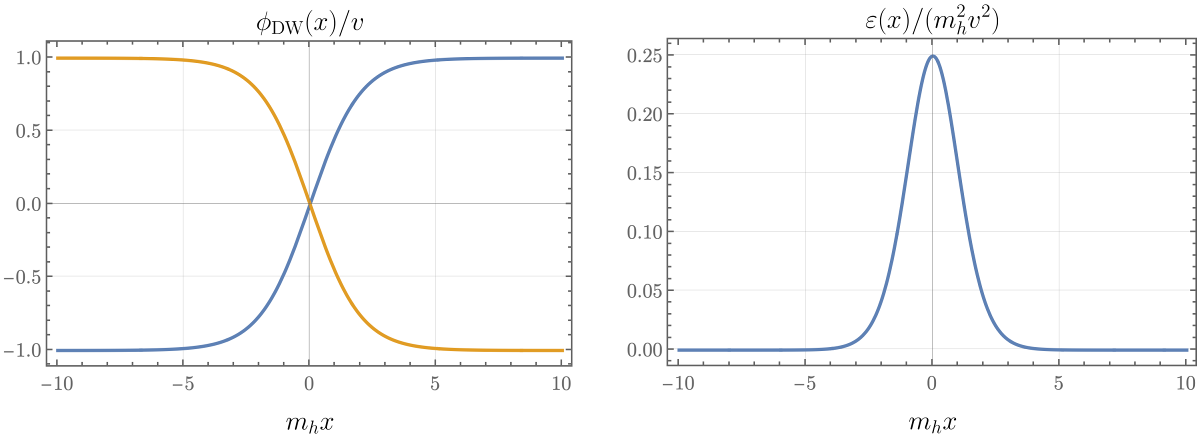

Figure 2.1: This figure shows the kink and anti-kink solutions (left) together with their energy density (right) for $x_0 = 0$.

charge. This charge is conserved for topological reasons and is therefore insensitive to continuous deformations of the field configuration. For the theory above, the topological current can be written as

$$J^\mu = -\frac{1}{2v}\varepsilon^{\mu\nu}\partial_\nu\phi\,, \tag{2.8}$$

where $\varepsilon^{\mu\nu}$ is the 2-dimensional Levi-Civita symbol[1]. Because the Levi-Civita symbol is anti-symmetric in the indices, this current is obviously conserved, $\partial_\mu J^\mu = 0$. The corresponding topological charge, n, is given by

$$n = \int_{-\infty}^{\infty} \mathrm{d}x\; J^0 = \frac{1}{2v}\left(\phi(x\to\infty) - \phi(x\to-\infty)\right). \tag{2.9}$$

For the domain wall solutions given in equation (2.5), the charge is $n = \pm 1$. Due to its conservation, the wall is stable and cannot decay.

2.1.3 Sine-Gordon Domain Walls

Another model in which domain walls appear is the Sine-Gordon model, where the potential is given by

$$V(\phi) = \frac{m^4}{\lambda}\left(1 - \cos\left(\frac{\sqrt{\lambda}}{m}\phi\right)\right), \tag{2.10}$$

with m being the mass of the scalar field and λ is a constant with an energy dimension of two.

---

[1] We will use the convention $\varepsilon^{01} = -1$

In high-energy physics, this model is particularly relevant in axion physics, since axions are expected to be described by such a potential [31]. Therefore, the study of the properties of the domain walls appearing in this model is of great interest for understanding phenomena that may arise in our Universe.

The minima of the potential (2.10) are given by $\phi_{\mathrm{min}} = 2\pi m N/\sqrt{\lambda} \equiv Nv$, where N is an integer. Consequently, the vacuum manifold of the theory consists of an infinite set of disconnected points. All these vacuum field values can be connected by one or multiple domain walls.

Similarly to the discussion above, the domain wall solutions that connect two neighbouring vacua of the vacuum manifold can be obtained by solving the Bogomol'nyi equation (2.4) using the boundary conditions $\phi(x \to -\infty) = nv$ and $\phi(x \to \infty) = (n \pm 1)v$. The resulting solutions are

$$\phi(x) = nv + \frac{2v}{\pi} \arctan\left(e^{m(x-x_0)}\right), \tag{2.11}$$

where x_0 denotes the position of the centre of the domain wall. The total mass of these walls is given by $m_{\mathrm{DW}} = 2mv^2/\pi^2$, and the corresponding topological charge is again $n = \pm 1$.

In the ϕ^4 model, it is possible to connect the vacua $\phi = \pm v$ with each other, and configurations with multiple domain walls can be constructed. However, an anti-wall must always follow a wall and vice versa. In contrast, the Sine-Gordon model allows for more freedom in the ordering of walls and anti-walls. Since the vacuum manifold contains infinitely many distinct vacua, it is possible to have more than one wall (or anti-wall) directly after each other.

A characteristic feature of solitons is the possible presence of massive bound modes that can be excited. While ϕ^4 domain walls possess such resonant modes, leading to clearly observable changes in their dynamics, Sine-Gordon domain walls do not exhibit this behaviour due to the absence of massive bound modes. Massive bound modes and their role in the dynamics of multi-soliton collisions will be discussed in detail in Chapter 3.

2.1.4 Domain Walls in Higher Dimensions

In the previous sections, domain walls were treated as one-dimensional objects. However, such walls can also arise in higher spatial dimensions. A flat ϕ^4 domain wall in three spatial dimensions can be realised by the field configuration

$$\phi_{\mathrm{DW}}(x, y, z) = \pm v \tanh\left(\frac{m_h}{2}(x - x_0)\right). \tag{2.12}$$

Here it was assumed that the wall is flat, but in principle the wall may also be deformed. Nevertheless, it is always energetically preferred for the wall to flatten. This property is commonly described by stating that the domain wall has a so-called tension, which characterises the energy per unit area of the domain wall. For the ϕ^4 domain wall, the tension is given by

$$\sigma_{\mathrm{DW}} = \frac{2}{3} m_h v^2 \,, \tag{2.13}$$

where v has mass dimension one in the $3+1$-dimensional setup.

If the domain wall is taken to fill the entire infinite space, the total energy will of course diverge. However, in cosmological phase transitions these objects typically appear as closed domain wall bubbles. Due to the wall tension, such bubbles tend to collapse unless there exists an additional source that generates an outward pressure on the bubble wall from inside. Further aspects of phase transitions and the formation and evolution of domain wall bubbles will be discussed in Chapter 4.

Another interesting feature of higher-dimensional domain walls are their gravitational properties. Recall that the Newtonian limit of the Einstein equations of General Relativity gives the Poisson equation

$$\Delta V_{\mathrm{grav}} = 8\pi G \left(T_{00} - \frac{1}{2} T \right) , \tag{2.14}$$

where V_{grav} denotes the gravitational potential, G is Newton's constant, and $T_{\mu\nu}$ is the energy-momentum tensor describing the gravitational source (with T being its trace). The energy-momentum tensor for a flat domain wall parallel to the $x = 0$ plane is given by

$$\begin{aligned} T_{\mu\nu} &= 2 \frac{\partial \mathcal{L}}{\partial g^{\mu\nu}} - g_{\mu\nu} \mathcal{L} \\ &= \varepsilon_{\mathrm{DW}} \, \mathrm{diag}(1, 0, -1, -1) \,. \end{aligned} \tag{2.15}$$

Inserting this expression into equation (2.14) yields

$$\Delta V_{\mathrm{grav}} = -4\pi G \, \varepsilon_{\mathrm{DW}} \,. \tag{2.16}$$

Due to the overall minus sign, this implies that test masses are repelled by domain walls. In this sense, domain walls “anti-gravitate”.

2.2 Vortices and Strings

As discussed in the previous section, domain walls are objects that are stable due to their topological structure. Due to the possibility of different vacuum expectation values (VEVs) in different regions of space, they carry a non-zero conserved topological charge. This concept can be extended to theories in higher dimensions with a larger number of propagating degrees of freedom. In $2 + 1$-dimensional theories with two scalar degrees of freedom, where a $U(1)$ symmetry is spontaneously broken, the spectrum of the theory can contain vortices as topological defect solutions. In $3 + 1$ dimensions, these solutions can be extended, similarly to domain walls, to higher-dimensional structures, the so-called (cosmic) strings. In this section, the vortex and string solutions will be introduced.

2.2.1 Topological Charge of Vortices

Before we analyse the full vortex solution, we now apply the concept of topological charge to vortices. The simplest theories in which vortex solutions exist are scalar field theories with a single complex scalar field, ϕ, and a single $U(1)$ symmetry. The spontaneous symmetry breaking of this $U(1)$ symmetry requires a vacuum manifold that contains a circular structure. The minimal choice is $\mathcal{M} \cong S^1$. Therefore, there are infinitely many scalar field configurations that minimize the energy of the theory. Analogously to domain walls, we can assign different values from the vacuum manifold to different regions in space. This can be implemented through a mapping of the form

$$\phi(r \to \infty, \theta) \propto e^{i\alpha(\theta)}\,, \tag{2.17}$$

where θ is the polar angle and α is a function of θ.

The topological current can be defined by

$$J^\mu = \frac{-i}{2\pi} \varepsilon^{\mu\alpha\beta}\, \partial_\alpha \phi^*\, \partial_\beta \phi\,. \tag{2.18}$$

This current is topologically conserved, $\partial_\mu J^\mu = 0$, and the topological charge can be calculated by

$$\begin{aligned} Q &= \int \mathrm{d}^2x\; J^0 \\ &= \frac{-i}{2\pi} \int \mathrm{d}^2x\; \varepsilon_{0ij}\, \partial_i(\phi^* \partial_j \phi) \\ &= \frac{1}{2\pi} \oint_C \mathrm{d}l_j\; \partial_j \alpha\,, \end{aligned} \tag{2.19}$$

where the last integral is a contour integral over the contour C, which represents the circular boundary of the two-dimensional space. Since ϕ is a continuous function, $\alpha(\theta)$ must be a periodic function of θ, with $\alpha(\theta + 2\pi) = \alpha(\theta) + 2\pi n$, where n is an integer. Hence, the topological charge is given by $Q = n$. This number indicates how many times the mapping from the circular boundary to the vacuum manifold winds around the vacuum manifold. For this reason, the topological charge is also called the *winding number*.

As an illustrative example for visualising the winding number, one can consider a vector whose direction represents the phase α at infinity. As the vector moves along the circle at infinity, its direction changes continuously. The winding number then describes how many times the vector completes a full rotation during one complete circular orbit.

2.2.2 Global Vortex

The simplest model involving vortices is a theory of a complex scalar field with a Lagrangian of the form

$$\mathcal{L} = \frac{1}{2} \partial_\mu \phi^*\, \partial^\mu \phi - V(|\phi|)\,. \tag{2.20}$$

This theory is symmetric under global $U(1)$ transformations, $\phi \mapsto e^{i\alpha}\phi$, where α is a constant.[2] The equations of motion of this theory are given by

$$\partial_\mu \partial^\mu \phi + 2\frac{\partial V}{\partial \phi^*} = 0\,. \tag{2.21}$$

By an appropriate choice of the potential, the $U(1)$ symmetry of the theory can be spontaneously broken. For the following discussion, we will use a quartic potential of the form

$$V(|\phi|) = \frac{\lambda}{8}\left(|\phi|^2 - v^2\right)^2, \tag{2.22}$$

where λ and v are constants of energy dimensions one and 1/2, respectively. The vacuum of the potential fully breaks the $U(1)$ symmetry. The particle spectrum in the spontaneously broken phase (which we will refer to as the Higgsed phase) contains one massive Higgs boson with mass $m_h = \sqrt{\lambda} v$ and one massless Goldstone degree of freedom. For a detailed introduction to spontaneous symmetry breaking, we refer to the standard textbooks [32, 33].

The vacuum manifold of the theory is given by $\mathcal{M} = \{\phi_0 = v\, e^{i\alpha} : \alpha \in [0, 2\pi)\}$ and has the topology of a circle, S^1. Therefore, this theory has the required structure to support solutions with non-zero winding number. The simplest choice is[3]

$$\phi(r,\theta) = v\, H_n(r)\, e^{in\theta}\,, \tag{2.23}$$

where n is the winding number and $H_n(r)$ is a profile function. At infinity, the scalar field must approach the vacuum of the theory, $|\phi| \xrightarrow{r\to\infty} v$, and therefore the profile function satisfies the boundary condition $H_n(r\to\infty) = 1$. For $r \to 0$, we require continuity, and thus the scalar field must vanish, implying $H_n(r \to 0) = 0$.

The total energy of the global vortex is given by

$$\begin{aligned} E &= \int \mathrm{d}^2x \, \left(\frac{1}{2}|\partial_i \phi|^2 + V(\phi)\right) \\ &= \int \mathrm{d}^2x \, \left(\frac{1}{2}|\partial_r \phi|^2 + \frac{n^2}{2r^2}|\phi|^2 + V(\phi)\right), \end{aligned} \tag{2.24}$$

where we have explicitly separated the radial and angular contributions. While the integration of the first and the last term yields finite values, the second term diverges logarithmically,

$$E = \pi n^2 \int \mathrm{d}r \; \frac{|\phi|^2}{r} \xrightarrow{r\to\infty} \pi n^2 v^2 \ln(r_{\mathrm{max}})\,, \tag{2.25}$$

---

[2] Note that this convention is unusual in the high-energy physics community, since it is not canonically normalized. However, most of the work on vortices in this thesis originates from collaborations within the solitons community, where the convention used here is standard. These conventions are also used in standard textbooks like [24, 25].

[3] Notice that instead of θ, one can choose an arbitrary periodic function $\alpha(\theta)$, which can even be nonlinear. For the quartic potential (2.22), however, it turns out that the minimal-energy winding-1 solution requires a linear function $\alpha(\theta) = \theta$.

where $r_{\max}$ is a large distance cut-off scale. This logarithmic divergence implies that an isolated global vortex has infinite energy. More generally, the energy in this model diverges whenever there is a non-zero total winding number. Notice that while there are configurations with higher-charged vortices that solve the field equations, these objects are highly unstable and will decay into multiple charge-1 vortices.

In a configuration containing one vortex and one anti-vortex, the total winding number vanishes. Consequently, the total energy of the system is finite. More precisely, for large separation distances d, it scales as

$$E \approx 2\pi v^2 \ln(d)\,. \tag{2.26}$$

Due to this logarithmic scaling, the force between the vortex and anti-vortex is long-ranged and scales as $\propto 1/d$. This long-range interaction is mediated by the massless Goldstone boson.

2.2.3 Nielsen–Olesen Vortex

In the previous section it was shown that the energy of the global vortex diverges logarithmically, due to the gradient energy arising from the winding of the ϕ field. As we will see in the following, this divergence can be compensated by introducing a gauge field into the theory. The model we analyse now is a $U(1)$ gauge theory with a single complex scalar field. The Lagrangian is

$$\mathcal{L} = -\frac{1}{4}F_{\mu\nu}F^{\mu\nu} + \frac{1}{2}D_\mu\phi^* D^\mu\phi - V(|\phi|)\,, \tag{2.27}$$

where the potential is again given by equation (2.22) and the covariant derivative is defined as $D_\mu\phi = \phi - igA_\mu\phi$, with g being the gauge coupling.[4] The field equations of this theory are given by

$$D_\mu D^\mu\phi + \frac{\lambda}{2}\left(|\phi|^2 - v^2\right)\phi = 0\,, \tag{2.28}$$

$$\partial_\mu F^{\mu\nu} - \frac{ig}{2}\left(\phi\,(D^\nu\phi)^* - \phi^*(D^\nu\phi)\right) = 0\,. \tag{2.29}$$

The spontaneous symmetry breaking of the $U(1)$ gauge symmetry results in one massive Higgs boson with mass $m_h = \sqrt{\lambda}v$ and two massive gauge degrees of freedom with mass $m_v = gv$.

The vacuum manifold of the theory remains the same as in the global vortex case and, therefore, the scalar field structure of the vortex solution in this model is unchanged. The difference is that the gauge field now compensates the logarithmic divergence of the energy. The total energy of the system is

$$E = \int \mathrm{d}^2x\,\left(\frac{1}{2}(E_i^2 + B^2) + \frac{1}{2}|D_t\phi|^2 + \frac{1}{2}|D_i\phi|^2 + V(|\phi|)\right), \tag{2.30}$$

---

[4] As in the global theory, we follow the conventions of the solitons community, which is why the Lagrangian is not canonically normalized.

where $E_i = F_{0i}$ is the electric field and $B = \frac{1}{2}\varepsilon_{ij}F_{ij}$ is the magnetic field. For a finite energy configuration, each term in the integrand has to fall off faster than with $1/r^2$ as $r \to \infty$. In particular, this implies the condition $D_\theta\phi = \frac{1}{r}\partial_\theta\phi - igA_\theta\phi \xrightarrow{r\to\infty} 0$, which is necessary to eliminate the logarithmically divergent contribution. Therefore, for a vortex configuration the gauge field has to satisfy

$$A_\theta \xrightarrow{r\to\infty} \frac{-i}{gr}\frac{\partial_\theta\phi}{\phi} \,. \tag{2.31}$$

The full (static) vortex ansatz can be written as

$$\phi(r,\theta) = v\, H_n(r)\, e^{in\theta} \,, \tag{2.32}$$

$$A_\theta(r,\theta) = \frac{n}{gr}\, K_n(r) \,, \tag{2.33}$$

$$A_r(r,\theta) = 0 \,. \tag{2.34}$$

Similarly, one can express the gauge field as

$$A_i(r,\theta) = -\varepsilon_{ij}\frac{n}{g}\frac{x^j}{r^2}\, K_n(r) \,, \tag{2.35}$$

with $i \in \{x, y\}$. Notice that we will always work in the gauge where the static vortex satisfies $A_t = 0$. The boundary conditions for the profile functions are

$$H_n(r\to\infty) = 1 \,, \qquad H_n(r\to 0) = 0 \,, \tag{2.36}$$

$$K_n(r\to\infty) = 1 \,, \qquad K_n(r\to 0) = 0 \,. \tag{2.37}$$

Inserting the vortex ansatz into the field equations (2.28), (2.29) gives the differential equations for the profile functions

$$H_n'' + \frac{1}{\tilde{r}}H_n' - \frac{n^2(1-K_n)^2 H_n}{\tilde{r}^2} + \frac{1}{2}\frac{m_h^2}{m_v^2}\, H_n(1-H_n^2) = 0 \,, \tag{2.38}$$

$$K_n'' - \frac{1}{\tilde{r}}K_n' + (1-K_n)H_n^2 = 0 \,, \tag{2.39}$$

where $'$ denotes the derivative with respect to $\tilde{r} = m_v r$. These equations can be solved numerically. For $m_h/m_v = 1$, the profile functions and the energy density of the $n = 1$ and $n = 2$ solutions are shown in Figure 2.2. Note that the scalar field profile has the polynomial behaviour, $H_n(r) \propto r^n$, near the origin. This implies that the gradient energy in the origin vanishes, leading to a local minimum of the energy density. Since the theory is Higgsed, the profiles approach their asymptotic values exponentially fast as $r \to \infty$.

The Nielsen–Olesen vortex has the special property that it carries a magnetic flux. The magnetic field can be calculated by inserting the gauge field ansatz (2.33) into the definition of the magnetic field,

$$B = \frac{1}{2}\varepsilon_{ij}F_{ij} = \frac{1}{r}\frac{\partial(rA_\theta)}{\partial r} = \frac{n}{gr}K_n'(r) \,. \tag{2.40}$$

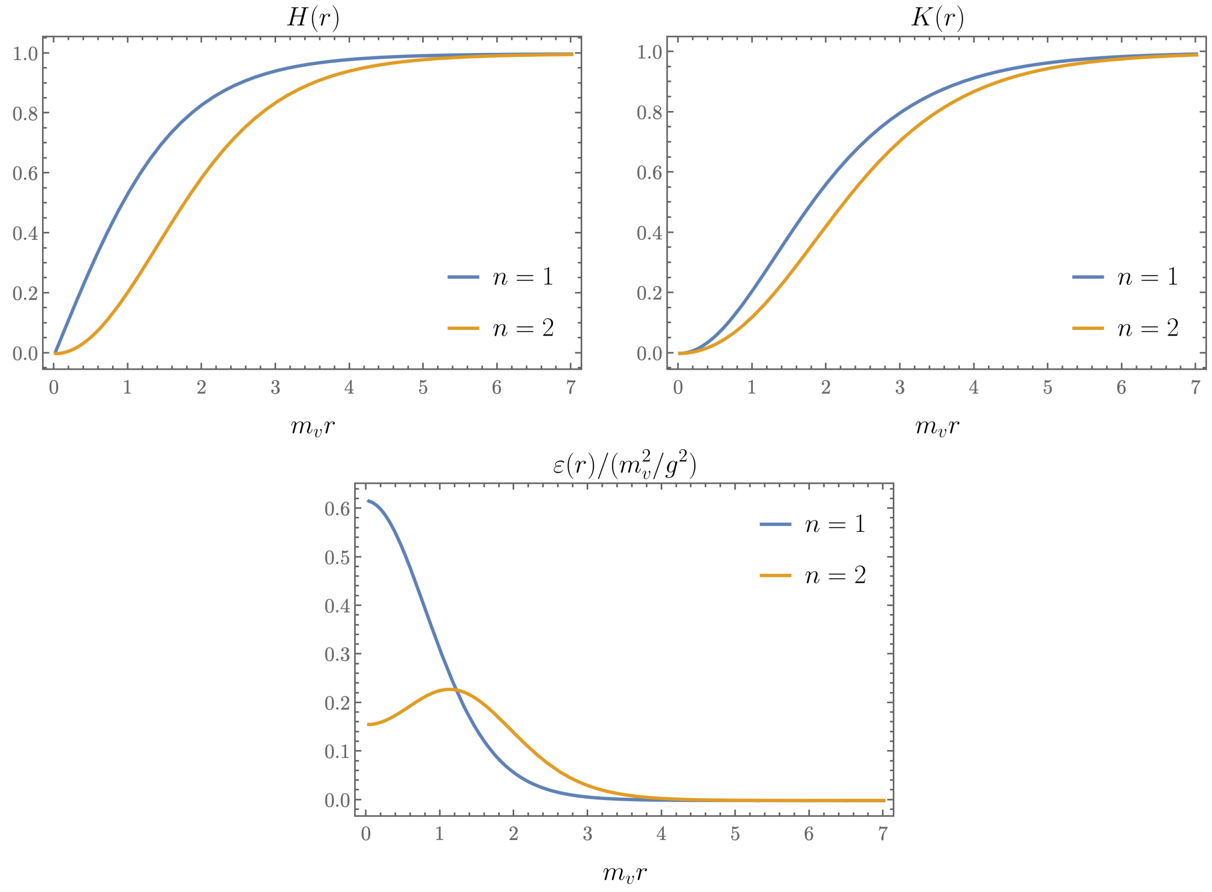
$H(r)$

$K(r)$

$\varepsilon(r)/(m_v^2/g^2)$

Figure 2.2: In the upper two figures, the numerically obtained profile functions for the Nielsen–Olesen vortex with $m_h/m_v = 1$ and winding numbers $n = 1$ and $n = 2$ are shown. The lower plot shows the corresponding energy density.

Since $K_n'(r)$ decreases exponentially fast to zero, the magnetic flux is fully localized within the vortex core. This localization can also be understood from the scalar field structure. Inside the vortex, the scalar field vanishes, i.e. the gauge boson mass is zero, whereas outside the scalar field acquires a VEV, i.e. the gauge boson becomes massive. Therefore, it is energetically preferred for the flux to be within the scalar core, where the gauge boson mass vanishes. The total magnetic flux is given by

$$\Phi = \int \mathrm{d}^2x \; B = \oint_C \mathrm{d}\theta \; rA_\theta = \frac{-i}{g} \oint_C \mathrm{d}\theta \, \frac{\partial_\theta \phi}{\phi} = \frac{2\pi n}{g} \,, \tag{2.41}$$

where C represents the boundary of the two-dimensional space.

2.2.4 Bogomol'nyi Bound and the BPS Vortex

Let us now calculate the energy of the vortex. First, the vortex does not source an electric field and is completely time-independent. Therefore, the total energy is given by

$$E = \int \mathrm{d}^2 x \, \left(\frac{1}{2} B^2 + \frac{1}{2} |D_i \phi|^2 + \frac{\lambda}{8} (|\phi|^2 - v^2)^2 \right) . \tag{2.42}$$

The covariant derivative term can be rewritten as

$$|D_i \phi|^2 = |(D_1 \pm i D_2) \phi|^2 \pm g \, \varepsilon_{0ij} \, |\phi|^2 \partial_i A_j \mp i \, \varepsilon_{0ij} \, \partial_i (\phi^* D_j \phi) . \tag{2.43}$$

The last term contributes to the total energy only through a boundary term and can therefore be dropped in the integral. A further rewriting gives

$$E = \int \mathrm{d}^2 x \left[\frac{1}{2} \left(B \pm \frac{\sqrt{\lambda}}{2} (|\phi|^2 - v^2) \right)^2 + \frac{1}{2} |(D_1 \pm i D_2) \phi|^2 \mp \frac{|\phi|^2}{2} B \left(\sqrt{\lambda} - g \right) \pm \frac{\sqrt{\lambda}}{2} v^2 B \right] . \tag{2.44}$$

This result gives one special feature of vortices. For the limit $\sqrt{\lambda} = g$, which corresponds to $m_h = m_v$, the energy is bounded from below by

$$E \geq \frac{\sqrt{\lambda}}{2} v^2 \left| \int \mathrm{d}^2 x \; B \right| = |n| \pi v^2 , \tag{2.45}$$

where n is the winding number of the system. To saturate this energy bound, vortex configurations have to satisfy the equations [30]

$$B \pm \frac{\sqrt{\lambda}}{2} (|\phi|^2 - v^2) = 0 , \tag{2.46}$$

$$|(D_1 \pm i D_2) \phi| = 0 . \tag{2.47}$$

Vortices in the Bogomol'nyi–Prasad–Sommerfield (BPS) limit, $m_h = m_v$, satisfy these so-called BPS equations. We will refer to these vortices as BPS vortices or critical vortices. The BPS limit has several interesting consequences. First of all, the second-order differential equations reduce to first-order differential equations, which makes them easier to solve.

For the second feature, let us briefly discuss the forces between two equally-charged vortices. The total energy of two far-separated BPS vortices, each with mass $m_{\mathrm{V}} = \pi v^2$, is given by $E = 2 m_{\mathrm{V}} = 2 \pi v^2$. This is exactly the same as the energy of a charge-2 BPS vortex, as can be seen from the BPS bound (2.45). This means that all configurations, regardless of their separation, are degenerate in energy and thus no force acts between them. Of course, there is both a scalar force and a gauge force, and in the vortex–vortex case the scalar force is attractive while the gauge force is repulsive. The very special property of BPS vortices (or, more generally, BPS solitons) is that these two forces exactly cancel.

This cancellation is only true for $m_h = m_v$. If $m_h < m_v$, the force between two equally charged vortices is attractive, while for $m_h > m_v$ it is repulsive [34]. This can be understood from the field profiles. One may think of the vortex core as consisting of a scalar field core of size $\sim m_h^{-1}$ and a gauge field core of size $\sim m_v^{-1}$. The strength of the scalar and gauge forces depends on how large the overlap of the scalar cores and gauge cores of two vortices is. For $m_h < m_v$, the scalar field core is larger than the gauge core, and thus the attractive scalar force dominates. For $m_h > m_v$, the gauge core is larger, and thus the repulsive gauge force dominates.

2.2.5 Cosmic Strings

So far, we have considered vortices in $2+1$ dimensions. However, just as domain walls can be extended to higher dimensions, vortices can also appear in higher dimensions in the form of so-called cosmic strings. An infinitely long cosmic string along the z-axis can be thought of as infinitely many copies of a vortex stacked on top of each other. Therefore, the solution is the same as for the vortex, but extended in the z-direction. The scalar field thus has the structure $\phi(r, \theta, z) \sim \exp(in\theta)$, where θ is the polar angle around the z-axis and r the radial distance from the z-axis. The magnetic flux of the Nielsen–Olesen vortex now runs along the entire string, forming a magnetic flux tube. Similar to the domain wall, the string has a tension that is given by $\mu \sim v^2$.

In the early Universe, cosmic strings may have formed during phase transitions (we will discuss phase transitions in more detail in Section 4.2). These strings appear as closed loops forming a full string network. Due to their tension, string loops tend to collapse. However, since their shape is typically not perfectly circularly symmetric, the dynamics is way more non-trivial. The strings dynamics and the observational consequences remain an active area of research [35, 36, 37, 38, 39, 40, 41, 42, 43].

Notice that such string networks can also appear for global cosmic strings. Although a single global vortex has infinite energy, a vortex–anti-vortex configuration does not, since the total winding of the system is zero. In this case, the energy has a logarithmic cut-off that depends on the separation distance between the two vortices. Considering a string loop, one can think about a plane cutting through the string. In this plane, the scalar field has the structure of a vortex–anti-vortex configuration, and thus the energy integrated over this plane is finite. This argument applies to the entire string loop, meaning that a string loop even if it is part of a global theory has always finite energy.

2.3 Magnetic Monopoles

The last topological defect discussed in this thesis is the magnetic monopole. Magnetic monopoles can arise in $3+1$-dimensional theories in which the vacuum manifold has the topology of a 2-sphere, S^2. As the name suggests, these objects carry a magnetic charge, which originates from a coupling to a gauge field. However, similarly to vortices, it is also possible to consider global monopoles that consist solely of a scalar field. Before discussing the minimal gauge theory in which the so-called ’t Hooft–Polyakov magnetic monopoles can appear, we first introduce the notion of topological charge and discuss global monopoles.

2.3.1 Topological Charge of Magnetic Monopoles

The most minimal theories in which magnetic monopole solutions exist are scalar field theories with three scalar field components, ϕ^a with $a = 1, 2, 3$, and an $SU(2)$ symmetry[5]. Once one component (or a linear combination of them) acquires a VEV, the $SU(2)$ symmetry gets spontaneously broken to $U(1)$. This type of symmetry breaking requires the vacuum manifold to have the shape of a 2-sphere, $\mathcal{M} \cong S^2$. Again, we can define a mapping that assigns different points at the boundary of space to different values in the vacuum manifold. In spherical coordinates (r, θ, φ), the simplest mappings take the form

$$\hat{\phi}^a = \begin{pmatrix} \cos(n\varphi)\sin\theta \\ \sin(n\varphi)\sin\theta \\ \cos\theta \end{pmatrix} , \tag{2.48}$$

where n is an integer.

Similarly to vortices and domain walls, this construction can give rise to a conserved topological charge. A topologically conserved current satisfying $\partial_\mu J^\mu = 0$ can be written as

$$J^\mu = -\frac{1}{8\pi}\varepsilon^{\mu\alpha\beta\gamma}\,\varepsilon_{abc}\,\partial_\alpha\hat{\phi}^a\,\partial_\beta\hat{\phi}^b\,\partial_\gamma\hat{\phi}^c\,. \tag{2.49}$$

Here $\varepsilon^{\mu\nu\alpha\beta}$ is the 4-dimensional Levi-Civita symbol and ε_{abc} is the 3-dimensional Levi-Civita symbol. The corresponding topological charge can be rewritten as

$$\begin{aligned} Q &= \int \mathrm{d}^3x\; J^0 \\ &= \frac{1}{8\pi}\int \mathrm{d}^3x\;\varepsilon_{ijk}\,\varepsilon_{abc}\,\partial_i\left(\hat{\phi}^a\,\partial_j\hat{\phi}^b\,\partial_k\hat{\phi}^c\right) \\ &= \frac{1}{4\pi}\int \mathrm{d}\theta\mathrm{d}\varphi\;\varepsilon_{abc}\,\hat{\phi}^a\,\partial_\theta\hat{\phi}^b\,\partial_\varphi\hat{\phi}^c\,, \end{aligned} \tag{2.50}$$

where in the first step we made use of the antisymmetry of the Levi-Civita symbol, and in the second step we applied Stokes’ theorem. Inserting (2.48) into this expression yields the topological charge $Q = n$. Therefore, n characterizes the winding number of the monopole configuration.

2.3.2 Global Monopoles

The Lagrangian of a global $SU(2)$ theory with a scalar field, ϕ, transforming in the adjoint representation and a quartic potential is given by

$$\mathcal{L} = \mathrm{Tr}\left((\partial_\mu\phi)^\dagger(\partial^\mu\phi)\right) - V(\phi)\,, \tag{2.51}$$

---

[5] Notice that for the global version of the magnetic monopole an $SO(3)$ symmetry would be sufficient.

where we will use the following quartic potential,

$$V = \lambda \left(\mathrm{Tr}\big(\phi^\dagger \phi\big) - \frac{v^2}{2} \right)^2 , \tag{2.52}$$

with λ and v being constants of energy dimensions zero and one, respectively. The scalar field ϕ can be expressed in terms of its $SU(2)$ components $\phi = \phi^a T^a$, with T^a being the three generators of $SU(2)$.[6] The field equations of this model are given by

$$(\partial^\mu \partial_\mu \phi)^a + \frac{\partial V}{\partial \phi^a} = 0 \, . \tag{2.53}$$

Due to the shape of the potential, the $SU(2)$ symmetry is spontaneously broken to $U(1)$. Consequently, the particle spectrum contains one Higgs boson with mass $m_h = \sqrt{2\lambda} v$ and two massless Goldstone bosons.

The vacuum manifold of this theory has the form of a 2-sphere, S^2, and therefore it is possible to construct a one-to-one map from the boundary of the three-dimensional space to the vacuum manifold. Such a map may, for instance, be written as

$$\phi^a(r, \theta, \varphi) = v \, H_n(r) \begin{pmatrix} \cos(n\varphi)\sin(\theta) \\ \sin(n\varphi)\sin(\theta) \\ \cos(\theta) \end{pmatrix} , \tag{2.54}$$

with n being the winding number and $H_n(r)$ the profile function with boundary conditions $H_n(r \to \infty) = 1$ and $H_n(r \to 0) = 0$.

The total energy of the global monopole is

$$\begin{aligned} E &= \int \mathrm{d}^3 x \left(\frac{1}{2} \partial_i \phi^a \partial_i \phi^a + V(\phi^a) \right) \\ &= \int \mathrm{d}^3 x \left(\frac{1}{2} \partial_r \phi^a \partial_r \phi^a + \frac{1}{2} \frac{(1+n^2)}{r^2} \phi^a \phi^a + V(\phi^a) \right) \\ &\xrightarrow{r \to \infty} 2\pi v^2 (1+n^2) \, r_{\max} \, , \end{aligned} \tag{2.55}$$

where $r_{\max}$ is a large distance cut-off scale. Therefore, as in the case of the global vortex, we find that an isolated global monopole has infinite energy. The difference is that here the divergence is linear rather than logarithmic, as it is for the vortex.

The linear divergence leads to an interesting phenomenon. Consider a configuration consisting of a monopole and an anti-monopole. In this case, the total winding number vanishes, and the energy remains finite. For a separation distance d, the energy scales as $E \propto d$, which implies a constant force between the two objects. Thus, independently of their separation, the monopole and anti-monopole always feel the same force between each other. This can result in rather unintuitive dynamics. For example, consider a configuration in which a monopole and an anti-monopole are very close to each other, with

---

[6] The generators are normalised by $\mathrm{Tr}\big(T^a T^b\big) = \frac{1}{2}\delta_{ab}$.

the monopole located at the origin and the anti-monopole placed slightly on the negative x-axis. Now add two additional anti-monopoles located far away along the positive x-axis. Due to the constant force, the monopole will accelerate towards the positive x-direction, rather than towards the nearby anti-monopole on the negative x-axis.[7] More information on the evolution of global monopole networks can be found in [44, 45].

2.3.3 ’t Hooft–Polyakov Magnetic Monopoles

As we will see in the following, similar to vortices, the divergence of the energy can be compensated by introducing a gauge field that couples to the scalar field. The Lagrangian of an $SU(2)$ gauge theory with an adjoint scalar field is given by

$$\mathcal{L} = -\frac{1}{2}\,\mathrm{Tr}(G_{\mu\nu}G^{\mu\nu}) + \mathrm{Tr}\left((D_\mu\phi)^\dagger(D^\mu\phi)\right) - V(\phi)\,, \tag{2.56}$$

with the scalar potential given in equation (2.52). The $SU(2)$ field strength tensor and the covariant derivative are defined as

$$G_{\mu\nu} = \partial_\mu W_\nu - \partial_\nu W_\mu - ig[W_\mu, W_\nu]\,, \tag{2.57}$$
$$D_\phi = \partial_\mu\phi - ig[W_\mu\phi]\,, \tag{2.58}$$

where g denotes the gauge coupling constant. The gauge field W_μ and the scalar field ϕ can be expressed in terms of their $SU(2)$ components as $W_\mu = W^a_\mu T^a$ and $\phi = \phi^a T^a$, respectively, with T^a being the three generators of $SU(2)$. Using this component notation we can write the Lagrangian as

$$\mathcal{L} = -\frac{1}{4}G^a_{\mu\nu}G^{\mu\nu}_a + \frac{1}{2}(D_\mu\phi)^a(D^\mu\phi)^a - V(\phi)\,, \tag{2.59}$$

with

$$G^a_{\mu\nu} = \partial_\mu W^a_\nu - \partial_\nu W^a_\mu + g\varepsilon_{abc}\,W^b_\mu W^c_\nu\,, \tag{2.60}$$
$$(D_\mu\phi)^a = \partial_\mu\phi^a + g\varepsilon_{abc}\,W^b_\mu\phi^c\,, \tag{2.61}$$
$$V(\phi) = \frac{\lambda}{4}(\phi^a\phi^a - v^2)^2\,. \tag{2.62}$$

The field equations of this model are given by

$$(D^\mu D_\mu\phi)^a + \frac{\partial V}{\partial\phi^a} = 0\,, \tag{2.63}$$
$$(D_\mu G^{\mu\nu})^a + g\varepsilon_{abc}\phi^b(D^\nu\phi)^c = 0\,. \tag{2.64}$$

As in the global theory, the $SU(2)$ symmetry is spontaneously broken to $U(1)$. The two massless Goldstone bosons are now “eaten” by two of the three gauge fields and consequently, two gauge bosons, which we will call W-bosons, acquire a mass $m_v = gv$, while

---

[7] I would like to thank Jon Urrestilla for providing this example.

one boson remains massless. We refer to this massless boson as the photon. In the scalar sector, there is only one physical degree of freedom, namely the Higgs boson, with mass $m_h = \sqrt{2\lambda}v$.

The static energy of a system described by this theory is given by

$$E = \int \mathrm{d}^3x \left(\frac{1}{4} G^a_{ij} G^a_{ij} + \frac{1}{2} (D_i\phi)^a (D_i\phi)^a + V(\phi) \right) . \tag{2.65}$$

Each term in this expression must have a finite integral to ensure finite energy. The divergence in the case of the global monopole originates from the scalar gradient term. To avoid this in the gauge model, we must require $(D_i\phi)^a \xrightarrow{r\to\infty} 0$ faster than with $1/r^3$. This, in turn, implies that the gauge field must have the following structure

$$W^a_i \xrightarrow{r\to\infty} \frac{1}{g} \varepsilon_{abc} \, (\partial_i \hat{\phi}^b) \hat{\phi}^c + c_i \hat{\phi}^a \, , \tag{2.66}$$

with c_i being a constant vector. The last term depends on the choice of gauge. We will set it to zero, which corresponds to the Coulomb gauge $\partial_i W^a_i = 0$.

In principle, one could now insert a winding-n scalar field configuration and multiply the fields by appropriate profile functions. However, it turns out that there are no spherically symmetric solutions with $n > 1$ that have finite energy [46]. In this case, the divergence in the energy does not originate from the asymptotic winding structure, but rather from a divergence in the monopole core. Hence, while the asymptotic field configuration remains valid, the ansatz breaks down near the core. Nevertheless, higher-charged magnetic monopoles without spherical symmetry exist. The short distance structure of such magnetic monopoles will be discussed further in Section 3.7.

Let us now focus on the finite-energy solution with winding $n = 1$. This corresponds to the 't Hooft–Polyakov magnetic monopole solution, which was first written down independently from each other by 't Hooft and Polyakov in 1974 and is given by [2, 3]

$$\phi^a = v \, \frac{x^a}{r} H(r) \, , \tag{2.67}$$

$$W^a_i = \frac{1}{g} \varepsilon_{aij} \, \frac{x^j}{r^2} (1 - K(r)) \, , \tag{2.68}$$

$$W^a_t = 0 \, , \tag{2.69}$$

where $H(r)$ and $K(r)$ are profile function with the boundary conditions

$$H(r \to \infty) = 1 \, , \qquad H(r \to 0) = 0 \, , \tag{2.70}$$

$$K(r \to \infty) = 0 \, , \qquad K(r \to 0) = 1 \, . \tag{2.71}$$

2.3.4 Magnetic Charge of Magnetic Monopoles

As the name suggests, the magnetic monopole carries a magnetic charge. To compute it, we first need to define the $U(1)$ magnetic field. A naive approach is to project out the massless $U(1)$ component of the gauge field by $A_\mu = \hat{\phi}^a W^a_\mu$, with $\hat{\phi}^a = \phi^a/\sqrt{\phi^b\phi^b}$, and to use the standard definition of the field strength from Maxwell electrodynamics, $F_{\mu\nu} = \partial_\mu A_\nu - \partial_\nu A_\mu$. However, this expression is not $SU(2)$ gauge invariant. To restore the gauge invariance, one needs to add an additional term,

$$F_{\mu\nu} = \partial_\mu(\hat{\phi}^a W^a_\nu) - \partial_\nu(\hat{\phi}^a W^a_\mu) - \frac{1}{g}\varepsilon_{abc}\hat{\phi}^a(\partial_\mu\hat{\phi}^b)(\partial_\nu\hat{\phi}^c)\,. \tag{2.72}$$

This expression can be rewritten to the 't Hooft field strength [2]

$$F_{\mu\nu} = \hat{\phi}^a G^a_{\mu\nu} - \frac{1}{g}\varepsilon_{abc}\,\hat{\phi}^a(D_\mu\hat{\phi})^b(D_\nu\hat{\phi})^c\,. \tag{2.73}$$

This definition of the field strength satisfies two conditions. First, it is gauge invariant and second, for a constant VEV, for example $\langle\phi\rangle = vT^3$, it reduces to the familiar expression $F_{\mu\nu} = \partial_\mu W^3_\nu - \partial_\nu W^3_\mu$. Therefore, it is the right field strength describing the $U(1)$-electric and -magnetic fields.

We can now insert the 't Hooft–Polyakov monopole ansatz. Substituting it into the $SU(2)$ field strength yields

$$G^a_{ij} = \frac{1}{g}\varepsilon_{ijk}\frac{1}{r}(\delta_{ka} - \hat{n}^k\hat{n}^a)K' + \frac{1}{g}\varepsilon_{ijk}\frac{\hat{n}^k\hat{n}^a}{r^2}(K^2-1)\,, \tag{2.74}$$

where $\hat{n}^a = x^a/r$, and we used the identity $\varepsilon_{ija} = \varepsilon_{ijk}\,\hat{n}^k\hat{n}^a + \varepsilon_{jak}\,\hat{n}^k\hat{n}^i + \varepsilon_{aik}\,\hat{n}^k\hat{n}^a$. The covariant derivative is given by

$$(D_i\hat{\phi})^a = \frac{1}{r}(\delta_{ai} - \hat{n}^a\hat{n}^i)K\,. \tag{2.75}$$

Combining these two results we obtain the photon field strength

$$F_{ij} = -\frac{1}{g}\varepsilon_{ijk}\frac{\hat{n}^k}{r^2}\,, \tag{2.76}$$

which results in the monopole magnetic field

$$B_i = \frac{1}{g}\frac{\hat{n}^i}{r^2}\,. \tag{2.77}$$

Therefore, the magnetic charge of the 't Hooft–Polyakov magnetic monopole is $Q_m = 4\pi/g$.

Notice that in all of the equations above we have used equalities. The calculation leading to the same long-range magnetic field can be simplified by considering only the limit $r \to \infty$. In this limit, one can drop the second term in the 't Hooft field strength (2.73), such that $F_{\mu\nu} \xrightarrow{r\to\infty} \hat{\phi}^a G^a_{\mu\nu}$, and one can neglect the profile function $K(r)$, since it drops to zero exponentially fast as $r \to \infty$.

In particular, for higher-charged magnetic monopoles, the long-range field approximation is especially useful. As mentioned earlier, these configurations are not spherically symmetric at short distances, whereas their magnetic field becomes spherically symmetric asymptotically. Let us use the relation [29]

$$\varepsilon^{\mu\alpha\beta\gamma}\,\partial_\alpha F_{\beta\gamma} = -\frac{1}{g}\varepsilon_{abc}\,\varepsilon^{\mu\alpha\beta\gamma}\,\partial_\alpha\hat{\phi}^a\partial_\beta\hat{\phi}^b\partial_\gamma\hat{\phi}^c\,, \tag{2.78}$$

which is straightforward to prove by inserting equation (2.66). Notice that for $n > 1$ this relation is only an equality in the limit $r \to \infty$. The right-hand side is proportional to the topological current (2.49). Therefore, after integration, one obtains $Q_m = 4\pi n/g$. Hence, the asymptotic magnetic field of a magnetic monopole with arbitrary winding number n is given by

$$B_i \xrightarrow{r\to\infty} \frac{n}{g}\frac{\hat{n}^i}{r^2}\,. \tag{2.79}$$

2.3.5 Bogomol'nyi Bound and the BPS Magnetic Monopole

Let us now perform the Bogomol'nyi completion for the magnetic monopole energy, analogous to the case of vortices. The total static energy is given by equation (2.65). Completing the square yields

$$E = \int \mathrm{d}^3x\,\left(\frac{1}{2}(B_i^a - (D_i\phi)^a)^2 + B_i^a(D_i\phi)^a + \frac{\lambda}{4}(\phi^a\phi^a - v^2)^2\right). \tag{2.80}$$

The first term and the potential energy term are always positive. Therefore, the energy is bounded by

$$E \geq \int \mathrm{d}^3x\,|B_i^a(D_i\phi)^a| = \int \mathrm{d}^3x\,|\partial_i(\phi^a B_i^a)| = \frac{4\pi v}{g}|n|\,, \tag{2.81}$$

where we used the Bianchi identity. This bound is saturated in the BPS limit $\lambda \to 0$ (while keeping v fixed) [30, 47] and for

$$B_i^a = (D_i\phi)^a\,, \tag{2.82}$$

which is known as the BPS equation for the magnetic monopole. In this way, the second-order field equations are reduced to first-order differential equations. Notice that this equation makes it particularly clear that, in the BPS limit, the scalar force has the same magnitude as the magnetic force. This was first shown by Manton in 1977 [4]. Therefore, the force between two equally-charged BPS magnetic monopoles cancels.

In general, the mass of the monopole is given by

$$m_{\mathrm{M}} = f\left(\frac{m_h}{m_v}\right)\frac{m_v}{g^2}\,, \tag{2.83}$$

where $f(m_h/m_v)$ is a monotonically increasing function with the limits $f(m_h/m_v \to 0) = 1$ (BPS limit) and $f(m_h/m_v \to \infty) \approx 1.787$ [48].

2.3.6 Profile Functions

Inserting the magnetic monopole ansatz (2.67) into the field equations (2.63) and (2.64) results in second-order differential equations for the profile functions

$$H'' + \frac{2}{\tilde{r}}H' - \frac{2K^2H}{\tilde{r}^2} - \frac{m_h^2}{m_v^2}(H^2-1)H = 0\,, \tag{2.84}$$

$$K'' - \frac{K(K^2-1)}{\tilde{r}^2} - KH^2 = 0\,, \tag{2.85}$$

where $'$ denotes the derivative with respect to $\tilde{r} = m_v r$. The first observation is that the shape of the profile functions depends only on the parameter m_h/m_v. This is for the same reason as in the case of vortices. We start with three parameters, g, v, and λ. By a well-chosen rescaling of the fields, one parameter can be eliminated. A second parameter can be absorbed into the definition of length and time scales (here encoded in the dimensionless $\tilde{r}$).

The profile equations cannot, in general, be solved analytically. However, their structure already provides insight into the scaling behaviour. The equations show that K always decays exponentially fast to zero. For this reason, in the large $\tilde{r}$ limit, the coupling between K and H disappears in the scalar field profile equation. The potential term acts as a damping term, implying that H approaches 1 exponentially fast. The larger the damping factor m_h^2/m_v^2, the faster the scalar field profile H approaches unity, corresponding to the VEV. The exponential scaling starts at $r \sim m_h^{-1}$. Therefore, we can say that the scalar field interactions are only relevant for distances $r \lesssim m_h^{-1}$. Hence, well-separated magnetic monopoles interact only via magnetic interactions.

Physically, this can be interpreted as follows. Interactions mediated by a massive field are always exponentially suppressed. Here, the mediator of the scalar interaction is the Higgs boson with non-zero mass m_h. In contrast, since the photon in the theory is massless, the magnetic interaction is unsuppressed. In the limit of vanishing Higgs boson mass, $m_h \to 0$, corresponding to the BPS limit, the scalar interactions also become long-range. In the profile equations, this is reflected by the fact that the damping term disappears completely, resulting in a scalar field profile equation of $H'' + 2H'/\tilde{r} = 0$ for large $\tilde{r}$. This equation indicates a $1/r$ scaling. Consequently, in this limit the scalar interactions can compete with the magnetic interactions. As mentioned in the previous section, it turns out that the interactions have exactly the same magnitude, meaning that two magnetic monopoles of the same charge neither attract nor repel [4].

In the BPS limit an analytic solution for the profile functions exists. It is given by [47]

$$H(r) = \coth(m_v r) - \frac{1}{m_v r}\,, \tag{2.86}$$

$$K(r) = \frac{m_v r}{\sinh(m_v r)}\,. \tag{2.87}$$

These functions reflect the properties we have just discussed above. The profile functions for the BPS limit and for the value $m_h/m_v = 1$, which we will use often in this thesis, are shown in Figure 2.3.

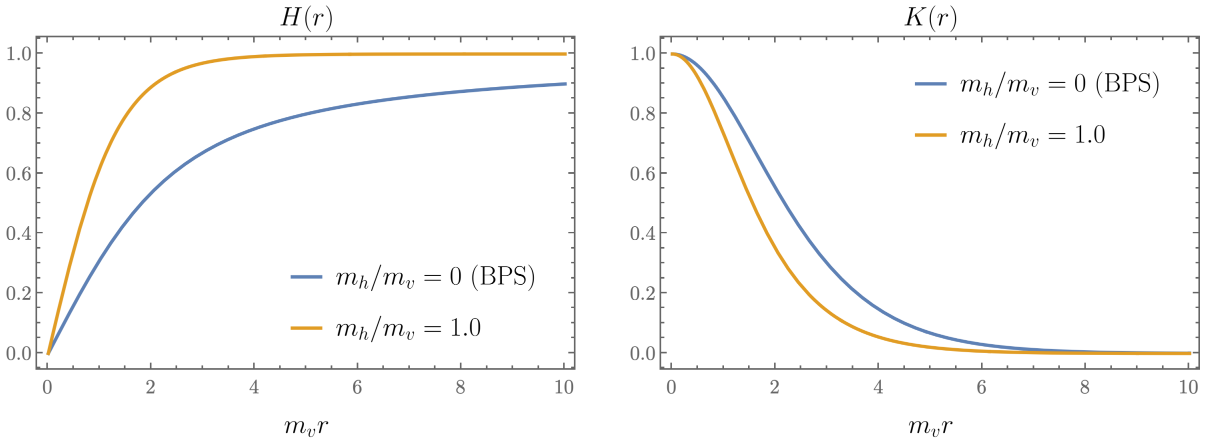

Figure 2.3: This figure shows the profile functions for the 't Hooft–Polyakov magnetic monopole. While the BPS solution is given by equations (2.86) and (2.87), the solution for $m_h/m_v = 1$ is obtained numerically using relaxation.

2.3.7 Julia–Zee Dyons

Before we finish the introduction to magnetic monopoles, we briefly mention monopoles that, in addition to magnetic charge, also carry electric charge, so-called dyons. In this section, we specifically introduce the Julia–Zee dyon [49]. The solution has the same ϕ^a and W_i^a structure as the 't Hooft–Polyakov magnetic monopole in equation (2.67), with the only difference being that the time component of the gauge field is no longer vanishing, but instead given by

$$W_t^a = v\,\frac{x^a}{r}J(r)\,, \tag{2.88}$$

where $J(r)$ is a profile function. This modification leads to the profile equations

$$H'' + \frac{2}{\tilde{r}}H' - \frac{2K^2H}{\tilde{r}^2} - \frac{m_h^2}{m_v^2}(H^2-1)H = 0\,, \tag{2.89}$$

$$K'' - \frac{K(K^2-1)}{\tilde{r}^2} - K(H^2-J^2) = 0\,, \tag{2.90}$$

$$J'' + \frac{2}{\tilde{r}}J' - \frac{2K^2J}{\tilde{r}^2} = 0\,. \tag{2.91}$$

As we can see from these equations, in contrast to the equation for H, the equation for J does not possess a damping term. Therefore, in the long-range limit, J always exhibits a $1/r$ scaling. This means that if $J \neq 0$, there will always be a long-range electric field given by

$$E_i = \hat{\phi}^a G^a_{0i} = -v\,\hat{n}^i J'(r) \xrightarrow{r\to\infty} \frac{Q_e}{4\pi}\frac{\hat{n}^i}{r^2}\,, \tag{2.92}$$

where Q_e is the electric charge of the dyon.

The electric charge depends on the asymptotic behaviour of the profile. It turns out that the maximal possible electric charge of the dyon is, in general, not arbitrarily large. This can again be seen from the profile equations. The equation for K contains a term proportional to $H^2 - J^2$. If this term changes sign, an exponentially growing mode appears, leading to an instability. Therefore, the function J is bounded from above by $J \leq H$. At small distances, both profile functions, H and J, increase linearly, and in the case of maximal charge these two functions are nearly identical. However, once the exponential scaling of H sets in at around $r \sim m_h^{-1}$, the functions begin to differ. This implies that the maximally allowed electric charge depends on the parameter m_h/m_v [50, 51].

In the BPS limit, $m_h \to 0$, the maximal electric charge becomes unbounded and can indeed be arbitrarily large. The solution to the profile equations in the BPS limit is given by [47, 24]

$$H(r) = \coth(\tilde{m}_v r) - \frac{1}{\tilde{m}_v r}\,, \tag{2.93}$$

$$K(r) = \frac{\tilde{m}_v r}{\sinh(\tilde{m}_v r)}\,, \tag{2.94}$$

$$J(r) = -\tanh(\alpha) H(r)\,, \tag{2.95}$$

where $\tilde{m}_v = m_v / \cosh(\alpha)$, and α is an arbitrary parameter. Notice that for $\alpha = 0$ we get again the BPS 't Hooft–Polyakov magnetic monopole profiles. The electric field of the BPS dyon is

$$E_i = \frac{\sinh(\alpha)}{g} \frac{\hat{n}^i}{r^2}\,, \tag{2.96}$$

and thus the electric charge is given by $Q_e = 4\pi \sinh(\alpha)/g$, which increases up to infinity as $\alpha \to \infty$. This limit corresponds to the case in which the profile function bound $J \leq H$ is saturated, i.e. the profile functions H and J become identical.

Physically, the existence of a maximal electric charge can be understood from the fact that an electric field above the Schwinger threshold, $|\boldsymbol{E}| \sim m_v^2/g$, leads to instabilities through W-boson pair production [49]. The Schwinger bound also explains why the maximal charge increases as m_h decreases. By a simple rescaling, one can express length and time units in terms of m_h^{-1} instead of m_v^{-1}. Then, decreasing m_h corresponds to increasing m_v. Consequently, the Schwinger threshold increases with increasing m_v, which agrees with the observation that the maximal electric charge grows with increasing m_v. The BPS limit then corresponds to $m_v \to \infty$. In this case, Schwinger pair production is fully suppressed, allowing for an arbitrarily large electric dyon charge.[8]

---

[8] The discussion on the maximal electric charge of the Julia–Zee dyon is not widely known, with most of the relevant information scattered across the papers [49, 50, 51]. The review presented in this section arose from work in collaboration with Giacomo Contri and Gia Dvali.

2.4 Virial Identities

In this section, we want to use energetic arguments to determine whether topological defects in a theory are allowed or not. These arguments are usually known under the name *Derrick's theorem* [52].

Let us first consider a global theory of the form

$$\mathcal{L} = \frac{1}{2}\partial_\mu \phi^a \partial^\mu \phi^a - V(\phi^a)\,, \tag{2.97}$$

where a runs over all scalar fields in the theory. The total static energy is then given by $E = T + U$, with

$$T = \int \mathrm{d}^d x\; \frac{1}{2}\partial_i \phi^a \partial_i \phi^a\,, \tag{2.98}$$

$$U = \int \mathrm{d}^d x\; V(\phi^a)\,, \tag{2.99}$$

being the gradient and potential energy, respectively, and d denotes the number of spatial dimensions. A soliton is stable if small deformations do not lead to configurations with lower energy. In particular, consider the so-called Derrick's scaling $\phi^a_{\mathrm{s}}(x) \to \phi^a_{\mathrm{s}}(\lambda x)$ of a soliton solution ϕ^a_{s}. The configuration at $\lambda = 1$ must then correspond to a minimum of the energy. Implementing this scaling in the total energy gives

$$E_\lambda = \lambda^{2-d}\, T + \lambda^{-d}\, U\,. \tag{2.100}$$

We can find the minimum by imposing that the derivative should be zero for $\lambda = 1$:

$$0 = \left.\frac{\mathrm{d}E_\lambda}{\mathrm{d}\lambda}\right|_{\lambda=1} = \Big((2-d)\,\lambda^{1-d}\, T - d\,\lambda^{-d-1}\, U\Big)\Big|_{\lambda=1}\,. \tag{2.101}$$

This results in the virial identity for global solitons

$$(2-d)\, T - d\, U = 0\,. \tag{2.102}$$

Now remember that $T, U \geq 0$. This implies that for $d > 2$ the only solution to the virial equation is $T = U = 0$. Hence, the configuration describes the trivial vacuum. For $d = 2$ the virial identity requires $U = 0$ and thus only configurations are allowed that carry solely gradient energy. Notice that for $d = 2$, global vortices that carry gradient but also potential energy can exist and are topologically stable. Homotopy arguments allow for such vortex solutions (see Appendix B), whereas the energetic arguments discussed here do not, since the energy of a global vortex is infinite. The only remaining possibility for global solitons with finite energy is therefore $d = 1$, for which one finds $T = U$. As we know, these solitons are domain walls, which are topologically stable and have finite energy.

We can repeat the calculations for a gauged theory with the Lagrangian

$$\mathcal{L} = -\frac{1}{4}F^b_{\mu\nu}F^{\mu\nu}_b + \frac{1}{2}\partial_\mu \phi^a \partial^\mu \phi^a - V(\phi^a)\,, \tag{2.103}$$

where a runs over all scalar fields and b runs over all gauge fields. The total static energy is now $E = G + T + U$, where

$$G = \int \mathrm{d}^d x \; \frac{1}{4} F_{ij}^b F_{ij}^b \, . \tag{2.104}$$

Then Derrick's scaling, $\phi_{\mathrm{s}}^a(x) \to \phi_{\mathrm{s}}^a(\lambda x)$ and $A_{\mathrm{s},\mu}^a(x) \to \lambda A_{\mathrm{s},\mu}^a(\lambda x)$, gives

$$E_\lambda = \lambda^{4-d}\, G + \lambda^{2-d}\, T + \lambda^{-d}\, U \, . \tag{2.105}$$

The minimisation of the energy now yields the virial identity

$$(4-d)\, G + (2-d)\, T - d\, U = 0 \, . \tag{2.106}$$

This relation shows that finite-energy configurations can also exist for $d = 2$ and $d = 3$, which is consistent with the existence of Nielsen–Olesen vortices and 't Hooft–Polyakov magnetic monopoles. For $d = 4$, the virial equation can only be satisfied if $T = U = 0$, while G may remain non-zero. The $G \neq 0$ case corresponds, for example, to Yang–Mills instantons in four Euclidean space-time dimensions. For $d > 4$, the virial identity is satisfied only by the trivial vacuum with $G = T = U = 0$.

In this section, we have seen that there are strong energetic constraints on the existence of solitons in a given theory. In addition to these energetic considerations, topology can tell us whether topological defects can exist. These topological aspects are typically discussed within homotopy theory. A brief introduction to this topic is provided in Appendix B.

Chapter 3

Dynamics of Topological Defects

So far we have considered topological defects as static configurations. However, they can of course also move. Their dynamics becomes particularly interesting when they collide with each other. In this chapter, the dynamics of such collisions will be introduced.

One long-term goal of magnetic monopole research is to understand their dynamics in the early Universe. This includes understanding how an entire system of magnetic monopoles behaves. In this chapter, we want in particular to understand what happens when monopoles collide with each other. However, the topological structure of magnetic monopoles is rather complicated compared to lower-dimensional defects such as vortices or kinks. For this reason, the dynamics of these lower-dimensional objects will be discussed first. It turns out that defects of different dimensionalities often share similar phenomena.

For instance, we will observe that in a head-on collision of a kink and an anti-kink, the pair can either annihilate and form a bound state or recreate after the collision. Which of these two outcomes occurs depends on the initial velocity and this dependence is chaotic. A similar chaotic behaviour can be observed in vortex–anti-vortex collisions.

Another example where the dynamics are similar for two different types of topological defects is the right-angle scattering for vortices and magnetic monopoles. Two vortices of the same charge scatter at 90° in a head-on collision. The same is true for magnetic monopoles.

Motivated by the considerations above, this chapter is structured as follows. First (Section 3.1), excitations of topological defects are introduced. It turns out that internal resonances of solitons play a crucial role in soliton collisions, as we will see throughout this chapter. Subsequently (Section 3.2), the dynamics of multi-kink configurations is discussed. In Section 3.3, the relativistic scattering of a vortex with an anti-vortex is discussed. In particular, we analyse the recreation and multi-bounce phenomena. Afterwards in Section 3.4, monopole–anti-monopole collisions are briefly presented.

Following the discussion of soliton–anti-soliton collisions, the focus turns to the scattering of solitons with the same charge. For this purpose, we first introduce the moduli space approximation (Section 3.5), which is required to understand multi-soliton dynamics from a topological point of view. Subsequently, the collision of multiple equally-charged vortices (Section 3.6) is presented. We first focus on simple, non-excited configurations and afterwards analyse collisions of excited vortices. Last but not least in Section 3.7, the dynamics of magnetic monopole collisions is presented.

3.1 Excited Topological Defects

In nature, solitons are never truly isolated objects. Interactions with their surroundings can significantly influence their dynamics. In particular, thermal and quantum fluctuations are expected to occur throughout space and can therefore interact with solitons. It turns out that solitons can possess resonance modes which may be excited by such fluctuations [53, 54]. Therefore, a full understanding of soliton dynamics requires understanding these modes.

To introduce these resonance modes, let us first discuss them in the context of ϕ^4 kinks, described by the Lagrangian given in equation (2.1) with the potential (2.2).[1] We begin by rescaling the field, $\phi \to v\phi$, and expressing all length and time values in units of m_h^{-1}. This yields

$$\mathcal{L} = v^2 m_h^2 \left(\frac{1}{2}(\partial_\mu \phi)^2 - \frac{1}{8}(\phi^2 - 1)^2 \right) . \tag{3.1}$$

The overall prefactor $v^2 m_h^2$ does not influence the classical dynamics, since it drops in the equation of motion

$$\partial_\mu \partial^\mu \phi + \frac{1}{2}(\phi^2 - 1)\phi = 0 . \tag{3.2}$$

The rescaling shows that all dynamical properties are fully encoded in this parameter-independent equation of motion. For different values of m_h, one can simply take the solutions of this equation and rescale back the dimensionful quantities accordingly.

We now consider small perturbations around the domain wall solution of the form

$$\phi = \phi_{\mathrm{DW}} + \xi\, f(x) \cos(\omega t) , \tag{3.3}$$

where $\xi \ll 1$ denotes the amplitude of the perturbation and ω is its frequency. Inserting this ansatz into the equation of motion and keeping only terms up to linear order in f gives

$$-\frac{\mathrm{d}^2 f}{\mathrm{d}x^2} + \frac{1}{2}\left(3\phi_{\mathrm{DW}}^2 - 1\right) f = \omega^2 f . \tag{3.4}$$

The frequency ω is given in units of m_h. Therefore, we do not expect long-lived excitations for $\omega > 1$, since at these frequencies the energy is high enough to radiate massive Higgs bosons. For $\omega < 1$, however, the equation admits two bound solutions. The first solution is given by

$$f_1 = \sqrt{\frac{3}{2}}\, \frac{\mathrm{d}\phi_{\mathrm{DW}}}{\mathrm{d}x} = \frac{\sqrt{3}}{2\sqrt{2}} \operatorname{sech}^2\left(\frac{x}{2}\right) , \tag{3.5}$$

---

[1] This example is a standard textbook example that is discussed in great detail in the books [26, 24].

for $\omega = 0$, where we applied the normalization condition

$$\int \mathrm{d}x \, f(x)^2 = 1 \,. \tag{3.6}$$

Since $\omega = 0$, this mode does not carry energy. It is a so-called zero mode, associated with a collective coordinate that describes the position of the domain wall. We will return to this mode in Section 3.5. For now, we focus only on the massive modes with $\omega \neq 0$.

The only massive bound mode for the kink is given by the solution

$$f_2 = \frac{\sqrt{3}}{2} \sinh\left(\frac{x}{2}\right) \operatorname{sech}^2\left(\frac{x}{2}\right) , \tag{3.7}$$

with frequency $\omega^2 = 3/4$. Analysing the time dependence of this solution shows that the mode corresponds to a wobbling of the kink. The kink energy density periodically spreads out and contracts. Note that in deriving equation (3.4) we assumed small amplitudes ξ and therefore neglected non-linear interactions. These non-linear effects couple the linear modes, for example the shape mode with the continuum spectrum, and thus lead to a slow decay of the mode over time. Nevertheless, the mode is very long-lived.

The shape and existence of a mode is strongly model-dependent. Here, we have analysed the ϕ^4 kink. For a different choice of the potential, the massive mode can have a different frequency or may disappear completely. For instance, in the ϕ^6 model [55] and in the Sine-Gordon model [56], the kinks possess only the zero mode and no massive bound modes. However, if one deforms these theories, massive modes can reappear [57, 58]. In the next section, we will see that these modes play a crucial role in the collision of multiple kinks.

Last but not least, one comment is worth mentioning that is relevant for moving kinks, or solitons in general. The frequency above corresponds to the mode frequency of a static kink. When the kink is Lorentz-boosted, due to time dilation, the frequency changes to ω/γ. We took this explicitly into account in the simulations presented in this thesis.

Let us now turn to Nielsen–Olesen vortices. The results on resonances of vortices presented in the following were obtained within the projects [59, 60] in close collaboration with Alberto Alonso-Izquierdo and Andrzej Wereszczynski. We adopt the conventions used in the Lagrangian (2.27). Performing the rescaling $x^\mu \to x^\mu/(gv)$, we find that the dynamical properties of the theory depend on a single parameter, which can be taken to be the Higgs mass $m_h = \sqrt{\lambda} v$. For different values of g and v, one can take the solutions of the rescaled Lagrangian and simply rescale back the dimensionful quantities accordingly. Thus, without loss of generality, we can set $g = 1$ and $v = 1$, so that the theory is fully parametrized by λ. In these conventions, the BPS limit is given by $\lambda = 1$.

To find a mode, we can follow the same procedure as for the ϕ^4 kink. First, we add perturbations to the vortex solution

$$\phi_{\mathrm{V}}(r,\theta,t) = H_n(r)\, e^{in\theta} + \xi\, f_n(r)\, e^{i\omega_n t}\, e^{in\theta} \,, \tag{3.8}$$

$$A_{\mathrm{V},\theta}(r,\theta,t) = n\frac{K_n(r)}{r} - \xi\, g_n(r)\, e^{i\omega_n t} \,, \tag{3.9}$$

where $f_n(r)$ and $g_n(r)$ are the profile functions of the modes and ξ denotes the amplitude.[2] Notice that the perturbed ansatz has to satisfy the Gauss constraint. Since we are working in the gauge $A_t = 0$, this leads to the so-called background gauge condition [63] for the fluctuations,

$$\partial_i(\delta A_i) - \frac{i}{2}(\phi_{\mathrm{V}}\,\delta\phi^* - \phi_{\mathrm{V}}^*\,\delta\phi) = 0\,. \tag{3.10}$$

We will discuss the background gauge in more detail in Section 3.5. Inserting the perturbed solution into the equations of motion (and imposing the background gauge) yields the following differential equations for the mode profile functions

$$-\frac{\mathrm{d}^2 f_n}{\mathrm{d}r^2} - \frac{1}{r}\frac{\mathrm{d}f_n}{\mathrm{d}r} + \left(\frac{n^2(1-K_n)^2}{r^2} + \frac{3\lambda}{2}H_n^2 - \frac{\lambda}{2}\right) f_n + \frac{2n}{r}(1-K_n)H_n g_n = \omega^2 f_n\,, \tag{3.11}$$

$$-\frac{\mathrm{d}^2 g_n}{\mathrm{d}r^2} - \frac{1}{r}\frac{\mathrm{d}g_n}{\mathrm{d}r} + \left(\frac{1}{r^2} + H_n^2\right) g_n + \frac{2n}{r}(1-K_n)H_n f_n = \omega^2 g_n\,. \tag{3.12}$$

Since the system of differential equations is linear, it can be solved numerically by reducing the equations to an eigenvalue problem. The method used to obtain the solutions is presented in Appendix A.2.3. In Figure 3.1, the solutions for the mode of the charge-1 vortex and the lowest mode of the charge-2 vortex for $\lambda = 1$ are shown. The mode profiles are normalized by

$$\int \mathrm{d}^2x\,\left(f(r)^2 + g(r)^2\right) = 1\,. \tag{3.13}$$

In the BPS limit, the frequencies of these two modes are $\omega_{10}^2 \approx 0.77788$ and $\omega_{20}^2 \approx 0.53898$, respectively.[3] The frequencies of the 1-vortex mode for other values of λ are illustrated in Figure 3.2. We observe that the frequency of the vortex mode grows with λ. For the charge-1 vortex, the frequency curve hits the continuum spectrum ($\omega^2 > 1$) at $\lambda \approx 1.5$. Above this value, there exist no massive bound modes.

It turns out, however, that in the regime where no massive bound modes exist, there can still be long-lived resonances. In particular, this becomes clear if we consider the limit $\lambda \to \infty$, which corresponds to the limit in which the vortex can be treated as a global vortex. It is known that the global vortex has infinitely many bound modes [64]. The transition from the gauge vortex without bound modes to the global vortex with bound modes can be understood as follows. Even if there are no bound modes, the modes do not necessarily vanish completely. Instead, there can be a half-bounded mode that lives only

---

[2] Notice that one can also consider fluctuations with a different scalar field structure. These modes have higher frequencies and are discussed in detail in [61, 62]. In this thesis, we focus only on the linear mode, which is the lowest (massive) frequency mode.

[3] The notation ω_{ni} is standard. The first index, n, denotes the winding of the vortex, while the second index, i, labels the non-degenerate modes of a charge-n vortex. The case $i = 0$ corresponds to the lowest mode. Notice that for $n > 1$, vortices also exhibit modes at higher frequencies [61, 62]. We will not consider them here.

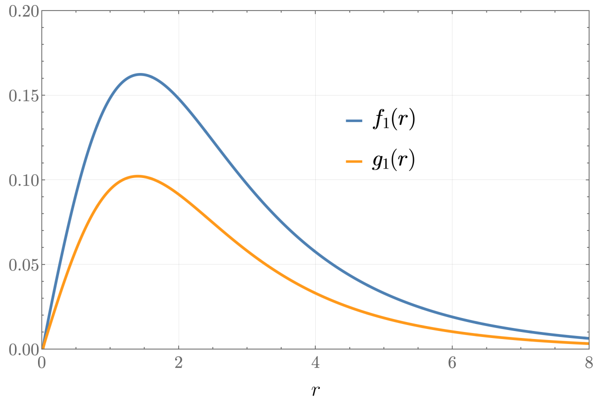

Figure 3.1: This plot shows the normalized mode functions for the charge-1 vortex (left) and the charge-2 vortex (right) in the BPS limit, $\lambda = 1$.

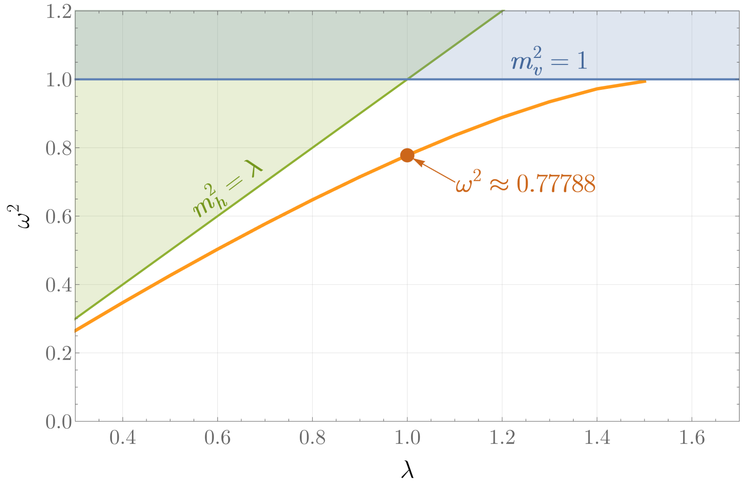

Figure 3.2: This figure shows the mode frequency of the charge-1 vortex for different values of λ.

in the scalar sector. The scalar field can still fluctuate with frequencies below the Higgs boson mass, $m_h = \sqrt{\lambda}$, but above the gauge boson mass threshold. These resonances are called Feshbach resonances [65] and are long-lived if the interaction between the scalar mode and the gauge sector is suppressed. Now, in the limit $\lambda \to \infty$, the gauge sector fully decouples, and thus the Feshbach resonances approach the bound modes of the global vortex.[4] We can approximately find such a Feshbach resonance mode by setting $g_n(r) = 0$

---

[4] These modes of the global vortex correspond to radial excitations and are entirely localized in the radial channel. It should be noted, however, that the global theory possesses a massless Goldstone degree of freedom. This degree of freedom corresponds to an angular channel with a mass threshold at $\omega = 0$. Therefore, more precisely, the modes of the global vortex should be interpreted as Feshbach resonances, since their frequency lies above the Goldstone boson mass threshold but below the Higgs boson mass threshold.

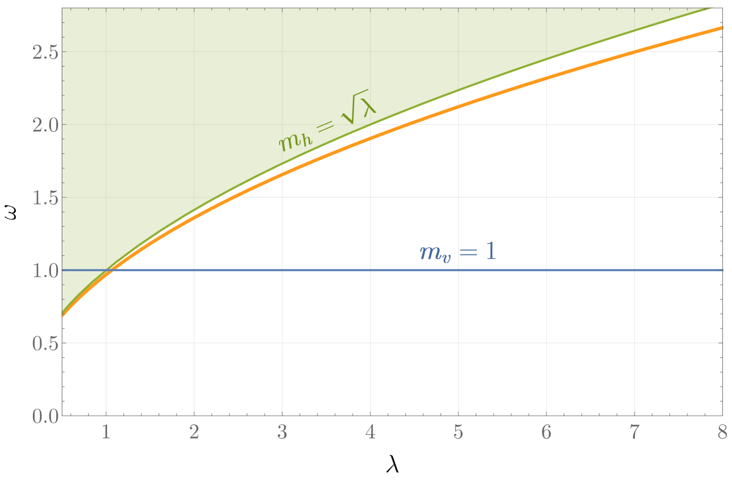

Figure 3.3: This figure shows the frequencies of the lowest Feshbach resonance of the charge-1 vortex for different values of λ.

in equation (3.11). This gives the equation

$$-\frac{\mathrm{d}^2 f_n}{\mathrm{d}r^2} - \frac{1}{r}\frac{\mathrm{d}f_n}{\mathrm{d}r} + \left(\frac{n^2(1-K_n)^2}{r^2} + \frac{3\lambda}{2}H_n^2 - \frac{\lambda}{2}\right) f_n = \omega^2 f_n\,, \tag{3.14}$$

which can be solved numerically. We find that there are indeed solutions with frequencies $\omega^2 < m_h^2$. The frequencies of the lowest 1-vortex Feshbach resonance for different values of λ are illustrated in Figure 3.3. We observe that the frequency increases with λ and remains close to the Higgs boson mass threshold, but never crosses it. In Section 3.3, we will find that such Feshbach modes can be excited in vortex–anti-vortex collisions.

The 't Hooft–Polyakov magnetic monopole does not possess true bound modes. This can be understood from the fact that after the symmetry breaking of the $SU(2)$ symmetry there is still a massless gauge field associated with the residual $U(1)$ symmetry. Therefore, the gauge field mass threshold is at $\omega = 0$. However, similarly to the vortex, there can be Feshbach resonances (very often also called quasi-normal modes), which decay faster than usual bound modes but are still long-lived [66, 67, 68, 69]. A long-term goal is to understand how these Feshbach resonances influence the dynamics of magnetic monopoles. As we will see in Section 3.6, excitations of modes on vortices influence the vortex dynamics significantly. In [70] it was suggested that the Feshbach resonances of magnetic monopoles will alter the monopole dynamics. Whether this indeed happens is an open question and needs to be confirmed numerically. In Section 3.7, we will study the collision of magnetic monopoles, which serves as a preparatory step for the collision of excited magnetic monopoles.

In this introductory section, it was shown that solitons can have long-lived resonances. It turns out that such modes play a crucial role in the dynamics of soliton scattering, as we will see in the next sections.

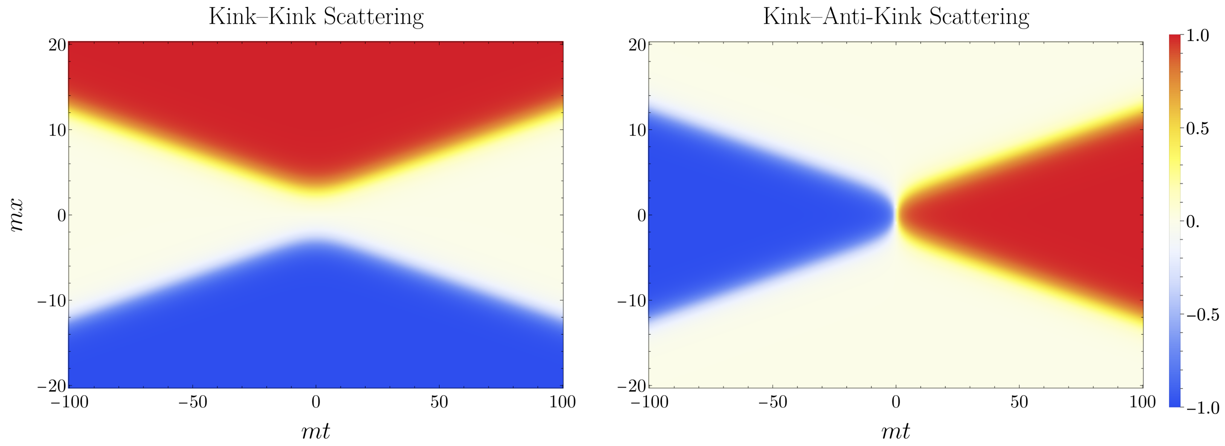

Figure 3.4: This figure shows the time evolution of a kink–kink collision (left) and a kink–anti-kink collision (right). In both cases, the initial velocities are chosen as $u = 0.1$. The colour scale represents the scalar field value ϕ.

3.2 Multi-Kink Dynamics

In this section, we focus on two types of domain walls, the Sine-Gordon kink and the ϕ^4 kink. The special feature of the Sine-Gordon model is that it is integrable. In particular, besides the single Sine-Gordon kink solution, multi-kink solutions are also known analytically [71, 24], some of which will be presented in the following. Let us begin with the kink–kink configuration. The solution is given by

$$\phi_{\mathrm{kk}}(x,t) = \frac{4m}{\sqrt{\lambda}} \arctan\left(u \frac{\sinh(\gamma m x)}{\cosh(\gamma m u t)} \right), \tag{3.15}$$

where $\gamma = 1/\sqrt{1-u^2}$ is the Lorentz factor corresponding to the velocity u. For $u \neq 0$, this solution describes two kinks located at the positions

$$x_{1,2} = \frac{\pm 1}{\gamma m} \operatorname{arcsinh}\left(\frac{1}{u} \cosh(\gamma m u t) \right). \tag{3.16}$$

One can show that the energy of this configuration is exactly twice the mass of the Sine-Gordon kink, $m_{\mathrm{DW}} = 2mv^2/\pi^2$, multiplied by the Lorentz factor, that is, $E = 2m_{\mathrm{DW}}\gamma$.

As time runs from $t < 0$ to $t = 0$, the two kinks approach each other until they collide around $t = 0$. At this moment, the configuration resembles a single kink of topological charge 2. When the system evolves further, $t > 0$, the kinks bounce back and move in opposite directions. This collision is elastic, since no kinetic energy is lost in the process. In Figure 3.4 (left), the time evolution of the kink–kink scattering is shown.

Another analytic solution of the Sine-Gordon model is given by

$$\phi_{\bar{\mathrm{k}}\mathrm{k}}(x,t) = \frac{4m}{\sqrt{\lambda}} \arctan\left(\frac{1}{u} \frac{\sinh(\gamma m u t)}{\cosh(\gamma m x)} \right), \tag{3.17}$$

which describes a kink–anti-kink configuration. For $m|t| \geq \mathrm{arcsinh}(u)/(\gamma u)$, the kinks are located at

$$x_{1,2} = \frac{\pm\mathrm{sign}(t)}{\gamma m} \operatorname{arccosh}\left(\frac{1}{u}\sinh(\gamma m u|t|)\right), \tag{3.18}$$

where the + sign corresponds to the anti-kink position and the − sign to the kink position. We observe that initially, for $t < 0$, the anti-kink is on the left (negative x) and the kink is on the right (positive x). At $t = 0$, they collide and the solution is given by $\phi_{\bar{\mathrm{k}}\mathrm{k}} = 0$, so that at this moment it seems that the kink–anti-kink pair is annihilated. The full potential energy disappears and the entire energy is given by the kinetic energy. As time evolves further, $t > 0$, the kinks reappear at the opposite sides and move apart. Overall, one can summarize that the kink and anti-kink pass through each other. In Figure 3.4 (right), the time evolution of the kink–anti-kink collision is illustrated.

Another solution that should be mentioned is the so-called breather solution. It can be obtained by the substitution $u \to is$ in equation (3.17), resulting in

$$\phi_{\mathrm{breather}}(x,t) = \frac{4m}{\sqrt{\lambda}} \arctan\left(\frac{1}{s}\frac{\sin(\tilde{\gamma} m s t)}{\cosh(\tilde{\gamma} m x)}\right), \tag{3.19}$$

where $\tilde{\gamma} = 1/\sqrt{1+s^2}$. This configuration is an oscillating solution with period $T = 2\pi/(\tilde{\gamma} m s)$. For $s \ll 1$, the configuration at $t = -T/2$ resembles that of a kink–anti-kink configuration. As time evolves from $t = -T/2$ to $t = 0$, these two kinks move towards each other until they “annihilate” at $t = 0$. Then, similarly to the kink–anti-kink case, they recreate and move apart again as if they pass through each other. However, at $t = T/2$, the velocity of the kinks becomes zero and they change their direction of motion. This process repeats periodically. The larger s is, the smaller the distance between the kink and the anti-kink at maximal separation and the larger the frequency of the oscillation is. For sufficiently large s, the two kinks do not fully separate and the configuration looks like an oscillating lump. In Figure 3.5, the time evolution for two different values of s is displayed.

The Sine-Gordon model is very special because it is integrable and therefore, there is no transfer of the energy to the continuous modes. As a result, analytic solutions describing collisions of multiple kinks are known and fully under control. In other theories, however, the situation changes completely. As an illustrative example, let us consider kink–anti-kink collisions in the ϕ^4 model. Such collisions were already studied in [72, 73, 74]. For a detailed review, the interested reader is referred to [75].

First of all, in the ϕ^4 model a kink–kink configuration does not exist, since there are only two vacua, $\langle\phi\rangle = \pm v$. A single kink solution is given in equation (2.5). An important advantage of this model is that the scalar field approaches its VEV exponentially fast, since the scalar degree of freedom is massive. Therefore, it is an excellent approximation to describe a kink–anti-kink configuration using, for instance, an additive ansatz [72] given by

$$\phi_{\bar{\mathrm{k}}\mathrm{k}} = v - \tanh\left(\frac{m_h}{2}\left(x + \frac{d}{2}\right)\right) + \tanh\left(\frac{m_h}{2}\left(x - \frac{d}{2}\right)\right), \tag{3.20}$$

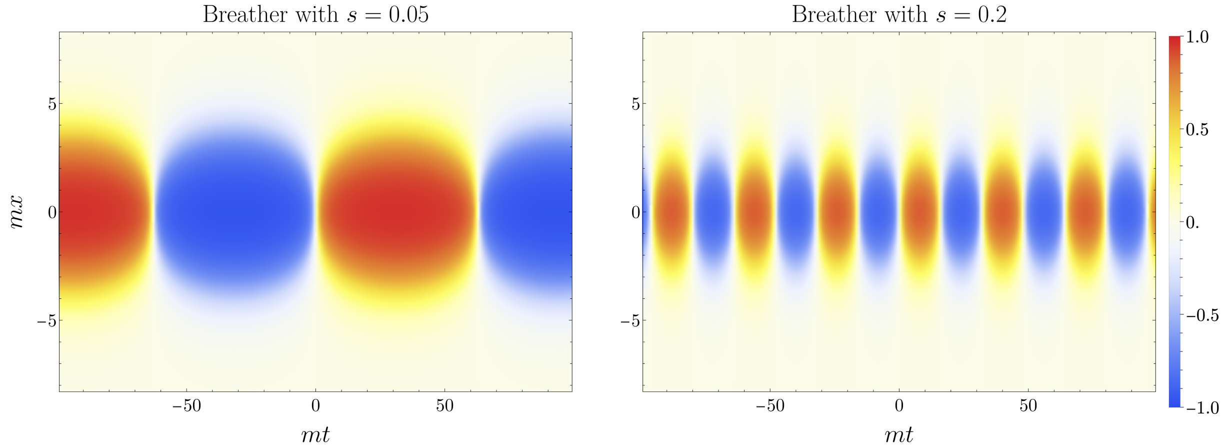

Figure 3.5: This figure shows the time evolution of the breather solution given in equation (3.19) for $s = 0.05$ (left) and $s = 0.2$ (right). The colour scale represents the scalar field value ϕ.

where d denotes the distance between the anti-kink at $x = -d/2$ and the kink at $x = +d/2$. To construct an initial configuration for a simulation, the two kinks can be Lorentz-boosted towards each other by replacing $x \pm d/2$ with $\gamma_{1,2}(x \mp u_{1,2} t \pm d/2)$, where u_1 (u_2) is the velocity of the anti-kink (kink), and $\gamma_{1,2}$ are the corresponding Lorentz factors. One finds that the outcome of the collision is highly sensitive to the initial velocity. For very low velocities, the kink–anti-kink pair annihilates and forms an oscillating bound state, the so-called bion (or oscillon). This bion is very similar to the Sine-Gordon breather solution (3.19) for large s. The difference is that the Sine–Gordon breather is stable and lives forever, whereas the bion decays very slowly. For very high velocities, $|u_{1,2}| \gtrsim 0.26$, the kink–anti-kink pair always recreates and the two solitons separate forever. In the intermediate velocity range, roughly between 0.1 and 0.26, the dynamics becomes much more chaotic. In this regime, a variety of outcomes can occur. The kinks may form a bion, but they can also bounce two, three, or more times before eventually separating. A summary of the possible scenarios is shown in Fig. 3.6, where the time evolution of the scalar field value ϕ at the origin is displayed for different initial velocities. One can clearly observe distinct windows in which the kinks undergo multiple bounces before separating, as well as regions in which a bionic bound state is formed.

The origin of such structures lies in the excitation of internal kink modes. In the previous section, we found that the ϕ^4 kink possesses a massive bound mode, which can be excited during a collision. Through the so-called resonant energy transfer mechanism [72, 73, 74, 76], energy is exchanged between the kinetic energy of the kinks and the energy stored in the internal degree of freedom, namely the massive bound mode. If not enough kinetic energy is transferred into the mode, the kinks can eventually overcome the attractive kink–anti-kink interaction barrier and re-emerge after the collision. In contrast, if too much kinetic energy is transferred into the mode, the kinks cannot overcome the barrier and eventually annihilate.

Although it is qualitatively understood that the origin of the multi-bounce windows

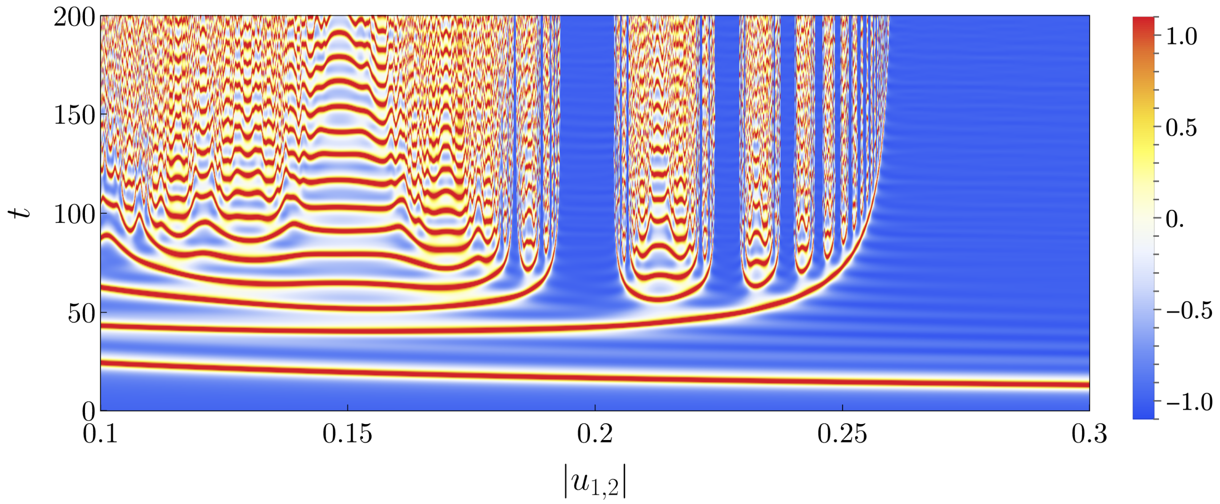

Figure 3.6: This figure shows the scalar field value ϕ/v at the origin ($x = 0$) for a colliding kink–anti-kink configuration as a function of time t, measured in units of m_h, for different initial kink velocities $u_{1,2}$. Initially, the scalar field is in the vacuum state $\phi = -v$. Whenever the kink and anti-kink overlap, the scalar field at the origin changes up to $\phi = v$. The initial distance between the kink and the anti-kink was chosen to be $d = 10\, m_h^{-1}$. The lattice properties and numerical details of the kink–anti-kink simulation are provided in Appendix A.

lies in the existence of an internal mode, the detailed structure of the resulting fractal pattern is not yet fully understood. For this reason, kink–anti-kink collisions remain an active area of research. For instance, relatively recently, an effective collective coordinate model for kink–anti-kink collisions in the ϕ^4 model was developed in [76], in which the mode amplitude is treated as an independent dynamical variable.

Furthermore, it is actively investigated how these patterns change for different scalar potentials. For example, as discussed above, the Sine-Gordon kink does not possess a massive bound mode and the theory is fully integrable. Consequently, such chaotic behaviour does not occur. However, for modifications of the Sine-Gordon model, these chaotic structures can reappear [77].

Multi-kink scattering and the appearance of multi-bounce windows have also been studied in ϕ^6 models [78, 79] and ϕ^8 models [80, 81]. In particular, kink–anti-kink collisions in the ϕ^6 model present an interesting case, since the ϕ^6 kink does not possess a shape mode [55]. Nevertheless, it turns out that the kink–anti-kink configuration supports bound modes that can be excited during the collision, leading to multi-bounce scattering [78].

In [82], more exotic modifications of scalar potentials are considered. The authors refer to these as *Frankensteinian potentials*. These potentials are non-smooth combinations of linear and quadratic functions that possess two discrete minima. The resulting kink solution, however, remains differentiable. Studying such models may provide further insight into which pieces of the potential are responsible for the emergence of the fractal structure.

3.3 Resonance Phenomena in Vortex–Anti-Vortex Collisions

Although some new aspects were added and discussions were rephrased, this section is an ad verbatim reproduction with respect to equations and figures of the paper "Resonance phenomena in vortex-antivortex collisions" [59] that I published with my collaborator Andrzej Wereszczynski.

In the previous section we discussed the appearance of multi-bounce windows in kink–anti-kink collisions. A natural question is whether similar multi-bounce patterns also arise for higher-dimensional solitons. In this section, we focus on Nielsen–Olesen vortices in the Abelian-Higgs model. Recently, it has been shown that the scattering of two BPS vortices [83, 84, 85] and three BPS vortices [86] can be strongly influenced by excitations of the vortex modes. In particular, in [83] it was demonstrated numerically that collisions of two initially excited vortices can lead to fractal chaotic patterns with multi-bounce right-angle scatterings.[5] The outcome of the scattering is highly sensitive to the collision velocity as well as to the initial amplitude and phase of the vortex excitations. The origin of this multi-scattering behaviour is similar to that in kink–anti-kink collisions. It can be understood in terms of a resonant energy transfer mechanism [84], in which energy is exchanged between the kinetic energy of the vortices and the energy of their internal excitations.

In this section, we do not focus on vortex–vortex collisions. Instead, we discuss vortex–anti-vortex collisions and show that the resonant energy transfer mechanism also plays a crucial role here. While it has long been known that a vortex–anti-vortex pair annihilates at low collision velocities and can recreate at high relativistic velocities [87], we demonstrate that the underlying pattern is far more non-trivial. In close analogy to kink–anti-kink collisions, we find that multi-bounce windows exist in vortex–anti-vortex scatterings.

3.3.1 Simulations of Vortex–Anti-Vortex Collisions

For our analysis of vortices, we use the Abelian-Higgs model in $2+1$ dimensions, described by the Lagrangian density given in equation (2.27) with $v = 1$ and $g = 1$. As an initial configuration for head-on vortex–anti-vortex scattering, we take the standard product ansatz [34]

$$\phi_{\text{v-av}}(t,x,y) = \phi_+(\gamma_1(x-u_1t-d/2),y)\cdot\phi_-(\gamma_2(x-u_2t+d/2),y)\,, \tag{3.21}$$

where ϕ_+ denotes the vortex solution (positive winding) Lorentz-boosted with velocity u_1, and ϕ_- the anti-vortex solution (negative winding) Lorentz-boosted with velocity u_2. The corresponding Lorentz factors are γ_1 and γ_2, and the separation between the vortices is given by d. Due to the exponential suppression of the gauge field outside the vortex core,

---

[5] The right-angle scattering of vortices will be discussed in more detail in Section 3.6.

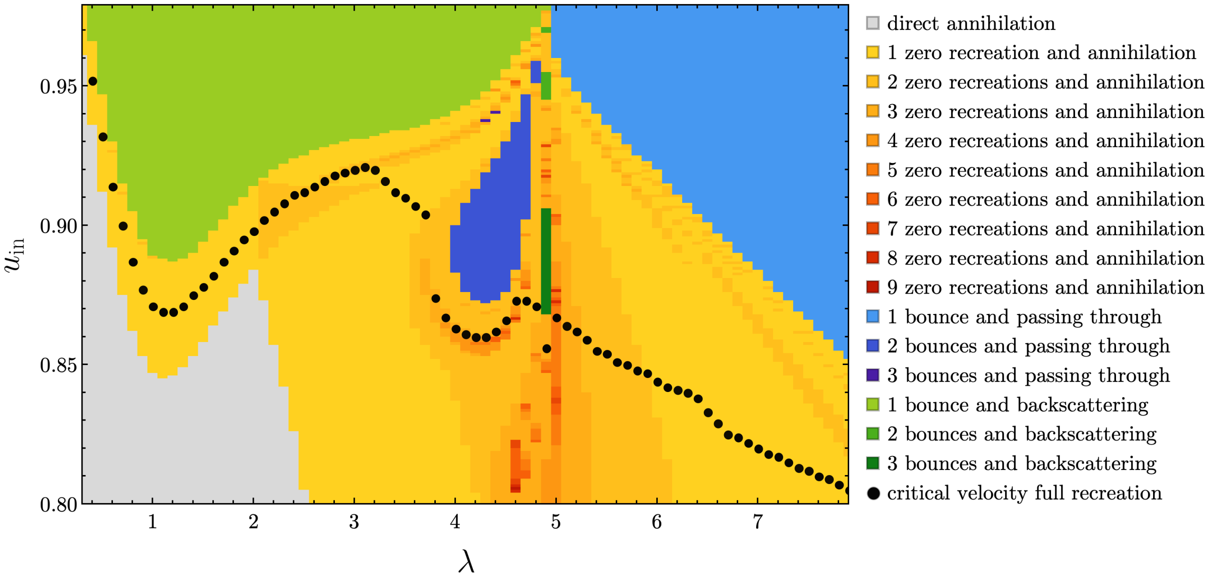

Figure 3.7: This figure summarizes the different final states that arise in vortex–anti-vortex collisions. The values of λ are shown on the x-axis, while the initial velocities are given on the y-axis.

an additive ansatz provides a good approximation,

$$A_\mu(t,x,y) = \begin{pmatrix} -u_1\gamma_1 A_x^+(\gamma_1(x-u_1t-d/2),y) \\ \gamma_1 A_x^+(\gamma_1(x-u_1t-d/2),y) \\ A_y^+(x,y) \end{pmatrix} + \begin{pmatrix} -u_2\gamma_2 A_x^-(\gamma_2(x-u_2t+d/2),y) \\ \gamma_2 A_x^-(\gamma_2(x-u_2t+d/2),y) \\ A_y^-(x,y) \end{pmatrix}, \tag{3.22}$$

where A^+ and A^- are the gauge field solutions of the vortex and anti-vortex, respectively.

For the numerical simulations presented in this section, we choose $d = 30$. We vary λ in the interval $[0.1, 8]$ with step size $\Delta\lambda = 0.1$. The initial velocities are scanned over the range $|u_1| = |u_2| \in [0.8, 0.98]$, using step sizes $\Delta u_1 = \Delta u_2 = 0.01$ for the results shown in Figure 3.7, and $\Delta u_1 = \Delta u_2 = 0.001$ for Figures 3.10, 3.10, and 3.11.

For the simulations, we use a slightly modified version of the second-order Runge–Kutta integration scheme (RK2), supplemented by natural boundary conditions and adiabatic damping near the boundaries. As a gauge-fixing condition, we choose the Lorenz gauge. Further details of the numerical methods are provided in Appendix A. As a lattice size we used 60×60 with spacing 0.05, and the time interval we investigated was $[0, 100]$ with time step 0.02.

The numerical results presented in this section are summarized in the following video: `https://youtu.be/1o__huMd13o`
The outcome of head-on vortex–anti-vortex collisions depends on both the value of λ and the collision velocity $u_1 = u_2$. By scanning over these parameters, we constructed the map shown in Figure 3.7 that summarizes the different possible outcomes of the collisions.

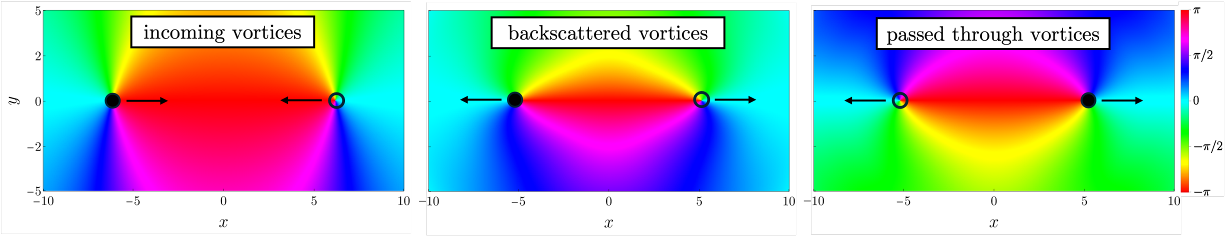

Figure 3.8: This figure illustrates the terms “backscattered vortices” and “passed through vortices”. The colour indicates the phase of the complex scalar field ϕ, while the circles mark the core positions of the vortex (filled circle) and anti-vortex (empty circle).

As already noted in [87], for collision velocities above a λ-dependent critical value, the vortices collide, recreate, and then separate forever. There are two possibilities, allowed by the system's symmetry, for how the vortices can recreate. On the one hand, they can backscatter, meaning that the vortex and anti-vortex leave the collision in the direction from which they initially came. On the other hand, they can pass through each other, meaning that they leave the collision in the opposite direction. This terminology is illustrated in Figure 3.8. We observe that there is a critical value at around $\lambda_{\mathrm{cr}} \approx 4.9$. Below this value, at high velocities, the vortices backscatter. This regime is illustrated by the large green region in the upper left of Figure 3.7. For $\lambda > \lambda_{\mathrm{cr}}$, the vortices pass through each other, as shown by the large blue region in the upper right of the map. This is also consistent with the observation that, in the global vortex–anti-vortex system (in the limit $\lambda \to \infty$), the zeros, although they never fully recreate and separate forever due to the strong attraction, always pass through each other at high velocities and never backscatter [88]. At $\lambda = \lambda_{\mathrm{cr}}$, the critical velocity for full recreation and separation has a local maximum.

Another possible outcome of the collision is annihilation. The corresponding regimes are illustrated by the gray, yellow, orange, and red regions in Figure 3.7. For $\lambda \lesssim 2$, the vortex and anti-vortex annihilate directly (gray region), even at relativistic initial velocities. There is only a small velocity window in which the vortices undergo a single bounce before annihilating. For very small values of $\lambda \lesssim 0.1$, which are not shown in the map, we observed the formation of an oscillon after annihilation. This type of oscillon is a flux-swapping oscillon, which has previously been observed in vortex–anti-vortex collisions in [89].

In the map we use the terms “bounce” and “zero recreation” to describe the reappearance of vortex zeros after they have disappeared for a short finite time. Zero recreation does not necessarily imply that the vortex and anti-vortex are fully recreated, since their overlap can still be large. We define full recreation as the stage at which the separation of the vortex zeros exceeds the vortex size $2R$, where R is the radius of a region around the zero that contains 90 percent of the static vortex energy. The critical velocity above which the vortices are fully recreated after the first bounce is indicated by the black dots in Figure 3.7. We observe that this velocity is very high for $\lambda \ll 1$, and that it has a local maximum around $\lambda \approx 3.2$. For larger values of λ, the critical velocity decreases. The

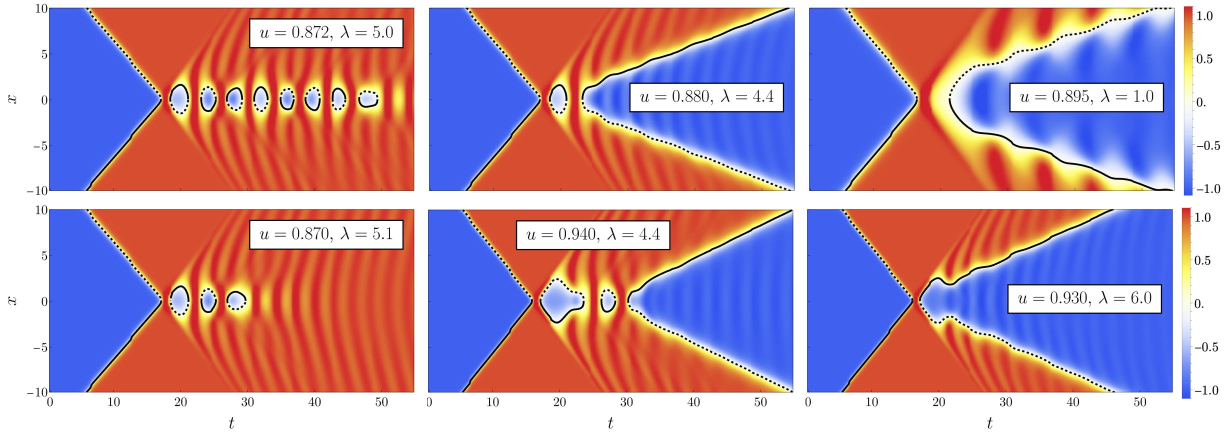

Figure 3.9: This figure shows the time evolution for several examples of vortex–anti-vortex scattering. The colour illustrates the real part of the scalar field, $\mathrm{Re}(\phi)$, along the x-axis. The solid and dashed lines represent the positions of the zeros of the vortex and anti-vortex, respectively.

reason why it increases for $\lambda \gtrsim 3.2$ lies in the appearance of Feshbach resonances, which will be discussed in Subsection 3.3.2.

The bounce window, which is narrow for $\lambda \lesssim 2$, increases by a lot for $\lambda \gtrsim 2$, and the recreation scenarios begin to dominate. For $\lambda < 4$, the possible outcomes are relatively simple. At sufficiently high velocities, the vortices backscatter and separate forever, at very low velocities (not shown in the map) the vortex–anti-vortex pair annihilates directly, and in between these two extremal regimes, they undergo one or two bounces before annihilation. For $\lambda \gtrsim 4$, the situation becomes much more complex. We observe that the vortices can bounce up to nine times before annihilation. In addition, new windows appear in which the vortices bounce up to three times and subsequently separate forever. These regions are indicated by darker blue and darker green colours in Figure 3.7. Figure 3.9 shows several examples of the scattering scenarios described above.

Analogous to Figure 3.6 for multi-bounce kink scattering, we can construct a similar plot for specific choices of λ. In Figure 3.10, we show the time evolution of the real part of the scalar field at the origin for different initial velocities. In this plot, the different bounce windows are clearly visible. There is a two-bounce window in the interval $u_{\text{in}} \in [0.8718, 0.9238]$ and a three-bounce window in $u_{\text{in}} \in [0.9397, 0.9409]$. Next to these windows are regions in which the vortex–anti-vortex pair annihilates. Thereby the vortices can undergo multiple bounces before annihilation.

In Figure 3.11, we show the case $\lambda = 4.9$. We find several distinct bouncing windows. In addition to the larger two- and three-bounce windows, there are smaller windows in which the vortices bounce and then separate. As before, these windows are next to regions where the vortices annihilate after multiple bounces. Note that for highly relativistic velocities, $u_{\text{in}} \gtrsim 0.95$, the lattice resolution may be insufficient to fully resolve the dynamics reliably.

Many of the outcomes observed in vortex–anti-vortex collisions are similar to those found in one-dimensional setups. The resulting fractal patterns closely resemble those seen

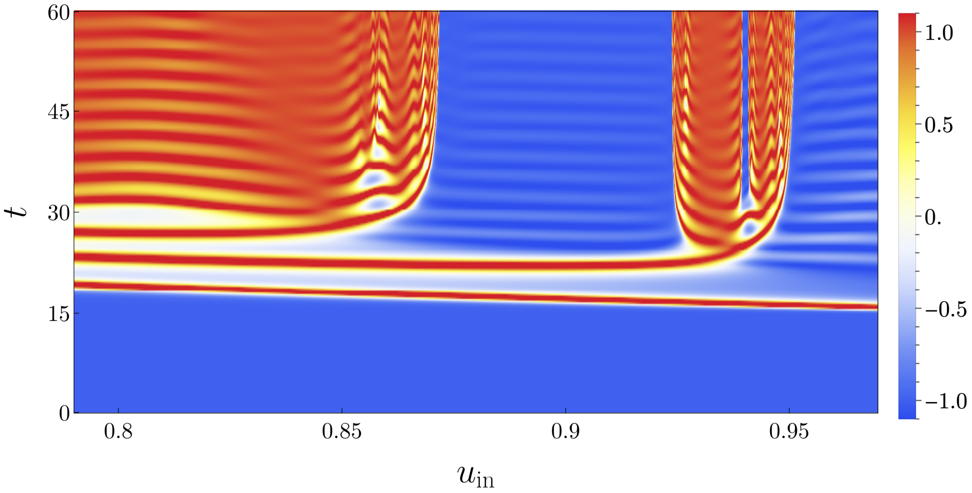

Figure 3.10: This figure shows the value of $\mathrm{Re}(\phi)$ at the origin as a function of time t and initial velocity u_{in} for $\lambda = 4.4$.

in kink–anti-kink collisions [72, 73, 74, 76], oscillon–oscillon collisions [90], and Q-ball–anti-Q-ball collisions [91].

3.3.2 Emergence of Resonances

The appearance of fractal patterns in soliton–anti-soliton collisions typically requires the presence of an internal mode that enables the resonant energy transfer mechanism. It is therefore surprising that, in vortex–anti-vortex collisions, multi-bounce windows emerge for $\lambda > 1.5$, a regime in which the Nielsen–Olesen vortex does not possess a massive bound mode. That the multi-bounce behaviour at large λ exists still due to the presence of some form of resonances can be seen from two observations.

First, for the case $\lambda = 4.4$, we measure the velocity of the recreated vortices in the bounce windows with final separation. The result is shown in Figure 3.12. As can be seen, the final velocity is clearly smaller than the initial velocity. This supports the picture of a resonant energy transfer mechanism, in which a part of the kinetic energy is converted into the energy of an internal mode.

Second, we also observe that the vortices are excited after the recreation, based on direct measurements. Due to the energy transfer, different contributions to the total energy of the system exhibit oscillatory behaviour. Using the numerical simulation data, we measure the total potential energy of the system as a function of time and extract the oscillation frequency from it. Since the accessible time interval is relatively short due to the high velocities of the recreated vortices and the limited lattice size, it is not feasible to perform a Fourier analysis of the oscillations. Instead, we determine the frequency by calculating the average time separation between two successive peaks of the potential energy. The results are shown in Figure 3.13.

We observe that for $\lambda \lesssim 1.5$, the frequency of the vortices agrees well with the frequency

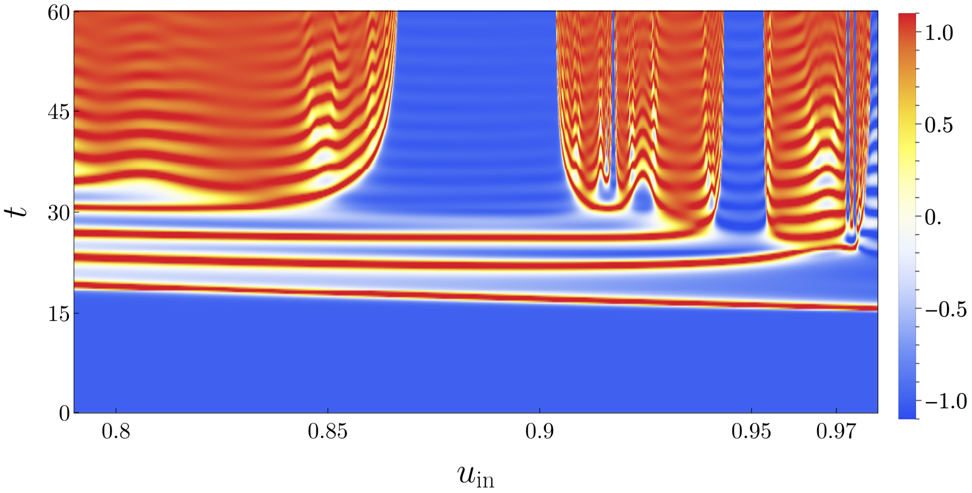

Figure 3.11: This figure shows the value of $\mathrm{Re}(\phi)$ at the origin as a function of time t and initial velocity u_{in} for $\lambda = 4.9$.

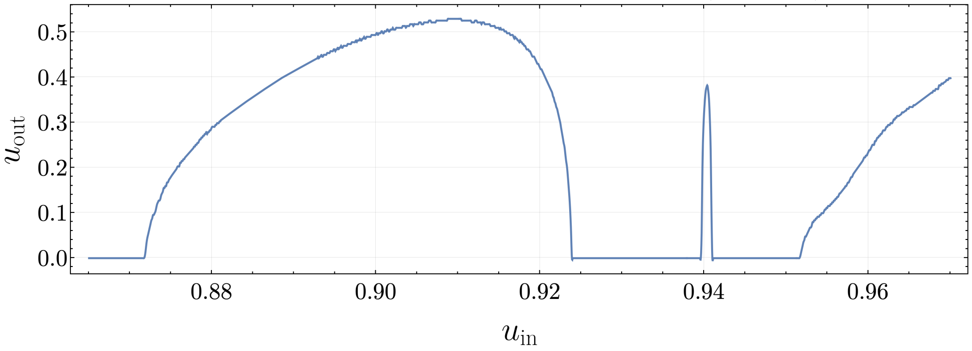

Figure 3.12: This figure shows the velocity of the recreated vortices with respect to the initial velocity u_{in} for the case $\lambda = 4.4$.

of the massive bound mode of the Nielsen–Olesen vortex. In the interval $\lambda \approx 1.7$ to $\lambda \approx 3.2$, the vortices after recreation exhibit only very weak oscillations, making it difficult to extract a reliable frequency. For $\lambda \gtrsim 3.2$, however, clear excitations become visible. This also explains why the critical velocity for full recreation, shown in Figure 3.7, decreases in this regime. The energy transfer mechanism turns on and allows for efficient recreation. For $\lambda \gtrsim 3.2$, we find that the observed frequencies lie well above the gauge boson mass threshold, but still below the scalar boson mass threshold. As discussed in Section 3.1, this is precisely the regime in which so-called Feshbach resonances can appear. In the discussion of the mentioned section, we neglected mixing terms between scalar and gauge field excitations for simplicity. The corresponding Feshbach resonance frequencies within this approximation are shown as the orange line in Figure 3.13. Within the uncertainties of our measurements and approximations, the agreement is very good. Therefore, we can conclude that the observed excitations of the recreated vortices are indeed Feshbach

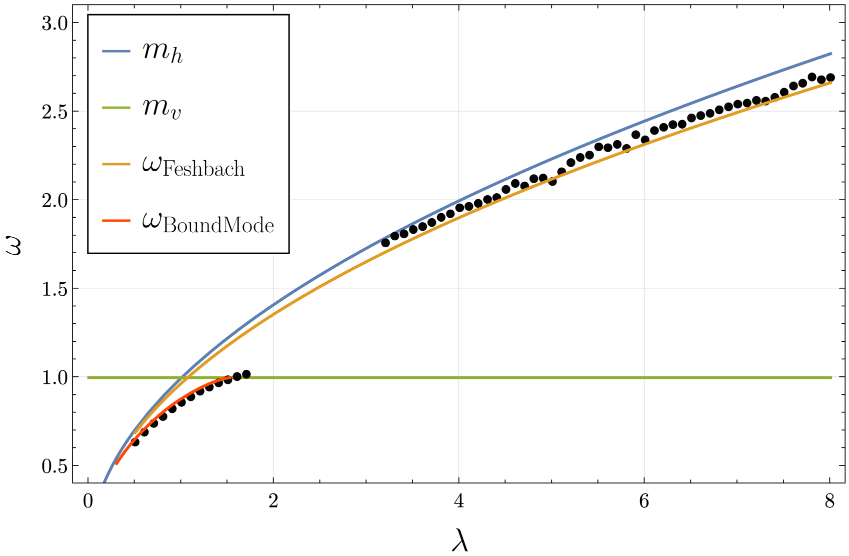

Figure 3.13: The black dots in this figure show the measured frequencies of the excited vortices after a one-bounce collision. The blue and green lines indicate the scalar and gauge mass thresholds, respectively. The red curve represents the frequency of the massive bound mode, while the orange line shows the approximate frequency of the Feshbach resonance.

resonances. We also find that these Feshbach resonances become longer-lived as λ increases. This can be understood from the fact that the gap between the scalar boson mass and the resonance frequency grows with λ. This observation is consistent with the fact that in the limit $\lambda \to \infty$, the vortices approach global vortices, which are known to possess massive long-lived modes.

3.3.3 Conclusion and Outlook

In this section, we have confirmed that the chaotic multi-bounce behaviour of solitons can arise for Nielsen–Olesen vortex–anti-vortex pairs. This addresses the long-standing question of whether the fractal pattern formation is unique to one-dimensional solitons such as kinks. With the example presented here, we clearly demonstrate that such a behaviour can also occur in theories with two spatial dimensions. A natural question that follows is whether a similar multi-bounce behaviour can also occur for magnetic monopole–anti-monopole pairs. So far such behaviour has not been observed. In the next section, we provide further discussion on this point.

A surprising observation from the simulations is that it seems that fractal patterns do not appear in the regime where the vortices possess massive bound modes, $\lambda \leq 1.5$. In this regime, we observe at most two recreations of the vortex zeros. In contrast, for $\lambda \gtrsim 4$, where no massive bound modes are present, multi-bounce behaviour emerges. This can be understood from the observation that the resonant energy transfer mechanism is driven by the Feshbach resonances of the vortices.

There are many possibilities what can be done next in this research direction. It is important to achieve a more fundamental understanding of the appearance of multi-bounce windows. This requires, first, further numerical investigations, and second, a more analytic treatment. For a more analytic understanding, it would be useful to develop a collective coordinate model, as has already been done for ϕ^4 kink–anti-kink collisions [76]. This is a highly non-trivial task, because, first, the model is more complex than the ϕ^4 model, and second, the multi-bounce windows appear in the highly relativistic regime. Therefore, Lorentz contractions have to be taken into account in the moduli space structure (a general discussion on the moduli spaces of solitons will be given later in this chapter).

Also numerically, there are many points that need to be explored in future studies. For example, it would be interesting to investigate collisions of a vortex and an anti-vortex when the vortices are already excited initially. Such an analysis is currently under investigation for ϕ^4 kink–anti-kink collisions [92]. It turns out that multi-bounce windows can be shifted to lower velocities. It would be interesting to see whether the same applies to vortices. Furthermore, it may happen that, due to an initial excitation, the resonant energy transfer mechanism becomes active even in the bound mode regime for $\lambda \lesssim 1.5$. In nature, initial excitations are very natural, since vortices can become excited through interactions with the background. This excitation can occur, for example, through thermal fluctuations or, as shown recently, through an oscillating background originating from an inflation field [93].

Within this thesis project, we focused on head-on collisions. A natural continuation of the analysis is to investigate small impact parameters. We performed first simulations and found that, for small impact parameters, recreation and bouncing are still feasible. All multi-bounce and recreation windows are, however, significantly deformed. For example, in the case with $\lambda = 1$ and a collision velocity of $u_{\text{in}} = 0.9$, the vortices end in annihilation for an impact parameter of $\Delta y = 1$, instead of backscattering as for $\Delta y = 0$.

Due to the non-zero angular momentum of configurations with non-zero impact parameter, we observe an additional new phenomenon. It seems that part of the angular momentum is transferred into an internal excitation of the vortex that carries angular momentum. For this to occur, it is not necessary for the vortex zeros to annihilate. It is sufficient that the vortices pass by each other at a small distance. This new type of vortex excitation, and its role in vortex collisions, requires further investigation and is left for future work.

Finally, it would also be interesting to explore whether such chaotic structure formation can appear in models beyond the Abelian-Higgs model. Simple modifications would include deformations of the potential. However, it would also be interesting to investigate whether multi-bounces occur for semi-local strings [94, 95], semi-global strings [96], or electroweak flux tubes [97]. Furthermore, one may wonder whether multi-bounce scattering can arise in cosmological setups. In particular, the multi-bouncing behaviour may be relevant for cosmic strings in $3 + 1$ dimensions.

3.4 Monopole–Anti-Monopole Collisions

In the previous sections, we discussed kink–anti-kink and vortex–anti-vortex collisions. A natural continuation is the study of monopole–anti-monopole collisions. It turns out that, apart from the simulations themselves, already the construction of the initial configuration for a monopole–anti-monopole system is more involved than for kinks and vortices. This has two main reasons. First, the topological structure is more complicated, as it is described by a three-component $SU(2)$ adjoint scalar field. Therefore, the standard product ansatz used for vortices cannot be applied to monopoles. Second, magnetic monopoles possess a long-range magnetic field. This implies that the gauge fields cannot simply be added together, as was done in the vortex case.

Fortunately, a monopole–anti-monopole configuration has already been constructed and analysed in a series of works [98, 99, 100, 101]. The corresponding scattering processes have also been studied numerically in [99, 101]. This section does not present major new results and partially reproduces the findings of these works. However, the monopole–anti-monopole ansatz exhibits several properties that will become relevant throughout this thesis, and therefore cannot be left unmentioned.

The monopole–anti-monopole ansatz is approximately given by [98, 99]

$$\begin{aligned}
\hat{\phi}_1 &= \big(\sin\bar{\theta}\cos\theta - \sin\theta\cos\bar{\theta}\cos\alpha\big)\cos\left(\varphi - \alpha/2\right) \\
&\quad + \sin\theta\sin\alpha\sin\left(\varphi - \alpha/2\right), \\
\hat{\phi}_2 &= \big(\sin\bar{\theta}\cos\theta - \sin\theta\cos\bar{\theta}\cos\alpha\big)\sin\left(\varphi - \alpha/2\right) \\
&\quad - \sin\theta\sin\alpha\cos\left(\varphi - \alpha/2\right), \\
\hat{\phi}_3 &= -\cos\theta\cos\bar{\theta} - \sin\theta\sin\bar{\theta}\cos\alpha\,,
\end{aligned} \tag{3.23}$$

where $\hat{\phi}^a = \phi^a/\sqrt{\phi^b\phi^b}$ and α is a relative twist angle. The monopole and anti-monopole are placed along the z-axis at the positions z_{M} and $z_{\bar{\mathrm{M}}}$, respectively. The angles θ and $\bar{\theta}$ denote the polar angles measured from the z-axis with respect to the monopole and anti-monopole positions. φ is the azimuthal angle around the z-axis. The final monopole–anti-monopole ansatz can be then written in form of a product ansatz of the profile functions

$$\phi^a = \frac{1}{g}\frac{H(r_{\mathrm{M}})}{r_{\mathrm{M}}}\frac{H(r_{\bar{\mathrm{M}}})}{r_{\bar{\mathrm{M}}}}\,\hat{\phi}^a, \tag{3.24}$$

$$W^a_\mu = -\frac{1}{g}(1-K(r_{\mathrm{M}}))(1-K(r_{\bar{\mathrm{M}}}))\,\varepsilon_{abc}\,\hat{\phi}^b\partial_\mu\hat{\phi}^c\,. \tag{3.25}$$

Here $H(r)$ and $K(r)$ are the profile functions for a single monopole. The radii r_{M} and $r_{\bar{\mathrm{M}}}$ are measured from the monopole core and anti-monopole core and are given by $r_{\mathrm{M}} = \sqrt{x^2 + y^2 + (z - z_{\mathrm{M}})^2}$ and $r_{\bar{\mathrm{M}}} = \sqrt{x^2 + y^2 + (z - z_{\bar{\mathrm{M}}})^2}$, respectively.

The relative twist parameter provides an additional degree of freedom, which can give rise to non-trivial phenomena, as we will see in this section. It ranges from zero twist, $\alpha = 0$, to maximal twist, $\alpha = \pi$. Let us first focus on the untwisted case. In this limit, the scalar field orientation reduces to

$$\begin{aligned}\hat{\phi}_1 &= \sin\left(\bar{\theta}-\theta\right)\cos\left(\varphi\right),\\ \hat{\phi}_2 &= \sin\left(\bar{\theta}-\theta\right)\sin\left(\varphi\right),\\ \hat{\phi}_3 &= -\cos\left(\bar{\theta}-\theta\right).\end{aligned} \tag{3.26}$$

In Figure 3.14 (left), we sketch the scalar field and the corresponding magnetic field of this configuration using a vector plot. The magnetic field lines exhibit the characteristic shape expected for a charge–anti-charge configuration. Note that this ansatz is only an approximation and requires numerical relaxation to obtain a configuration that solves the field equations. This has been carried out in [100]. However, for a qualitative analysis, this approximate ansatz is sufficient. We can now modify it by applying a Lorentz boost to the monopole and anti-monopole, allowing us to study their collisions, as it was done in [99, 101]. We reproduced these results using numerical simulations. Details of the numerical methods used here are provided in Appendix A. One improvement of our results compared to previous simulations lies in the efficiency of the numerical implementation. We observed that the monopole–anti-monopole configuration is axially symmetric. This symmetry can be used to solve the equations of motion in a single central plane. For monopoles, this approach was first used in simulations of monopole erasure in [102]. In this thesis, the method is extended to monopole–anti-monopole configurations. A detailed description of the method is given in Appendix A.6.

A few snapshots of the scattering are shown in Figure 3.15. We observe that when the monopole and anti-monopole collide, they annihilate, and their energy is radiated away from the collision point. The dominant radiation channel is electromagnetic radiation, as it corresponds to the massless photons. We considered collision velocities up to 0.98 and several values of m_h/m_v, and consistently found that the monopoles annihilate directly [6]. We never observed recreation like for kinks or vortices. It is possible that monopole–anti-monopole recreation does not occur at all. Although monopoles do not possess massive bound modes, they can exhibit long-lived Feshbach resonances [67]. In principle, this could enable a resonant energy transfer mechanism, which is essential for a multi-bounce behaviour. However, it may be that, for monopoles, recreation is strongly suppressed due to the dominance of radiation into massless photons[7]. From the vortex–anti-vortex simulations discussed in Section 3.3, we know that recreation typically occurs only at highly relativistic velocities. It is therefore possible that the velocities required for monopole–anti-monopole recreation are even higher and not accessible within our simulations. Further investigation in this direction is required and is left for future work.

---

[6] For the maximal velocities we have checked, the numerical accuracy may be problematic. We used a minimal lattice spacing of 0.034 and a time step of 0.0125, which provide good precision, but may still be insufficient.

[7] This is quite similar to the global vortex case, where massless Goldstone modes are present. It was found that, for a quartic potential, a global vortex–anti-vortex always annihilate, even at highly relativistic collision velocities [88].

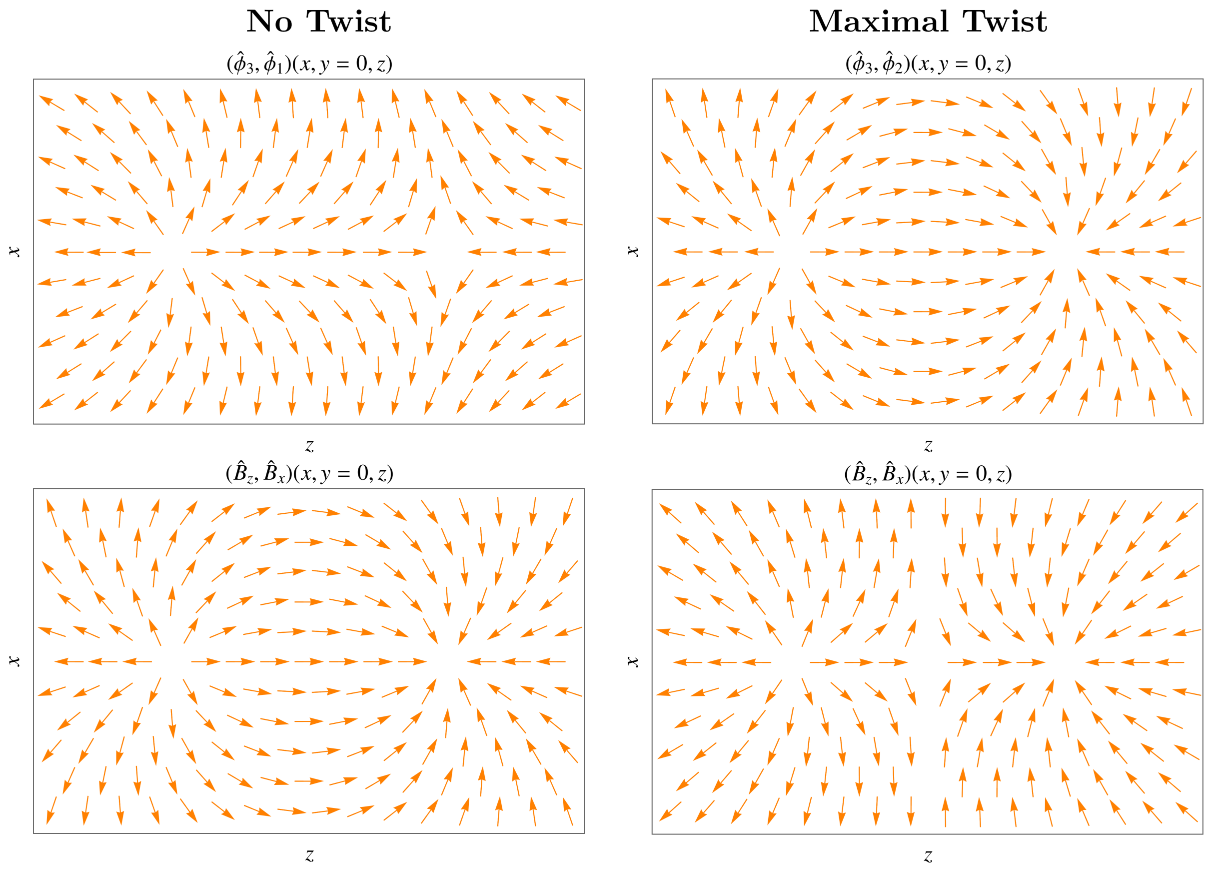

Figure 3.14: This figure shows the internal scalar field orientation and magnetic field in the $y = 0$ plane of a monopole–anti-monopole configuration for zero twist (left) and maximal twist (right).

Let us now turn to the maximally twisted scenario, $\alpha = \pi$. In this case, the scalar field orientation reduces to

$$\begin{aligned} \hat{\phi}_1 &= \sin\left(\bar{\theta} + \theta\right) \sin\left(\varphi\right), \\ \hat{\phi}_2 &= -\sin\left(\bar{\theta} + \theta\right) \cos\left(\varphi\right), \\ \hat{\phi}_3 &= -\cos\left(\bar{\theta} + \theta\right). \end{aligned} \tag{3.27}$$

The field vector and the corresponding magnetic field are sketched in Figure 3.14 (right). We observe that the magnetic field has a qualitatively different structure compared to the non-twisted case. Close to the monopole and anti-monopole, the field spreads radially outwards as usual. However, there is a plane exactly between the two objects where the magnetic field becomes parallel to this plane and the vectors flip by 180°. Note that this discontinuity is an artifact of the ansatz. After numerical relaxation, one can find that the actual solution of the field equations exhibits smoothly connected magnetic field lines [100], although the overall magnetic field is more spread compared to the untwisted case.

The maximally twisted configuration is a saddle point solution and corresponds to a so-called sphaleron [103]. It is unstable, since it has higher energy than the untwisted

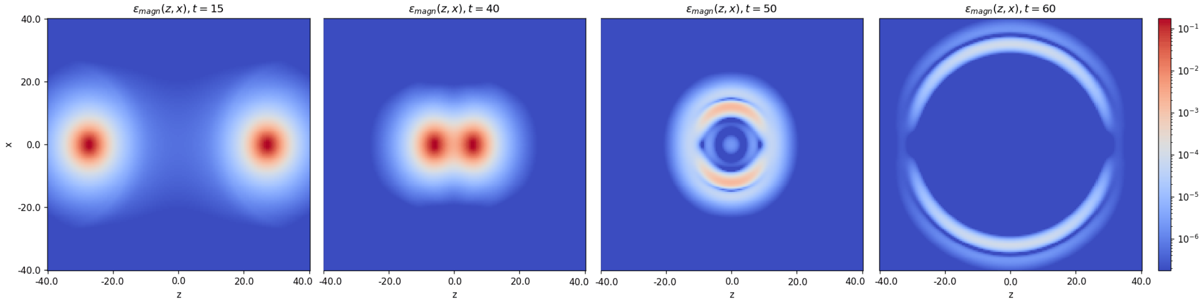

Figure 3.15: This figure shows four snapshots of the magnetic energy density in the $y = 0$ plane for a colliding monopole–anti-monopole pair. All time and length scales are given in units of m_v^{-1}. The energy density is expressed in units of m_v^4/g^2. We chose $m_h = m_v$, the initial separation distance was $d = 40\, m_v^{-1}$, and the initial velocities were $|u_{1,2}| = 0.4$. The numerical details for this simulation are given in Appendix A.

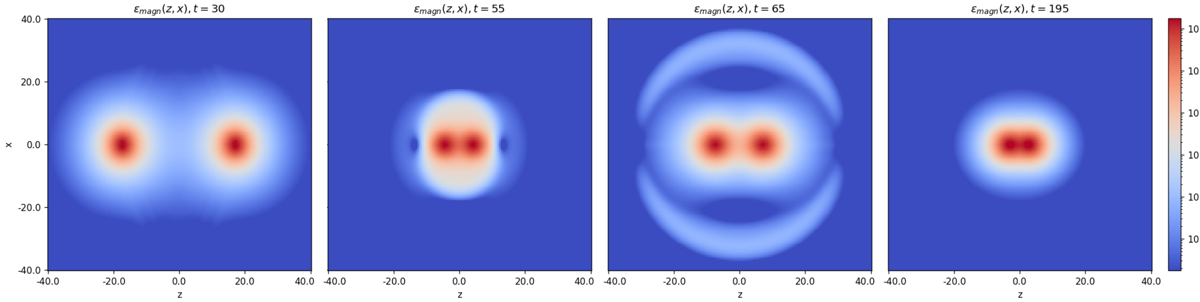

Figure 3.16: This figure shows four snapshots of the magnetic energy density in the $y = 0$ plane for a monopole–anti-monopole collision with maximal twist. The second and third frames show the configuration shortly after the first bounce. The last frame shows an almost static configuration, which formed after six bounces. The parameters for the simulation are the same as in Figure 3.15. The numerical details for this simulation are given in Appendix A.

configuration and there exists a smooth transition from $\alpha = \pi$ to $\alpha = 0$ [100]. The collision of a maximally twisted monopole–anti-monopole pair exhibits an interesting behaviour. Several time snapshots from our simulations are shown in Figure 3.16. When the monopole and anti-monopole collide, they do not annihilate. Instead, they bounce back and move apart. Subsequently, they are attracted again and bounce once more. This process repeats several times until the configuration relaxes to a static monopole–anti-monopole pair with a small separation distance (see the last frame of Figure 3.16). The backscattering behaviour was previously observed in [99]. However, no multi-bounce events were reported there. The reason we are able to observe them here is that, by employing the axial symmetry method in our simulations, the system remains perfectly axially symmetric, which typically is not true on fully three-dimensional lattices. In such cases, even small numerical fluctuations can already lead to untwisting.

It is also interesting to note that the twist can be related to a Chern–Simons number [104]. This opens up several directions for future studies. In particular, the untwisting process generates non-zero values of $G^a_{\mu\nu}\tilde{G}^{\mu\nu}_a$, where $\tilde{G}^{\mu\nu} = \frac{1}{2}\varepsilon^{\mu\nu\alpha\beta}G_{\alpha\beta}$ is the dual field strength. Its coupling to an axion could provide an axion production mechanism in the early Universe. Further investigations in this direction are planned for future work.

3.5 Moduli Space Approximation

In this section, the so-called *moduli space approximation* is introduced. This concept is essential for developing a clear intuition about what happens during multi-soliton collisions. In the previous sections, we discussed collisions between solitons and anti-solitons. From now on, we will restrict our attention to solitons of the same charge. In particular, this short section serves as a preparatory step towards understanding multi-vortex and multi-monopole collisions. This section follows the textbooks [25, 24, 26].

Let us first introduce the terminology by analysing the ϕ^4 kink solution (2.5). The solution contains a constant x_0, which represents the position of the domain wall. In this chapter, the position of the soliton is always defined as the point where the scalar field vanishes. For the domain wall this means that $\phi_{\mathrm{DW}}(x = x_0) = 0$. Changing x_0 leads to a translation of the kink, while the total energy remains unchanged. Parameters that describe different solutions which are degenerate in energy will be called *collective coordinates*. Therefore, x_0 is a collective coordinate of the domain wall. The space spanned by all collective coordinates is the so-called *moduli space*.

The *moduli space approximation* assumes that, for slow soliton motion, the field configurations are completely described by geodesics on the moduli space. Therefore, the geometry of this space contains all information about the dynamics of solitons in the non-relativistic (and unexcited) regime. In the case of the kink, there is one collective coordinate, which can take any real value. Hence, the moduli space is flat and is simply given by $\mathcal{M} = \mathbb{R}$.

Let us now introduce a time dependence of the collective coordinate, $x_0 = a(t)$. The scalar field configuration for a single kink is then given by $\phi(x,t) = \phi_{\mathrm{DW}}(x - a(t))$. Recall that for all choices of $a(t)$, the energy remains the same. Taking this into account, the action of the theory can be reduced to an effective action for a point particle:

$$S = \int \mathrm{d}t \, \left(\frac{1}{2} m_{\mathrm{DW}} \dot{a}(t)^2 - m_{\mathrm{DW}}\right), \tag{3.28}$$

where m_{DW} denotes the mass of the kink. This action shows that the kink behaves like a free point particle, which is reflected in the fact that the moduli space has no curvature.

A collective coordinate can always be related to a mode. To see this, let us proceed as in Section 3.1. For the ϕ^4 kink, we obtain the mode equation (3.4). Since $\phi_{\mathrm{DW}}(x - a)$ has the same energy as $\phi_{\mathrm{DW}}(x)$ for all values of a, there exists a mode

$$\delta\phi(x) = \left.\frac{\mathrm{d}\phi_{\mathrm{DW}}(x-a)}{\mathrm{d}a}\right|_{a=0} = -\frac{\mathrm{d}\phi_{\mathrm{DW}}(x)}{\mathrm{d}x}\,, \tag{3.29}$$

which does not carry any energy and therefore solves equation (3.4) with $\omega = 0$. This mode is called the *zero mode*. There is a one-to-one correspondence between collective coordinates and zero modes[8].

Let us apply this knowledge to the Nielsen–Olesen vortex. In this case we have one additional spatial dimension and thus two collective coordinates, a_x and a_y, corresponding to the position of the vortex. We can make the vortex solution time-dependent by writing

$$\phi(\boldsymbol{x}, t) = \phi_{\mathrm{V}}(\boldsymbol{x} - \boldsymbol{a}(t)) \approx \phi_{\mathrm{V}}(\boldsymbol{x}) - a_i(t)\, \partial_i \phi_{\mathrm{V}}(\boldsymbol{x})\,, \tag{3.30}$$

$$A_i(\boldsymbol{x}, t) = A_{\mathrm{V},i}(\boldsymbol{x} - \boldsymbol{a}(t)) \approx A_{\mathrm{V},i}(\boldsymbol{x}) - a_j(t)\, \partial_j A_{\mathrm{V},i}(\boldsymbol{x})\,, \tag{3.31}$$

where we assume small a_i. Notice that we can always apply a translation, $\boldsymbol{x} \mapsto \boldsymbol{x} + \delta\boldsymbol{x}$, to the solution. Therefore, even though we analyse small a_i, the result holds in general.

However, introducing this time dependence violates the Gauss constraint

$$\partial_i F_{i0} + \frac{ig}{2}\, \phi^*(D_0\phi) - \frac{ig}{2}\, \phi(D_0\phi)^* = 0\,, \tag{3.32}$$

which corresponds to the $\nu = 0$ component of the gauge field equation (2.29). To satisfy the constraint, the time-dependent solution requires

$$A_t(\boldsymbol{x}, t) = -\dot{a}_i(t)\, A_{\mathrm{V},i}(\boldsymbol{x})\,. \tag{3.33}$$

In order to work in time gauge, we perform an infinitesimal gauge transformation

$$\phi \mapsto \phi - i\alpha\phi\,, \qquad A_\mu \mapsto A_\mu - \frac{1}{g}\partial_\mu \alpha\,, \tag{3.34}$$

with $\alpha = -g\, a_i(t)\, A_{\mathrm{V},i}(\boldsymbol{x})$. This sets $A_t = 0$, and the time-dependent vortex configuration becomes

$$\phi(\boldsymbol{x}, t) = \phi_{\mathrm{V}}(\boldsymbol{x}) - a_i(t)\, (D_i\phi)^{(\mathrm{V})}\,, \tag{3.35}$$

$$A_i(\boldsymbol{x}, t) = A_{\mathrm{V},i}(\boldsymbol{x}) - a_j(t)\, F_{ji}^{(\mathrm{V})}\,, \tag{3.36}$$

where the label (V) indicates that the static vortex solution is inserted.

Let us now insert this into the kinetic energy of the system,

$$\begin{aligned} E_{\mathrm{kin}} &= \int \mathrm{d}^2x \left(\frac{1}{2}F_{0i}^2 + \frac{1}{2}|D_0\phi|^2\right)^{(\mathrm{V})} \\ &= \frac{1}{2}\left(\int \mathrm{d}^2x\, (F_{ik}F_{jk} + (D_i\phi)^*(D_j\phi))\right)^{(\mathrm{V})} \dot{a}_i\dot{a}_j \\ &= \frac{1}{2}\left(\int \mathrm{d}^2x \left(B^2 + \frac{1}{2}(D_k\phi)^*(D_k\phi)\right)\right)^{(\mathrm{V})} \dot{a}_i\dot{a}_i\,, \end{aligned}$$

---

[8] Notice that this statement applies to the (canonical) moduli space construction, where the moduli space is built from static solutions that are degenerate in energy. However, it is also possible to treat other quantities as collective coordinates that are not associated with zero modes. For example, in [76], the amplitude of the massive kink mode is treated as a collective coordinate.

where in the last step we used $F_{ij} = \varepsilon_{ij} B$, together with the rotational symmetry of the vortex solution. In particular, under a 90° rotation we can replace $D_x \to D_y$ and $D_y \to -D_x$ without changing the value of the integral. Using the virial identity (2.106) for vortices finally yields

$$E_{\text{kin}} = \frac{1}{2} m_{\text{V}}\, g_{ij}\, \dot{a}_i \dot{a}_j \,, \tag{3.37}$$

where m_{V} denotes the vortex mass and $g_{ij} = \delta_{ij}$. Since the metric is simply the identity, the moduli space of a single vortex is flat. This means that the vortex can be treated as a point-like particle moving with velocity $\dot{\boldsymbol{a}}$.

Finally, let us briefly comment on the translational zero modes of the vortex. As seen above, there are infinitely many ways to construct the time-dependent vortex solution due to the gauge invariance of the theory. Consequently, there are also infinitely many possible representatives of the translational zero modes. Strictly speaking, this originates from the fact that gauge invariance itself generates a zero mode. A gauge transformation is a symmetry of the theory and therefore leaves the energy unchanged. However, all gauge-transformed configurations are physically equivalent, and we therefore exclude them from the moduli space. This is achieved by fixing the gauge through an appropriate gauge condition. Since the standard vortex solution satisfies $A_t = 0$, it is natural to require that the zero mode has a vanishing time component of the vector field, as already imposed in equations (3.35) and (3.36). Equivalently, we can demand that the zero modes satisfy the background gauge condition given in equation (3.10). The translational zero modes are thus given by

$$\delta_i \phi = -(D_i \phi)^{(\text{V})} \,, \qquad \delta_i A_j = -F_{ij}^{(\text{V})} \,. \tag{3.38}$$

Last, the same analysis can be applied to the 't Hooft–Polyakov magnetic monopole. The background gauge condition is now given by

$$(D_j^{(\text{M})}(\delta_i W_j))^a + g\, \varepsilon_{abc}\, \phi_{\text{M}}^b\, \delta_i \phi^c = 0 \,. \tag{3.39}$$

The translational zero modes satisfying this gauge condition are then given by

$$\delta_i \phi = -(D_i \phi)^{a,(\text{M})} \,, \qquad \delta_i W_j^a = -G_{ij}^{a,(\text{M})} \,. \tag{3.40}$$

We can again compute the kinetic energy, and simplify the resulting expression by using that the monopole solution is spherically symmetric,

$$\begin{aligned} E_{\text{kin}} &= \int \mathrm{d}^3 x \left(\frac{1}{2} G_{0i}^a G_{0i}^a + \frac{1}{2} (D_0 \phi)^a (D_0 \phi)^a \right)^{(\text{M})} \\ &= \frac{1}{2} \left(\int \mathrm{d}^3 x \left(G_{ik}^a G_{jk}^a + (D_i \phi)^a (D_j \phi)^a \right) \right)^{(\text{M})} \dot{a}_i \dot{a}_j \\ &= \frac{1}{2} \left(\int \mathrm{d}^3 x \left(\frac{1}{3} G_{jk}^a G_{jk}^a + \frac{1}{3} (D_j \phi)^a (D_j \phi)^a \right) \right)^{(\text{M})} \dot{a}_i \dot{a}_i \,. \end{aligned}$$

Using the virial identity (2.106) for magnetic monopoles results in

$$E_{\text{kin}} = \frac{1}{2} m_{\text{M}}\, \tilde{g}_{ij}\, \dot{a}_i \dot{a}_j \,, \tag{3.41}$$

where m_{M} is the monopole mass and $\tilde{g}_{ij} = \delta_{ij}$.

In addition to the translational zero modes, there is another mode corresponding to global $U(1)$ transformations

$$\phi_{\text{M}} \mapsto U \phi_{\text{M}} U^\dagger \,, \tag{3.42}$$

$$W_{\text{M},\mu} \mapsto U W_{\text{M},\mu} U^\dagger + \frac{i}{g} U \partial_\mu U^\dagger \,, \tag{3.43}$$

with $U = \exp(i\alpha\phi^a_{\text{M}}/v)$. Notice that under this transformation ϕ_{M} remains unchanged. The only change is in δW^a_i, which is given by

$$\delta W^a_i = \frac{1}{gv} \alpha(t) (D_i\phi)^{(\text{M}),a} \,. \tag{3.44}$$

By promoting α to be time-dependent, we get an additional contribution to the kinetic energy

$$\Delta E_{\text{kin}} = \frac{1}{2} \frac{\dot{\alpha}^2}{v^2 g^2} \left(\int \mathrm{d}^3x \; (D_i\phi)^a (D_i\phi)^a \right)^{(\text{M})} \,, \tag{3.45}$$

which in the BPS limit simplifies to

$$\Delta E_{\text{kin}} = \frac{1}{2} \frac{m_{\text{M}}}{v^2 g^2}\, \dot{\alpha}^2 \,. \tag{3.46}$$

Therefore, the full moduli space metric is $g_{ij} = \text{diag}(1,1,1,g^{-2}v^{-2})$. The moduli space itself has the structure

$$\mathcal{M} = \mathbb{R}^3 \times S_1 \,, \tag{3.47}$$

where S_1 corresponds to the collective coordinate α, which ranges from 0 to 2π.

This new collective coordinate has a very special meaning. This becomes apparent when we analyse the electric field of the configuration,

$$E_i \xrightarrow{r\to\infty} \hat{\phi}^a G^a_{i0} = \frac{\dot{\alpha}}{vg} \hat{\phi}^a (D_i\phi)^a \,. \tag{3.48}$$

In the BPS limit, this simplifies to

$$E_i \xrightarrow{r\to\infty} \frac{\dot{\alpha}}{vg} B_i \,. \tag{3.49}$$

We observe that for $\dot{\alpha} \neq 0$, an electric field is generated that is proportional to the magnetic field of the monopole. Therefore, exciting the S^1 zero mode corresponds to giving the magnetic monopole an electric charge. This configuration is the Julia–Zee dyon [49].

So far, we have considered only single solitons. For all three types of solitons discussed above, the moduli space is flat. This, however, changes once multiple solitons are taken into account. This will be discussed for vortices and monopoles in the next two sections.

3.6 Collision of Vortices with the Same Charge

Although some new aspects were added and discussions were rephrased, this section is an ad verbatim reproduction with respect to equations and figures of the paper "From BPS geodesics to mode-driven dynamics in the scattering of multiple BPS vortices" [60] that I wrote with my collaborators Alberto Alonso Izquierdo and Andrzej Wereszczynski.

So far, we have mainly focused on soliton–anti-soliton collisions. For the rest of this chapter, we turn our focus to interactions between solitons of the same charge. We begin with the Nielsen–Olesen vortices of the Abelian-Higgs model, described by the Lagrangian (2.27). It is well-known that two vortices of the same charge repel for $\lambda > 1$ and attract for $\lambda < 1$. In the BPS limit, $\lambda = 1$, all long-range interactions between equally charged vortices cancel [34]. Due to the absence of such forces, the moduli space approximation can be used to determine vortex trajectories by identifying geodesics on the moduli space [8]. In particular, this explains the well-known right-angle scattering observed in head-on collisions of two vortices [105, 106].

Recently, it has been found that BPS geodesic motion on the moduli space can be significantly modified when vortices are initially excited [83, 84, 85]. The underlying mechanism is the emergence of a mode-generated force. In particular, the lowest mode of a vortex–vortex configuration induces an attractive force. This can result in multiple right-angle scatterings, as observed numerically in [83]. A similar behaviour has also been shown for the collision of three vortices [86].

In all cases studied in the mentioned works, the motion was confined to the geodesic of the moduli space corresponding to the unexcited system. While the dynamics may proceed back and forth along this geodesic, the geodesic itself is not deformed. This can be understood from the enhanced symmetry of the configurations considered. In this section, we also investigate less symmetric configurations and show that, in such cases, excitations of internal modes can indeed deform the BPS geodesic.

The structure of this section on multi-vortex collisions is as follows. In Section 3.6.1, we review the moduli space structure for two vortices, and in Section 3.6.2, we summarise the current understanding of collisions of two excited vortices. We then turn to the charge-3 sector. In Section 3.6.3, we analyse the geodesic motion, and in Section 3.6.4, we study the role of excitations. The same program is carried out for the charge-4 sector in Sections 3.6.5 and 3.6.6.

3.6.1 Moduli Space Structure for Two Vortices

This subsection follows the explanations of [25]. We observed already that a single vortex has two collective coordinates corresponding to its position. When we add a second vortex, the number of collective coordinates can increase, since both vortices can in principle be placed at arbitrary positions. However, recall that collective coordinates parametrize configurations that are degenerate in energy. For two vortices, their separation distance is a true collective coordinate only in the BPS limit, $\lambda \to 1$, because in this limit the interaction energy between them vanishes. For $\lambda \neq 1$, there is a force between the vortices, so changing the distance between them changes the energy. Notice that the force between two vortices may violate the requirement of the moduli space approximation that solitons move slowly. Furthermore, the moduli space approximation cannot be applied to vortex–anti-vortex configurations, since there is always an attractive force between them. In the following, we restrict our analysis to the BPS case, in which the two-vortex configuration is described by four collective coordinates.

Let us denote the positions of the vortices by two complex numbers z_1 and z_2, such that the vortices are located at $(\mathrm{Re}(z_1), \mathrm{Im}(z_1))$ and $(\mathrm{Re}(z_2), \mathrm{Im}(z_2))$. If we then parametrize the positions according to $z_1 = z_\mathrm{c} + w$ and $z_2 = z_\mathrm{c} - w$, where z_c denotes the centre-of-mass coordinate, the metric of the moduli space can be written as

$$\mathrm{d}s^2 = \mathrm{d}z_\mathrm{c}^* \, \mathrm{d}z_\mathrm{c} + f(w, w^*) \, \mathrm{d}w^* \, \mathrm{d}w \, . \tag{3.50}$$

Notice that the centre-of-mass term in the metric has no position-dependent prefactor, since changing z_c simply corresponds to moving around the full two-vortex configuration. The w term in the metric, however, requires a position-dependent prefactor $f(w, w^*)$, because for small w the two vortex cores overlap, and the vortices can no longer be treated as two separate point-like particles.

Let us reduce our analysis to the centre-of-mass frame. There the system is invariant under rotations. Therefore, the prefactor f depends only on one parameter, which is given by the distance between a vortex and the centre of mass, $\rho = |w|$. The moduli subspace metric reduces to

$$\mathrm{d}\tilde{s}^2 = f^2(\rho) \left(\mathrm{d}\rho^2 + \rho^2 \mathrm{d}\varphi^2 \right) , \tag{3.51}$$

where φ is the polar angle.

Note that the two vortices are indistinguishable. Hence, the two-vortex configuration is symmetric under exchanging them, which corresponds to $w \to -w$, or equivalently $\varphi \to \varphi + \pi$. This symmetry must be taken into account in describing the moduli space. As a result, φ only ranges from 0 to π. Thus, the half-plane spanned by r and φ is sufficient to describe the positions of both vortices. The two lines extending from $\rho = 0$ to $\rho \to \infty$ at $\varphi = 0$ and $\varphi = \pi$ represent the same configurations. Therefore, the half-plane should be "glued" along these two lines, which leads to a moduli space with the structure of a cone. A more detailed analysis of the function $f(r)$ shows that the tip of this cone is not sharp but rounded [106]. The appearance of the cone is illustrated schematically in Figure 3.17.

The motion of the vortices is then described by geodesics on the cone. The simplest geodesic is the one that passes directly through the tip of the cone. Translating this trajectory back to the position space of the vortices shows that the vortices scatter at a right angle (see Figure 3.18) [106].

This behaviour was numerically confirmed in [105, 107]. We reproduce these results using the multi-vortex ansatz of [34], which corresponds to the configurations in equations (3.21) and (3.22) with ϕ_- and A_μ^- replaced by ϕ_+ and A_μ^+, respectively. The result of the simulation is shown in Figure 3.19. Initially, the vortices move towards each other along the x-axis. When they meet at the origin, they form a charge-2 vortex configuration,

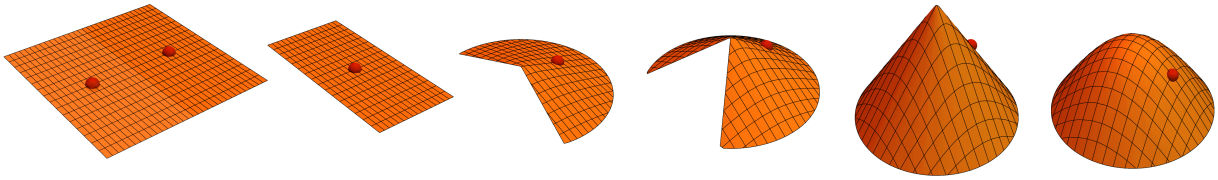

Figure 3.17: This figure schematically shows how the conic moduli space structure for a vortex–vortex configuration arises. The red dots illustrate the vortices. First, a half-plane is sufficient to describe the full configuration. This half-plane can then be glued together such that a cone forms. The tip at the end needs to be rounded, as shown in [106].

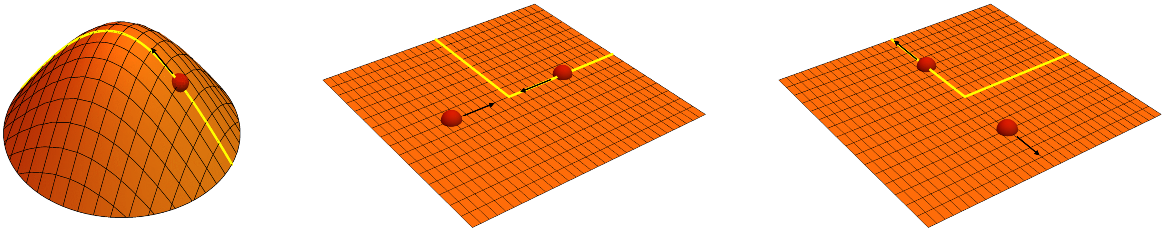

Figure 3.18: This figure schematically shows how the right-angle scattering of two vortices arises. The yellow line on the cone corresponds to a geodesic on the moduli space. Translated into the target space, this corresponds to a trajectory that changes the direction by 90° when the two vortices collide, as illustrated in the second and third figure.

with the energy density distributed in a circularly symmetric manner. Subsequently, they separate along the y-axis and move apart. This motion is in perfect agreement with the behaviour predicted in [106].

At the beginning of this section, we noted that the BPS limit, $\lambda \to 1$, is required for the vortex separation distance to be a true collective coordinate. This is because, in this limit, the forces between vortices vanish. Nevertheless, right-angle scattering persists even for $\lambda \neq 1$. Since in these cases the interaction force is exponentially suppressed (for $\lambda \nrightarrow \infty$), its effect remains small for moderate collision velocities, $u \sim 0.1$.

3.6.2 Collision of Two Excited Vortices

As discussed in Section 3.1, vortices can possess massive bound modes. These modes carry an energy that depends on both their frequency and amplitude. In multi-vortex configurations, the frequency changes as vortices approach each other, leading to variations in the mode-dependent potential energy and, consequently, to a mode-dependent force between vortices. Recently, it was shown in [83, 108, 85] that this mode-dependent force allows excitations of massive bound modes to significantly affect the dynamics in head-on

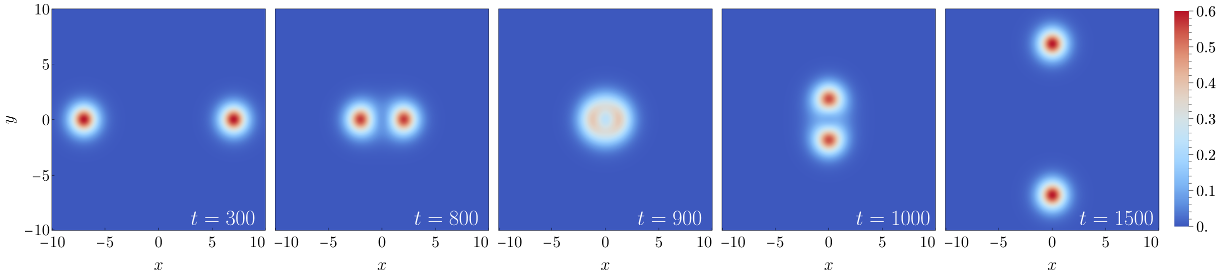

Figure 3.19: This figure shows the energy density at five moments during a vortex–vortex collision. The numerical details of the simulations are given in Appendix A.

vortex–vortex collisions. These results will be briefly reviewed in this section.

In the following, we work entirely in the centre-of-mass frame and we will only focus on BPS vortices. For head-on collisions of two vortices, the only relevant collective coordinate is the separation distance. As an initial setup for the numerical simulation, we consider two vortices separated along the x-axis and Lorentz-boost them towards each other. The numerical details are provided in Appendix A.[9]

A useful tool for understanding the mode-dependent force is the spectral flow, which describes the dependence of the mode frequencies of the two-vortex configuration on the separation distance. This spectral flow was computed in [108, 85] and is shown in Figure 3.20.

Using numerical simulations, we confirmed the spectral flow (see light-gray lines in Figure 3.20), as already done in [85], by studying the scattering of vortices with initial excitations. For that we added perturbations as in equations (3.8) and (3.9) to each of the two vortices. While the η_1 mode can be excited by an in-phase excitation of the two vortices, the η_2 mode is excited by an out-of-phase excitation. Here, out-of-phase means that one of the vortices carries an excitation with a phase shift $i\omega t \to i\omega t + i\pi$.

From the spectral flow, one can see that the frequency of the η_1 mode decreases as the separation distance becomes smaller. This implies that the mode-dependent potential energy decreases with decreasing separation, and hence two vortices attract due to the η_1 mode excitation. When two vortices of the same charge collide, they scatter at 90°, as discussed in the previous section. Since the mode excitation induces an additional attractive force, this right-angle scattering can occur multiple times. This behaviour has been demonstrated in [83, 108]. It turns out that the resulting multi-bounce dynamics is highly chaotic and very sensitive to the initial parameters, such as the separation distance, initial velocity, and phase shift of the excitation. In [83], it was shown that this multi-bounce scenario can exhibit a fractal structure, similar to the fractal patterns observed in kink–anti-kink [72, 74] and vortex–anti-vortex collisions [59].

---

[9] This section on the scattering of two excited vortices is included for completeness. Since the numerical codes for the simulations were developed within the project of [60] for the charge-3 and charge-4 sectors, more detailed information on the numerics is also provided in the following sections on higher-charged systems.

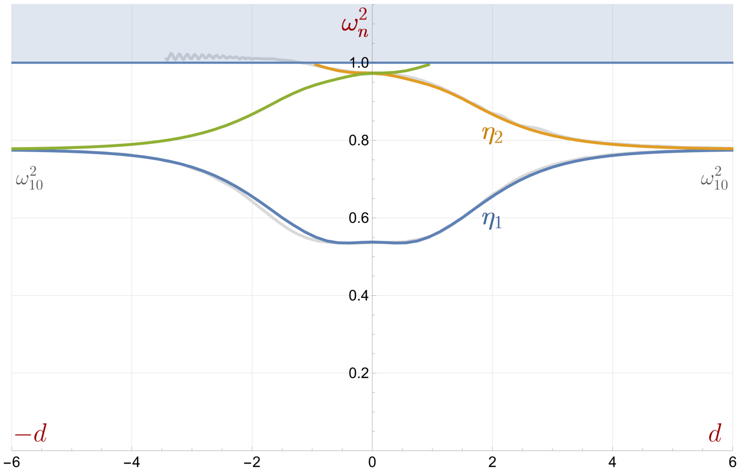

Figure 3.20: This figure shows the spectral flow of a vortex–vortex configuration as a function of the separation distance d. The positive half-plane corresponds to vortices separated along the x-axis, while the negative half-plane corresponds to vortices separated along the y-axis. The light-gray lines in the background illustrate the measurements from the simulations (Notice that the frequency along the light-gray lines changes from right to left as time passes, since we start with $d > 0$ at $t = 0$.). The spectral flow data were provided by Alberto Alonso Izquierdo and was computed by him and collaborators in [108, 85].

The origin of this fractal behaviour lies in the resonant energy transfer mechanism, which we have already discussed for vortex–anti-vortex collisions in Section 3.3. Due to the mode excitation, there is an oscillatory exchange between different constituents of the vortex energy. For example, energy can oscillate back and forth between the kinetic energy and the mode-dependent potential energy. If after a collision the kinetic energy dominates over the mode energy, the vortices can escape from each other. If, however, the attractive mode-dependent potential dominates, the vortices move again towards each other, leading to another collisions.

Excitations of the η_2 mode lead to the opposite behaviour, since they induce a repulsive force. As can be seen from the spectral flow in Figure 3.20, the frequency increases for smaller separation distances. Therefore, the mode-dependent potential energy increases, resulting in a repulsive interaction. Furthermore, one observes that the mode reaches the mass threshold. This can also be seen in the simulations. When the two vortices are excited out-of-phase, corresponding to an excitation of the η_2 mode, and move towards each other, they can still scatter at a right-angle. After the collision, however, the mode enters the continuum spectrum, meaning that it is no longer bound and the excitation disappears. The point at which this occurs is referred to as the spectral wall and has been discussed for vortex–vortex collisions in [85]. At the position of the spectral wall, the vortices nearly stop moving. The reason is that the resonant energy transfer mechanism continuously transfers energy between the kinetic and the mode-dependent potential energy. However, since the mode energy is damped by excitations into the continuum spectrum, the energy pumped from the kinetic sector to the mode sector is subsequently absorbed.

The vortex–vortex configuration is special (in the centre-of-mass frame, where both vortices are placed on the x- or y-axes), since it obeys reflection symmetry with respect to both the x- and y-axes. This symmetry must be preserved at all times. Therefore, excitations can only lead to deformations of the dynamics along the geodesic, but cannot cause deviations of the trajectories away from motion along the x- and y-axes. In this sense, the motion is confined to the BPS geodesic. This situation changes completely for multi-vortex systems with reduced symmetry, as we will see in the following subsections.

3.6.3 Geodesic Motion of Charge-3 Configurations

In the charge-3 sector, there are six collective coordinates describing the positions of the three vortex zeros. These positions can be described in a compact way by a third-degree complex polynomial,

$$\begin{aligned} P_3(z) &= (z-z_1)(z-z_2)(z-z_3) \\ &= z^3 + w_2 z^2 + w_1 z + w_0 \,, \end{aligned} \tag{3.52}$$

where $z = x + iy$ parametrizes the x- and y-coordinates in the complex plane, and

$$w_2 = -(z_1 + z_2 + z_3)\,, \tag{3.53}$$

$$w_1 = z_1 z_2 + z_2 z_3 + z_3 z_1\,, \tag{3.54}$$

$$w_0 = -z_1 z_2 z_3\,. \tag{3.55}$$

The roots of $P_3(z)$ correspond to the vortex positions. To simplify the analysis, we work in the centre-of-mass frame, which imposes $w_2 = 0$ and reduces the number of collective coordinates to four. The corresponding moduli space is then described by the polynomial

$$P_3(z) = z^3 + w_1 z + w_0\,. \tag{3.56}$$

The number of collective coordinates can be further reduced by imposing some symmetry. We focus on configurations with reflection symmetry $y \to -y$, which requires w_1 and w_0 to be real. The resulting moduli subspace is therefore only two-dimensional.

A useful parametrization of the zero positions is [86]

$$z_1 = 2a\,, \qquad z_2 = -a + \sqrt{3}b\,, \qquad z_3 = -a - \sqrt{3}b\,, \tag{3.57}$$

with $a \in \mathbb{R}$ and $b \in \mathbb{R}_+ \cup i\mathbb{R}_- \cup \{0\}$. In Figure 3.21, we show four representative examples of configurations within this parametrisation. The first two examples correspond to configurations where the vortices are arranged in a collinear way along the x-axis ($b \in \mathbb{R}_+$). The last two plots describe configurations in which one vortex remains on the x-axis, while the other two have non-zero y-coordinates ($b \in i\mathbb{R}_-$). The coefficients w_1 and w_0 are given in terms of a and b by

$$w_1 = -3(a^2 + b^2)\,, \qquad w_0 = -2a(a^2 - 3b^2)\,. \tag{3.58}$$

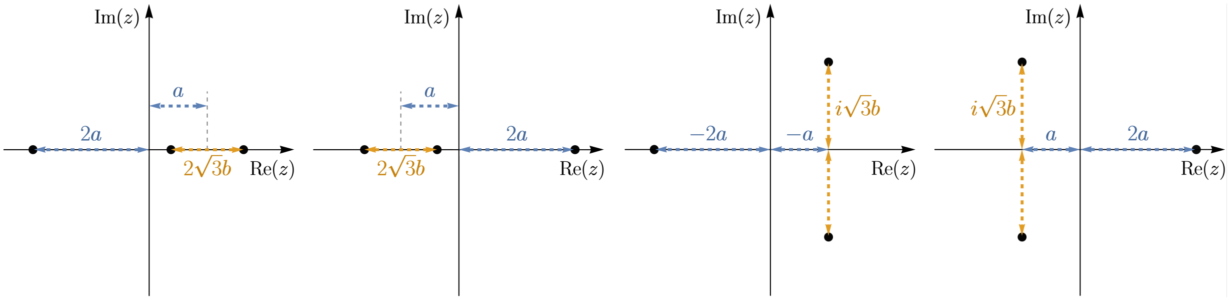

Figure 3.21: This plot shows a few examples of configurations in the reduced moduli space, described by the coordinates in the parametrisation of equation (3.57).

Remember that in the two-vortex case, it was sufficient to consider only half of the space to reconstruct the full configuration. This observation motivated the conical structure of the moduli space. A similar exclusion applies here. The region $b > |a|/3$ corresponds to configurations that are already represented elsewhere in the a-b-space. Therefore, we can exclude this region and “glue” the resulting boundaries together, leading again to a conically structured moduli space. For illustrative purposes, we will keep the a-b-plane unfolded and highlight the excluded region, as shown in Figure 3.22. When analysing geodesics on this moduli space, it is important to keep in mind that the boundaries of the excluded region, $b = a/\sqrt{3}$ with $a > 0$ and $b = -a/\sqrt{3}$ with $a < 0$, correspond to the same physical configurations.

There are two setups with enhanced symmetry that have already been studied in [109, 86]. Due to these additional symmetry restrictions, the moduli spaces are reduced to one-dimensional subspaces. The first case, the equilateral triangle configuration, possesses an additional $\mathcal{C}_3$ rotational symmetry (rotations by 120°), which in the a-b-parametrisation imposes the condition $b = ia$. The positions of the vortices are then given by

$$z_1 = 2a\,, \qquad z_2 = -a + i\sqrt{3}a\,, \qquad z_3 = -a - i\sqrt{3}a\,. \tag{3.59}$$

When three vortices that are obeying this cyclic symmetry collide, they form an intermediate charge-3 vortex configuration, which subsequently splits again. The scattering occurs at an angle of 60°, corresponding to a sign flip in a. The geodesic describing this process is given by the blue curve in Figure 3.22.

The second setup exhibiting enhanced symmetry is obtained by imposing a reflection symmetry $x \to -x$. In terms of the parameters a and b, this results in the submanifold

$$\begin{aligned} b &= \frac{a}{\sqrt{3}}\,, && \text{for} \ \ a \in \mathbb{R}_+\,, \\ a &= 0\,, && \text{for} \ \ b \in i\mathbb{R}_-\,. \end{aligned} \tag{3.60}$$

This one-dimensional moduli subspace describes collinear configurations, in which one vortex is always located at the origin, while the other two vortices lie either on the x-axis or on the y-axis. At the collision, two vortices moving towards each other along the x-axis

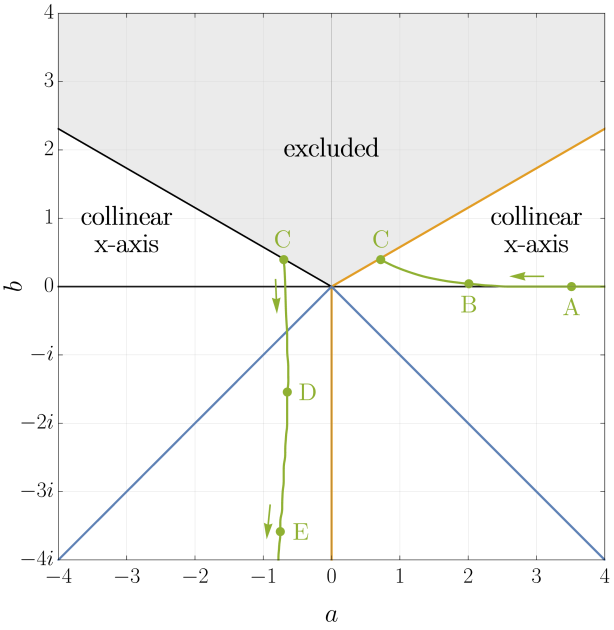

Figure 3.22: This figure illustrates a moduli subspace for three vortices. The BPS geodesics for the equilateral triangle (blue), collinear (orange), and $2+1$ collisions (green) are shown. The green labelled dots indicate the time frames displayed in Figure 3.23.

collide simultaneously with the vortex at the origin. After the collision, one vortex remains at the origin, while the other two separate along the y-axis. The geodesic describing this scattering process is given by the orange line in Figure 3.22.

Last but not least, we describe a scattering process that is quite natural, but does not possess an enhanced symmetry that reduces the moduli space to a one-dimensional subspace. This is the head-on collision of a charge-2 vortex with a charge-1 vortex. The geodesic of this scenario cannot be determined as easily as in the symmetric three-body cases, and we therefore obtain it numerically using simulations.

For all simulations in this and the following sections, we employed a modified version of the second-order Runge–Kutta method (RK2) together with absorbing boundary conditions. These are implemented by combining natural boundary conditions with a damping region near the boundary. For gauge fixing, we chose the Lorenz gauge. More details on the numerical methods are provided in Appendix A. The lattice we used has size 60×60, with spatial resolution $\Delta x = 0.05$ and time step $\Delta t = 0.025$. The total simulated time is 4000.

For the initial conditions of the 2-vortex–1-vortex collision, we again use a product ansatz for the scalar field and add together the vector field configurations of the individual vortex solutions. To place the centre of mass at the origin, we position the 1-vortex at $x = -7$ and the 2-vortex at $x = 14$. We can then apply Lorentz boosts with velocities $u_1 = -0.02$ and $u_2 = 0.01$, respectively, such that the vortices move towards each other.

Before presenting the results, we comment on some numerical subtleties. A minimum

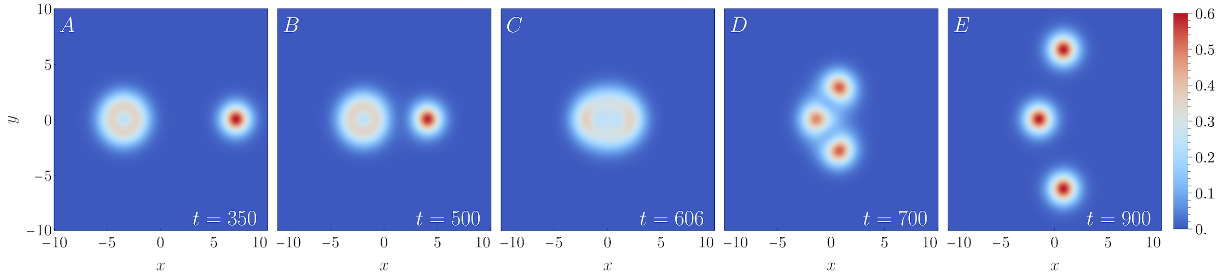

Figure 3.23: This sequence of plots shows five moments in time of the energy density during a head-on collision of a 2-vortex with a 1-vortex.

separation distance of $d \approx 20$ is required for the chosen lattice to avoid a too large overlap of the vortices. For smaller separations we observed small instabilities in the late-time evolution ($t \gtrsim 1000$). On the other hand, too large separation distances are also problematic. Although the BPS charge-2 vortex is stable, small numerical fluctuations can induce a splitting into two charge-1 vortices. While this effect is very small and does not affect the qualitative behaviour of the time evolution, we minimise it by avoiding too large initial separations. This motivates the choice of the initial separation given above.

A second comment concerns the choice of the vortex velocities. The moduli space approximation is valid only for small, non-relativistic velocities. For larger velocities, $u \gtrsim 0.1$, two effects may arise. First, Lorentz contractions can deform the configuration, potentially influencing the outcome of the collision compared to the non-relativistic case. Second, the increased kinetic energy can excite internal vortex modes via the resonant energy transfer mechanism, which has already been discussed previously for vortex–anti-vortex collisions in Section 3.3. Numerically, we can observe such excitations for collision velocities $u \gtrsim 0.1$, while for $u \lesssim 0.02$ no such effects are visible.

The animated result of the 2-vortex–1-vortex collision is shown in the following video: `https://youtu.be/o-0fQn-0wlE`
Furthermore, in Figure 3.23, we show five time frames of the full time evolution. By tracking the positions of the zeros of the scalar field (for details see Appendix A.8), we can determine the time dependence of the coordinates $a(t)$ and $b(t)$. This, in turn, allows us to extract an approximate geodesic curve $b(a)$, which is illustrated by the green line in Figure 3.22.

Initially, the vortices are located at $z_1 = 2a$ and $z_2 = z_3 = -a$, with $a = 7$. As the vortices approach each other, the charge-2 vortex begins to split along the x-axis. This results in a non-zero real b, such that $z_2 = -a + \sqrt{3}b$ and $z_3 = -a - \sqrt{3}b$. As long as the single vortex remains entirely in the positive x-half-plane, a stays positive. Once one of the vortices originating from the negative x-direction passes the origin towards the positive x-half-plane, a flips the sign. In Figure 3.22, this corresponds to the moment when the green geodesic hits the boundary of the excluded region at point C. This occurs at approximately $a \approx 0.7068$ and $b \approx 0.4080$. Subsequently, the vortex that initially came from the positive x-direction collides with one of the vortices coming from the negative

x-direction. They undergo right-angle scattering, leave the x-axis, and move apart along the y-direction. In the a-b-plane, this right-angle scattering is visible by the crossing of the a-axis. The remaining vortex, originating from the initial charge-2 configuration, slows down significantly and stays near the origin on the x-axis.

3.6.4 Collision of Excited Vortices in Charge-3 Configurations

Now that we have found the BPS geodesics, we want to investigate how the dynamics are modified if the vortices are initially excited. For the equilateral triangle and the collinear collision, this has already been studied in great detail in [86]. It was observed that excitations of the modes can generate either attractive or repulsive forces. The attractive interaction can lead to multiple scattering events. Due to the enhanced symmetry, the motion in these cases always remained along the BPS geodesic. In the collision of a charge-2 vortex with a charge-1 vortex, however, such enhanced symmetry is absent, and we will see that the trajectories can leave the BPS geodesic when a mode is excited.

Before studying the time evolution of these excited configurations for the 2-vortex–1-vortex scattering, we first need to understand which bound modes exist in multi-vortex configurations and can be excited. Furthermore, we need to understand how these modes evolve along the geodesic.

When the charge-2 vortex and the charge-1 vortex are far separated, the modes correspond to those of the isolated vortices. The charge-1 vortex has one massive bound mode with frequency $\omega_{10}^2 \approx 0.77788$, while the charge-2 vortex has three massive bound modes, one with frequency $\omega_{20}^2 \approx 0.53898$ and two degenerate modes with frequency $\omega_{21}^2 \approx 0.97256$ [61]. Notice that the latter degenerate modes carry angular momentum. Since these modes are rather non-trivial to excite, we will restrict ourselves to the lowest bound mode with frequency ω_{20}.

After the 2-vortex–1-vortex collision, there are three well-separated charge-1 vortices, each supporting one mode corresponding to the frequency ω_{10}. The modes of the 1-vortices can be excited with a relative phase shift. This leads to infinitely many possible excitations, which can be constructed as superpositions of the individual modes. We will see that it is convenient to describe these superpositions in terms of the following normalized orthogonal eigenstates [86],

$$\xi_1 = \frac{1}{\sqrt{3}} \left(|1\rangle + |2\rangle + |3\rangle \right), \tag{3.61}$$

$$\xi_2 = \frac{1}{\sqrt{2}} \left(|1\rangle - |3\rangle \right), \tag{3.62}$$

$$\xi_3 = \frac{1}{\sqrt{6}} \left(|1\rangle - 2\,|2\rangle + |3\rangle \right), \tag{3.63}$$

where $e^{i\alpha}\,|i\rangle$ schematically describes the excitation of one of the three vortices, and α corresponds to the phase shift between the excitations. Hence, in the above eigenstates, the plus sign corresponds to $\alpha = 0$, while the minus sign corresponds to $\alpha = \pi$. Along

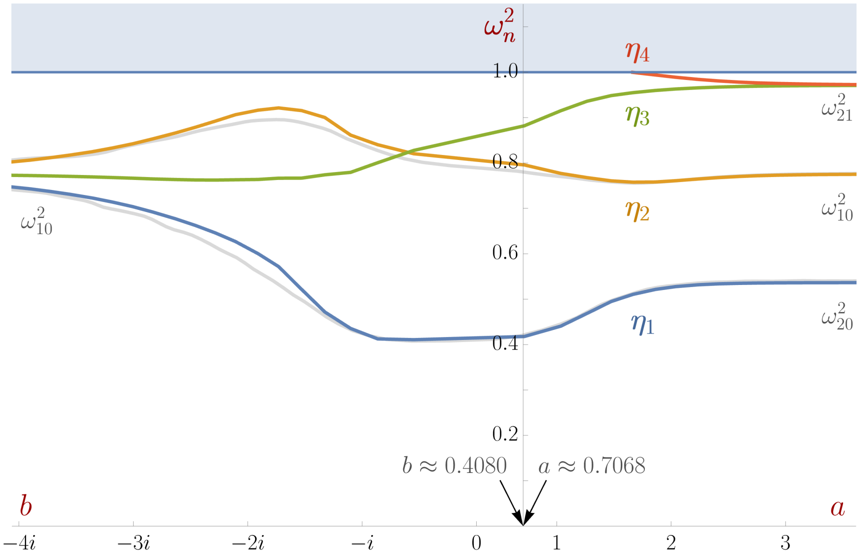

Figure 3.24: In this figure, the numerically obtained spectral flow for the 2-vortex–1-vortex collision is illustrated. To the left of the frequency axis, the flow along the geodesic with $a < 0$ is shown, while to the right of the frequency axis, the flow along the geodesic with $a > 0$ is plotted. The light-gray curves correspond to the frequencies measured in the numerical simulation.

the BPS geodesic, the spectral flow should exhibit a continuous transition from the modes of the separated charge-2 and charge-1 vortices to superpositions of the three separated charge-1 vortex modes.

The complete spectral flow of the modes can be computed numerically. For this we take the numerically obtained geodesic $b(a)$ and determine, for the different points along the moduli space geodesic, the corresponding static 3-vortex solutions using numerical relaxation. Using these numerical solutions, one can introduce small fluctuations and reduce the resulting differential equations to an eigenvalue problem, which can then be solved numerically to obtain the frequencies of the corresponding modes. For further details, we refer to [108, 62][10]. The final result is shown in Figure 3.24.

As a cross-check, we can measure the spectral flow directly from the numerical simulation. For this purpose, we excite the vortices with very small mode amplitudes, such that the modification of the dynamics remains small. Since there is a continuous flow between the different energy contributions of the system, we use the time dependence of the potential energy to extract the time dependence of the oscillation frequency.[11] Applying a Gaussian filter to the obtained data in order to reduce numerical noise then yields the frequency flow lines shown in light-gray in Figure 3.24.

We checked two curves of the spectral flow. The lowest mode, η_1, is obtained by exciting

---

[10] In this thesis, we will not go further into the numerical details of the spectral flow calculation, since these computations were not performed by myself, but by my collaborator Alberto Alonso Izquierdo.

[11] When modes are excited out-of-phase, it is sometimes not possible to extract a certain frequency from the total potential energy. This issue can be resolved by calculating the potential energy only of one half of the lattice.

only the charge-2 vortex. The η_2 mode, on the other hand, is obtained by exciting only the charge-1 vortex. We observe that the measured frequencies follow the predicted spectral flow very well.

The numerical simulation also provides information about the excitation of the final state. We find that for the η_1 mode all vortices are excited in-phase in the final state, which corresponds to the excitation given by the eigenstate ξ_1. In contrast, when the charge-1 vortex is excited initially, corresponding to the η_2 mode, the final state shows that the single vortex remaining on the x-axis is excited out-of-phase with respect to the other two vortices. This corresponds to the ξ_3 mode. We have not tested the η_3 mode in the simulation. However, we expect that the final state will exhibit the excitation given by ξ_2.

The η_4 mode hits the continuous spectrum at $a \approx 1.6651$ and $b \approx 0.0867$. Notice that such behaviour of a mode can lead to spectral walls [85, 110]. The fact that one mode must reach the mass threshold can also be understood from a simple counting argument. As mentioned above, the charge-2 vortex has three bound modes and the charge-1 vortex has one bound mode. Thus in total there are four bound modes. In contrast, the final state with three separated charge-1 vortices admits only three independent superpositions of modes. Therefore, one mode must disappear when the configuration transitions from a 2-vortex–1-vortex system to three separated 1-vortices.

Finally, we want to mention that there is a level crossing at $b \approx -0.5489i$, which means that the η_2 and η_3 modes are degenerate at this point. Such behaviour is expected due to the known results for the spectral flow of the equilateral triangle [86], where it was found that this configuration always has two degenerate modes. Since the 2-vortex–1-vortex collision passes through the equilateral triangle configuration (see the crossing of the blue and green trajectories in Figure 3.22), the frequencies in our collision scenario should match those of the equilateral triangle configuration at this point.

In the simulation, we can now excite the vortices using equations (3.8) and (3.9). By choosing different amplitudes, ξ, we can observe how the dynamics change. Besides attractive and repulsive forces, which have already been observed in [83, 86], we can additionally see a deformation of the BPS geodesic. Such a deformation arises from two effects. First, there is a mode-generated force [84]. The excitation of the modes leads to an additional potential energy, which is higher for higher frequencies and lower for lower frequencies. Since the frequency changes during the motion, as seen in the spectral flow plot, this induces a force that pushes the configuration towards regions of lower frequency. The second effect is the so-called Coriolis effect [111], which describes a velocity-dependent force resulting from a coupling between the zero mode and the massive modes. Through this effect, the moduli space becomes deformed, leading to a moduli space metric that depends on the mode amplitude. For the 1-vortex, such a modification has been computed recently in [112].

Excitation of the η_1 Mode

Let us first focus on the modification of the dynamics due to the excitation of the lowest mode, the η_1 mode. The trajectories in the a-b-parametrisation are shown in Figure 3.25

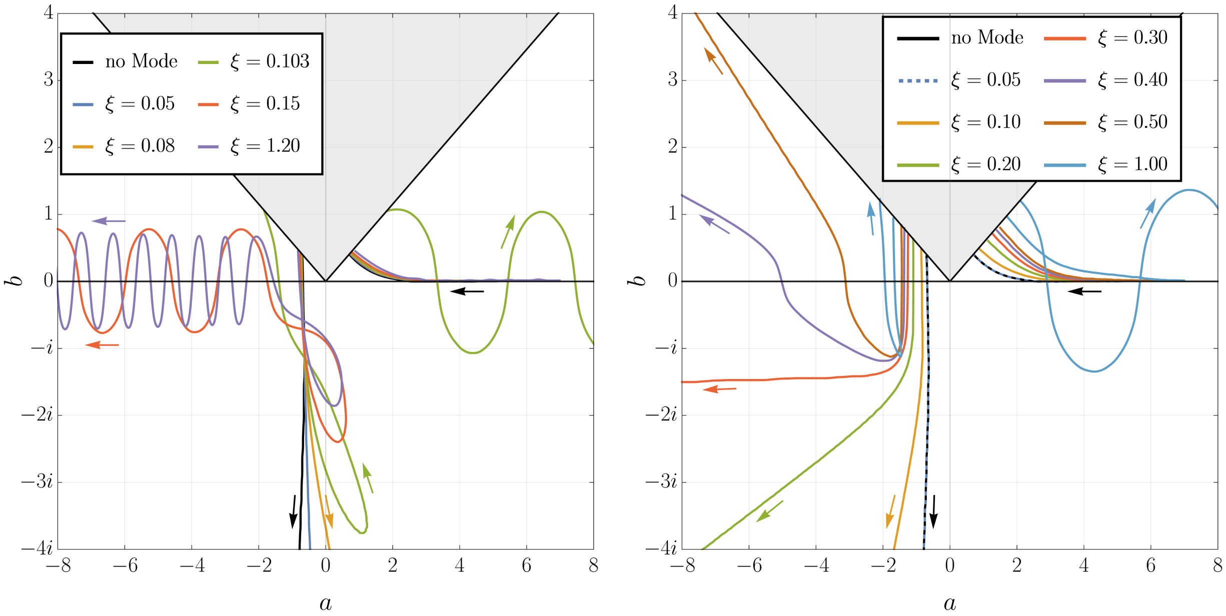

Figure 3.25: In this figure, the trajectories of the 2-vortex–1-vortex scattering are shown in the a-b-plane. The black curve represents the BPS geodesic, while all other coloured curves correspond to cases in which the vortices are initially excited with different amplitudes ξ. In the left plot, trajectories are shown where the 2-vortex is initially excited, whereas the right plot displays trajectories where the 1-vortex is initially excited. The dark blue lines correspond to the lowest amplitudes we tested. These low amplitude cases were used to measure the spectral flow corresponding to the light-gray lines in Figure 3.24. Animated results of some displayed trajectories can be found in the following video: `https://youtu.be/o-0fQn-0wlE` .

(left). From this plot, it is clearly visible that the motion is no longer confined to the BPS geodesic. Already small amplitudes ξ lead to noticeable deviations of the trajectories. At the beginning of the motion, the trajectories follow the BPS geodesic quite closely, meaning that the 2-vortex and the 1-vortex approach each other. Subsequently, the 2-vortex splits along the x-axis into two charge-1 vortices. One of them then scatters at a right angle with the 1-vortex coming from the positive x-direction. Up to this point, the dynamics remain very similar to the unexcited scenario.

However, starting from around $b \approx -i$, the trajectories begin to deviate significantly. This is due to the strong change in the spectral flow at approximately the same value of b. The curves bend towards the a-axis and, for sufficiently large amplitudes, even cross the b-axis. This corresponds to a sign flip in the x-coordinates of the three vortices. If the amplitude is large enough, the vortices located off the x-axis reverse their direction of motion after reaching a maximal separation. This can be understood from the behaviour of the potential energy of the modes, as can be seen in the spectral flow shown in Figure 3.24 for $\mathrm{Im}(b) \lesssim -1$. The mode energy increases as the separation of the vortices in the y-direction grows (i.e. for more negative imaginary values of b).

After the two vortices reverse their direction of motion, the trajectory re-enters the negative a-half-plane, and the two vortices off the x-axis undergo another right-angle scattering. Subsequently, two different outcomes can be observed. The first possibility occurs within a very small amplitude window around $\xi \sim 0.1$ (green line in Figure 3.25 (left)), in which the trajectory can hit the excluded region once more and then leave towards the positive a-direction. While the 1-vortex moves towards positive x, i.e. in the direction from which it initially came, the other two vortices move towards negative x and undergo multiple right-angle scatterings, forming a bound charge-2 state. The second possibility, which is the dominant scenario for amplitudes $\xi \gtrsim 0.11$, corresponds to trajectories that move towards the negative a-direction (red and purple lines in Figure 3.25 (left)). The final state then consists of a charge-1 vortex moving towards the negative x-axis and a bound, multi-bounce charge-2 state moving towards the positive x-axis. The frequency of the multi-bounce behaviour increases with increasing amplitude. Surprisingly, the maximal separation distance of the oscillating multi-bouncing remains the same.

As already mentioned earlier, the deviations of the trajectories are due to two effects, the mode-generated force and the Coriolis effect. Qualitatively, we can say that the Coriolis effect leads to a bending of the curves as a result of the deformation of the moduli space metric, while the mode-generated force induces an effective attraction between the charge-1 vortex constituents.

In the final state, when the multi-bounce charge-2 structure appears, the mode-generated force becomes the dominant effect. This multi-bounce behaviour is the same as that studied in [83, 84] and arises due to the resonant energy transfer mechanism [76, 72, 74], which we have already discussed for vortex–anti-vortex collisions in Section 3.3. Whenever the vortices collide, energy is exchanged between the kinetic energy and the energy stored in the excitation. If the kinetic energy is sufficiently small, the attractive interaction between the vortices dominates, leading to the formation of a bound, bouncing state.

Finally, it should be briefly mentioned that the dynamics also change under slight variations of the initial separation distance or small changes of the phase of the excitation, $i\omega t \to i\omega t + i\alpha$. This arises due to the energy exchange between the different contributions to the total energy. For instance, at the moment when the first two vortices collide, the distribution of energy among the different energy constituents can vary depending on the initial phase, which in turn affects the outcome of the collision. This behaviour was already observed in [83]. Overall, however, our simulations show that qualitatively the trajectories and their behaviour remain unchanged.

Excitation of the η_2 Mode

We can excite the η_2 mode by exciting the 1-vortex in the initial configuration. Similarly to the η_1 mode, we simulate the collision for different amplitudes ξ of the initial excitation. The resulting trajectories are shown in Figure 3.25 (right).

In contrast to the previous case, the trajectories start to deviate from the BPS geodesic already at early times. Due to the excitation, the 1-vortex induces an attractive force that pulls one constituent of the charge-2 vortex towards it. As a result, the trajectories hit the excluded region at larger values of a. Afterwards, the two vortices that collide perform the right-angle scattering, which is again visible in the crossing with the a-axis. In the lower left quadrant of the a-b-plot, we observe that stronger excitations lead to a stronger bending of the trajectories towards the negative a-direction, until, for sufficiently large amplitudes, the trajectories change their direction by 180°.

This behaviour can be understood from the spectral flow shown in Figure 3.24. The η_2 mode exhibits a maximum at around $b \sim -1.5i$. If the amplitude is sufficiently small, such that the kinetic energy dominates over the mode energy, the trajectories can bend slightly (see for example, the orange line in Figure 3.25 (right)), but the overall motion still proceeds towards more negative imaginary values of b. As the amplitude of the excitation increases, more kinetic energy can be transferred into the potential energy of the modes, which slows down the vortices in the y-direction (i.e. along the imaginary b-direction). For sufficiently large amplitudes, the maximum in the spectral flow cannot be overcome, and the vortices reverse their direction of motion (see the light blue line in Figure 3.25 (right)). Notably, this change in direction occurs approximately at the point where the spectral flow of the η_2 mode reaches its maximum.

When the vortices reverse their direction, they can cross the a-axis again, leading to another right-angle scattering. For sufficiently large mode amplitudes, they can even hit the excluded region once more, such that the final state consists of a charge-1 vortex moving towards the positive x-direction and a bouncing charge-2 state moving towards the negative x-direction.

We can summarize that the structure of the trajectories is rather organized and can be partially understood from the spectral flow. Of course, the dynamics of the charge-2 bouncing states remain chaotic and highly sensitive to the initial ansatz, but the overall way in which the trajectories deform is very robust.

3.6.5 Geodesic Motion of Charge-4 Configurations

A natural continuation of the above study is to perform the same analysis for four BPS vortices. Before discussing the collision of vortices in the charge-4 sector, we first describe the reduced moduli space on which we will focus.

Similarly to the configurations with three vortices, we can encode the positions of the vortices as the roots of a complex polynomial of fourth order

$$\begin{aligned} P_4(z) &= (z - z_1)(z - z_2)(z - z_3)(z - z_4) \\ &= z^4 + w_3 z^3 + w_2 z^2 + w_1 z + w_0 \,, \end{aligned} \tag{3.64}$$

with

$$w_3 = -(z_1 + z_2 + z_3 + z_4)\,, \tag{3.65}$$

$$w_2 = z_1 z_2 + z_1 z_3 + z_1 z_4 + z_2 z_3 + z_2 z_4 + z_3 z_4\,, \tag{3.66}$$

$$w_1 = -(z_2 z_3 z_4 + z_1 z_3 z_4 + z_1 z_2 z_4 + z_1 z_2 z_3)\,, \tag{3.67}$$

$$w_0 = z_1 z_2 z_3 z_4\,. \tag{3.68}$$

Therefore, the moduli space depends on four complex parameters, i.e. it has eight dimensions. We again restrict our analysis to the centre-of-mass frame, which sets $w_3 = 0$ and thus reduces the number of dimensions by two. Furthermore, we focus on a subspace that satisfies the symmetries $x \to -x$ and $y \to -y$. This implies that the polynomial must be invariant under the transformations $z_i \to -z_i^*$ and $z_i \to z_i^*$. As a consequence, we obtain $w_1 = 0$, while w_0 and w_2 are restricted to be real, resulting in the reduced polynomial

$$\tilde{P}_4(z) = z^4 + w_2 z^2 + w_0 \,, \tag{3.69}$$

where $w_0, w_2 \in \mathbb{R}$. Therefore, the moduli subspace has only two dimensions.

We can again introduce a useful parametrisation that allows us to understand the dynamics on the moduli space in an illustrative way. For one part of the moduli subspace, we use

$$\begin{aligned} z_1 &= a + b \,, \qquad & z_2 &= a - b \,, \\ z_3 &= -a + b \,, \qquad & z_4 &= -a - b \,, \end{aligned} \tag{3.70}$$

where a and b are complex numbers. Using $a \in \mathbb{R}$ and $b \in i\mathbb{R}$ yields configurations in which the vortices are located at the corners of a rectangle. However, since exchanging vortices leads to the same configuration, it is sufficient to restrict to $a \in \mathbb{R}_+$ and $b \in i\mathbb{R}_-$. We will refer to these as *rectangle configurations*. The choices $a \in \mathbb{R}_+$ and $b \in \mathbb{R}_+$ (and similarly $a \in i\mathbb{R}_-$ and $b \in i\mathbb{R}_-$) describe configurations in which all four vortices lie on the x-axis (or the y-axis). We will refer to these as *collinear x-axis (y-axis) configurations*. As before, we want to avoid double counting in the moduli space. In this case, exchanging vortices, corresponding to $a \leftrightarrow b$, yields the same configuration. Therefore, one of the regions separated by the line $b = a$ can be excluded.

One last class of vortex arrangements is missing, which we refer to as *cross configurations*. These describe situations in which two vortex zeros lie on the x-axis and the other two on the y-axis. For this, we can use the parametrisation

$$\begin{aligned} z_1 &= \sqrt{2}a \,, \qquad & z_2 &= \sqrt{2}b \,, \\ z_3 &= -\sqrt{2}a \,, \qquad & z_4 &= -\sqrt{2}b \,, \end{aligned} \tag{3.71}$$

with $a \in i\mathbb{R}_-$ and $b \in \mathbb{R}_+$.

Illustrative examples of this parametrisation are shown in Figure 3.26 (left). In Figure 3.26 (right), the a-b-plane representing the moduli subspace we are considering is displayed.

We consider three scattering scenarios. The first, which we call square scattering, describes four vortices placed at the corners of a square and moving towards each other such that they collide at the origin. The corresponding geodesic is given by $b = -ia$, which describes vortices initially in a cross configuration. Upon collision, the vortices scatter at 45° [109], enter the rectangle configuration regime, and then move apart again. This geodesic is shown as the blue line in Figure 3.26 (right).

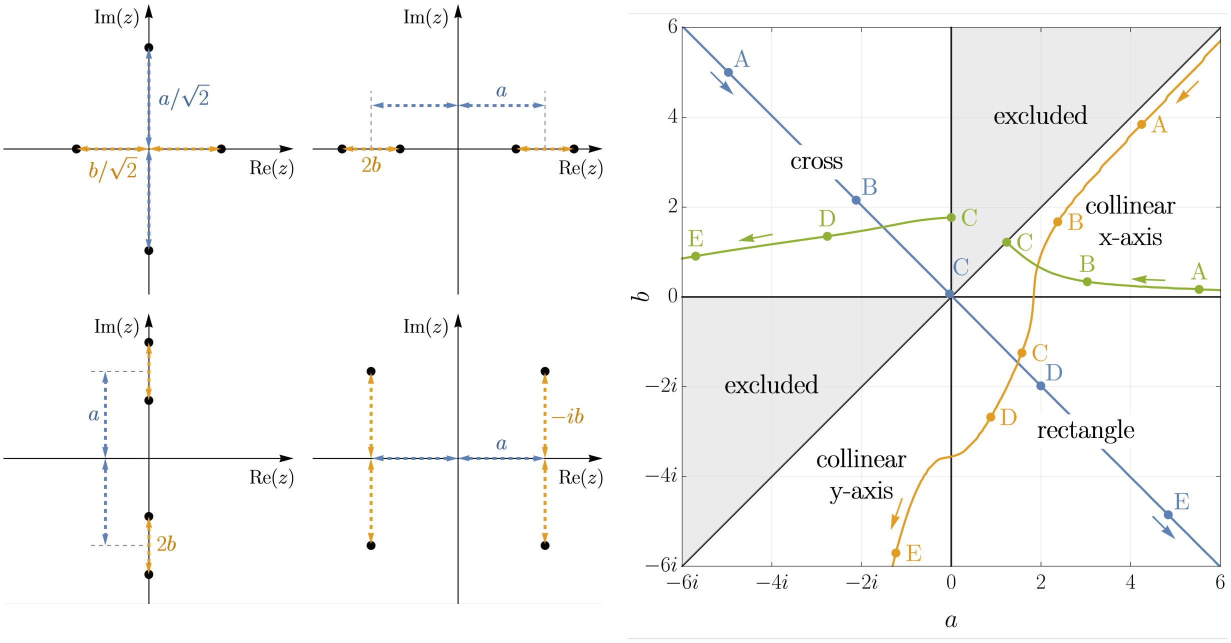

Figure 3.26: The figure on the left shows representative examples of the four different configurations that can be described by the parametrisation introduced in the text. The subfigures are arranged in the same order as the four different quadrants of the a-b-plot shown in the right figure. The right figure also displays three different BPS geodesics corresponding to square (blue), collinear $1+2+1$ (orange), and $2+2$ (green) vortex scatterings. The labelled dots indicate the points corresponding to the snapshots shown in Figure 3.27.

The second scenario we consider is the collinear $1+2+1$ scattering, which corresponds to a charge-2 vortex at the origin and two charge-1 vortices located on the x-axis away from the origin. The two outer vortices move towards the central 2-vortex and collide with it. The third scenario is the $2+2$ scattering, i.e. two charge-2 vortices undergoing a head-on collision along the x-axis.

The BPS geodesics for the latter two cases have to be determined numerically. We utilize the same numerical methods as for the 2-vortex–1-vortex scattering. As before, we choose the initial separation between the vortices to be at least 20. Specifically, we place the vortices at $\{(15,0);(0,15);(-15,0);(0,-15)\}$, $\{(-20,0);(0,0);(20,0)\}$, and $\{(-10,0);(10,0)\}$ for the square collision, the collinear $1+2+1$ collision, and the $2+2$ collision, respectively. The velocities of the moving vortices are taken to be $|u| = 0.01$ in all cases. The lattice properties are the same as in the 2-vortex–1-vortex case, with the only difference that for configurations where the vortices are initially close to the boundary, the lattice size is increased to 80×80.

The animated results of the collisions are shown in the following video:
`https://youtu.be/o-0fQn-0wlE`
Additionally, we display several snapshots of the time evolution for the three scattering cases in Figure 3.27. Using the numerical data, we again determine the BPS geodesic

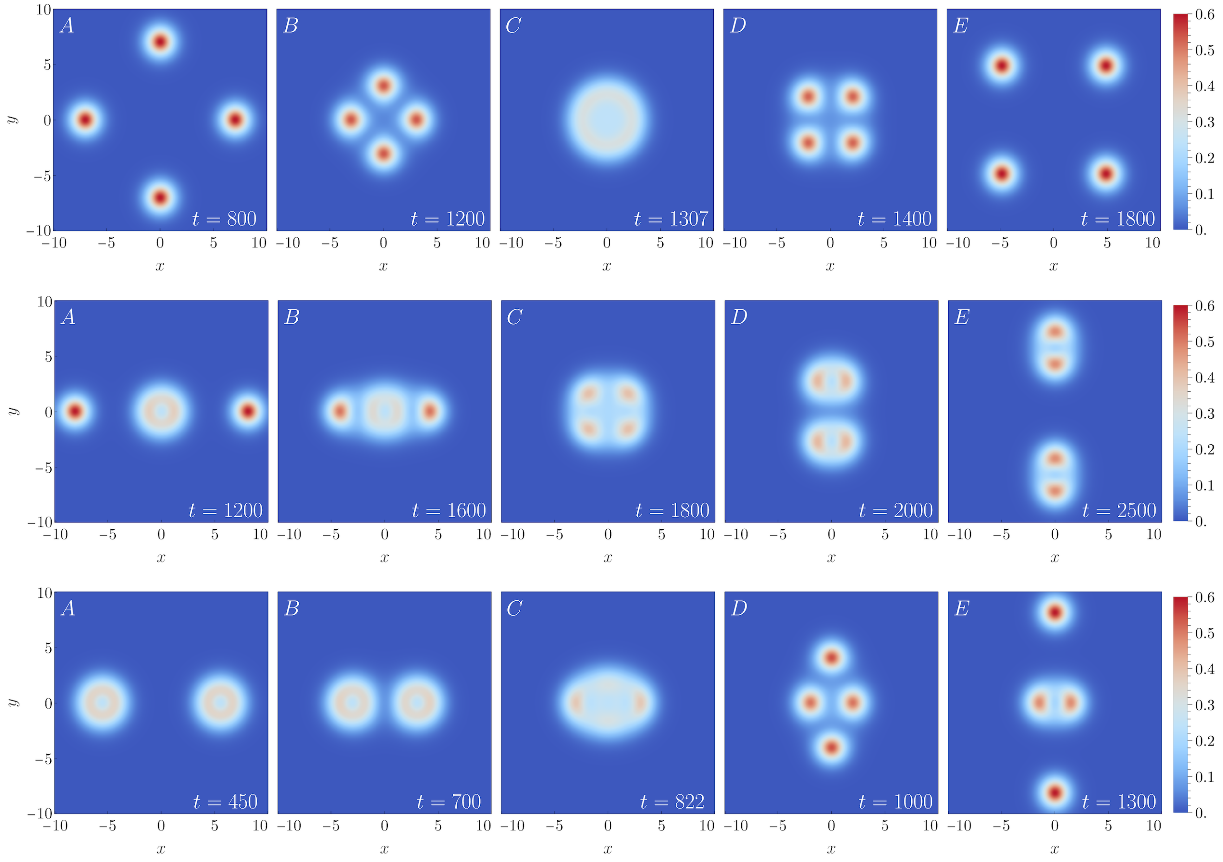

Figure 3.27: This figure displays five snapshots of the energy density for square scattering (first row), collinear $1+2+1$ scattering (second row), and $2+2$ scattering (third row).

motion in terms of the coordinates a and b. The corresponding trajectories are shown in Figure 3.26.

The dynamics of the $1+2+1$ scattering proceeds as follows. First, the two vortices located on the x-axis away from the origin move towards the origin, where the charge-2 vortex is located. As they approach, the 2-vortex begins to split into two charge-1 vortices along the x-axis. Subsequently, this leads to two simultaneous right-angle scatterings. In Figure 3.26, this corresponds to the point where the orange trajectory crosses the a-axis. At this stage, the four vortices are located at the corners of a rectangular configuration. The two upper vortices move towards each other and collide, ending up on the positive y-axis. The same happens simultaneously for the two lower vortices. In the a-b-plot, this is visible as the crossing of the orange trajectory with the b-axis. Afterwards, all vortices move apart along the y-axis.

In the $2+2$ scattering, the two charge-2 vortices initially move towards each other. As they approach, they begin to split along the x-axis. The two charge-1 vortices closer to the origin scatter first at a right angle and continue moving apart along the y-axis. This corresponds to the point where the green trajectory hits the excluded region in Figure 3.26.

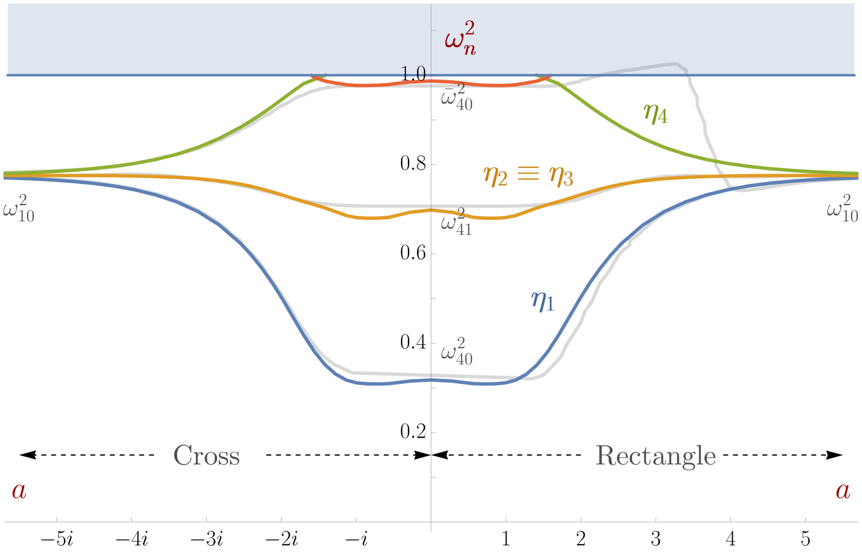

Figure 3.28: The spectral flow along the BPS geodesic for the square scattering is shown in this figure. The light-gray lines correspond to the frequencies obtained from measurements in the numerical simulations. Notice that in contrast to Figures 3.20, 3.24, and 3.29, the frequency along the light-gray lines changes from left to right as time passes, since we start with the cross configuration at $t = 0$.

At a later stage, the remaining two vortices on the x-axis also collide at a right angle and subsequently move along the y-direction.

3.6.6 Collision of Excited Vortices in Charge-4 Configurations

With the setup for the collision of four vortices introduced in the previous section, we can now analyse what happens when the vortices are initially excited. For this, we follow the same procedure as in the scattering of a 2-vortex with a 1-vortex. We first discuss the possible excitation combinations and the spectral flow, and then analyse the resulting change in the dynamics.

Let us begin with the square collision. The spectral flow is shown in Figure 3.28, and was determined using the same methods described earlier. In addition, we again measured the frequencies directly in the simulations (see light-gray curves) to verify the predicted behaviour of the spectral flow.

In the initial and final state, we expect the frequency to approach that of the 1-vortex mode, $\omega_{10}^2 \approx 0.77788$, since the vortices are well-separated and can be treated as isolated objects. Furthermore, because the configurations before the scattering coincide with those after the scattering up to a rotation of 45°, the spectral flow is symmetric with respect to the frequency axis. The lowest mode, the η_1 mode, can be obtained by a symmetric excitation of all four vortices

$$\xi_1 = \frac{1}{2}\left(|1\rangle + |2\rangle + |3\rangle + |4\rangle\right). \tag{3.72}$$

As the vortices approach each other, the frequency decreases and reaches that of the lowest 4-vortex mode, $\omega_{40}^2 \approx 0.31928$ [61], when the configuration forms the intermediate state of a charge-4 vortex. After the 45° scattering, the frequency increases again towards its initial value. Notice that the measured frequency of the simulation agrees very well with the predicted behaviour of η_1.

The highest-frequency mode, η_4, can be obtained by exciting the vortices with the state

$$\xi_4 = \frac{1}{2}\left(|1\rangle - |2\rangle + |3\rangle - |4\rangle\right). \tag{3.73}$$

This corresponds to the two vortices located on the x-axis being excited out-of-phase with respect to the two vortices on the y-axis. Notice that this excitation respects the symmetry of the moduli subspace that we are considering, but does not preserve the cyclic $\mathcal{C}_4$ symmetry of the unexcited square configuration. As a result, in simulations with very small excitation amplitudes, we can measure the frequencies, but they do not perfectly match the predicted behaviour of the spectral flow. In the simulations, we clearly observe that the flow of this mode reaches the mass threshold. At this point, the excitation of the η_4 mode disappears. The configuration then effectively reduces to one with excitation in the η_1 mode, as can be seen from the light-gray curve in Figure 3.28. It initially follows the green and red curves, but after hitting the mass threshold, it falls down to the blue curve. The origin of this behaviour lies in non-linear interactions, through which all modes are weakly coupled. Consequently, even if only the η_4 mode is initially excited, the η_1 mode can also become excited during the collision. Once the η_4 mode disappears, i.e. its energy radiated into the continuum spectrum, only the η_1 mode remains, even though with a small amplitude.

Notice that, through such non-linear interactions between the modes, the $\eta_2 = \eta_3$ mode cannot be excited, since this mode corresponds to orthogonal superpositions

$$\xi_2 = \frac{1}{2}\left(|1\rangle + |2\rangle - |3\rangle - |4\rangle\right), \tag{3.74}$$

$$\xi_3 = \frac{1}{2}\left(|1\rangle - |2\rangle - |3\rangle + |4\rangle\right), \tag{3.75}$$

which do not obey the symmetry of the moduli subspace, $x \to -x$ and $y \to -y$. Since the excitations ξ_1 and ξ_4 respect this symmetry, it must be preserved at all times. Nevertheless, in the simulations we still excited the η_2 and η_3 modes by hand with small amplitudes, such that the deviation from the symmetry remains small. This allowed us to reconstruct the spectral flow, which agrees very well with the predicted behaviour.

The spectral flow for the collinear $1+2+1$ collision is shown in Figure 3.29. Due to the reduced symmetry compared to the square scattering, the behaviour of the flow is

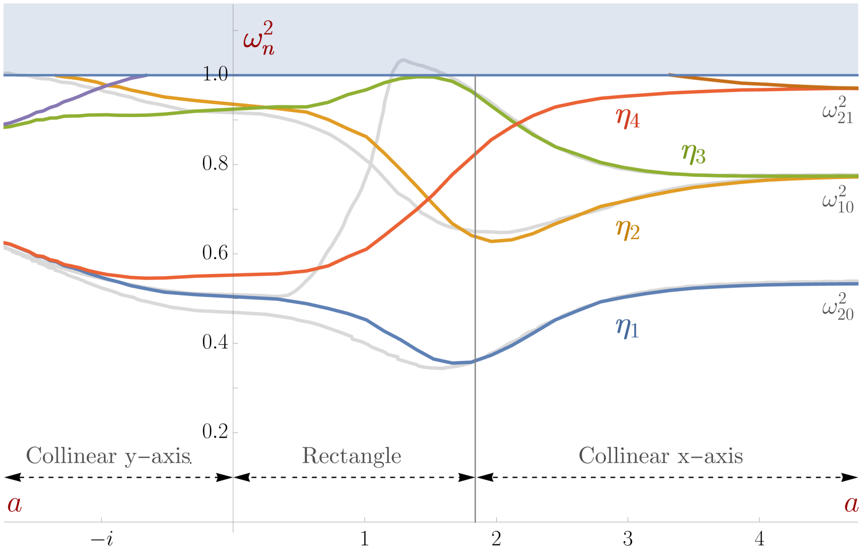

Figure 3.29: This plot shows the spectral flow along the BPS geodesic corresponding to the collinear $1+2+1$ scattering. The light-gray curves represent the frequencies extracted from the numerical simulations.

more involved, and there are several different ways in which the vortices can be excited. One possibility is to excite only the 2-vortex through its modes. The simplest excitation corresponds to the lowest mode with frequency $\omega_{20}^2 \approx 0.53898$. We observe that the frequency initially decreases, reaching a minimum approximately when the first right-angle scattering occurs. Subsequently, it increases again and eventually approaches the frequency of the 1-vortex mode, since at late times the vortices are well-separated.

The highest mode, η_4, is non-trivial to excite, which is why we have not considered it in the simulations. Its behaviour can be described as follows. Initially, the mode is excited at the frequency of the two degenerate modes of the 2-vortex, $\omega_{21}^2 \approx 0.97256$ [61]. These two degenerate modes then split. One disappears into the continuum spectrum (brown curve), while the other, the η_4 mode, falls down, crossing the η_2 and η_3 modes, and approaches the η_1 mode. The level crossing with the η_2 mode can be attributed to the fact that the configuration passes through a square configuration. As seen in the spectral flow for the square case in Figure 3.28, there are only three distinct modes, since η_2 and η_3 are degenerate. This explains why, at this stage of the spectral flow for the $1+2+1$ collision, the η_2 and η_4 modes become degenerate.

The η_2 and η_3 modes can be obtained by exciting the 1-vortices in the $1+2+1$ configuration. They can be excited either out-of-phase or in-phase. In the simulations, we find that the out-of-phase excitation corresponds to the η_2 mode. Notice that this mode breaks the symmetry of the moduli subspace, $x \to -x$. Nevertheless, the simulated results and the predicted spectral flow agree quite well. This mode first decreases, reaching a minimum at the point where the first right-angle scattering occurs. Afterwards, the frequency increases and hits the mass threshold. The shape of the flow at the end is similar to the out-of-phase excitation of a vortex–vortex configuration [85].

The η_3 mode, obtained from the in-phase excitation of the two 1-vortices, initially increases and approaches the mass threshold very closely. In the simulations, we observe that the excitation indeed reaches the continuum spectrum, where the η_3 mode becomes strongly damped. Subsequently, the η_1 excitation with small amplitude remains. As in the square scattering case, this can be attributed to non-linear interactions between the modes, through which the η_1 mode becomes excited.

Next, we analyse the dynamics of the excited configuration using numerical simulations. We restrict ourselves to excitations that respect the symmetry of the moduli subspace, $x \to -x$ and $y \to -y$. Other cases are difficult to interpret, since the motion leaves the two-dimensional a-b-space.

In the square scattering, there are two possible excitations that obey this symmetry, namely ξ_1 and ξ_4. The ξ_1 excitation, corresponding to the η_1 mode, fully preserves the cyclic $\mathcal{C}_4$ symmetry, and therefore, even in the presence of the excitation, the trajectories remain confined to the BPS geodesic. We can again observe multiple bounces due to the attractive force generated by the mode. This behaviour is very similar to the scattering of two vortices [83, 108, 85], as well as to the equilateral triangle and collinear scattering in the three-vortex sector [86]. The ξ_4 excitation, corresponding to the η_4 mode, leads to deviations from the BPS geodesic, as shown in Figure 3.30. This mode generates an energetic barrier, making it energetically costly to increase the value of a. This effect is clearly visible in the behaviour of the trajectories. The larger the mode amplitude ξ is, the more the trajectories are bent. For sufficiently large amplitudes, the mode interactions can even prevent the configuration from leaving the crossed configuration (see, for instance, the red line).

In the collinear $1+2+1$ scattering, the two modes η_1 and η_3 can be excited without violating the symmetries of the moduli subspace. The η_1 mode is excited through the lowest mode of the 2-vortex, while the η_3 mode arises from the in-phase excitation of the two 1-vortices. The trajectories for these two cases are shown in Figure 3.31. We observe that, for small amplitudes, the deviations are similar in both scenarios. Initially, the trajectories follow the BPS geodesic quite closely, but at later times they begin to bend towards the crossed-configuration region.

At high amplitudes, the η_1 mode leads to final states in which two vortices leave the collision along the y-axis, while the other two vortices form a multi-bounce state at the origin. For very large amplitudes, the final configuration closely resembles a collinear $1+2+1$ configuration oriented along the y-direction.

The η_3 mode exhibits a repulsive behaviour at high amplitudes, as expected from the spectral flow shown in Figure 3.29. In particular, this repulsive behaviour is clearly visible in the red trajectory. First, the two strongly excited 1-vortices approach the 2-vortex at the origin. Initially, the 2-vortex splits slightly into two 1-vortices along the x-axis, but due to the strong repulsive interaction, the incoming vortices change their direction of motion and scatter at a right angle at the origin. At this point, the η_3 mode reaches the mass threshold and falls down to the η_1 mode (see the light-gray curve behind the η_3 mode in Figure 3.29).

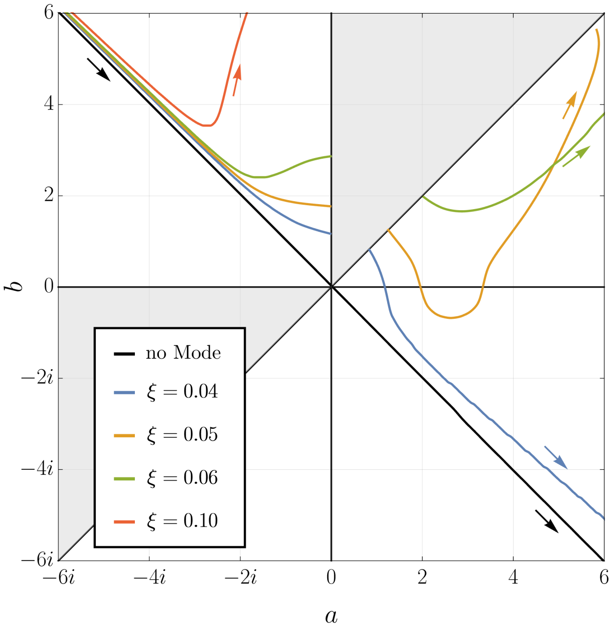

Figure 3.30: This a-b-plot shows the trajectories of the square collision with the η_4 mode excited. The blue line indicates the trajectory used to measure the spectral flow, corresponding to the light-gray curve (behind the η_4 mode) in Figure 3.28.

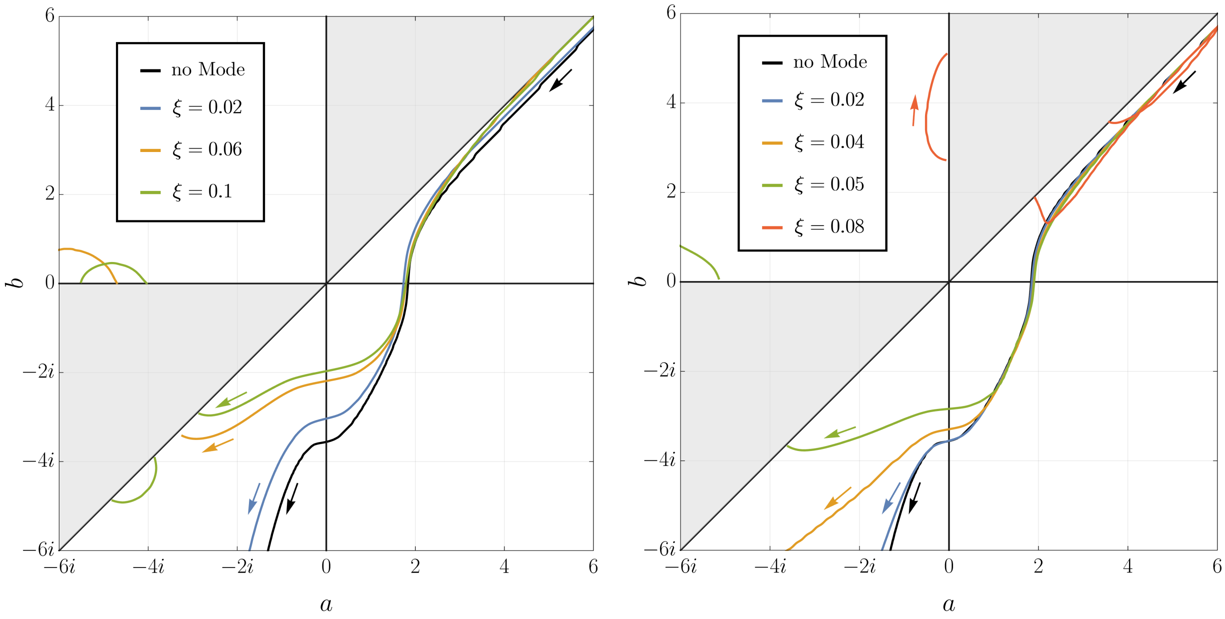

Figure 3.31: These two plots show the trajectories of the collinear $1 + 2 + 1$ scattering with the η_1 mode excited (left) and the η_3 mode excited (right). The blue lines indicate the cases used to measure the spectral flow, corresponding to the light-gray curves behind the η_1 and η_3 modes in Figure 3.29.

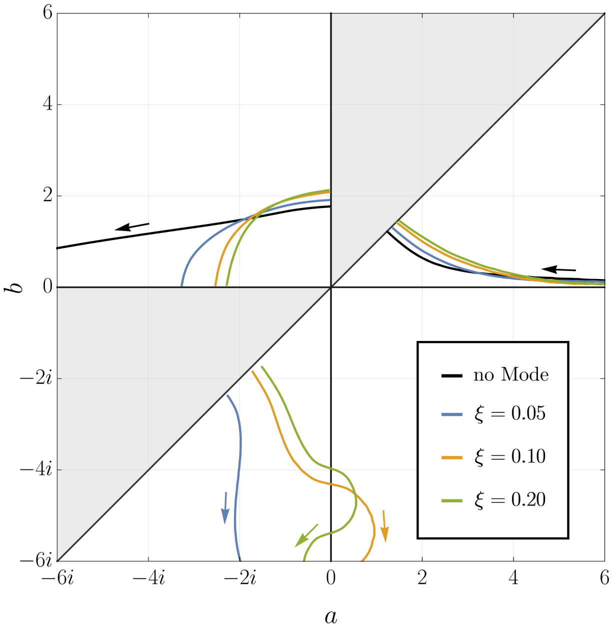

Figure 3.32: This a-b-plot shows the trajectories of the 2+2 collision, where both charge-2 vortices are initially excited with their lowest modes.

This, in turn, causes the two vortices near the origin to attract and to scatter once more, finally resulting in an overall collinear $1 + 2 + 1$ configuration that closely resembles the initial state.

Finally, we briefly comment on the $2 + 2$ scattering. One possible excitation that respects the symmetry of the moduli subspace is given by an in-phase excitation of the lowest charge-2 vortex mode. The resulting trajectories are shown in Figure 3.32. We observe that this mode corresponds to an attractive interaction. After the trajectories enter the cross configuration region, they bend strongly towards the negative imaginary b-direction. Subsequently, the two vortices on the x-axis scatter at a right angle at the origin and move apart along the y-axis. For sufficiently large amplitudes, the vortices in the positive and negative y-half-planes form two multi-bounce bound states that move apart along the y-direction. At very high amplitudes, the maximal bouncing separation becomes rather small, and the final state is approximately given by two charge-2 vortices that are moving apart.

3.6.7 Conclusion and Outlook

In this section, we studied the modification of BPS vortex dynamics due to excitations of massive bound modes. The focus was primarily on scenarios without enhanced symmetry. In particular, we focused on 2-vortex–1-vortex scattering in the charge-3 sector, as well as on square, collinear $1 + 2 + 1$, and $2 + 2$ scatterings in the charge-4 sector. Our analysis proceeded in three steps. First, the BPS geodesic was determined. Second, the spectral flow was analysed. Finally, the modification of the geodesic induced by these excitations was studied qualitatively.

In cases with enhanced symmetry, namely the head-on collision of two vortices, the equilateral triangle and collinear collisions of three vortices, and the square collision of four vortices, the vortices always move along the BPS geodesic with no excitations. The motion along this geodesic can nevertheless change significantly, in the sense that the vortices can move back and forth along the geodesic due to attractive and repulsive mode-generated forces. This can lead to chaotic multi-bounce dynamics. In these cases, a change of the trajectory in the moduli space has never been observed, since the enhanced symmetry of the system cannot be violated by excitations that respect this symmetry.

In less symmetric setups the situation changes fully. We found that the dynamics are significantly affected by mode excitations. In particular, we showed that the behaviour of the trajectory modifications is much more involved than in cases with enhanced symmetry, which have been studied previously [83, 108, 85, 86]. The modification arises mainly from two effects, the mode-generated force and the Coriolis effect. The former originates from a potential on the moduli space, while the latter describes the modification of the moduli space due to non-linear interactions between the bound modes and the zero modes.

An interesting observation from our simulations is that multi-vortex systems appear to prefer final states in which two vortices form a bound multi-bounce configuration. In other words, it seems that excited vortices tend to pair up into long-lived bound states.

Phenomenologically, the change in the dynamics of vortices, or rather strings, due to excitations can have important implications in cosmology. First of all, the appearance of excitations is very natural, since during phase transitions vortices and strings can already form in excited states. Furthermore, thermal and quantum fluctuations, or vortex–vortex collisions as we saw in our numerical simulations, can also excite these modes. Since massive bound modes of vortices and strings generally decay slowly [113], vortices and strings should generically be considered to be excited in cosmological settings. Excitations may also explain the differences observed between string network simulations based on the Nambu–Goto theory [36], where bound modes are not included, and fully field-theoretic simulations [40, 41, 42, 43]. Notice that mode excitations of strings play a crucial role in gravitational radiation emission from string networks and may significantly affect the resulting spectrum.

The work presented in this thesis provides a qualitative study of the mode-driven dynamics of vortices. However, for a more complete understanding of the trajectory modifications, a more detailed analysis of the Coriolis effect is required, which so far has only been studied in detail for a single vortex [112]. Furthermore, a collective coordinate model that implements these excitations would be desirable, as it could predict the spectral structure of the full moduli space.

In addition to vortices and strings, we expect that the dynamics of higher-dimensional solitons, such as non-BPS vortices [114, 115, 116], non-Abelian vortices [117], chiral skyrmions [118], and BPS magnetic monopoles [8, 119], may also be affected by the excitation of massive bound modes or other resonances. For magnetic monopoles, the first fully field-theoretic simulations of the unexcited dynamics were performed within this thesis (see next section). Extending this analysis by including mode excitations is non-trivial, but feasible in the near future. Moreover, it was recently pointed out in [120] that the excitation of "memory modes" can modify the dynamics of black holes. This suggests that the study of the mode-driven dynamics in solitons may also give a better understanding of black hole dynamics.

3.7 Simulations of Magnetic Monopoles Collisions

Although some new aspects were added and discussions were rephrased, this section is an ad verbatim reproduction with respect to equations and figures of the paper "Simulations of Magnetic Monopole Collisions" that I published together with my collaborators Gia Dvali, Josef E. Seitz, and Juan Sebastián Valbuena-Bermúdez [12].

The final part of this chapter continues the analysis of soliton–soliton collisions by turning to the collision of magnetic monopoles. Compared to vortices, monopoles share several similarities, as we will see throughout this section, but they also exhibit important differences that make the analysis more involved.

Since magnetic monopoles carry magnetic charge, they source a long-range magnetic field associated with the massless photon in the theory. The Higgs boson provides another channel for interactions. However, due to its non-zero mass, the corresponding scalar-mediated force is typically suppressed and thus of short range. In the Bogomol'nyi–Prasad–Sommerfield (BPS) limit [47, 30], the Higgs boson mass $m_h \to 0$ (with the VEV fixed), the Higgs-mediated interaction becomes long-range and can compete with the magnetic force. Manton showed that for two equally charged magnetic monopoles, the attractive scalar force exactly cancels the repulsive magnetic force [4]. This motivates the study of collisions of slowly moving magnetic monopoles.

Similar to vortices, their dynamics can be approximated by geodesics on their moduli space, which exhibits a particularly rich structure in the BPS limit due to the absence of forces between equally charged monopoles. This moduli space framework for describing monopole dynamics was introduced by Manton [8] and later mathematically confirmed by Stuart [121]. For the case of two monopoles, the corresponding moduli space is given by the Atiyah–Hitchin manifold [9, 10]. This manifold sets the basis for studying monopole collisions within the moduli space approximation. In [10], the scattering of two magnetic monopoles was analysed, including the famous right-angle scattering in a head-on collision. Subsequently, a variety of further scattering scenarios for monopole configurations with particular symmetries have been investigated [5].

The aim of this section is to verify these predictions within a fully field-theoretic description by solving the complete equations of motion through numerical simulations. To enable accurate simulations, we developed several approximate analytic configurations for different multi-monopole setups. The scattering processes we investigated include planar 90°, 60°, and 45° scatterings for systems of two, three, and four monopoles, respectively. In addition, we simulated non-planar scatterings involving toroidal higher-charged monopoles which interact with a single charge-1 monopole or with another toroidal monopole.

The structure of this section is as follows. First, in Section 3.7.1, we review the fundamentals of the moduli space approximation for 't Hooft–Polyakov magnetic monopoles. In Section 3.7.2, we numerically compute the toroidal structure of static charge-N monopoles. The approximate initial configurations used in our simulations are presented for two monopoles in Section 3.7.3, and for more than two monopoles in Section 3.7.4. Finally, the results of our numerical simulations are discussed: planar scattering scenarios in Section 3.7.5, and non-planar scattering in Section 3.7.6.

3.7.1 Moduli Space Structure for Two Magnetic Monopoles

Magnetic monopoles are solutions to the classical field equations that represent localized, finite-energy configurations. For a fixed total magnetic charge, there exists a continuous family of solutions that are degenerate in energy. In the moduli space approximation, we focus on those configurations that are related to each other through continuous transformations, like for example spatial translation. In Section 3.5, we have already found the moduli space structure for a single magnetic monopole. Here we want to focus on two magnetic monopoles. It turns out that in the BPS limit, the moduli space is particularly interesting, because in this limit there is no long-range interaction force [4].

In the low-energy regime, the dynamics of monopoles can be approximated by promoting the collective coordinates to time-dependent variables. Within this moduli space approximation, the monopole behaves like a point particle, and its low-energy motion is governed by geodesics on the moduli space [8].

As mentioned earlier, in the case of a single monopole, three collective coordinates describe the position of the monopole core. In addition, there is a fourth coordinate associated with a global $U(1)$ transformation. Exciting the mode corresponding to this coordinate gives rise to an electric charge on the monopole. The full moduli space structure of a single monopole is $\mathcal{M} = \mathbb{R}^3 \times S^1$.

For two magnetic monopoles, there are four collective coordinates analogous to the single-monopole case: three describing the centre of mass and one associated with the global $U(1)$ transformation responsible for electric charge. In the BPS regime, where long-range forces are not present, there are four additional collective coordinates. One corresponds to the separation between the monopoles and the remaining three describe rotations around the three spatial axes. As we will see explicitly later, a two-monopole configuration is not axially symmetric and so the rotation around the axis connecting the two monopoles is non-trivial. Therefore, all three rotational coordinates must be included. It can be shown that the moduli space describing the low-energy dynamics of two monopoles is [10, 25]

$$\mathcal{M} = \mathbb{R}^3 \times \frac{S^1 \times \mathcal{M}_{AH}}{\mathbb{Z}_2}\,, \tag{3.76}$$

where the Atiyah–Hitchin manifold $\mathcal{M}_{AH}$ is spanned by the four last mentioned coordinates.

A submanifold of the Atiyah–Hitchin manifold that is particularly relevant for our discussion is the surface[12] with the metric

$$\mathrm{d}s^2 = f^2(\rho)\,\mathrm{d}\rho^2 + a^2(\rho)\,\mathrm{d}\varphi^2\,, \tag{3.77}$$

where $\varphi \in [0, \pi]$, and $f(\rho) \to 1$ and $a(\rho) \to \rho$ as $\rho \to \infty$. This surface is $\mathbb{R}^2/\mathbb{Z}_2$ and has the geometry of a cone. A more detailed analysis [10] shows that $a(\rho) \to 0$ faster than linear as $\rho \to 0$, meaning the tip of the cone is rounded. Because we are considering two identical monopoles, interchanging them leaves the physical configuration unchanged. That's why we have to include the $\mathbb{Z}_2$, which in turn gives rise to the conical structure of the submanifold. This moduli subspace has a similar structure as the moduli space for two vortices described in Subsection 3.6.1.

This submanifold fully captures the monopole dynamics when their motion is restricted to a plane, which we will refer to as the x-y-plane. Scattering within this plane corresponds to the geodesic that passes through the tip of the smoothed cone (see Figure 3.33 (left)). Since φ ranges from 0 to π, the angle φ changes by $\Delta\varphi = \pi/2$ when passing over the tip. As a result, a head-on collision of monopoles in the x-y-plane leads to right-angle scattering similar to the right-angle scattering of vortices [106].

Another relevant submanifold is the one describing monopole motion in the x-z- and y-z-planes[13]. For both planes, we can apply the same symmetry argument as in the x-y-case. Since the two monopoles are identical, the submanifold should again have a conic structure. However, a more detailed analysis [10] shows that, in both cases, the tip of the cone opens up, giving the shape of a hopper. As a result, the origin of the moduli space is given by a full circle. The circular tip of the hopper describing the x-z-plane can be identified with that of the y-z-plane. Combining these two geometries yields the so-called "Atiyah–Hitchin trumpet", which is illustrated in Figure 3.33 (right).

For a head-on collision, the geodesic corresponds to the path passing straight through the throat of the trumpet. As the monopole crosses the midpoint of the throat, it changes the plane of its motion, resulting in a change of the direction by 90°, which is consistent with the previous description on the smoothed cone. If the monopoles collide with a small impact parameter along the z-direction, there is angular momentum within the x-z-plane. The geodesic motion in the moduli space would have the form of a spiral entering the throat of the trumpet, and upon emerging on the other side, this angular momentum becomes visible as an electric charge. Therefore, two monopoles colliding with a small impact parameter can scatter into dyons [9, 122]. For larger impact parameters, the monopoles remain in their original plane and deflect slightly when they pass each other.

In the low energy regime, the kinetic energy of a monopole is $\sim m_{\mathrm{M}} u^2$, with u being the velocity and m_{M} being the monopole mass. The moduli space approximation doesn't include the emission of radiation and thus, the velocity of the monopoles before and after the scattering should be the same. However, because we can think of the monopoles as a composite object that consists by parts of charged W-bosons, this cannot be completely right and so during the scattering, there should be radiation emitted. Nevertheless, it was found in [123] that this radiation emission is suppressed by a factor of $\sim u^5$.

---

[12] denoted as Σ_1 in the notation of [10].

[13] denoted as Σ_2 in the notation of [10].

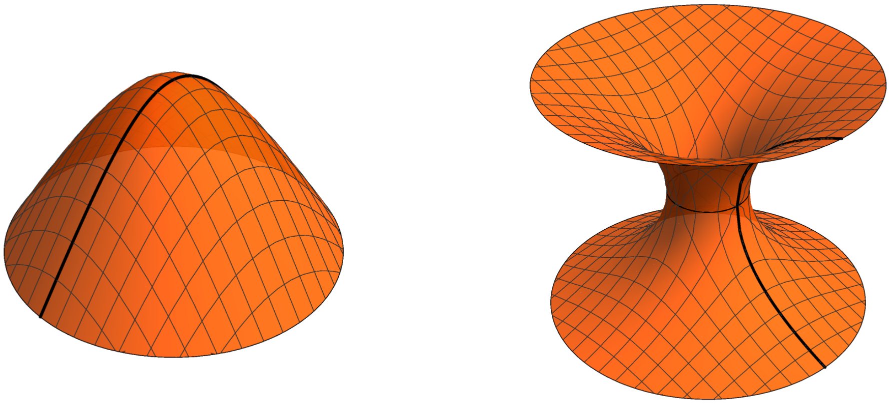

Figure 3.33: These two illustrations depict the structure of the moduli space for two magnetic monopoles. The cone with the rounded tip represents the monopole trajectories within the x-y-plane. The trumpet-shaped manifold characterizes the monopole motion within the x-z- and y-z-planes.

Another limitation of the moduli space approximation comes from classical decoherence effects, which occur when monopoles approach each other at distances $\sim 1/m_v$. In this regime, the individual monopole profiles begin to overlap. According to [121], such decoherence becomes relevant when monopoles remain close together for times $t \gtrsim 1/v$.

In conclusion, the moduli space approximation is only valid if the inner structure of the monopoles remains approximately undeformed. In Section 3.7.5, we will test these statements by using relativistic collision velocities in our numerical simulations.

This section provided a brief overview of the essential concepts needed to understand the right-angle scattering of magnetic monopoles, which is investigated numerically in this work. For more details, we refer the reader to the reviews [25, 10] and the lecture notes [124]. Furthermore, an illustrative explanation of the moduli space for two magnetic monopoles, summarizing some of the above discussion, is provided in the following video: `https://youtu.be/2DfE9ty727c`

3.7.2 Charge-n Magnetic Monopoles

After the discovery of the magnetic monopole solution, Weinberg and Guth [46] asked the question whether monopoles with higher magnetic charge could exist. They proved that a spherically symmetric configuration carrying multiple units of magnetic charge cannot have finite energy. However, later it was found that higher-charged monopoles do exist, if the energy distribution breaks spherical symmetry. The simplest realizations exhibit toroidal symmetry [125, 126, 127]. Using a numerical relaxation method (see Appendix A.3), we computed toroidal solutions for BPS monopoles with charges two, three, and four in units of $4\pi/g$. Energy contour plots of these configurations are shown in Figure 3.34. We can observe that the radius of the torus increases with magnetic charge. For the numerical

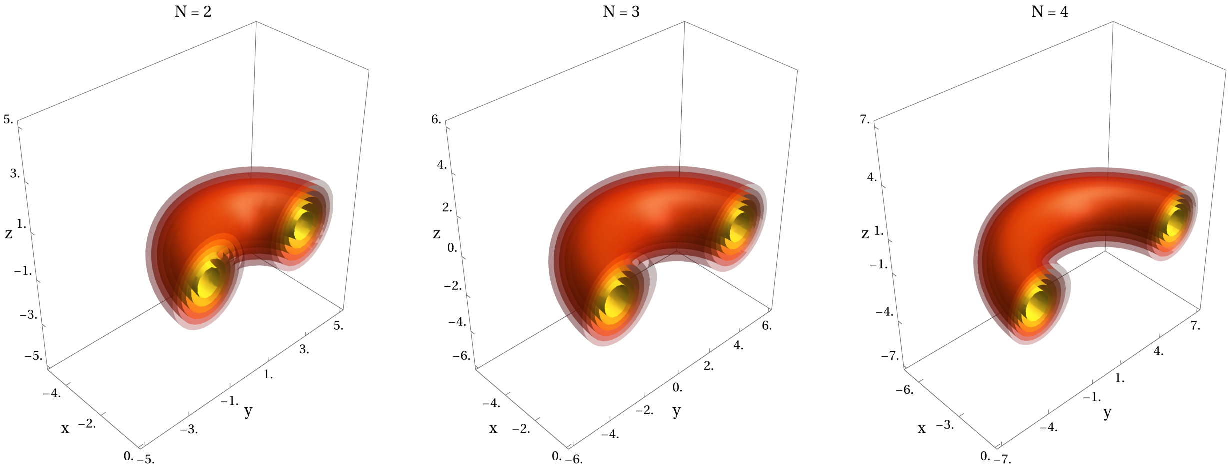

Figure 3.34: In this figures three contour plots for the distribution of the energy density of toroidal charge-2, -3, and -4 monopoles in the BPS limit are presented. The contours show energy densities within the intervals $[0.045, 0.07]$, $[0.032, 0.053]$, and $[0.03, 0.045]$ (in units of m_v^4/g^2), respectively. The length values are given in units of m_v^{-1}.

relaxation, we used an initial configuration of the form

$$\begin{aligned}\hat{\phi}^1 &= \cos(n\varphi)\sin\theta\,,\\ \hat{\phi}^2 &= \sin(n\varphi)\sin\theta\,,\\ \hat{\phi}^3 &= \cos\theta\,.\end{aligned} \tag{3.78}$$

For ensuring finite energy ($(D_i\phi)^a \to 0$ for $r \to \infty$), we took the gauge field to be

$$W_i^a \xrightarrow{r\to\infty} -\frac{1}{g}\varepsilon_{abc}\,\hat{\phi}^b\partial_i\hat{\phi}^c\,. \tag{3.79}$$

Taking parameters beyond the BPS limit does not lead to stable higher-charged monopoles. Nevertheless, we can still investigate the structure of these objects using the numerical relaxation method. Figure 3.35 shows a contour plot of the energy density for a charge-2 monopole with $m_h/m_v = 0.1$. In contrast to the BPS case, we observe that energy appears at the centre of the torus. As m_h/m_v increases, this central energy density grows, and the overall size of the monopole shrinks. The total energy of this configuration is larger than that of two well-separated charge-1 monopoles, meaning that the charge-2 configuration is unstable and decays into two individual monopoles.

3.7.3 Two-Monopole Configuration

Remarkably, an exact solution describing two separated BPS monopoles was constructed in [128]. However, it does not directly give an expression for an initial configuration of two Lorentz-boosted monopoles, which is required in the simulations. In this section, we present an approach for constructing an approximate solution describing charge-2 monopoles.

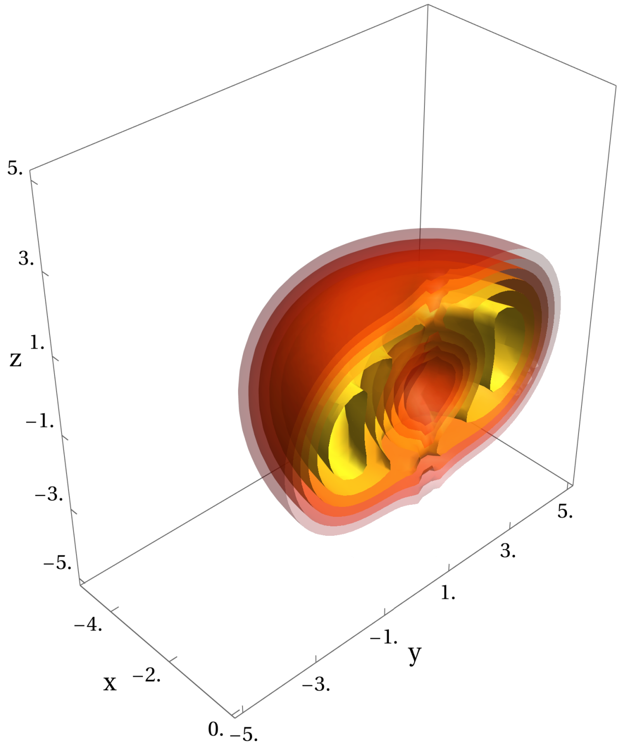

Figure 3.35: This contour plot illustrates the energy density of a non-BPS charge-2 monopole with $m_h/m_v = 0.1$. The contours represent energy densities within the range $[0.04, 0.065]$ (in units of m_v^4/g^2). As visible in the plot, energy appears in the centre of the torus. The length scales in the plot are given in units of m_v^{-1}.

The motivation came from starting with a winding-2 scalar field configuration (see previous section). In the limit where the distance between the two monopoles is zero or equivalently, for $r \to \infty$, the configuration should reduce to that of a single winding-2 monopole. This observation led to the idea of splitting 2φ into $\varphi_1 + \varphi_2$, where φ_1 and φ_2 are the azimuthal angles around the first and second monopole, respectively. The ansatz is then given by

$$\begin{aligned} \hat{\phi}^1 &= \cos(\varphi_1 + \varphi_2)\sin\theta\,, \\ \hat{\phi}^2 &= \sin(\varphi_1 + \varphi_2)\sin\theta\,, \\ \hat{\phi}^3 &= \cos\theta\,, \end{aligned} \tag{3.80}$$

with

$$\begin{aligned} \varphi_{1,2} &= \operatorname{arctan2}(y, x - x_{1,2})\,, \\ \theta &= \arccos\left(\frac{z}{r_1}\right)\Theta_H(-x) + \arccos\left(\frac{z}{r_2}\right)\Theta_H(x)\,, \\ r_{1,2} &= \sqrt{(x - x_{1,2})^2 + y^2 + z^2}\,, \end{aligned}$$

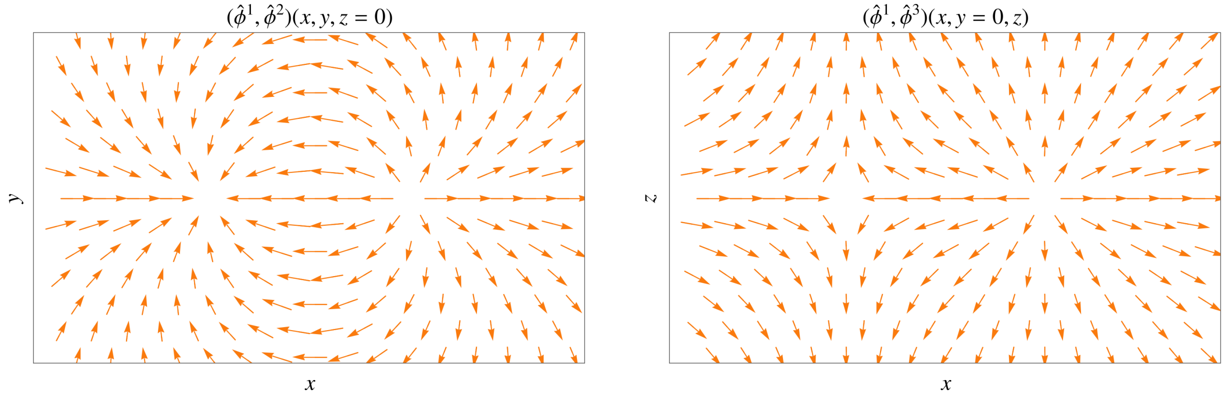

Figure 3.36: These vector plots illustrate the direction of the scalar field: $(\hat{\phi}^1, \hat{\phi}^2)^T$ in the x-y-plane (top) and $(\hat{\phi}^1, \hat{\phi}^3)^T$ in the x-z-plane (bottom).

where Θ_H is the Heaviside step function, and $x_1 = -x_2 < 0$.

A vector plot of $\hat{\phi}^a$ in the x-y- and x-z-planes is shown in Figure 3.36. In contrast to an axially symmetric monopole–anti-monopole configuration, the figure clearly shows that a configuration with two separated, equally-charged monopoles has no axial symmetry. Once a good behaviour of the scalar field is found, one can write down a complete approximate ansatz:

$$\phi^a = \frac{1}{m_v g} \frac{H(r_1)}{r_1} \frac{H(r_2)}{r_2} \hat{\phi}^a \,, \tag{3.81}$$

$$W_i^a = -\frac{1}{g}(1 - K(r_1))(1 - K(r_2)) \, \varepsilon_{abc} \, \hat{\phi}^b \partial_i \hat{\phi}^c \,, \tag{3.82}$$

where $H(r)$ and $K(r)$ are the profile function given by the BPS solution (2.86), (2.87).

Another possibility to obtain a configuration with two magnetic monopoles is by modifying the monopole–anti-monopole ansatz with maximal twist, given in equation (3.27). As can be seen from Figure 3.14 (right), the shape of the magnetic field lines resembles that of a monopole–monopole configuration, with the only difference being that the direction of the field lines has the wrong sign in one half-plane. This incorrect sign can be compensated by introducing a sign flip at $z = 0$ in the definition of the angle φ. The resulting configuration indeed describes two magnetic monopoles of the same charge. However, it turns out that this construction is slightly less accurate than the one presented above. For this reason, we do not use this ansatz and instead focus on the previous method.[14]

3.7.4 n-Monopole Configuration

Using the insights from the two-monopole configuration, one can generalize the setup to n monopoles arranged with cyclic symmetry around the z-axis in the x-y-plane. The idea

---

[14] For more details on the modification of the monopole–anti-monopole ansatz to obtain a monopole–monopole configuration, the interested reader is referred to [12].

remains the same. In the limit where the separation distance between the monopoles goes to zero, we should recover a winding-n scalar field configuration. To achieve this, we replace $n\varphi$ with $\sum_{k=1}^{n}\varphi_k$, where each φ_k denotes the azimuthal angle around the kth monopole. Inserting this into the normalized scalar field vector yields

$$\begin{aligned}\hat{\phi}^1 &= \cos\left(\sum_k \varphi_k\right)\sin\theta\,,\\ \hat{\phi}^2 &= \sin\left(\sum_k \varphi_k\right)\sin\theta\,,\\ \hat{\phi}^3 &= \cos\theta\,,\end{aligned}\tag{3.83}$$

with

$$\begin{aligned}\varphi_k =& \operatorname{arctan2}(y_k, x_k)\,,\\ \theta =& \sum_k \arccos\left(\frac{z}{r_k}\right)\\ &\cdot\Theta_H\left(\cos\left(\alpha_k-\Delta\alpha/2\right)x+\sin\left(\alpha_k-\Delta\alpha/2\right)y\right)\\ &\cdot\Theta_H\left(\cos\left(\alpha_k+\Delta\alpha/2\right)x+\sin\left(\alpha_k+\Delta\alpha/2\right)y\right),\\ r_k =& \sqrt{x_k^2+y_k^2+z^2}\,.\end{aligned}\tag{3.84}$$

The positions of the monopoles in the x-y-plane are given by the coordinates x_k and y_k. They have to be chosen such that the monopoles are arranged in a cyclically symmetric way:

$$\begin{aligned}x_k &= \cos(\alpha_k)x+\sin(\alpha_k)y-R\,,\\ y_k &= \cos(\alpha_k)y-\sin(\alpha_k)x\,,\end{aligned}\tag{3.85}$$

with R being the radial distance from the origin to each monopole, and α_k is the azimuthal angle around the z-axis specifying the position of the kth monopole. The angular separation between two neighbouring monopoles is given by $\Delta\alpha$. To ensure cyclic symmetry, we set $\Delta\alpha = 2\pi/3$ for a configuration with three monopoles. In this case, we choose the angular positions $\alpha_k = \{\pi/3, \pi, 5\pi/3\}$. For four monopoles, we have to choose $\Delta\alpha = \pi/2$ and take $\alpha_k = \{0, \pi/2, \pi, 3\pi/2\}$.

3.7.5 Numerical Simulations

The information about the motion of the magnetic monopoles can be included by applying Lorentz boosts to the initial configurations. Since we have an analytic approximate ansatz that includes the positions of the monopoles, these boosts can be implemented straightforwardly and analogously to the previously discussed setups in this chapter. In the case of two monopoles, one can simply replace $x - x_{1,2}$ with $\gamma(x - x_{1,2} - u_{1,2}t)$, where u_1 and u_2 are the velocities of the two monopoles. In all processes, we assume that the magnitudes of the velocities are the same. Therefore, the Lorentz factor γ is identical for all monopoles. For a general ansatz of n monopoles in planar scattering, the coordinates x_k in equation (3.85) are boosted according to

$$x_k = \gamma\big(\cos(\alpha_k)x + \sin(\alpha_k)y - R - ut\big)\,, \tag{3.86}$$

with u being the absolute value of the velocity towards the origin of each monopole. Using the boosted scalar field ansatz provides the full approximate initial configuration, including the time derivatives of the scalar fields. Furthermore, by inserting the boosted scalar field direction into the gauge field ansatz

$$W_i^a = -\frac{1}{g}\left(\prod_{k=1}^{n}(1 - K(r_k))\right)\varepsilon_{abc}\,\hat{\phi}^b\partial_i\hat{\phi}^c\,, \tag{3.87}$$

we can also obtain the boosted ansatz for the gauge field.

For the time iteration we employed the Crank–Nicolson method with two iterations. Dirichlet boundary conditions were chosen and the results were cross-checked using absorbing boundaries and larger lattice sizes. The standard lattice size used was a cubic lattice with 240^3 lattice points and a lattice spacing of $0.25\,m_v^{-1}$. For the time step, we used $\Delta t = 0.1\,m_v^{-1}$. For fixing the gauge, we used the Lorenz gauge, $\partial_\mu W_a^\mu = 0$. More details on the numerical methods can be found in Appendix A.

Using the approximate solutions from the previous two subsections, we were able to simulate head-on collisions of monopoles. Let us begin with the scattering of two monopoles. In the first simulation, the monopole velocity was set to 0.2. Three snapshots of the scattering are shown in Figure 3.37, and full animations of all simulations are available at:
`https://youtu.be/a2wOOo2AAHI`
From the simulation, we observe that the monopoles scatter by 90° within the x-y-plane. When the two monopoles meet at the origin, the energy density distributes in a toroidal shape, forming the intermediate charge-2 monopole configuration, which we have already discussed in Section 3.7.2. All these observations are in perfect agreement with the predictions from the moduli space approximation [10].

Initially, when the monopoles are far apart, the configuration seems to exhibit axial symmetry. However, as already seen in Figure 3.36, it becomes clear that the configuration has no axial symmetry. This becomes even more apparent when the monopoles form the toroidal intermediate state during the scattering process. Therefore, the internal structure of the scalar field sets the specific plane in which the monopoles will scatter, here the x-y-plane. Analysing the scalar field direction in two-dimensional slices of the two-monopole configuration, as shown in Figure 3.36, we observe similarities with the scattering behaviour of vortices. Considering the complex scalar field $\psi = \mathrm{Re}(\psi) + i\mathrm{Im}(\psi)$ for two vortices of same winding, a vector plot reveals a structure similar to Figure 3.36 (left). In Section 3.6.1 we showed already that two vortices scatter at 90°, due to a similar moduli space structure. Applying this analogy to the two-monopole case suggests that, within the x-y-plane, the

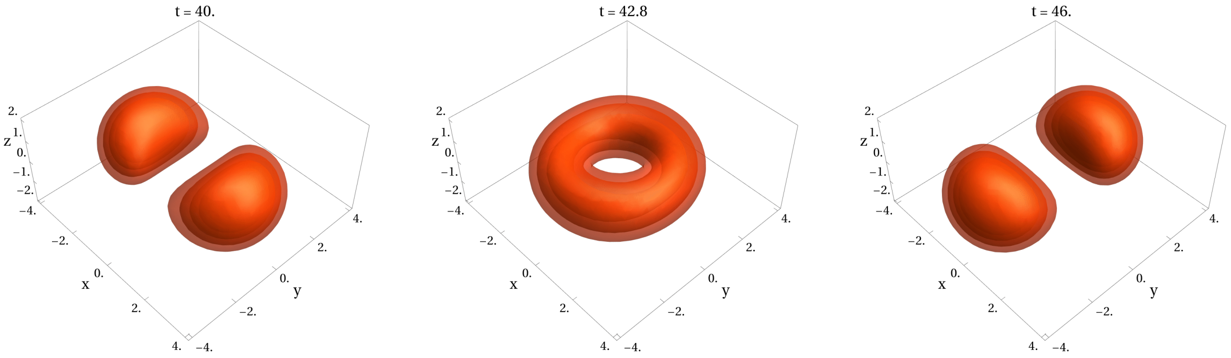

Figure 3.37: This figure shows the energy density for three snapshots of the two-monopole head-on collision in contour plots. We observe that the monopoles scatter with a right-angle, and when they meet at the origin, they briefly form a toroidal state. Length and time are given in units of m_v^{-1}, and the energy densities shown are above $0.06\, m_v^4/g^2$.

two-dimensional winding must be preserved and thus leading to the 90° scattering. In contrast, the scalar field direction in the x-z-plane (Figure 3.36 (right)) resembles that of a vortex–anti-vortex pair. In this system, one expects annihilation of the vortices. While the monopoles obviously don't annihilate, they leave the x-z-plane in a perpendicular direction, so that the effective two-dimensional winding vanishes. This analogy with vortex dynamics may help for constructing more complicated monopole configurations. Some ideas will be discussed in Section 3.7.6.

We used the simulation data to track the monopole zeros, i.e. the points where all components of the scalar field vanish ($\phi^a = 0$). We observed that, for a large separation between the monopoles, the zeros are localized in the centre of the monopole cores. As the monopoles approach each other, the zeros leave the cores and move towards the origin, where they meet when the torus forms. At this point, they change the direction of motion by 90°, and once the monopoles are again sufficiently far apart, the zeros re-enter the cores. This behaviour is in complete agreement with theoretical expectations, as the two-monopole system has a Z_2 symmetry that must be preserved throughout the time evolution. Tracking the position of the zeros also allowed us to determine the monopole speeds before and after the collision. The trajectory of the zeros for an initial monopole velocity of $u = 0.2$ is shown in Figure 3.38. We found that the velocity change after the scattering is about $\Delta u \approx 0.01$, meaning that almost no radiation is emitted during the process. Even for a relativistic initial velocity of $u = 0.62$, the velocity change is only $\Delta u \approx 0.04$. Manton and Samols showed in [123] that radiation emission is suppressed in this scenario, because the two-monopole configuration has no dipole moment. The leading contribution arises from the quadrupole term.

In the figure, it can also be seen that the velocities of the zeros become very large when the monopoles approach each other to form the torus. We observed that the velocities can even exceed the speed of light. However, since the zeros do not correspond to physically measurable quantities like energy, this is not in contradiction with special relativity. The energy of the system still propagates at speeds below the speed of light along the torus.

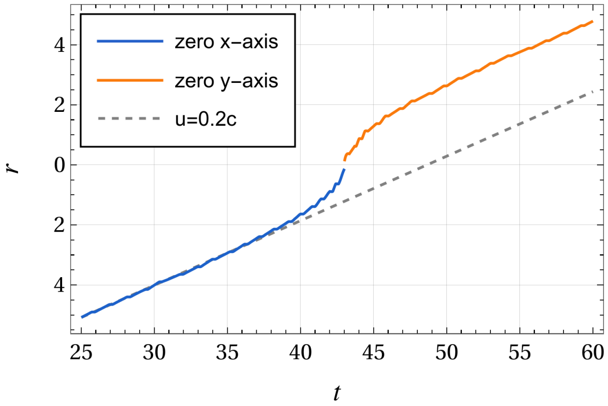

Figure 3.38: This figure shows the radial distance between the zeros of the scalar field and the origin with respect to time. The blue line illustrates the initial motion along the x-axis and the orange line shows the motion of the zeros after the right-angle scattering along the y-axis. Length and time are given in units of m_v^{-1}.

An advantage of our fully field-theoretic simulations is that they allow us to test the robustness of the moduli space predictions beyond the BPS limit and at relativistic velocities. As discussed in Section 3.7.1, in these regimes the moduli approximation ceases to be valid.

We investigated velocities up to $u = 0.8$, for which the characteristic right-angle scattering remained consistently present. However, we observed that the axially symmetric toroidal structure becomes distorted. While the energy of the intermediate charge-2 monopole is still distributed around the origin, with no energy at the origin itself, the torus shape becomes more rectangular, with slightly flattened edges. In addition, the overall size of the charge-2 object is smaller. The deformation of the torus is clearly visible in Figure 3.39. The deformation arises due to the Lorentz contraction of the initially separated monopoles. Rather than remaining spherically symmetric, the energy density takes on an ellipsoidal form.

Besides relativistic velocities, we went beyond the moduli approximation by considering non-BPS regimes, i.e. cases with a finite Higgs mass, $m_h \neq 0$. In this scenario, the scalar force is exponentially suppressed for separations $r > m_h^{-1}$, thus leaving the magnetic repulsion as the dominant force. Hence, an energy barrier emerges that the monopoles have to overcome before the scalar attraction becomes relevant.

Imagining the monopoles as point particles, one can estimate the energy required to overcome the barrier. The magnetic potential takes the form

$$\Delta E_{\mathrm{magn}} \sim \frac{q_m^2}{r} \sim \frac{1}{g^2 r} \,. \tag{3.88}$$

Therefore, bringing the monopoles with mass m_{M} to separations of order $r \sim m_h^{-1}$ requires

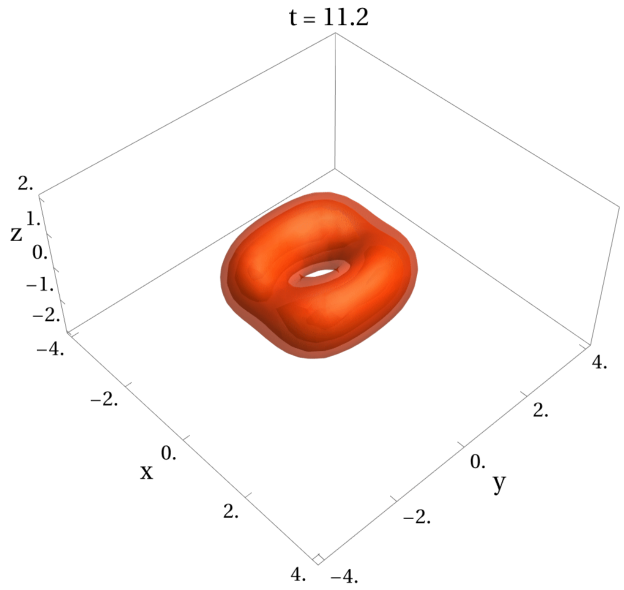

Figure 3.39: This figure shows the energy density for a relativistic scattering (velocity $u = 0.6$) of two monopoles in a contour plot. A torus-like structure is still forming, but the distribution of the density is not axially symmetric as in the low energy scattering. The contours show energy densities bigger than $0.015\, m_v^4/g^2$. The length and time values are given in units of m_v^{-1}.

an energy of

$$\Delta E_{\text{magn}} \sim \frac{m_h}{g^2} \sim \frac{m_h}{m_v}\, m_{\text{M}}\,.$$

Consequently, the Lorentz factor necessary to overcome the magnetic barrier, and thus to allow for right-angle scattering, is

$$\gamma - 1 \sim \frac{m_h}{m_v}\,. \tag{3.89}$$

Here we assumed that the magnetic repulsive $1/r^2$ force is present for separations $r \gtrsim m_h^{-1}$. However, this is only valid for $m_v \gtrsim m_h$. For $m_v \lesssim m_h$, the Coulomb-like interaction exists only for $r \gg m_v^{-1}$. When the monopole separation is within the range $m_h^{-1} \lesssim r \lesssim m_v^{-1}$, they experience a strong constant repulsive force. This regime can be viewed as the limit $g \to 0$ for $r \ll m_v^{-1}$, and thus resembles the interaction between global monopoles, where the interaction potential is linear.

In the above estimates we treated the monopoles as point-like objects and neglected non-linear interactions. In particular, we did not account for their extended structures, which are compressed by Lorentz contraction before and after the collision, and are deformed into a torus-like structure during the collision. Moreover, non-linear effects can also play a significant role at short distances, which we have also neglected in the estimations. Nonetheless, our numerical simulations show that velocities below $u = 0.8$ are sufficient to produce 90° scattering in the interval $m_h/m_v \in [0, 1.0]$. We also observed the strong repulsive force characteristic for global monopoles. In this case, however, the interaction is so strong that right-angle scattering could not be realized in the simulation.

The ansatz developed in Section 3.7.4 allowed us to study the planar scattering of n monopoles arranged to preserve a cyclic symmetry $\mathcal{C}_n$. We observed that three monopoles scatter by 60°, while four monopoles scatter by 45°, consistent with the expectations from the moduli space approximation. As in the two-monopole case, the monopoles form a toroidal charge-n configuration during the collision. Animated results of our simulations are available in the following video: `https://youtu.be/a2wOOo2AAHI`

All the observations made for two monopoles also hold for three and four monopoles. This includes the deformation of the toroidal structure at relativistic velocities. Furthermore, the behaviour of the zeros is similar. Initially, they are in the cores of the separated monopoles. As the three or four monopoles approach each other, the zeros leave their cores and form a single zero of winding three or four, respectively, in the origin. The velocities of the zeros can again be superluminal.

3.7.6 Non-planar Scattering

All the scattering processes described above were planar, meaning that the monopoles remained in the x-y-plane throughout the entire process. However, there also exist non-planar scattering processes, in which the monopoles can leave the x-y-plane after the collision. Although the energy density in the infinite separation limit always appears identical for all scalar field orientations, the outcome of a scattering process depends very sensitively on the internal structure of the scalar field. This we already observed in the scattering of two monopoles. While the energy density of two monopoles at infinite separation seems to be axially symmetric, it provides no information about the plane in which the monopoles will scatter. Here, the knowledge of the internal structure is essential to determine the scattering plane. In the case of an N-monopole scattering process with $N > 2$, the monopoles do not need to remain in a single plane and can acquire momentum in the perpendicular z-direction.

A useful tool to study how monopoles scatter are rational maps. In [5], Hitchin, Manton, and Murray discussed several special cyclically symmetric configurations. For example, three monopoles placed cyclically symmetrically around the z-axis in the x-y-plane can scatter with three different outcomes. One of these is the planar scenario discussed in the previous section. Another possibility is a configuration in which the monopoles scatter into a single monopole that moves along the positive z-axis while a toroidal charge-2 monopole moves along the negative z-axis. The third outcome is the mirror image of this process: a single monopole moving in the negative z-direction and a toroidal charge-2 monopole moving in the positive z-direction. When the monopoles meet at the origin, the energy density takes the form of a tetrahedral structure, which is discussed in more detail in [6].

Another example discussed in [5] is a configuration of four monopoles arranged cyclically symmetrically. In this case, there are four possible scattering outcomes. The first is the planar scenario, as described in the previous section. Two further possibilities correspond to a scattering into a single monopole and a toroidal charge-3 monopole moving in opposite

z-directions. In this case, the monopoles pass through an intermediate state with the shape of a pyramid. The final possibility is a scattering into two toroidal charge-2 monopoles moving in opposite z-directions. During the collision, the intermediate state has a cubic structure [6].[15]

For simulating such processes, an initial configuration that has the correct orientation of the scalar field is needed. Such configurations are not known yet, but before explaining how we solved this issue, we want to present some ideas of how these configurations should look like. Here, the concept of the $2D$ winding in the x-y-plane can be used. In the previous section, we already mentioned that for two monopoles the scalar field carries a conserved $2D$-dimensional winding number of two in the x-y-plane. This explains why the two monopoles remain in the x-y-plane. As an explicit example for a non-planar case, consider four monopoles. In the planar case, each monopole contributes with a $2D$ winding number of one. If these are the only windings present in the x-y-plane, the total winding number is four, which must be conserved, and the four monopoles will therefore undergo planar 45° scattering. To obtain a non-planar behaviour such as the cubic scattering, $2D$ anti-windings must be introduced. In this case, two of the monopoles contribute with a $2D$ winding of one and the other two monopoles with a $2D$ anti-winding of one, yielding a total $2D$ winding number of zero. This allows the monopoles to leave the x-y-plane to perform non-planar scattering. This way of interpreting the role of the $2D$ winding number is fully consistent with the behaviour observed in our numerical simulations presented below. Understanding these structures can help for finding explicit approximate analytic configurations that can be used for simulations of non-planar scatterings.

Another useful tool for constructing such configurations may be rational maps. For simple non-toroidal multi-monopole configurations, such as the tetrahedral charge-3 monopole or the cubic charge-4 monopole, explicit rational maps describing the correct structures are already known [7]. These rational maps can provide a starting point for deriving the corresponding scalar and gauge field solutions. For multiple separated charge-1 monopoles, these solutions should be recovered in the limit where the distance between the monopoles goes to zero. Therefore, rational maps may offer valuable guidance in identifying the correct configurations.

Since finding these solutions is still work in progress, we simulated non-planar processes by starting from the outgoing configurations: a toroidal charge-n_1 monopole and a toroidal charge-n_2 monopole separated along the z-axis. Scattering them in a head-on collision along the z-axis results in a splitting into $n_1 + n_2$ charge-1 monopoles arranged with cyclic symmetry.

---

[15] Note that other structures can also arise in multi-monopole configurations without cyclic symmetry [129].

The scalar field configurations $\hat{\phi}_1^a$ and $\hat{\phi}_2^a$ of the charge-n_1 and -n_2 monopole configurations placed at z_1 and z_2 respectively are

$$\begin{aligned} \hat{\phi}_1^1 &= \cos(n_1\varphi)\sin\theta_1\,, & \hat{\phi}_2^1 &= -\cos(n_2\varphi)\sin\theta_2\,, \\ \hat{\phi}_1^2 &= \sin(n_1\varphi)\sin\theta_1\,, & \hat{\phi}_2^2 &= \sin(n_2\varphi)\sin\theta_2\,, \\ \hat{\phi}_1^3 &= \cos\theta_1\,, & \hat{\phi}_2^3 &= -\cos\theta_2\,, \end{aligned} \tag{3.90}$$

with

$$\begin{aligned} \varphi &= \operatorname{arctan2}(y,x)\,, \\ \theta_{1,2} &= \arccos\left(\frac{z-z_{1,2}}{r_{1,2}}\right), \\ r &= \sqrt{x^2+y^2+(z-z_{1,2})^2}\,. \end{aligned} \tag{3.91}$$

We can combine these two configurations using an exponential smoothing function to ensure that the scalar field remains continuous:

$$\hat{\phi}^a = \frac{1}{1+e^{\beta m_v z}}\,\hat{\phi}_1^a + \frac{1}{1+e^{-\beta m_v z}}\,\hat{\phi}_2^a\,. \tag{3.92}$$

Notice that the relative minus signs in equation (3.90) are crucial for obtaining the correct field orientation and for ensuring smooth continuity across the $z = 0$ plane.

We performed the simulations with the smoothing parameter $\beta = 0.5$ and the monopole positions $z_1 = -20\,m_v^{-1}$ and $z_1 = 20\,m_v^{-1}$. The collision velocity was set to 0.2. The animated results for all non-planar cases that we simulated are given in the video:
`https://youtu.be/a2wOOo2AAHI`

The resulting dynamics agree with the description of Hitchin, Manton, and Murray [5] in the language of rational maps. In the case of three monopoles, we observed that the single monopole colliding with the toroidal charge-2 monopole splits into three charge-1 monopoles (see Figure 3.40). The intermediate state, when all three monopoles meet at the origin, takes the form of a tetrahedral structure. In the case of four monopoles, we observed that a single monopole colliding with a toroidal charge-3 monopole splits into four separated monopoles, with the intermediate state being a pyramid. Finally, when two toroidal charge-2 monopoles collide along the z-axis, they also split into four separated monopoles, with the energy density distributing in a cubic structure during the collision (see Figure 3.41).

Since the simulation is performed for all field components of the theory, we are able to use the simulation data for analysing the dynamics of the zeros of the scalar field ϕ^a. Around each zero one can determine the local winding of the field. In the planar scattering the behaviour of the zeros was rather simple. Initially, each monopole contains one zero in its centre. At the collision when the axially symmetric toroidal state is formed all zeros meet at the origin and form a single zero of winding n, where n depends on the number of monopoles that are involved in this process. After the collision, there is a again one

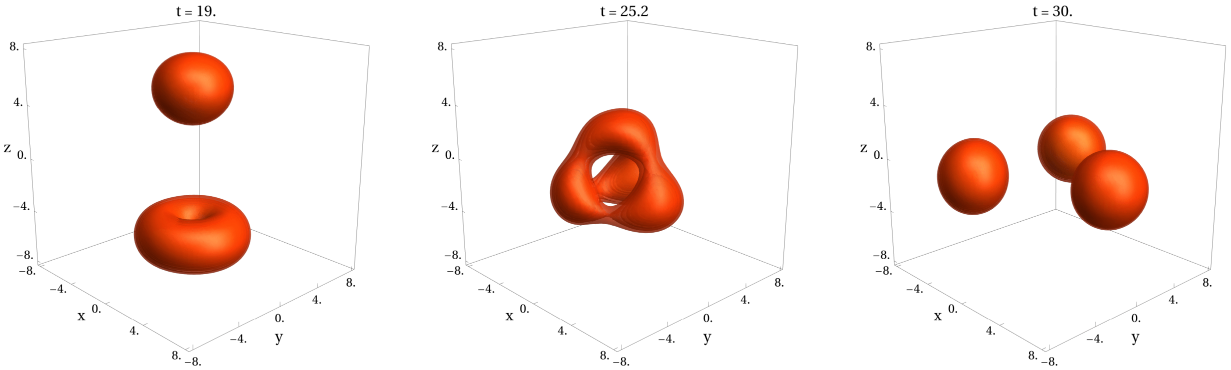

Figure 3.40: Three time frames of the collision between a charge-1 monopole and a charge-2 monopole are shown. During the collision, a tetrahedral intermediate state is formed, after which the monopoles split into three separated charge-1 monopoles. Length and time values are given in units of m_v^{-1}. The energy contours correspond to energy densities greater than $0.025\, m_v^4/g^2$.

zero of winding one per monopole. This behaviour is the only possibility to ensure cyclic symmetry throughout the full process.

In non-planar scatterings, this cyclic symmetry must also be preserved all the time. However, the formation of special structures like the tetrahedron sometimes requires additional zeros with negative local winding (anti-zeros) [130]. The behaviour of the zeros in the non-planar scattering of three monopoles is as follows. Initially, there is one zero of winding one within the charge-1 monopole and one zero of winding two within the toroidal charge-2 monopole. When these monopoles approach each other, the winding-2 zero splits into three zeros of winding one arranged cyclically symmetric and another single zero of winding minus one. As the tetrahedral state forms, there are four zeros of winding one at the corners of the tetrahedron, and one anti-zero in its centre. Afterwards, the tetrahedron splits into three separated monopoles, each containing one zero of winding one. The anti-zero then annihilates with the zero originating from the initial charge-1 monopole. Notice that the overall winding is preserved throughout the process, as expected from the conservation of topological charge.

The non-planar scattering of four monopoles with an intermediate pyramidal structure is very similar. The zero with winding three at the centre of the toroidal charge-3 monopole splits into four zeros of winding one and a single anti-zero. When the pyramid forms, the zeros are located in the corners, while the anti-zero remains at the centre. Subsequently, the monopoles split into four separated monopoles, each containing one zero of winding one, and the anti-zero annihilates with the zero originating from the initial charge-1 monopole.

In the cubic scattering, no anti-zeros appear. Here, the two zeros of winding two originating from the toroidal charge-2 monopoles overlap at the origin, forming a single zero of winding four when the cubic structure is formed. Afterwards, when the monopoles split, the zeros become localized at the centres of the four separated monopoles.

The dynamics of the zeros observed in our simulations align perfectly with the predictions of Sutcliffe in [130].

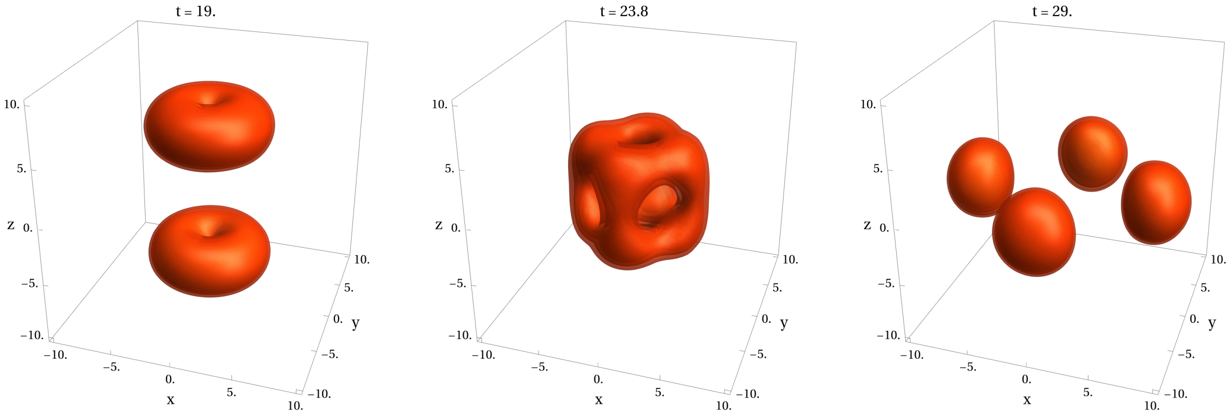

Figure 3.41: Three time frames for the collision of two charge-2 monopoles are shown. After they formed an intermediate cubic state they split into four separated monopoles of charge one. Length and time values are given in units of m_v^{-1}. The energy contours correspond to energy densities greater than $0.025\, m_v^4/g^2$.

3.7.7 Conclusions and Outlook

In this section on magnetic monopole collisions, we simulated several multi-monopole scattering processes that had previously been predicted using the moduli space approximation. Specifically, we studied the scattering of two, three, and four monopoles. In the planar case, the monopoles remain confined to a single plane and scatter at angles of 90°, 60°, and 45°, respectively. During the collision, a toroidal intermediate state is formed. We also investigated non-planar scattering scenarios. In these cases, we observed the formation of tetrahedral and cubic structures in the scattering of three and four monopoles, respectively. Notice that all of these observed structures resemble those for higher-charged skyrmions [7].

Since our simulations solve the full field equations, we were able to explore parameter regimes beyond the moduli space approximation. In particular, we simulated scatterings at relativistic velocities and with a non-vanishing Higgs boson mass. The similar behaviour observed in all these cases, besides the magnetic repulsion for $m_h \neq 0$, demonstrates the robustness of the moduli space approximation for monopole collisions.

Many of these observations were already known from the moduli space approximation. Nevertheless, our work on monopole collisions provides meaningful progress towards developing a complete field-theoretic level description of multi-monopole systems. The analytic approximate solutions for planar scatterings, presented in Sections 3.7.3 and 3.7.4, offer an intuitive picture of how the field structure looks and evolves. As mentioned in Section 3.7.6, such analytic approximate solutions for multiple charge-1 monopoles scattering in a non-planar way is not yet known and remains work in progress.

Another ongoing work concerns the behaviour of monopoles in collisions that are not head-on. An offset within the x-y-plane should lead to deflections of the monopoles, as predicted in [10]. However, an offset in the z-direction is also possible. For sufficiently large z-separations, the monopoles scatter with some non-trivial scattering angle, whereas for small offsets the moduli approximation predicts that the monopoles still undergo right-angle scattering, with the angular momentum of the system becoming observable as electric charge [122, 10]. In this case, the initially purely magnetically charged monopoles turn into dyons with opposite electric charges. In [122], it was suggested that the induced electric charge might lead to a subsequent attraction of the monopoles after the collision. However, the actual outcome remains unknown and requires numerical investigation.

A further effect that can strongly modify the dynamics of monopoles are excited modes. In Section 3.6, it was already discussed that the excitation of massive modes can lead to a multi-bounce behaviour in the right-angle scattering or modification of the BPS geodesics. Even though magnetic monopoles do not have massive bound modes, they do have an infinite number of quasi-normal modes. Each mode by itself decays rather quickly, but in combination, such excitations can be long-lived [67]. These could give rise to multi-bounce windows similar to those observed for vortices. Some first ideas in this direction are discussed in [70]. Preliminary numerical tests with our simulations already indicate that such modes can generate both attractive and repulsive interactions between monopoles, and that the attraction can end in a right-angle scattering. A full exploration of the multi-bounce behaviour is left for future work.

Summarising, we want to emphasize once more that with this work we aim to start a new phase of research on multi-monopole configurations. We have demonstrated that simulations provide a powerful tool for understanding the dynamics of monopole collisions. On the one hand, they make it possible to test the predictions of the moduli space approximation, and on the other hand, they open the door to exploring new phenomena such as those outlined in the previous paragraphs.

Chapter 4

The Magnetic Monopole Problem and its Solutions

This chapter is devoted to the role of magnetic monopoles in the early Universe. We first explain why magnetic monopoles are expected to exist and how and why they are formed (see Sections 4.1 and 4.2). It turns out that the formation of monopoles may lead to a problem, since they are overproduced during phase transitions in the early Universe. This issue is discussed in Section 4.3. Finally, several possible solutions are presented. Inflation and symmetry non-restoration, as two potential solutions, are briefly reviewed in Section 4.3. Two further solutions, the erasure of magnetic monopoles through domain walls and the connection of monopoles by strings, are presented in detail in Sections 4.4 and 4.5, respectively.

4.1 Magnetic Monopoles in Grand Unified Theories

It is a well-known fact that the strengths of the three fundamental forces of particle physics – the electromagnetic, weak, and strong interactions – are energy scale-dependent. In other words, the corresponding coupling constants had different values in the early Universe, when the temperatures were much higher. It turns out that when one extrapolates the coupling constants to higher energies, they approach very similar values. In 1974, Georgi, Quinn, and Weinberg showed that the Standard Model (SM) coupling constants evolve in such a way that they possibly reach the same value at energy scales of order $\sim 10^{15}$–$10^{16}\,\mathrm{GeV}$ [131]. This observation motivated a new class of theories, the so-called Grand Unified Theories (GUTs). These theories assume that all interactions of the SM originate from a theory in which interactions are unified within a single gauge group. The minimal version of a GUT was proposed by Georgi and Glashow in 1974 and is based on the gauge group $SU(5)$ [13].

However, one should note that the $SU(5)$ theory has several problems. First, in its original form it predicts equal masses for the charged leptons and the down-type quarks. Second, in view of the today's stronger experimental constraints [132], it appears that the gauge couplings do not fully unify[1]. Beyond $SU(5)$, there exist other, non-minimal GUTs, such as those based on $SO(10)$ or $SU(6)$, which are not experimentally excluded. Nevertheless, even if the prospects for $SU(5)$ grand unification have become less promising, it still serves as an excellent prototype model for grand unification.

Let us assume that an $SU(5)$ phase was present in the early Universe. Then, as the temperature drops, it has to be broken down to the SM. This breaking takes place via phase transitions (see Section 4.2). The only way to realize a spontaneous symmetry breaking of the form

$$SU(5) \to SU(3) \times SU(2) \times U(1)\,, \tag{4.1}$$

is to introduce a scalar field transforming in the adjoint representation of $SU(5)$. Now, using the rules of homotopy theory (see Appendix B), one finds that the second homotopy group of the $SU(5)$ vacuum manifold,

$$\pi_2\left(\frac{SU(5)}{\left(SU(3) \times SU(2) \times U(1)\right)/Z_6}\right) \cong \mathbb{Z}\,, \tag{4.2}$$

is non-trivial. Therefore, there exist non-trivial mappings from $\mathbb{R}^2$ to the vacuum manifold, implying the possibility of monopole solutions. The same idea can be applied to other GUTs beyond the $SU(5)$ theory.

Magnetic monopoles in the $SU(5)$ theory possess a variety of properties. Since the monopole solution can mix with different subgroups of the SM gauge group, monopoles may carry, in addition to the $U(1)$ magnetic charge, other charges, such as an $SU(3)$ colour charge. Many of these possibilities are discussed in detail in [24]. In this thesis, however, we focus on the simplest monopoles, which carry only a $U(1)$ magnetic charge. This allows us to study magnetic monopoles within $SU(2)$ gauge theories as prototype objects for GUT monopoles.

4.2 Phase Transitions

In this section, we briefly review the main concepts of phase transitions in the early Universe without detailed derivations. We use the equations provided in [27] and focus only on concepts which are relevant for this thesis. For a more detailed discussion, the interested reader is referred to the book by Vilenkin and Shellard [27].

In the previous section, it was shown that GUTs predict magnetic monopoles. However, to ensure a dynamical symmetry breaking in the early Universe, a phase transition is required. Such a phase transition usually occurs through a change in the shape of the effective potential of the theory. Since the shape of the effective potential is temperature-dependent [134, 135, 136], these phase transitions typically occur due to a change in temperature. Therefore, as the Universe cools down, phase transitions are expected to take place.

---

[1] Notice, however, that it was recently shown that this problem can be solved by introducing higher-dimensional effective operators, allowing for unification at scales of order $\sim 10^{14}$ GeV [133].

4.2.1 Second-Order Phase Transitions and Kibble Mechanism

As a simple example for a phase transition, we first focus on the model (2.20) with one complex scalar field ϕ. Thermal corrections result in the effective potential

$$V_{\text{eff}} = \lambda \left(|\phi|^2 - v^2\right)^2 + \frac{\lambda}{3} T^2 |\phi|^2 \,. \tag{4.3}$$

Therefore, the mass term of the theory becomes temperature-dependent. We also see that the temperature term has the opposite sign compared to the original zero-temperature mass term, $-2\lambda v^2 |\phi|^2$. Hence, the sign of the temperature-corrected mass term depends on the temperature T. The sign flip occurs at the critical value $T_{\text{c}} = \sqrt{6}\, v$.

For $T > T_{\text{c}}$, the potential has a single minimum at $\phi = 0$. Therefore, the vacuum manifold of the theory consists of only one point, and the entire system is filled with the VEV $\langle \phi \rangle = 0$.

For $T < T_{\text{c}}$, the potential obtains the Mexican hat shape. Hence, the vacuum manifold is a full circle with a non-zero VEV, resulting in the breaking of the $U(1)$ symmetry. As described in Section 2.2, this allows for a vortex solution.

We can summarize that when a system cools down below the critical temperature T_{c}, it undergoes a phase transition. In this specific example, the system starts at high temperatures in the symmetric $U(1)$ phase and enters the $U(1)$-Higgsed phase at low temperatures. Such a phase transition, in which at a critical temperature the potential minimum at $\phi = 0$ disappears and other minima at $\phi \neq 0$ emerge, is called a second-order phase transition.

While the structure of these vortices was already discussed in great detail in this thesis, it has not yet been explained how these vortices form during a phase transition. The idea was first proposed by Kibble in 1976 [137]. When a system undergoes a phase transition, different regions are causally disconnected[2], meaning that not enough time has passed for information about the vacuum expectation value to be transferred from one region to another. In the case of the vortex model, this implies that each region can independently choose an arbitrary point on the vacuum manifold. If the phases of the scalar field are aligned such that, at the intersection of several regions with different VEVs, a non-trivial winding occurs, a vortex will form. This process is illustrated schematically in Figure 4.1.

The same concept can be applied to domain walls and magnetic monopoles. Let us consider, for example, a domain wall model with a vacuum manifold consisting of two values, $\pm v$. When the phase transition occurs, two causally disconnected regions can get different VEVs. Thus, one region may get the value $-v$, while a neighbouring region obtains the value $+v$. In such a case, a domain wall forms between these two regions. It serves as a boundary separating the two vacua.

For monopoles, we need at least three scalar fields, usually realized as the components of an adjoint scalar field ϕ^a. The idea works similarly to the cases of domain walls and vortices. For example, if there is a region where the VEVs are such that all three components are

---

[2] In cosmology, instead of the term "causally disconnected regions" the word "horizons" is quite often used.

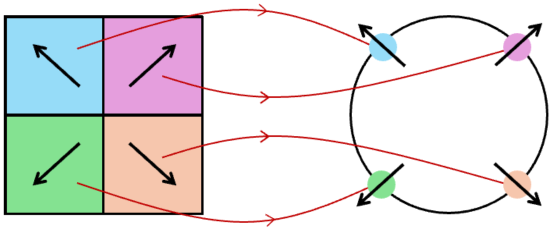

Figure 4.1: This figure sketches how the Kibble mechanism works for a vortex. The left square depicts a system with four different causally disconnected regions. In each region, the phase (illustrated by the vectors) of the scalar field can take a different value. These phases correspond to different points on the circular vacuum manifold, as illustrated by the mapping to a circle. If the configuration is oriented as shown in the figure, a vortex will form in a region around the centre of the square.

smaller than zero, $\phi^a < 0$, and a neighbouring region where all components are larger than zero, $\phi^a > 0$, then a magnetic monopole will form between these neighbouring regions. An example setup is illustrated schematically in Figure 4.2.

4.2.2 Dynamics of Vacuum Bubbles

Before we continue with phase transitions, a short discussion about vacuum bubbles is given. In this thesis so far, we have only considered flat domain walls and mainly focused on domain walls in one spatial dimension. But of course, domain walls exist also in higher dimensions. There, the wall doesn't have to be necessarily flat. It can also be curved and form full domain wall bubbles. As an example let us think of a real scalar field theory with a quartic potential (2.2) in $2+1$ dimensions. We want to find a rotationally symmetric configuration. Therefore, we can drop all derivatives with respect to the polar angle φ. The static field equation is then given by

$$\partial_r^2\phi + \frac{1}{r}\partial_r\phi = \frac{\partial V(\phi)}{\partial\phi}\,, \tag{4.4}$$

where r is the polar radius.

In the limit of large bubble radii, we can neglect the second term, and we are left with the same form of the differential equation as for a flat domain wall. The domain wall solution was already derived and is given in equation (2.5). By replacing the x-coordinate with r, we obtain

$$\phi_{\mathrm{DW}}(r) = \pm v \tanh\left(\frac{m_h}{2}(r - r_0)\right)\,, \tag{4.5}$$

where r_0 is now the radius of the bubble. Notice that this configuration solves the equations of motion only in the limit $r_0 \gg m_h^{-1}$, since only in this case we can neglect the second term

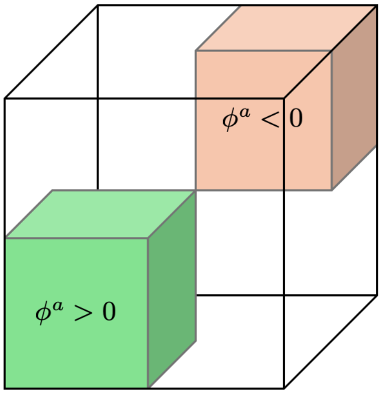

Figure 4.2: This figure shows two regions with opposite signs of the adjoint scalar field ϕ^a. The two boxes are meant to depict two causally disconnected regions. The idea for this illustration was taken from [138].

in equation (4.4). For small radii r_0, the solution receives corrections due to the curvature of the wall. These corrections can be found numerically.

Next, we want to understand how such a bubble evolves in time. For simplicity, we remain in the thin-wall limit $r_0 \gg m_h^{-1}$ and focus only on two spatial dimensions. The total energy of the bubble is then given by $E_0 = 2\pi r_0 \sigma$, where σ denotes the tension of the domain wall. If we now allow the bubble to grow or shrink, the energy more generally takes the form $E(t) = 2\pi r(t)\sigma\gamma(t)$, where $\gamma(t)$ is the Lorentz factor associated with $\dot{r}(t)$. Imposing energy conservation, $E(t) = E_0$, we obtain the differential equation

$$\left(\frac{r(t)}{r_0}\right)^2 = 1 - \dot{r}(t)^2\,, \tag{4.6}$$

which can be solved by $r(t) = r_0 \cos(t/r_0)$. We thus see that the bubble collapses at the time $t \simeq \pi r_0/2$. In more than two dimensions, the bubble also collapses. However, the collapse time becomes shorter as the number of spatial dimensions increases.

Let us now introduce a small potential difference, ΔV, between the two minima of the potential. The higher minimum is referred to as the false vacuum, while the global minimum is the true vacuum. If the false vacuum is inside the bubble, the collapse is further enhanced, since the vacuum energy can be converted into kinetic energy of the domain wall as the bubble shrinks. If the false vacuum is outside of the bubble, the collapse becomes slower, since the vacuum energy has to be created from the energy of the domain wall. If the tension of the wall is not high enough, the bubble can even start growing. For a domain wall with tension σ, the critical radius at which the domain wall bubble is static is given by $r_\mathrm{c} = \sigma/\Delta V$. For $r_0 > r_\mathrm{c}$, the bubble will expand, whereas for $r_0 < r_\mathrm{c}$, the bubble will collapse.

Notice that the same concepts described above can be applied to cosmic string loops in three spatial dimensions. In the limit of thin strings, the dynamics is exactly the same:

the string collapses within the time $t = \pi r_0/2$, where r_0 is now the radius of the string loop. Instead of vacuum energy, one can introduce a planar domain wall attached to the string [31, 139]. This wall can either lie inside the string loop, forming a disk of radius r_0, or outside the loop, forming an infinitely large wall with a hole of radius r_0. In the latter case, the string loop collapses or expands depending on its size. The critical radius is now given by $r_\mathrm{c} = \mu/\sigma$, where μ and σ are the string and wall tensions, respectively.

The formation of holes in domain walls can proceed either through a quantum tunnelling process [140] or through thermal fluctuations [141]. A numerical analysis of the thermal creation of holes in domain walls is a work in progress and will be published after the submission of this thesis [54].

4.2.3 First-Order Phase Transitions

Second-order phase transitions described earlier are phase transitions in which the symmetry is broken everywhere at approximately the same time, assuming that the temperature distribution is homogeneous. This is due to the sign flip of the temperature-dependent mass term, which changes the shape of the potential from having a single minimum to having multiple minima.

First-order phase transitions are more controlled than second-order phase transitions. The overall idea is that when the temperature drops, there is a critical value at which the vacuum at $\phi = 0$ becomes a false vacuum, but still remains a local (but not global) minimum of the potential. Once such a change occurs, vacuum bubbles can nucleate through quantum [142] or thermal [143] fluctuations. If the pressure difference between the outside and the inside of the bubble is sufficiently large, the bubbles grow until they fill the entire space.

In the following, we consider the Abelian-Higgs model as an example. We take the Lagrangian

$$\mathcal{L} = -\frac{1}{4} F_{\mu\nu} F^{\mu\nu} + (D_\mu \phi)^* (D^\mu \phi) - V(\phi)\,, \tag{4.7}$$

with the potential $V(\phi) = V_0 = m_0^2 |\phi|^2$. Through quantum and thermal corrections, the effective potential contains different types of contributions:

$$V_\mathrm{eff} = V_0 + V_\mathrm{quantum} + V_\mathrm{thermal}\,. \tag{4.8}$$

Coleman and Weinberg showed in 1973 [144, 145] that the quantum corrections at one-loop order give

$$V_\mathrm{quantum} = \frac{m_0^2}{v\sigma^2}\, |\phi|^4 \, \ln\left(\frac{|\phi|^2}{\sigma^2}\right), \tag{4.9}$$

where $v = 16\pi^2 m_0^2/(3g^4\sigma^2)$ and σ is the renormalisation scale. Thermal corrections yield the contribution [27]

$$V_\mathrm{thermal} = \frac{1}{4} g^2 T^2 |\phi|^2\,. \tag{4.10}$$

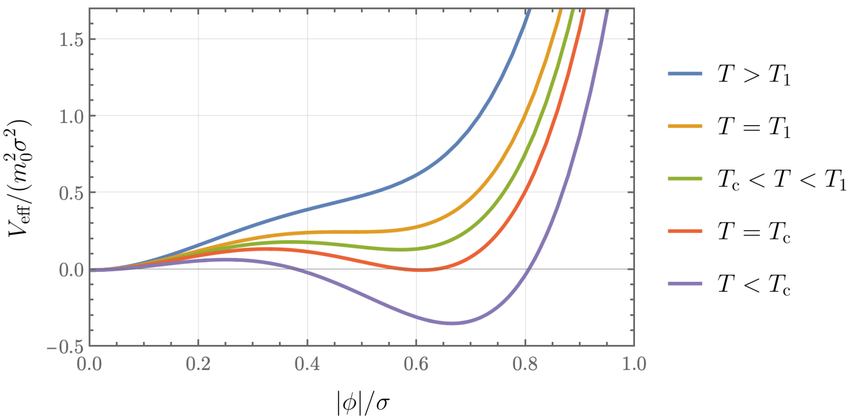

Figure 4.3: This figure shows the temperature-dependent Coleman–Weinberg potential of the Abelian-Higgs model for different temperatures.

In Figure 4.3, the effective potential is shown for different temperatures. The potential has several different regimes in which its shape exhibits different properties. Let us start with very high temperatures. In this case, the potential has a single minimum at $\phi = 0$. Below the temperature $T_1 = (2m_0/g)\sqrt{v_1/v - 1}$, with $v_1 = 2e^{-3/2}$, additional minima at $|\phi| \neq 0$ appear. As long as the temperature is still sufficiently high, these minima lie above the minimum at $\phi = 0$. Therefore, the true vacuum corresponds to $\phi = 0$.

However, at the critical temperature $T_{\rm c} = (2m_0/g)\sqrt{v_{\rm c}/v - 1}$, with $v_{\rm c} = e^{-1}$, all minima of the potential become degenerate. At this point, the vacuum manifold of the theory has its richest structure. It is a disconnected vacuum manifold, and therefore static domain walls separating vacua with $\phi = 0$ from vacua with $\phi \neq 0$ can exist. Since the vacua are degenerate, tunnelling processes from one vacuum to the other are also possible. This means that small vacuum bubbles can emerge through quantum and thermal fluctuations [142]. However, due to the tension of the domain walls, these vacuum bubbles collapse very quickly.

The situation changes when the temperature decreases further. For $T < T_{\rm c}$, the true vacuum corresponds to minima with $\phi \neq 0$. Therefore, the symmetric vacuum at $\phi = 0$ becomes a false vacuum. Again, this allows for the nucleation of bubbles through quantum and thermal fluctuations.

The nucleation rate through a quantum tunnelling process can be estimated by analysing the instanton solution for the vacuum bubble. The nucleation rate is then given by $\Gamma \sim e^{-B}$, where B is the bounce action, defined as $B = S - S_0$ [142, 146, 140]. Here, S denotes the action of the instanton, and S_0 is the action of the false vacuum. In $3+1$ dimensions, one finds $B = 27\pi^2\sigma^4/(2\Delta V^3)$, where ΔV is the potential difference between the true and the false vacuum, and σ is the domain wall tension.

The thermal nucleation rate is given by $\Gamma \sim e^{-E_{\rm sphaleron}/T}$ [141], where the sphaleron energy corresponds to the static vacuum bubble configuration with the critical radius, $E_{\rm sphaleron} = 4\pi r_{\rm c}^2\,\sigma$. The critical radius is given by $r_{\rm c} = 2\sigma/\Delta V$.

The vacuum energy outside of the nucleated bubble creates a pressure difference between the inside and the outside. This allows bubbles with radius $r > r_\mathrm{c}$ to grow and eventually fill the entire system with the true vacuum.

The Coleman–Weinberg potential has a rather non-trivial structure due to the logarithm. However, since in this thesis we focus only on scenarios around the critical temperature T_c, we can approximate the Coleman–Weinberg potential by a sextic potential,

$$V = \lambda \left(|\phi|^2 - v^2\right)^2 |\phi|^2 . \tag{4.11}$$

With this potential, the vacuum manifold is now given by a single point at $\phi = 0$ and a circle at $|\phi| = v$. The shape of this potential is very similar to the Coleman–Weinberg potential at the critical temperature T_c. By adding an extra quadratic term $\alpha|\phi|^2$, one can introduce a potential difference between the minima at $\phi = 0$ and $\phi \neq 0$. This makes it possible to study the dynamics of growing vacuum bubbles.

In this section, we focused on Abelian theories. The discussion is slightly modified for non-Abelian theories. However, the qualitative idea remains the same.

4.3 The Magnetic Monopole Problem

We saw that Grand Unified Theories predict the existence of magnetic monopoles. Through the Kibble mechanism, they may have been produced in phase transitions taking place in the early Universe. The most natural question one may ask is how many magnetic monopoles we expect in today's Universe. This question was first raised by Zeldovich and Khlopov in 1978 [15] and analysed in great detail by Preskill in 1979 [16]. It was found that the number of monopoles would exceed the present energy density of the Universe. In these studies, it was shown that the annihilation of monopole–anti-monopole pairs via their Coulomb attraction proceeds too slowly to sufficiently reduce the monopole abundance, which has recently been confirmed numerically in [147]. This issue is referred to as *the magnetic monopole problem.* For order-of-magnitude estimates, we neglect the Coulomb attraction in this section.

Let us assume that the GUT phase transition occurs at the temperature T_GUT and the monopole mass is given by m_M. Since magnetic monopoles interact very strongly with the surrounding plasma, their kinetic energy can be neglected and they behave as non-relativistic matter. Therefore, the magnetic monopole density parameter can be estimated as

$$\Omega_\mathrm{M} = \frac{\rho_\mathrm{M}}{\rho_0} \sim \frac{N m_\mathrm{M}}{R_\mathrm{H}^3} \left(\frac{a(T_\mathrm{GUT})}{a(T_0)}\right)^3 \frac{\Omega_\mathrm{rad}}{T_0^4} , \tag{4.12}$$

where we have assumed that magnetic monopoles redshift as matter. Here, $R_\mathrm{H} \sim M_\mathrm{P}/T_\mathrm{GUT}^2$ denotes the horizon size at temperature T_GUT, ρ_c is the critical energy density of the Universe, $\Omega_\mathrm{rad} \sim T_0^4/\rho_\mathrm{c}$ is today's radiation energy density parameter, and N is the number of monopoles per horizon at the time of their creation. Using $a(T) \propto 1/T$ and simplifying the expression, we finally obtain

$$\Omega_{\mathrm{M}} \sim N \, \frac{m_{\mathrm{M}} \, T_{\mathrm{GUT}}^3}{T_0 \, M_{\mathrm{P}}^3} \, \Omega_{\mathrm{rad}} \sim 10^{16} N \left(\frac{m_{\mathrm{M}}}{10^{17}\,\mathrm{GeV}} \right) \left(\frac{T_{\mathrm{GUT}}^3}{10^{16}\,\mathrm{GeV}} \right)^3 . \tag{4.13}$$

As a simple estimate, we follow Kibble's argument and assume that, during the phase transition, approximately one monopole per horizon, $N \sim 1$, is produced. Taking $m_{\mathrm{M}} \sim 10^{17}\,\mathrm{GeV}$ and $T_{\mathrm{GUT}} \sim 10^{16}\,\mathrm{GeV}$ then gives a density parameter of $\Omega_{\mathrm{M}} \sim 10^{16}$. For a fully homogeneous distribution, this would correspond to roughly one magnetic monopole per cubic meter. This is already in contradiction with the fact that we have not detected a magnetic monopole yet.[3] The even bigger problem is that the density parameter exceeds the current density of the Universe by 16 orders of magnitude, which is in strong disagreement with observations.

Several ideas have been proposed to solve the magnetic monopole problem. Already in [16], Preskill pointed out that if the phase transition is strongly first-order, monopole production can be significantly less efficient, such that the resulting monopole density could be compatible with current observations of the Universe.

The most famous solution to the magnetic monopole problem is probably inflation. Indeed, one of the original motivations for Guth's idea of inflation was the monopole problem [17]. During inflation, the exponential expansion of the Universe leads to an exponentially fast decrease of the monopole number density. In terms of equation (4.12), this corresponds to an additional exponential suppression factor. Hence, if the inflationary epoch takes place after the monopoles are created, during the GUT phase transition, the monopole density is expected to be sufficiently small so that it no longer exceeds the critical density.

However, there exist several inflationary scenarios in which inflation occurs before a GUT phase transition and thus before the creation of magnetic monopoles. In this case, inflation is not available to solve the magnetic monopole problem, and alternative solutions are required. A very minimal solution is, for example, symmetry non-restoration [22]. The idea is that even at high temperatures around the GUT scale the GUT symmetry group remains broken. Therefore, there is no phase transition during which magnetic monopoles are produced. In [22], it was shown that this is indeed possible in the context of $SU(5)$ grand unification. The actual realisability, however, depends on the structure of the Higgs sector and is therefore highly model-dependent.

There are two further ideas to solve the magnetic monopole problem by introducing other types of topological defects. In [23] it is suggested that during a phase transition, domain walls can form in addition to magnetic monopoles. When monopoles collide with these walls, they get erased. This erasure mechanism is discussed in great detail in Section 4.4. The second possibility involves a subsequent symmetry breaking, in which strings form

---

[3] Notice that on Valentine's Day 1982, Cabrera reported an experimental signal consistent with the detection of a single magnetic monopole [148]. However, this result could not be reproduced afterwards, and thus we can say that magnetic monopoles have not been detected so far.

that connect monopole–anti-monopole pairs. Due to the string tension, the monopoles are pulled together until they eventually collide and annihilate. This idea was introduced by Langacker and Pi in 1980 [18] and will be discussed in detail in Section 4.5. A modification of this idea in the form of the so-called slingshot effect is presented in Chapter 5.

4.4 Erasure of Magnetic Monopoles through Domain Walls

Although some new aspects were added and discussions were rephrased, this section is an ad verbatim reproduction with respect to equations and figures of the paper "Radiation emission during the erasure of magnetic monopoles" [149] that I wrote with my collaborators Gia Dvali and Juan Sebastián Valbuena-Bermúdez.

The erasure mechanism is a minimal solution to the magnetic monopole problem. In 1997, Dvali, Liu, and Vachaspati [23] pointed out that higher-dimensional topological defects can erase lower-dimensional ones. In particular, domain walls can erase magnetic monopoles when they encounter them. Since the $SU(5)$ GUT predicts both the existence of domain walls and of magnetic monopoles, this erasure phenomenon may occur in such a framework. The erasure mechanism allows for a reduction of the number of magnetic monopoles and, as pointed out in [23], may provide a possible solution to the magnetic monopole problem.

The main idea of the erasure mechanism described in [23] is that a domain wall can be viewed as a surface on which the symmetry is higher than in the surrounding vacuum. If the symmetry inside the wall is partially restored in such a way that the single $U(1)$ symmetry required for the existence of a magnetic monopole becomes embedded in a larger symmetry group, the monopole configuration can unwind. Although the $SU(5)$ kink solution, in which the full $SU(5)$ symmetry is restored, is unstable, other domain wall solutions, which do not fully restore the $SU(5)$ symmetry, are stable [150]. Within such walls, the symmetry is reduced compared to the symmetry outside. Nevertheless, it remains possible for them to eliminate magnetic monopoles if the embedding of the $U(1)$ symmetry changes within or behind the wall. Depending on the scalar field structure of the wall, a monopole may either pass through it or be erased. This behaviour has been studied numerically in [151].

The erasure mechanism has already been studied numerically in several different scenarios. These include the erasure of magnetic monopoles in $SU(5)$ [102, 151], in the Pati–Salam model [152], and in an $O(3)$ linear sigma model [153]. The erasure of vortices and strings has been discussed in [154, 155]. Finally, the erasure of skyrmions was studied numerically in [156, 157].

In this thesis, the erasure mechanism is presented for an $SU(2)$ gauge theory with a scalar field transforming in the adjoint representation. Instead of considering a single domain wall, we study an $SU(2)$-invariant vacuum layer, that is, a layer in the $SU(2)$-symmetric phase separated from the outer $U(1)$-invariant phase by two domain walls [158]. We again observe that the monopoles erase when they encounter the domain wall. The goal of this section is to gain a better understanding of what exactly happens during the erasure process. In particular, we want to clarify what happens to the magnetic charge after the monopole has been erased.

4.4.1 The Model and its Solutions

The Lagrangian describing an $SU(2)$ gauge theory with an adjoint scalar field ϕ and gauge fields W_μ is given by

$$\mathcal{L} = -\frac{1}{2}\,\mathrm{Tr}\,(G_{\mu\nu}G^{\mu\nu}) + \mathrm{Tr}\,\big((D_\mu\phi)^\dagger(D^\mu\phi)\big) - V(\phi)\,. \tag{4.14}$$

In this chapter, we follow the same conventions and notations as in Section 2.3.3. The potential $V(\phi)$ requires a specific choice, since in the original 't Hooft–Polyakov Lagrangian (2.56) with a quartic potential, a stable domain wall solution does not exist. However, because we want the theory to support both magnetic monopoles and domain walls, the potential has to be modified. In particular, we require a vacuum manifold that is, first, disconnected and, second, supports both an $SU(2)$-invariant vacuum and a $U(1)$-invariant Higgsed vacuum. These properties are realized by the sextic potential

$$V(\phi) = \lambda\left(\mathrm{Tr}\big(\phi^2\big) - \frac{v^2}{2}\right)^2 \mathrm{Tr}\big(\phi^2\big)\,. \tag{4.15}$$

The vacuum expectation value $\langle \mathrm{Tr}\big(\phi^\dagger\phi\big)\rangle = 0$ corresponds to the $SU(2)$-invariant vacuum, whereas $\langle \mathrm{Tr}\big(\phi^\dagger\phi\big)\rangle = v^2/2$ corresponds to the $U(1)$-invariant Higgsed vacuum in which the $SU(2)$ symmetry is Higgsed down to $U(1)$. The particle spectrum differs in these two phases. In the $SU(2)$-invariant vacuum, the three vector fields are massless and the three scalar degrees of freedom are massive. In the Higgsed vacuum, two of the vector fields acquire a mass $m_v = gv$, with g being the gauge coupling, while one remains massless. In addition, there is a Higgs boson with mass $m_h = \sqrt{\lambda}v^2$. In the following, we refer to the two massive vector fields as the W-bosons and to the massless vector field as the photon. Notice that, due to the ϕ^6 term, the theory is not renormalizable. However, as discussed in Section 4.2, the sextic potential can be treated as an effective potential. For instance, it may be taken as an approximation to the Coleman–Weinberg effective potential in the intermediate regime where the symmetric and broken phases are degenerate.

The field equations of this model are given by

$$(D_\mu D^\mu\phi)^a + \frac{\partial V}{\partial\phi^a} = 0\,, \tag{4.16}$$

$$(D_\mu G^{\mu\nu})^a - g\varepsilon_{abc}\,(D^\nu\phi)^b\phi^c = 0\,. \tag{4.17}$$

These equations contain domain wall solutions. For instance, the solutions for an infinite domain wall located at $z = 0$ are given by

$$\phi_{(v,0)}(z) = \frac{v}{\sqrt{1+e^{m_h z}}}\,n^aT^a\,, \tag{4.18}$$

$$\phi_{(0,v)}(z) = \frac{v}{\sqrt{1+e^{-m_h z}}}\,n^aT^a\,, \tag{4.19}$$

where n^a is a normalized $SU(2)$ vector describing the internal $SU(2)$ orientation of the wall. These walls interpolate between the Higgsed vacuum with VEV v and the $SU(2)$-invariant vacuum with VEV 0. For the erasure mechanism, we consider a combination of the wall solutions $\phi_{(v,0)}$ and $\phi_{(0,v)}$ in order to form an $SU(2)$-invariant vacuum layer [158]. The ansatz we use is

$$\phi_{\mathrm{VL}}(z) = \phi_{(v,0)}(z) + \phi_{(0,v)}(z-h)\,, \tag{4.20}$$

where h denotes the width of the vacuum layer. Notice that this configuration of a wall and an anti-wall is not static, because there is an attractive force between them. However, the interaction is exponentially suppressed with the separation h, and thus the attraction becomes negligible for $h \gg m_h^{-1} \sim m_v^{-1}$. For the value $h = 20\,m_v^{-1}$ used in our simulations, the vacuum layer can be considered as stable during the time interval we investigated.

The magnetic monopole solution has the usual 't Hooft–Polyakov structure [2, 3]

$$\begin{aligned} W_i^a &= \varepsilon_{aij}\frac{r^j}{r^2}\frac{1}{g}\big(1-K(r)\big)\,, \\ W_t^a &= 0\,, \\ \phi^a &= \frac{r^a}{r^2}\frac{1}{g}H(r)\,, \end{aligned} \tag{4.21}$$

where $K(r)$ and $H(r)$ are the usual profile functions. Their boundary behaviour remains unchanged, and their shape is only slightly modified compared to the case with a quartic potential.

4.4.2 Initial Configuration

We want to analyse the collision of a magnetic monopole with an $SU(2)$-invariant vacuum layer, using a numerical simulation. To achieve this, a good initial condition for the scalar and vector field is required. To combine the monopole solution with the domain wall solution we are taking the product ansatz

$$\phi^a(\boldsymbol{r}, t=0) = \frac{1}{v}\,\phi^a_{\mathrm{M}}(\boldsymbol{r})\,\phi_{\mathrm{VL}}(z-d)\,, \tag{4.22}$$

$$W^a_\mu(\boldsymbol{r}, t=0) = W^a_{\mathrm{M},\mu}(\boldsymbol{r})\,, \tag{4.23}$$

where d is the separation between the magnetic monopole, which is placed in the origin, and the vacuum layer.

Before introducing the Lorentz-boosted configuration, we should analyse the validity of this ansatz first. We observe that for small separations d the monopole is attracted to the vacuum layer. Such an attraction was already mentioned in [153]. However, it is exponentially suppressed and thus can be neglected for our study. Note that in this work we completely neglect gravitational interactions. Since any gravitational repulsion between the monopole and the wall is suppressed by M_{P}^2 (the Planck mass), this effect can be safely ignored.

Furthermore, Ambjørn and Olesen [159] showed that the W-bosons can condense in the presence of a uniform magnetic field with $B > m_v^2/g$. This effect arises from a bilinear term in the gauge fields that generates modes with imaginary frequencies. Since the Higgs profile vanishes inside the vacuum layer, the gauge boson masses also vanish there, which could in principle lead to instabilities. In our simulations, we confirmed this effect for a uniform magnetic field with $B < m_v^2/g$. As expected we found that there are no growing modes outside the layer, because the magnetic field is below the Ambjørn–Olesen critical value, whereas inside the layer such growing modes do appear. However, for a single monopole configuration, the situation is different. The eigenvalues of the gauge boson mass matrix in the background of the magnetic monopole are always positive. As a result, even in the presence of the wall, the Ambjørn–Olesen effect does not destabilize the vacuum inside the vacuum layer.

Finally, the ansatz should be examined with respect to possible quantum effects. In the Higgsed vacuum, the running of the gauge coupling g^2 stops at the scale $m_v \sim m_h$. Within the $SU(2)$-invariant vacuum layer, the scalar degrees of freedom remain massive and therefore also decouple at energy scales of order $\sim m_h$. However, because the Higgs profile vanishes inside the layer, the gauge boson mass term also vanishes. As a result, the gauge coupling continues to run down to the scale h^{-1}, where h denotes the width of the vacuum layer. Because we work in the regime $h \gg m_v^{-1}$, this running can be treated analogously to that in a pure $SU(2)$ gauge theory. Taking the running into account, one finds that the gauge coupling inside the layer, g^2_{inside}, is stronger than the coupling outside, g^2_{outside}:

$$g^2_{\text{inside}} = g^2_{\text{outside}} + \frac{11}{12\pi^2} g^4_{\text{outside}} \ln(m_v h) + \mathcal{O}(g^6_{\text{outside}}) \,. \tag{4.24}$$

As a consequence, the magnetic energy of the monopole is reduced inside the layer (see Figure 4.4). This results in an attractive interaction between the monopole and the vacuum layer. At one-loop order, the corresponding attractive potential can be estimated as

$$V(d) \approx -\frac{11}{24\pi} \frac{h}{d(d+h)} \ln(m_v h) \,. \tag{4.25}$$

The corresponding force therefore scales as $\sim (h/d^3) \ln(m_v h)$ for $h \ll d$. Hence, at large distances, as considered in our simulations, the force is strongly suppressed and can be neglected. Therefore, the classical analysis indeed captures the right physical behaviour.

When discussing quantum effects, one has to distinguish between the perturbative weak-coupling regime and the strong-coupling regime. In the present setup, these two regimes correspond to $h^{-1} \gg \Lambda$ and $h^{-1} < \Lambda$, respectively, where Λ denotes the strong-coupling scale of the $SU(2)$ gauge theory. The perturbative treatment which we discussed in detail above is valid only in the weak-coupling regime. For the strong coupling regime, $h^{-1} < \Lambda$, the $SU(2)$ vacuum inside the layer becomes confining and a mass gap of order Λ is generated. As a consequence, the $U(1)$ electric field is repelled, while the magnetic field is screened by the vacuum layer. This phenomenon was originally discussed in [160, 161, 158].

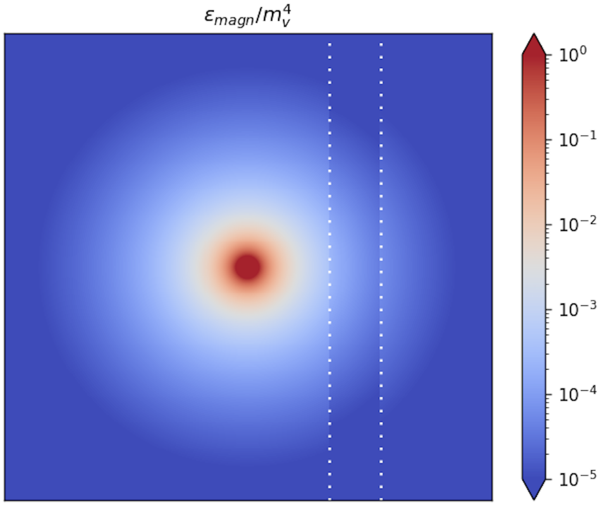

Figure 4.4: This figure shows the distribution of the magnetic energy density of a monopole located close to an $SU(2)$-invariant vacuum layer. Taking into account the quantum correction to the gauge coupling given in equation (4.24), one finds that the magnetic energy is reduced inside the layer.

In this work, we focus on the regime in which the thickness of the vacuum layer is much smaller than the inverse confinement scale Λ^{-1}, so that these strong-coupling effects can be neglected.

With all these potential effects of both classical and quantum origin in mind, we now know the regimes of validity of the ansatz given in equations (4.22) and (4.23). To analyse the collision of the monopole with the vacuum layer, we have to Lorentz boost the configurations. This can be implemented through the following modification of the ansatz:

$$\phi^a_{\mathrm{M}}(\boldsymbol{r}) \to \tilde{\phi}^a_{\mathrm{M}}(\boldsymbol{r}, t) = \phi^a_{\mathrm{M}}(x, y, \gamma_{\mathrm{M}}(z - u_{\mathrm{M}}t)) \,, \tag{4.26}$$

$$\phi_{\mathrm{VL}}(z - d) \to \tilde{\phi}_{\mathrm{VL}}(z, t) = \phi_{\mathrm{VL}}(\gamma_{\mathrm{VL}}(z - u_{\mathrm{VL}}t - d)) \,, \tag{4.27}$$

where u_{M} and u_{VL} denote the initial velocities of the monopole and the vacuum layer, respectively, and γ_{M} and γ_{VL} are the corresponding Lorentz factors. For the gauge field, we apply the same replacement of the z-coordinate as for the monopole scalar field. In addition, however, we must account for the Lorentz transformation of the vector field itself. This yields

$$W^a_{\mathrm{M},\mu}(\boldsymbol{r}) \to \tilde{W}^a_{\mathrm{M},\mu}(\boldsymbol{r}, t) = \begin{pmatrix} -u_{\mathrm{M}}\gamma_{\mathrm{M}} W^a_{\mathrm{M},z}(x, y, \gamma_{\mathrm{M}}(z - u_{\mathrm{M}}t)) \\ W^a_{\mathrm{M},x}(x, y, \gamma_{\mathrm{M}}(z - u_{\mathrm{M}}t)) \\ W^a_{\mathrm{M},y}(x, y, \gamma_{\mathrm{M}}(z - u_{\mathrm{M}}t)) \\ \gamma_{\mathrm{M}} W^a_{\mathrm{M},z}(x, y, \gamma_{\mathrm{M}}(z - u_{\mathrm{M}}t)) \end{pmatrix} . \tag{4.28}$$

Using this ansatz as the initial configuration allows us to numerically simulate the erasure mechanism.

4.4.3 Simulation and Results

The numerical simulation of the erasure was carried out by solving the field equations (4.16) and (4.17) in Lorenz gauge using the iterative Crank–Nicolson method. Moreover, we made use of the axial symmetry of the system and solved the field equations only in the $y = 0$ plane. This significantly improves the computational efficiency and allows the use of a smaller lattice spacing. As boundary conditions, we chose adaptive boundaries. Further details on the numerical methods are provided in Appendix A.

For the lattice, we chose a size of $120\, m_v^{-1} \times 120\, m_v^{-1}$ and analysed the time evolution up to $t = 150\, m_v^{-1}$. The lattice and time spacings were set to $\Delta x = 0.25\, m_v^{-1}$ and $\Delta t = 0.1\, m_v^{-1}$ for monopole velocities $u_{\mathrm{M}} < 0.8$. For monopole velocities $u_{\mathrm{M}} \geq 0.8$, we increased the resolution in the z-direction by a factor of two and reduced the time step accordingly by the same factor.

We varied all parameters of the theory. We find that the qualitative behaviour of the erasure mechanism does not depend on the theory parameter m_h/m_v. Therefore, for the cases presented here, we set $m_h/m_v = 1$. In addition, we varied the width of the vacuum layer, h, the distance between the monopole and the vacuum layer, d, and the initial velocities of the monopole, u_{M}, and of the vacuum layer, u_{VL}. For the figures shown in this thesis, we choose $h = 20\, m_v^{-1}$ and $d = 30\, m_v^{-1}$. We considered velocities up to $u_{\mathrm{M}} = 0.8$ and $u_{\mathrm{VL}} = 0.98$. These values represent the maximal velocities for which we can trust the results with the chosen lattice resolution. Note that, in particular for the maximal case, this corresponds to a relative Lorentz factor of about $\gamma \approx 15$. In earlier works [102, 151, 154], the erasure mechanism has not been studied in the highly relativistic regime. Our simulations therefore provide a first test of the erasure mechanism in this regime.

In all cases we analysed, we observe that the magnetic monopole is erased by the $SU(2)$-invariant vacuum layer. This confirms the prediction of the erasure mechanism of [23] for the $SU(2)$ gauge theory with a sextic potential. The results for two representative cases are shown in Figures 4.5, 4.6, 4.7, and 4.8. In all figures, length and time are given in units of m_v^{-1}, and the energy densities are expressed in units of m_v^4/g^2. The corresponding animated results can be found in the following video:
`https://youtu.be/JZaXUYikQbo`

One feature that can be observed in the figures is that the impact of the monopole on the wall leads to deformations of the vacuum layer. This effect can be separated into two parts, the deformation of the first wall and that of the second wall. Initially, the gauge field is localized around the core of the monopole. Since the gauge boson masses vanish inside the magnetic monopole, this configuration is energetically preferred. However, inside the vacuum layer the gauge boson masses also vanish. As a result, the gauge field spreads within the layer. This can be understood as a pulse of gauge bosons that become effectively free inside the vacuum layer. When this packet of gauge field radiation reaches the second wall, it transfers momentum to the wall and causes it to deform. This effect is best visible in the ultra-relativistic case shown in Figure 4.7.

The deformation of the first wall can be seen in the domain wall's potential energy

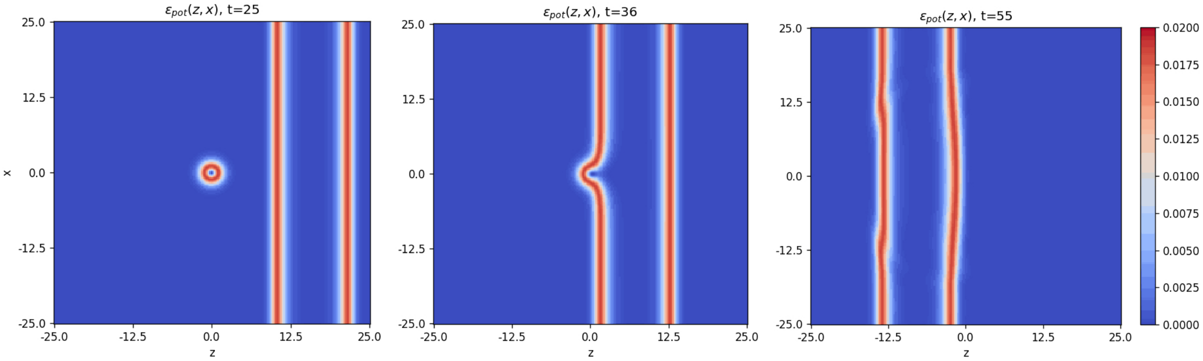

Figure 4.5: This figure shows the time evolution of the potential energy density of the erasure process in the $y = 0$ plane. For this case, the initial velocities are $u_{\mathrm{M}} = 0$ and $u_{\mathrm{VL}} = -0.8$. Length and time are given in units of m_v^{-1}, and the energy density is expressed in units of m_v^4/g^2.

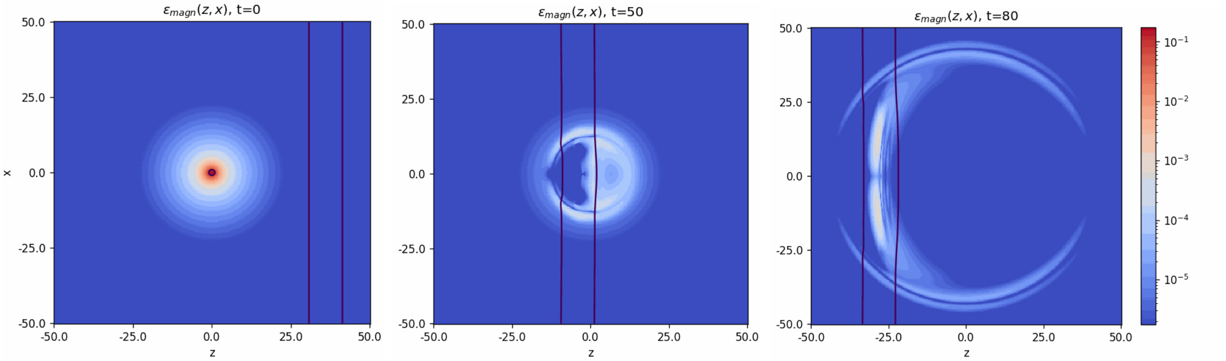

Figure 4.6: This figure shows the time evolution of the magnetic energy density during the erasure process in the $y = 0$ plane. For this case, the initial velocities are $u_{\mathrm{M}} = 0$ and $u_{\mathrm{VL}} = -0.8$. The black lines indicate the contour defined by $\sqrt{\phi^a \phi^a} = 0.5$, thus illustrating the positions of the two domain walls of the $SU(2)$-invariant vacuum layer.

density shown in Figure 4.5. This deformation occurs because the scalar field profile of the magnetic monopole merges with that of the vacuum layer. As a consequence, a travelling wave is generated on the domain wall, propagating radially outward from the collision point along the first wall. Such travelling waves on domain walls have been previously discussed in [162]. It was shown in [163] that the associated emission of electromagnetic and scalar radiation is negligible, with the dominant energy loss arising from gravitational radiation. Using the methods described in Section 5.4, we computed the emitted gravitational energy and observed a constant power of gravitational radiation associated with this travelling wave. Note that we do not include the back-reaction of the gravitational radiation on the propagating wave. Accounting for this effect would lead to a damping and eventual disappearance of the travelling wave.

Another observation from the simulation is the presence of a magnetic energy density that is roughly three orders of magnitude smaller than the energy density in the core of the monopole, which propagates radially outward from the collision point, even beyond

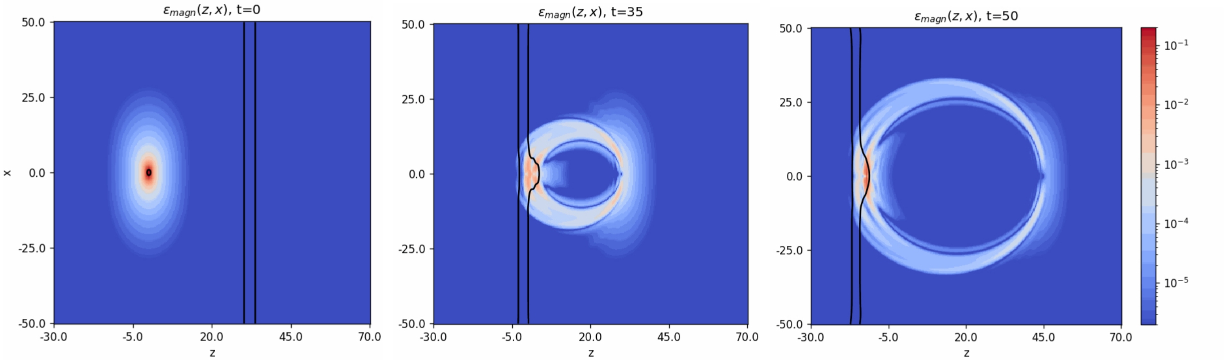

Figure 4.7: This figure shows the time evolution of the magnetic energy density for the maximal velocities we have simulated, $u_{\mathrm{M}} = 0.8$ and $u_{\mathrm{VL}} = -0.98$. The black lines illustrate the position of the vacuum layer.

the vacuum layer. This magnetic energy density corresponds to electromagnetic radiation. Several observations support this interpretation. First, we find that the radiation propagates at the speed of light. Second, the electric and magnetic fields show the characteristic structure of electromagnetic radiation, as shown in Figure 4.9. The electric field is perpendicular to the $y = 0$ plane and due to the axial symmetry we can conclude that it has circular symmetry around the z-axis. The magnetic field has no y-component in the $y = 0$ plane and exhibits a banana-shaped structure. This radiation pattern is characteristic for the electromagnetic radiation emitted during the acceleration of a magnetic point charge.[4] Indeed, by comparing the radiation direction for different initial monopole velocities, we find that its dependence on the initial velocity closely resembles the behaviour expected for electromagnetic radiation from an accelerated magnetic point charge.

Before interpreting these similarities, let us take a closer look at the direction of the magnetic field after the erasure of the monopole. In Figure 4.8, one can clearly see that initially the magnetic field lines point radially outward from the centre of the monopole. However, after the pulse of electromagnetic radiation has passed, the magnetic field arrows reorient and point to the right, i.e. perpendicular to the domain wall. The reason for this behaviour is that the magnetic charge, which was initially localized in the monopole core, becomes distributed over the entire vacuum layer. Effectively, the wall turns into a magnetically charged plane. The information about this redistribution of the magnetic charge is transported by the photon, and this is why the magnetic field reorients to the right after the erasure process.

This redistribution also explains the similarities in the radiation pattern between the erasure process and the acceleration of a magnetic point charge. In the erasure scenario, the magnetic charge spreads into the vacuum layer when the monopole hits the first domain wall. During this process, the entire magnetic charge begins to move into the $SU(2)$-

---

[4] Notice that the radiation pattern of an accelerated electric point charge is well-known. The radiation of an accelerated magnetic point charge is essentially the same, with the electric and magnetic fields exchanged.

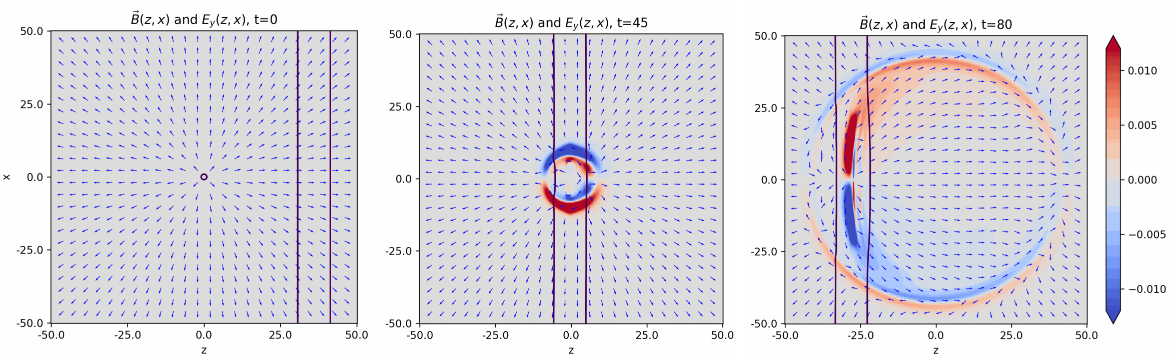

Figure 4.8: This figure shows the time evolution of the magnetic and electric fields in the $y = 0$ plane for the case of vanishing monopole velocity and a vacuum layer velocity of $u_{\mathrm{VL}} = -0.8$. The colour density plot represents the y-component of the electric field. The arrows indicate the direction of the magnetic field within this plane. Notice that the x- and z-components of the electric field and the y-component of the magnetic field vanish in the $y = 0$ plane.

invariant vacuum, i.e. it undergoes acceleration. Therefore, the resulting radiation characteristics resemble those of an accelerated magnetic point charge.

As already mentioned, we observe the erasure in all cases we analysed, and it appears impossible for the monopole to pass through the vacuum layer. In [23], this behaviour is explained in terms of a loss of coherence. After the monopole collides with the vacuum layer, the coherence required to reconstruct a localized magnetic monopole configuration is carried away by the emitted radiation. This phenomenon can also be understood from entropy arguments presented in [164]. A state containing radiation has a much larger entropy than a state with a single monopole. Consequently, the recreation of a monopole from the state with radiation is highly suppressed. Similar explanations have been used in previous works [154, 165].

4.4.4 Conclusion and Outlook

In this section, the erasure mechanism was presented for an $SU(2)$ gauge theory with an adjoint scalar field. Thereby, we collided a magnetic monopole with an $SU(2)$-invariant vacuum layer to prove the erasure using numerical simulations. With these simulations we deepened the understanding of the erasure process itself. In particular, we observed that during the erasure, electromagnetic radiation is emitted, which is sourced by an accelerated magnetic charge that is spreading from the monopole core into the vacuum layer.

Since the erasure mechanism can occur in the early Universe, it may contribute to the production of high-energy particles that could, in principle, be detectable today. In addition to the electromagnetic radiation emitted during the erasure process, gravitational radiation is also produced. From the radiation spectrum and the total emitted energy, it may be possible to derive constraints on the monopole abundance and on the grand unification scale in the early Universe. A more detailed investigation of these implications

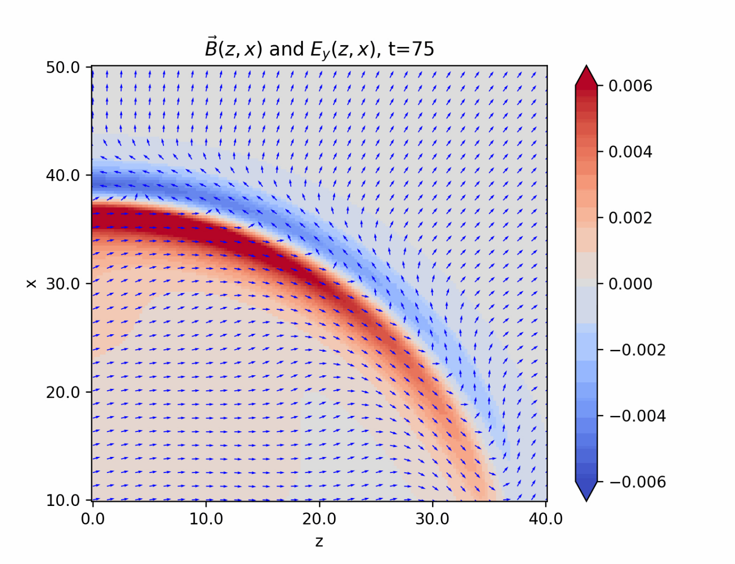

Figure 4.9: This figure shows a zoomed version of the magnetic and electric fields of the electromagnetic radiation emitted during the erasure process. The arrows indicate the x- and z-components of the magnetic field, while the colour represents the y-component of the electric field.

is left for future work.

Finally, we comment on the original motivation for the erasure mechanism, namely its role as a possible solution to the magnetic monopole problem. In this section, we have analysed a highly simplified setup consisting of a planar vacuum layer and a single magnetic monopole. In a realistic cosmological phase transition, however, the situation is considerably more complicated. Instead of a single monopole, there will be many monopoles and anti-monopoles. And instead of a single planar domain wall, closed domain wall bubbles can form. Due to the pressure difference between the interior and exterior, such bubbles may either collapse or expand and collide with other bubbles. During their expansion or collapse, they can encounter multiple monopoles and erase them in the process. As observed in our simulations, after the collision, the magnetic charge of a monopole spreads over the entire wall. In the presence of multiple monopoles and anti-monopoles, the magnetic charges distributed on the wall can neutralize each other. An analogy of this process is a conducting plate with an initially inhomogeneous charge distribution. Due to the conductive properties of the plate, positive and negative charges redistribute and neutralize.

However, one may ask what happens if the numbers of monopoles and anti-monopoles erased by a domain wall bubble are not equal. In that case, the magnetic charge cannot fully neutralize on the wall. By charge conservation, a net magnetic charge must remain, even if the bubble subsequently collapses or collides with other walls. A possibility supported by the theory is the recreation of magnetic monopoles that carry exactly this residual charge. In our numerical analysis, this scenario was explicitly tested. We found that if the domain wall collapses after erasing a single monopole, it is indeed possible for a monopole to be recreated, carrying its original magnetic charge.

Furthermore, for a monopole to be erased, it must collide with a wall. However, it remains unclear whether every monopole will indeed encounter a domain wall.

These thoughts imply that the erasure mechanism in the early Universe may not eliminate all magnetic monopoles permanently. A residual fraction of monopoles can, in general, remain. In [23], it was argued that the erasure mechanism can nevertheless be highly efficient. However, its viability as a solution to the magnetic monopole problem could in principle be strongly model-dependent. For instance, it depends on the velocities of the domain walls, as well as on the abundance of domain walls and magnetic monopoles. A complete understanding therefore requires a more detailed analysis, which is left for future work.

4.5 Magnetic Monopoles Connected by Cosmic Strings

The last solution to the magnetic monopole problem that will be presented in this thesis is the so-called Langacker–Pi mechanism. In 1980, Langacker and Pi suggested [18] that, after the phase transition from the grand unified phase down to the SM phase, there can be a subsequent phase transition that breaks the electromagnetic $U(1)_{\mathrm{em}}$ symmetry group for a finite period of time. One possible breaking pattern could be

$$SU(5) \to SU(3)_{\mathrm{c}} \times SU(2)_L \times U(1)_Y \to SU(3)_{\mathrm{c}} \times U(1)_{\mathrm{em}} \to SU(3)_{\mathrm{c}} \to SU(3)_{\mathrm{c}} \times U(1)_{\mathrm{em}} \,. \tag{4.29}$$

In [18], Langacker and Pi explicitly showed that such a breaking pattern can be realized. In the first symmetry breaking, where the $SU(5)$ symmetry is broken down to the SM gauge group, magnetic monopoles are produced. During the electroweak symmetry breaking, nothing happens to these monopoles, since an overall $U(1)$ symmetry remains unbroken. In the next step, when the electromagnetic symmetry group $U(1)_{\mathrm{em}}$ is broken, cosmic strings in the form of Nielsen–Olesen flux tubes [11] can form. These strings have the property that the $U(1)_{\mathrm{em}}$ symmetry is restored inside their core. Therefore, outside the string the photon becomes massive, while inside it remains massless. As a result, it is energetically favourable for the magnetic flux, originating from the monopoles, to become confined within the cosmic string. In this way, monopoles and anti-monopoles become connected by the strings. Due to the string tension, the monopoles are pulled toward each other, and when a monopole and an anti-monopole collide, they annihilate. In this way, all monopoles can disappear before the $U(1)_{\mathrm{em}}$ symmetry is fully restored at a later stage in the evolution of the Universe. In [166], it was shown that this Langacker–Pi mechanism is indeed efficient enough to solve the magnetic monopole problem.

There are several different ways in which magnetic monopoles can become connected by strings. In Section 4.5.1, magnetic monopole necklaces, which are monopoles with two strings attached to them, will be briefly discussed. In Section 4.5.2, magnetic monopole dumbbells, which are monopole–anti-monopole pairs connected by a string, will be analysed. Subsequently, we will study the gravitational radiation spectrum resulting from magnetic monopole dumbbells.

4.5.1 Magnetic Monopole Necklaces

The minimal model in which magnetic monopole necklaces can appear is an $SU(2)$ gauge theory with a gauge field W_μ and two adjoint scalar fields, ϕ and χ. The Lagrangian we will study is [11]

$$\mathcal{L} = -\frac{1}{2}\operatorname{Tr}(G_{\mu\nu}G^{\mu\nu}) + \operatorname{Tr}\left((D_\mu\phi)^\dagger(D^\mu\phi)\right) + \operatorname{Tr}\left((D_\mu\chi)^\dagger(D^\mu\chi)\right) - V(\phi,\chi)\,, \tag{4.30}$$

with the potential

$$V(\phi,\chi) = \lambda_\phi\left(\operatorname{Tr}\big(\phi^2\big) - \frac{v_\phi^2}{2}\right)^2 + \lambda_\chi\left(\operatorname{Tr}\big(\chi^2\big) - \frac{v_\chi^2}{2}\right)^2 + \beta\operatorname{Tr}(\phi\chi)^2\,. \tag{4.31}$$

Here, we take all constants to be positive, $\lambda_\phi\,, v_\phi\,, \lambda_\chi\,, v_\chi\,, \beta > 0$. In this chapter, we use the same conventions and notation as in Section 2.3.3. For the moment, let us assume the hierarchy $m_{h,\phi} = \sqrt{\lambda_\phi}\,v_\phi^2 > m_{h,\chi} = \sqrt{\lambda_\chi}\,v_\chi^2$. When the ϕ field obtains a non-zero VEV, the $SU(2)$ symmetry is broken down to $U(1)$. This remaining $U(1)$ symmetry can be further broken down to Z_2 by the field χ. Notice that the second breaking is only possible if $\beta > 0$, since only in this case the minimization of $\beta\operatorname{Tr}(\phi\chi)^2$ enforces that the two vectors ϕ^a and χ^a are perpendicular to each other. In contrast, if $\beta < 0$, the minimization of the β-term is achieved by having ϕ^a and χ^a parallel to each other. In this case, the $U(1)$ symmetry would remain unbroken. Since we are interested in the formation of strings we will continue the discussion with $\beta > 0$.

The string solution in this model is called a Z_2 string and is given by [167]

$$\phi^a = v_\phi\delta_{a3}\,, \qquad \chi^a = v_\chi H(r)\begin{pmatrix}\cos\varphi\\ \sin\varphi\\ 0\end{pmatrix}, \qquad W_\varphi^a = -\frac{1}{g}K(r)\delta_{a3}\,, \tag{4.32}$$

where φ denotes the azimuthal angle in spherical coordinates (r,φ,θ), and $H(r)$ and $K(r)$ are profile functions. These strings carry a magnetic flux, which can be calculated by $\Phi = \int_S \boldsymbol{B}\cdot \mathrm{d}\boldsymbol{S}$, where the $U(1)$ magnetic field is given by $B_i = -\frac{1}{2}\varepsilon_{ijk}\,\hat{\phi}^a G^a_{jk}$. One finds that the flux is given by $\Phi = 2\pi/g$ [11].

In addition to the string solution, this model contains a magnetic monopole solution. At scales below $m_{h,\phi}$, but above $m_{h,\chi}$, the $SU(2)$ symmetry is broken down to $U(1)$. Therefore, a magnetic monopole solution exists, which is given by the standard 't Hooft–Polyakov magnetic monopole. Its total flux is $4\pi/g$, i.e. twice the flux of the Z_2 string. Now, below the scales $m_{h,\chi}$, the $U(1)$ gets broken. Therefore, all the magnetic flux sourced by magnetic monopoles gets confined into magnetic flux tubes. The only way this can be achieved in this model is to attach two Z_2 strings to the monopole such that they carry away the full flux. Notice that it is necessary to have two strings with flux $2\pi/g$ to confine the full magnetic monopole flux $4\pi/g$. [168]

A possible scalar field ansatz for an infinite string with a single monopole located at the origin can have the following structure

$$\phi^a \propto \begin{pmatrix} \sin\varphi \sin\theta \\ -\cos\varphi \sin\theta \\ \cos\theta \end{pmatrix}, \qquad \chi^a \propto \begin{pmatrix} \cos\varphi \\ \sin\varphi \\ 0 \end{pmatrix}. \tag{4.33}$$

This configuration has a winding in ϕ around the origin. Furthermore, there is a winding in χ around the z-axis. Using numerical relaxation, one can use this ansatz to find the actual solution for such a configuration.

During phase transitions, multiple magnetic monopoles can end on string loops, forming magnetic monopole necklaces. Notice that there cannot be two magnetic monopoles of the same charge next to each other on the string. This implies that string loops always contain the same number of monopoles and anti-monopoles. In Figure 4.10, a numerically obtained monopole necklace system is shown.

Above we assumed the scaling hierarchy $m_{h,\phi} > m_{h,\chi}$. This implies that magnetic monopoles form in the ϕ field, while strings form in the χ field. For $m_{h,\phi} < m_{h,\chi}$, this would be the other way around, i.e. monopoles would form in the χ field and strings would form in the ϕ field. However, the overall behaviour remains the same.[5]

The dynamics of magnetic monopole necklaces was first simulated in [169]. It turned out that the evolution of necklaces is different from earlier predicted dynamics [170, 171]. The simulations showed that the relative velocity of the monopoles on the strings is negligible and, thus, the only way to annihilate magnetic monopoles is through the collapse of the necklaces. In this way, the magnetic monopole problem can be solved: In a first phase transition ($SU(2) \to U(1)$), magnetic monopoles form, which become confined in a second phase transition ($U(1) \to Z_2$), resulting in magnetic monopole necklaces. These necklaces can collapse, leading to the annihilation of the magnetic monopoles.

4.5.2 Magnetic Monopole Dumbbells

This section presents a brief and partial reproduction of the work [165] published by my collaborators Gia Dvali, Juan Sebastián Valbuena-Bermúdez, and Michael Zantedeschi. The simulation programs used to obtain the numerical results shown here were developed within the project [20].

Another possibility to annihilate magnetic monopoles is to connect a monopole–anti-monopole pair by a single cosmic string, forming a so-called magnetic monopole dumbbell. This may lead to very efficient annihilation, since the string induces a distance-independent force between the monopole and anti-monopole, resulting in a strong acceleration towards each other until they collide and annihilate.

---

[5] An interesting case is the regime with $\lambda_\phi = \lambda_\chi$ and $v_\phi = v_\chi$, which corresponds to $m_{h,\phi} = m_{h,\chi}$. In this case, single monopoles split into two so-called semipoles located on the string. More details can be found in [169].

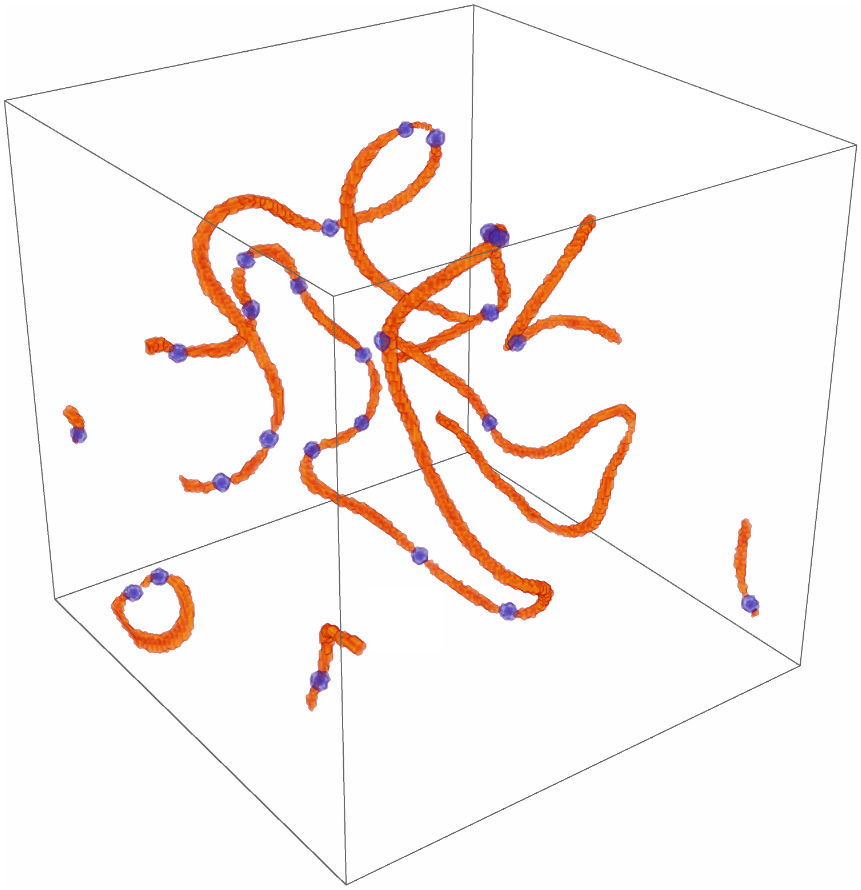

Figure 4.10: This figure shows a time frame of a magnetic monopole necklace system described by the Lagrangian (4.30). The figure shows a density plot of the scalar field profiles for ϕ and χ (values close to the vacuum expectation values are made transparent). The monopole–string structure is obtained dynamically. More details on how this is achieved numerically are given in the Appendix A.9.

As a prototype model we will consider an $SU(2)$ gauge theory with a scalar field ϕ transforming in the adjoint representation, which allows for the spontaneous symmetry breaking $SU(2) \to U(1)$. To further break $U(1) \to 1$, we introduce another scalar field, ψ, transforming in the fundamental representation of $SU(2)$. The Lagrangian of the theory is given by [172, 173]

$$\mathcal{L} = \mathrm{Tr}\left((D_\mu \phi)^\dagger \left(D^\mu \phi\right)\right) + (D_\mu \psi)^\dagger (D^\mu \psi) - \frac{1}{2}\,\mathrm{Tr}\left(G^{\mu\nu} G_{\mu\nu}\right) - V(\phi, \psi)\,, \tag{4.34}$$

with the potential

$$V(\phi, \psi) = \lambda_\phi \left(\mathrm{Tr}\left(\phi^\dagger \phi\right) - \frac{v_\phi^2}{2}\right)^2 + \lambda_\psi \left(\psi^\dagger \psi - v_\psi^2\right)^2 + \beta \psi^\dagger \phi \psi\,. \tag{4.35}$$

Again, we use the same conventions and notation as in Section 2.3.3. The covariant derivative for the ψ field can be defined as usual by $D_\mu \psi = \partial_\mu \psi - i g W_\mu \psi$.

We wish that the first symmetry breaking is triggered by the scalar field ϕ, and the second by ψ. Therefore, we assume the hierarchy $v_\phi > v_\psi$. The overall breaking pattern is then given by

$$SU(2) \xrightarrow{\langle\phi\rangle} U(1) \xrightarrow{\langle\psi\rangle} 1\,. \tag{4.36}$$

After the first breaking, only one of the three generators is generating the residual unbroken $U(1)$ symmetry. Hence, one gauge boson, the photon, remains massless. The other two gauge bosons acquire a mass $m_{v,\phi} = gv_\phi$. The remaining scalar degree of freedom, the Higgs boson, has a mass $m_{h,\phi} = \sqrt{2\lambda_\phi}v_\phi$. Through the VEV of the field ψ, the $U(1)$ symmetry gets also spontaneously broken. This gives an additional contribution of $m_{v,\psi} = gv_\psi/\sqrt{2}$ to all three gauge boson masses. The Higgs boson associated with the ψ field acquires a mass $m_{h,\psi} = 2\sqrt{\lambda_\psi}v_\psi$.

It is important to comment that the interaction term $\beta\psi^\dagger\phi\psi$ cannot be generated through quantum corrections. This is because for $\beta = 0$ the theory has a Z_2 symmetry, $\phi \mapsto -\phi$, which is preserved by quantum corrections. In the limit $g \to 0$, this term is required in order to realize the breaking pattern (4.36), while in the gauged case, $g \neq 0$, the non-linear structure of the gauge interactions with the scalar fields are sufficient to obtain the correct breaking. One might therefore ask why to include this β-term at all. Indeed, even without it, the magnetic flux can still become confined in cosmic strings. However, these strings are stable only for sufficiently small values of m_{h_ψ}. This becomes evident in the limit $v_\phi \to \infty$, where the strings reduce to known configurations of semi-local strings, which are stable only when m_{h_ψ} is sufficiently small [95, 94].[6] In what follows, we will thus restrict to the case $\beta \neq 0$.

From the Lagrangian (4.34), we can derive the classical field equations

$$(D_\mu G^{\mu\nu})^a = j_\phi^{a,\nu} + j_\psi^{a,\nu}\,, \tag{4.37}$$

$$(D_\mu D^\mu \phi)^a + \frac{\partial V(\phi,\psi)}{\partial \phi^a} = 0\,, \tag{4.38}$$

$$D_\mu D^\mu \psi + \frac{\partial V(\phi,\psi)}{\partial \psi^\dagger} = 0\,, \tag{4.39}$$

where the currents are given by $j_\phi^{a,\nu} = g\varepsilon^{abc}(D^\nu\phi)^b\phi^c$ and $j_\psi^{a,\nu} = ig\psi^\dagger T^a(D^\nu\psi) + h.c.$.

Let us first consider the case without a fundamental scalar field ($\psi = 0$). Since the adjoint scalar field ϕ acquires a VEV, the $SU(2)$ symmetry is spontaneously broken down to $U(1)$. As a consequence, the field equations contain a 't Hooft–Polyakov magnetic monopole solution [2, 3]. When the ψ field acquires a VEV, the magnetic flux originating from the monopoles becomes confined into Nielsen–Olesen flux tubes [11]. In contrast to the Z_2 string discussed in the previous section, these flux tubes now carry magnetic flux $\Phi = 4\pi/g$, i.e. the same flux as for a single magnetic monopole. Therefore, each monopole

---

[6] For the model considered here in this thesis, this has been analysed in detail in the Master's project of Deniz Ali Duru, which I supervised together with Gia Dvali and Giacomo Contri.

is attached to a single string. This results in a monopole–anti-monopole pair connected by a cosmic string.

In Section 3.4, we have already discussed an ansatz for a monopole–anti-monopole pair with arbitrary relative twist angle α. In this section we will focus on twist zero, $\alpha = 0$, giving us the scalar field ansatz [100, 99]

$$\hat{\phi}^a = \begin{pmatrix} \cos(\varphi)\sin\big(\theta - \bar{\theta}\,\big) \\ \sin(\varphi)\sin\big(\theta - \bar{\theta}\,\big) \\ -\cos\big(\theta - \bar{\theta}\,\big) \end{pmatrix} . \tag{4.40}$$

The monopole and anti-monopole are placed along the z-axis at the positions z_{M} and $z_{\bar{\mathrm{M}}}$, respectively. The angles θ and $\bar{\theta}$ denote the polar angles measured from the z-axis with respect to the monopole and anti-monopole positions. φ is the azimuthal angle around the z-axis.

To minimize the potential, the interaction term $-\beta\psi^\dagger\phi\psi$ has to be extremized. This can be achieved by choosing ψ such that the vector $\psi^\dagger T^a \psi$ is parallel to ϕ^a. This condition gives us [98]

$$\hat{\psi} = \begin{pmatrix} \sin\left(\frac{\theta-\bar{\theta}}{2}\right) \\ \cos\left(\frac{\theta-\bar{\theta}}{2}\right) e^{i\varphi} \end{pmatrix} . \tag{4.41}$$

With this orientation the ψ field will break the $U(1)$ symmetry.

Using the scalar field configurations (4.40), (4.41) and the gauge field orientation $W^a_\mu \sim \varepsilon_{abc}\hat{\phi}^b\partial_\mu\hat{\phi}^c$, we apply a numerical relaxation procedure to obtain a solution of the field equations (4.38), (4.37), (4.39). The resulting configuration can then be used as input for a numerical simulation to study the dynamics of a monopole dumbbell configuration. The results for a specific choice of parameters are illustrated in Figure 4.11.

Furthermore, for illustrative purposes, a full system of monopole dumbbells was obtained dynamically in a numerical simulation. One time frame of the time evolution is shown in Figure 4.12.

As expected, we observe that the string pulls the monopole and anti-monopole together. When they collide, they annihilate and emit a pulse of gauge and scalar radiation. In a point-like approximation, we can estimate the acceleration by assuming that the entire string energy is converted into kinetic energy of the monopoles. This yields a constant acceleration $a = \mu/m_{\mathrm{M}}$. Therefore, a larger string tension leads to a larger acceleration.

The constant acceleration has two cosmologically relevant consequences. First, such a system is expected to emit gravitational radiation. The form of the gravitational wave spectrum is discussed in Section 4.5.3. Furthermore, since the monopoles gain a large amount of kinetic energy, they may form a black hole upon collision [174].

The Schwarzschild radius of two monopoles connected by a string is given by $r_{\mathrm{S}} = 2M/M_{\mathrm{P}}^2$, where M denotes the total mass of the system, $M \sim \mu\, L + 2m_{\mathrm{M}}$. L is the initial length of the monopole dumbbell. As the monopoles accelerate towards each other, they emit gravitational and gauge radiation and also interact with the surrounding plasma.

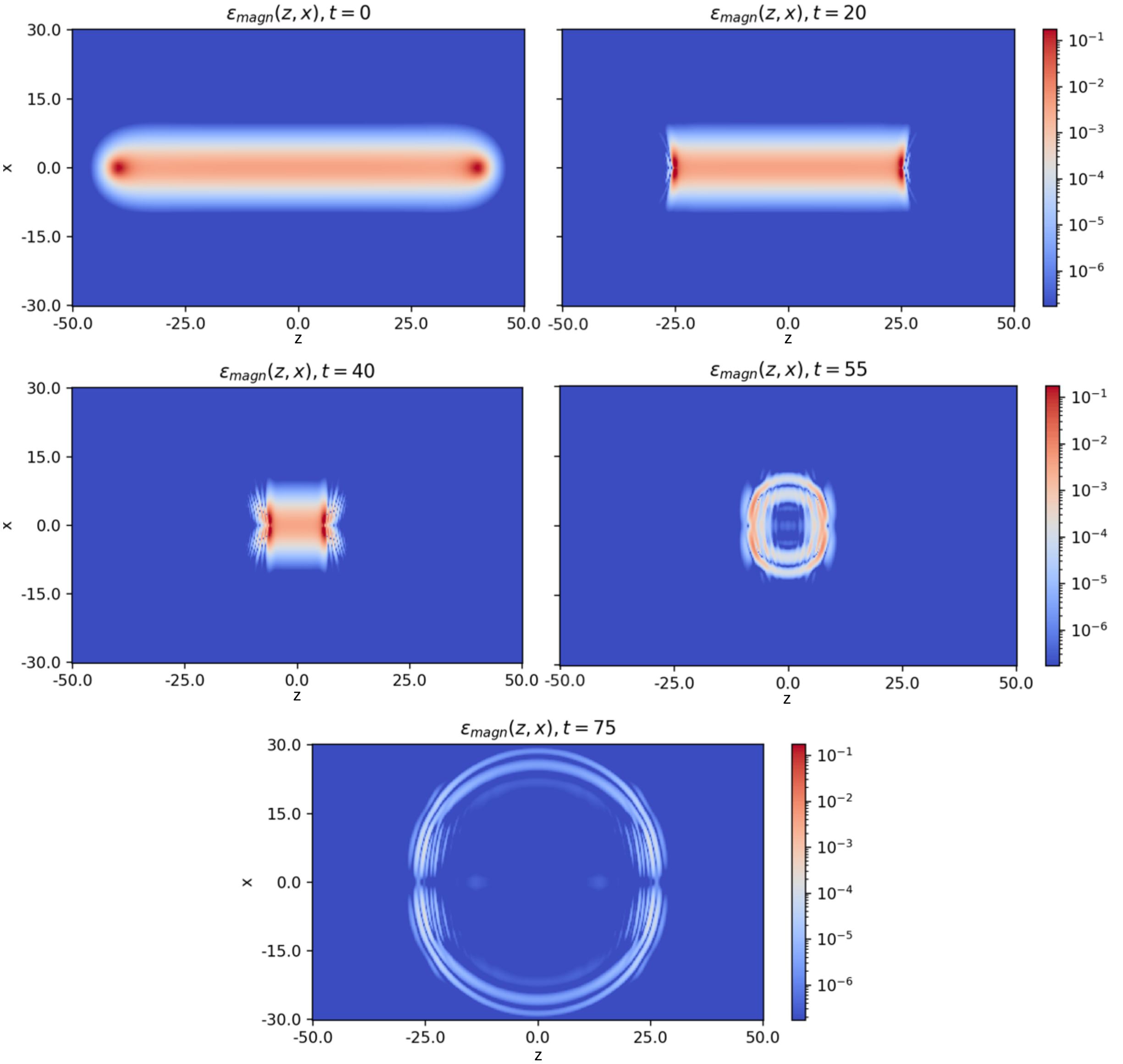

Figure 4.11: These figures show the time evolution of a confined monopole–anti-monopole pair. Here the energy density is illustrated in units of $m^4_{v,\phi}/g^2$. Time and space values are given in units of $m^{-1}_{v,\phi}$. For this figure we used the parameters $m_{h,\phi} = m_{v,\phi}$, $m_{v,\psi} = 0.4\, m_{v,\phi}$, $m_{h,\psi} = 0.4\, m_{v,\phi}$, and $\beta = 0.01\, m_{v_\phi}$.

Nevertheless, if we neglect these energy losses and assume that the total energy remains stored in the monopole–anti-monopole system, we can estimate the minimal initial length of the confined pair that is required for the formation of a black hole. For the occurrence of black hole formation, the Schwarzschild radius must exceed the string thickness, since this corresponds to the characteristic scale at which annihilation would take place. Hence,

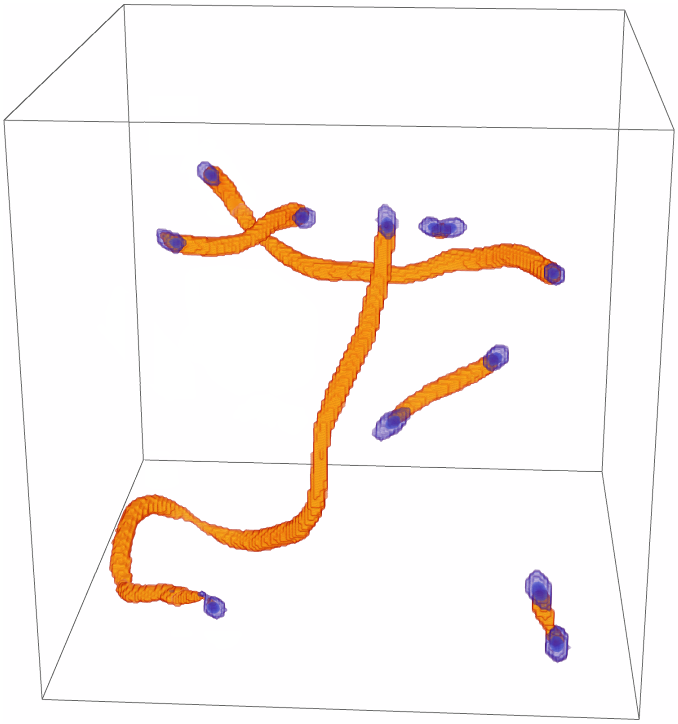

Figure 4.12: This figure shows a time frame of a system with magnetic monopole dumbbells described by the Lagrangian (4.34). The figure shows a density plot of the scalar field profiles for ϕ and ψ (values close to the vacuum expectation values are made transparent). The monopole–string structure is obtained dynamically. More details on how this is achieved numerically are given in Appendix A.9.

the string length at the moment of monopole–anti-monopole pair formation must satisfy $L \gtrsim M_{\mathrm{p}}^2/\mu^{3/2}$, where we have assumed that the string thickness is of order $\mu^{-1/2}$.

This required length is typically very large, making it possible for the string to split into smaller segments via monopole–anti-monopole pair production. Nevertheless, there remains a non-zero probability that the string does not break before the monopoles form a black hole. Thus, this provides a mechanism for black hole formation [174, 165]. Since such monopoles are expected to form very early in the Universe, this process may play an important role in primordial black hole physics.

So far, we have assumed scenarios in which the monopoles collide head-on. However, at high velocities it is quite possible that the monopoles miss each other and simply pass by. In this case, they do not collide and no black hole is formed. Instead, they form an oscillating monopole–anti-monopole pair connected by a string. Such a configuration was considered by Martin and Vilenkin [19], who estimated the corresponding gravitational radiation spectrum analytically. We will review their calculations in the next section.

Finally, we briefly comment on monopole–anti-monopole configurations with relative maximal twist. Above, we considered only the untwisted case, for which we observed that the pair annihilates upon collision. In contrast, for maximal twist ($\alpha = \pi$), the monopole

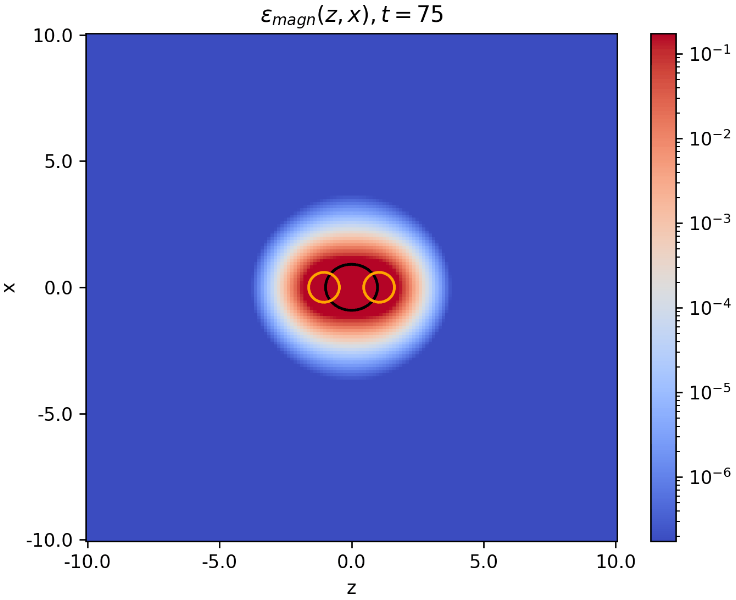

Figure 4.13: This figure shows one time frame of a simulation of a confined monopole–anti-monopole pair with maximal relative twist. The black and the orange lines show one contour, corresponding to half of the respective vacuum expectation value, of the ϕ and ψ profiles. Initially, the monopoles are pulled together. When they collide, they bounce. The time frame shown here corresponds to a stage after the monopoles have already bounced multiple times.

and anti-monopole bounce several times before annihilating [165]. We find that for a perfect axially symmetric setup, implemented in the simulations using the axial symmetry method described in Appendix A.6, the monopole–anti-monopole pair connected by a string does not annihilate within the investigated time interval. Instead, it bounces multiple times. It is very likely that the configuration relaxes to an unstable sphaleron configuration [103]. Notice that we observed the same phenomenon in the unconfined case in Section 3.4. In Figure 4.13, the twisted confined monopole–anti-monopole configuration after multiple bounces is shown. At this stage, the bouncing amplitude is already small compared to the monopole size. Therefore, we assume that the unstable static sphaleron configuration has the structure shown in the figure. Note again that we imposed axial symmetry in the simulation. Without this constraint, small numerical fluctuations are sufficient to cause the configuration to decay, as discussed in [165]. The decay of this configuration leads to a non-zero value of $G_{\mu\nu}\tilde{G}^{\mu\nu}$ during the untwisting. Therefore, this could find interesting applications in axion physics, since the untwisting may serve as a production mechanism for axions. A more detailed study is left for future work.

4.5.3 Gravitational Waves from Monopoles Connected by Cosmic Strings

In the previous section, we found that a monopole–anti-monopole pair connected by a cosmic string attracts with constant acceleration $a = \mu/m_{\mathrm{M}}$. Martin and Vilenkin showed in 1996 [19] that in the point-like approximation a pair of oscillating monopoles, accelerated towards each other with constant acceleration, emits, in the highly relativistic regime, a characteristic power spectrum given by $\mathrm{d}P/\mathrm{d}\omega = 2G\mu^2/\omega$, where G is the gravitational constant and ω is the frequency of the gravitational wave signal.[7]

In this section, we first want to review the calculations by Martin and Vilenkin. We then apply similar calculations to a non-oscillating confined monopole–anti-monopole pair. In particular, we consider two monopoles that are initially pulled together by the string, but whose velocities instantaneously become zero when they collide. The reason for analysing this case is that, in a fully field-theoretic setup as considered in the previous section, a confined monopole–anti-monopole pair will annihilate in a head-on collision and will not pass through each other. We will confirm that one can expect a similar power spectrum from pulling together the monopoles by the string. It should be noted that a monopole dumbbell can, in general, also undergo rotational motion. In such cases, the gravitational radiation spectrum we will calculate in the following would be modified. However, we will not consider these scenarios in this work. The interested reader is referred to [175] for a discussion of gravitational radiation from rotating monopole dumbbells.

Oscillating Confined Monopole–Anti-Monopole Pair

In the following, we review the calculations performed by Martin and Vilenkin [19] for the gravitational wave spectrum of an oscillating pair of monopoles connected by a cosmic string. We assume a point-like approximation, i.e. we treat the two monopoles as point masses of mass m_{M}. Furthermore, we neglect the string in the calculation and only assume that it induces a constant acceleration of the monopoles. The trajectories of such an oscillating pair of point masses can be described by

$$\begin{aligned} \tilde{y}(t) &= \tilde{z}(t) = 0\,, \\ \tilde{x}(t) &= \pm\mathrm{sign}(t)\,\frac{1}{a}\left(\gamma_0 - \sqrt{1 + (\gamma_0 v_0 - a|t|)^2}\right). \end{aligned} \tag{4.42}$$

At $t = 0$, the monopoles meet at the origin with maximal velocity v_0 and the corresponding Lorentz factor γ_0. At $t = \pm\gamma_0 v_0/a$, the distance between the monopoles is maximal and the monopoles are at rest. In this calculation, we only take into account gravitational effects and neglect any electromagnetic effects that may originate from the monopoles' magnetic charges. Therefore, a full period is described by the time interval from $t = -\gamma_0 v_0/a$ to $t = +\gamma_0 v_0/a$, and thus the period time is given by $T = 2\gamma_0 v_0/a$.

---

[7] Notice that at high frequencies $\omega \gtrsim \gamma_0^2/T$, where γ_0 is the maximal Lorentz factor of the monopoles and T is the period of oscillation, the power spectrum starts to fall off faster, scaling as ω^{-2}. In this thesis, we will only focus on lower frequencies.

To compute the gravitational radiation spectrum, one can use Weinberg's formula [176]

$$\frac{\mathrm{d}P_n}{\mathrm{d}\Omega} = \frac{G\omega_n^2}{\pi}\left(T^*_{\mu\nu}(\omega_n,\boldsymbol{k})T^{\mu\nu}(\omega_n,\boldsymbol{k}) - \frac{1}{2}\left|T_\mu{}^\mu(\omega_n,\boldsymbol{k})\right|^2\right), \tag{4.43}$$

where $\mathrm{d}\Omega$ is the differential solid angle and $\omega_n = 2\pi n/T$ is the frequency of the gravitational wave signal corresponding to the mode number n. Here, $T^{\mu\nu}(\omega_n,\boldsymbol{k})$ denotes the Fourier-transformed energy-momentum tensor,

$$T^{\mu\nu}(\omega_n,\boldsymbol{k}) = \frac{1}{T}\int_0^T \mathrm{d}t\, e^{i\omega_n t}\int \mathrm{d}^3x\, e^{-i\boldsymbol{k}\cdot\boldsymbol{x}}\, T^{\mu\nu}(\boldsymbol{x},t)\,. \tag{4.44}$$

For a point mass moving in the x-direction, only the components T^{00}, T^{01}, T^{10}, and T^{11} are non-vanishing. Using energy momentum conservation, $k_\mu T^{\mu\nu} = 0$, one can write $T^{00} = u\,T^{01}$ and $T^{11} = T^{01}/u$, where $u = k_x/\omega_n$. Making use of these relations and integrating (4.43) over all directions of radiation emission finally yields

$$P_n = 2G\omega_n^2\int_0^1 \mathrm{d}u\,\frac{(1-u^2)^2}{u^2}\left|T^{01}(\omega_n,\boldsymbol{k})\right|^2. \tag{4.45}$$

The energy-momentum tensor corresponding to the monopole motion (4.42) is

$$T^{01}(t,\boldsymbol{x}) = m_{\mathrm{M}}\left(\gamma_0 v_0 - a|t|\right)\delta(y)\,\delta(z)\left[\delta(x-\tilde{x}(t)) - \delta(x+\tilde{x}(t))\right]. \tag{4.46}$$

The Fourier-transformed energy-momentum tensor can then be calculated as

$$T^{01}(\omega_n,\boldsymbol{k}) = \frac{m_{\mathrm{M}}}{T}\int_0^T \mathrm{d}t\,\left(\gamma_0 v_0 - a|t|\right)\left[\cos(\omega_n t) + i\sin(\omega_n t)\right]\,(-2i)\sin(\omega_n u\tilde{x}(t))\,. \tag{4.47}$$

Due to the periodic motion, we can extend the integral to the lower boundary $-T$ and divide the full expression by a factor of two. We can then use that the imaginary part of the integrand is anti-symmetric under $t \to -t$ and thus can be dropped. The real part remains and, after using trigonometric identities, we find

$$T^{01}(\omega_n,\boldsymbol{k}) = \frac{m_{\mathrm{M}}}{T}\int_0^T \mathrm{d}t\,\left(\gamma_0 v_0 - a|t|\right)\left[\cos(\omega_n t - \omega_n u\tilde{x}(t)) - \cos(\omega_n t + \omega_n u\tilde{x}(t))\right]. \tag{4.48}$$

Next, we perform the substitution $\xi = 1 - at/(\gamma_0 v_0)$. Furthermore, we are interested in the highly-relativistic regime with $\gamma_0 v_0 \gg 1$ and $v_0 \sim 1$. In this limit, the $\tilde{x}$-trajectory can be approximated by $\tilde{x}(\xi) \approx (\gamma_0/a)(1-|\xi|)$. Inserting this into (4.48) yields

$$\begin{aligned} T^{01}(\omega_n,\boldsymbol{k}) &\approx \frac{m_{\mathrm{M}}\gamma_0^2}{Ta}\int_{-1}^1 \mathrm{d}\xi\,\xi\,\left[\cos(n\pi(1-\xi)(1-u)) - \cos(n\pi(1-\xi)(1+u))\right] \\ &= \frac{8m_{\mathrm{M}}\gamma_0}{n^2\pi^2}\,\frac{u\,\sin^2\left(\frac{n\pi}{2}(1-u)\right)}{(1-u^2)^2}\,. \end{aligned} \tag{4.49}$$

Inserting this into equation (4.45) finally gives, after integration and simplification,

$$P_n \approx \frac{16G\mu^2}{n\pi} \int_0^{n\pi/2} \mathrm{d}\tilde{u}\, \frac{\sin^4(\tilde{u})}{\tilde{u}^2 \left(1 - \frac{\tilde{u}}{n\pi}\right)^2} \approx \frac{4G\mu^2}{n} \,. \tag{4.50}$$

Notice that we used the substitution $\tilde{u} = n\pi(1-u)/2$ and the last integral has been performed numerically.

In summary, this result describes the gravitational radiation spectrum in the highly relativistic regime for frequency modes up to $n \sim \gamma_0^2$ [19].

Colliding Confined Monopole–Anti-Monopole Pair

Above, we analysed the gravitational radiation spectrum for an oscillating pair of monopoles. The oscillating pair is cosmologically well-motivated, since the probability that a pair of relativistic monopoles collides when pulled together by the string is very low, they instead tend to miss each other and fly by. This behaviour can be approximated by the oscillating pair described above [177]. Nevertheless, mainly in view of the discussion we will provide in Chapter 5, we also perform the same calculation for a colliding confined monopole–anti-monopole pair. In this case, we assume that the monopoles are first accelerated by the string, but at the moment of collision they stop immediately and do not pass through each other.

The motion describing this setup is the same as in equation (4.42). The difference is that we now consider the time interval from $t = -\gamma_0 v_0/a$ to $t = 0$. Thus, the monopoles start at rest and stop once they have reached their maximal velocity v_0. For the calculation, we assume that this process occurs periodically, i.e. after the monopoles collide and their velocity is reset to zero, they begin accelerating again. The period of this motion is therefore $T = \gamma_0 v_0/a$.

The Fourier-transformed energy-momentum tensor has the same form as the one we already had earlier,

$$T^{01}(\omega_{\bar{n}}, \boldsymbol{k}) = \frac{m_{\mathrm{M}}}{T} \int_0^T \mathrm{d}t\, (\gamma_0 v_0 - a|t|) \left[\cos(\omega_{\bar{n}} t) + i \sin(\omega_{\bar{n}} t)\right] (-2i) \sin(\omega_{\bar{n}} u \tilde{x}(t)) \,. \tag{4.51}$$

Here $\omega_{\bar{n}} = 2\pi\bar{n}/T$. Notice that since the period is only half of that in the oscillating monopole pair case, we have $n = 2\bar{n}$ corresponding to the same frequencies, $\omega_{\bar{n}} = \omega_n$. Furthermore, if we were to extend the integral to the lower boundary $-T$, the integrand would no longer be anti-symmetric under $t \to -t$, unlike in the previous case. Therefore, we cannot drop the imaginary part. However, since one term is purely imaginary while the other is purely real, we can treat them separately, because they give two additive contributions to the gravitational power, $P_{\bar{n}} = P_{\bar{n}}^{\mathrm{Re}} + P_{\bar{n}}^{\mathrm{Im}}$. Using substitutions and rewriting steps analogous to those in the previous calculation, we obtain for the real part

$$P_{\bar{n}}^{\mathrm{Re}} \approx \frac{32G\mu^2}{\bar{n}^3\pi^3} \int_0^{\bar{n}\pi} \mathrm{d}\tilde{u}\, \frac{\sin^4(\tilde{u})}{\left(1 - \frac{\tilde{u}}{\bar{n}^2\pi^2}\right)^2} \approx \frac{2G\mu^2}{\bar{n}} \,. \tag{4.52}$$

Again, the last integral has been performed numerically. Notice that, after using $n = 2\bar{n}$, the resulting power is exactly the same as the power obtained for the oscillating monopole pair. Now, however, we also have an additional contribution coming from the imaginary part of equation (4.51),

$$\begin{aligned} P_{\bar{n}}^{\mathrm{Im}} &\approx \frac{2Gm_{\mathrm{M}}^2\gamma_0^2 v_0^2}{\bar{n}^2\pi^2 T^2}\int_0^1 \mathrm{d}u\, \frac{1}{u^2}(1-u^2)^2 \left(\frac{2\bar{n}\pi u(1-u^2) + (1+u^2)\sin(2\bar{n}\pi u)}{(1-u^2)^2}\right)^2 \\ &\approx 8Gm_{\mathrm{M}}^2\gamma_0^2 v_0^2 \frac{1}{T^2}\,. \end{aligned} \tag{4.53}$$

Thus, we obtain a contribution to the power spectrum that is constant in the frequency. We can compute the energy spectrum $\mathrm{d}E^{\mathrm{Im}}/\mathrm{d}\omega_{\bar{n}} = P_{\bar{n}}\, T^2/2\pi$, which gives

$$\frac{\mathrm{d}E^{\mathrm{Im}}}{\mathrm{d}\omega_{\bar{n}}} = \frac{4}{\pi} Gm_{\mathrm{M}}^2\gamma_0^2 v_0^2\,. \tag{4.54}$$

This energy spectrum corresponds to two particles that change their velocity instantaneously at the origin. A similar example has already been calculated in [176].

Therefore, we can summarize the results for the power spectrum of the colliding confined monopole pair as follows. The dynamics we considered describe a monopole pair that accelerates towards each other with constant acceleration. When they collide, their velocity instantaneously drops to zero. The two contributions to the power spectrum can be directly associated with these two events. The term $P_n^{\mathrm{Re}} \approx 4G\mu^2/n$ corresponds to the phase of constant acceleration, while $P_n^{\mathrm{Im}} \approx \text{const.}$ corresponds to the instantaneous change in the velocity. We thus conclude that the power spectrum equation obtained by Martin and Vilenkin [19] can also be applied to a setup in which a confined monopole–anti-monopole pair annihilates.

Comparison to the Numerical Simulation

The programs used to calculate the gravitational radiation spectrum, which is presented in this subsection, were developed in close collaboration with Michael Zantedeschi.

For the numerical calculation of the gravitational energy spectrum, we follow the same procedure, which will be explained in detail in Section 5.4.1. In short, the procedure works as follows. From the numerical simulation, we determine the energy-momentum tensor of the system, then compute its Fourier transformation, and finally insert it into Weinberg's formula (5.18) and integrate over the solid angle. This yields the gravitational energy spectrum shown in Figure 4.14. First of all, we clearly observe the ω^{-1} behaviour of the spectrum, which was already predicted in the point-like approximation discussed above. Furthermore, we varied the parameters $m_{h,\psi}$ and $m_{v,\psi}$, and observed that the power spectrum exhibits the expected scaling $\propto \mu^2$. Therefore, we conclude that the result of Martin and Vilenkin, given in equation (4.50), provides a very good approximation for the fully field theoretic setup beyond the point-like approximation.

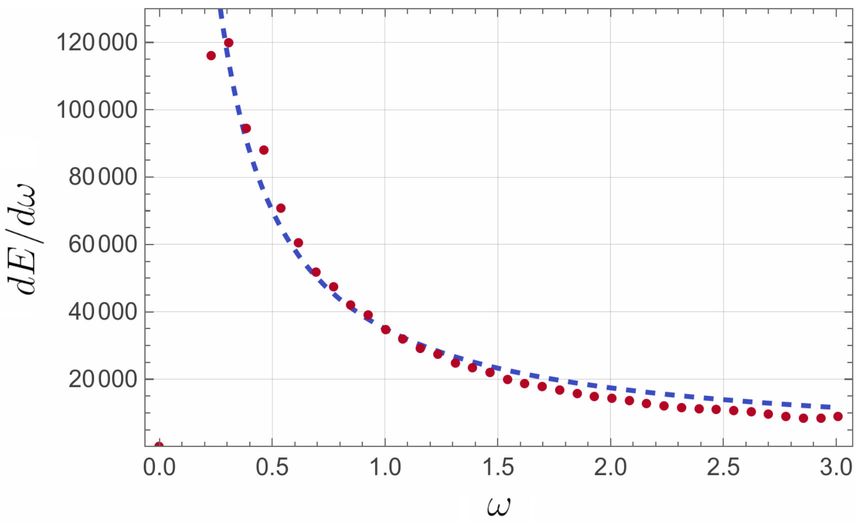

Figure 4.14: This figure shows the gravitational energy spectrum for a confined monopole–anti-monopole pair. The red dots show the measurements from the simulation, while the blue dashed line displays a ω^{-1} curve for comparison. The frequency is given in units of $m_{v,\phi}$. The parameters used in the simulation are the same as those listed in the caption of Figure 4.11.

4.5.4 Discussion and Outlook

In this section, it was shown that magnetic monopoles can connect by cosmic strings in phase transitions where the $U(1)$ symmetry, corresponding to the $U(1)$ magnetic field of the magnetic monopole, gets broken. The resulting structures can either be magnetic monopole necklaces or magnetic monopole dumbbells. Both cases provide an efficient mechanism to annihilate magnetic monopoles and thus may solve the magnetic monopole problem. For magnetic monopole dumbbells, we also saw that they can emit a characteristic signal of gravitational radiation, which could be detectable in future gravitational wave experiments.

Besides gravitational waves, monopoles connected by strings are phenomenologically interesting because their annihilation can be a source of ultra-high-energy cosmic rays [178]. Furthermore, their annihilation can lead to the formation of primordial black holes [179, 174], which may serve as dark matter candidates.

Models that involve magnetic monopoles and cosmic strings may also be relevant for the dynamics of cosmic string networks. A series of works on cosmic string networks [35, 36, 37, 38, 39] obtained promising results for a stochastic gravitational wave background that could be observable in future gravitational waves experiments. In [38], it was shown that the latest data from pulsar timing arrays already provide bounds on the parameters of theories involving cosmic strings. In particular, it was found that $\mu/M_{\mathrm{P}}^2 \gtrsim 10^{-11}$ is excluded, where μ is the string tension and M_{P} is the Planck mass. In minimal models, this would imply that cosmic strings from Grand Unified Theories are excluded, since their typical scale is of order $\mu/M_{\mathrm{P}}^2 \sim 10^{-8} - 10^{-6}$. In [180], however, it was argued that this regime can still be viable if one takes into account the metastability of cosmic strings in models that also contain magnetic monopoles. Through quantum tunnelling, a monopole–anti-monopole pair can nucleate on the string, causing it to break [181, 140]. For a single string loop, this means that the loop splits into a confined monopole–anti-monopole pair. This supports the idea of string networks originating from GUTs, since the late-time evolution of the network, which is responsible for the gravitational wave signal in the frequency range probed by pulsar timing arrays, is cut off at the scale where the strings decay, i.e. where they split into monopole–anti-monopole pairs.

In this section, we only analysed two prototype models, in which confined monopoles can appear. However, there are of course many more models in which such objects can arise. For example, in the SM, so-called electroweak dumbbells may exist [182]. Their structure and dynamics have been analysed numerically in great detail in [183, 184].

Furthermore, the structure of confined monopole–anti-monopole pairs can become far more non-trivial in larger gauge groups $SU(N)$ with $N > 2$. For example, in [185], it was argued that in a symmetry breaking $SU(3) \to (SU(2) \times U(1))\,/Z_2$, magnetic monopoles can appear that carry $U(1)$ magnetic charge and, in addition, $SU(2)$ colour-magnetic charge. In a subsequent symmetry breaking $SU(2) \to Z_2$, the colour-magnetic field becomes confined, leading to the formation of dumbbells. As long as the monopoles have opposite colour-magnetic charge, their $U(1)$ magnetic charges can have either the same sign or opposite signs. These objects share similar dynamics to confined quarks [186]. Therefore, constructing models in which multiple monopoles can become confined and form higher-charged "mesons" and "baryons" may provide a full dual picture of confinement and lead to a better understanding of its dynamics. Similarities between confined monopole–anti-monopole pairs and confined quarks have been discussed in detail in [165]. Furthermore, we will return to this topic in the next chapter.

Chapter 5

The Confinement Slingshot Effect

Although some new aspects were added and discussions were rephrased, this chapter is an ad verbatim reproduction with respect to equations and figures of the two papers "Confinement slingshot and gravitational waves" [20] and "Cosmological Implications of the Slingshot Effect: Gravitational Waves, Primordial Black Holes and Dark Matter" [21] that I wrote with my collaborators Gia Dvali, Juan Sebastián Valbuena-Bermúdez, and Michael Zantedeschi.

In this chapter, a new mechanism, the *confinement slingshot effect* is introduced. This phenomenon arises in theories that allow the coexistence of confined and unconfined vacua. It describes a charge that enters the confined region, where its flux becomes concentrated into flux tubes, producing a string that connects the charge with the wall that is separating the two different phases. Due to the string's tension, it pulls the charge back towards the unconfined vacuum.

These dynamics can appear in various fields of physics. For instance, in a QCD-like theory that supports coexisting confined and unconfined regions, heavy quarks entering the confined region stretch QCD flux tubes. A realization of such a scenario was first described in [160] and we will discuss some details in Section 5.5. Another example in which the slingshot mechanism can appear is in string cosmology, in particular in string-theoretic inflation scenarios [187, 188, 189]. In this context, the role of the slingshot is played by D-strings attached to D-branes of different dimensionalities. We will discuss such a D-brane realization in Section 5.6.

In this chapter, we will specifically focus on magnetic monopole models, in which the $U(1)$-Coulomb magnetic field of the monopole becomes confined within a $U(1)$-Higgsed domain. In the $U(1)$-Coulomb region, the photon is massless and the magnetic monopole can propagate freely. However, when the monopole enters the Higgsed region, where the photon is massive and the magnetic field is confined into flux tubes, it stretches a cosmic string that connects the monopole to the wall separating the Higgsed and Coulomb regions.

Such a scenario for magnetic monopoles can, for example, appear during phase transitions in Grand Unified Theories. As discussed in Chapter 4, it was predicted that, in the absence of a mechanism reducing their density, these monopoles would dominate the Universe today [15, 16]. Besides several other solutions [17, 23, 22], we discussed in great detail the idea by Langacker and Pi [18] in Section 4.5. They proposed that in the evolution of the Universe, there can be another phase during which the electromagnetic $U(1)$ symmetry is temporarily broken. This causes monopoles to become connected by strings that, due to their tension, pull the monopole and anti-monopole toward each other until they collide and annihilate. This provides an efficient mechanism to reduce the number of magnetic monopoles.

While Langacker and Pi assumed that all monopoles connect to strings approximately simultaneously (second-order phase transition), in this chapter, we will consider the possibility that this phase transition occurs as a phase transition of first-order type. In this case, there exists an intermediate stage during which the slingshot effect takes place, before all monopoles become connected in pairs.

Since the slingshot effect can appear in a variety of cosmological setups, it is important to understand the gravitational radiation produced by this effect. Focusing on magnetic monopoles arising from GUTs, we will investigate the gravitational wave spectrum for a single slingshot and extrapolate our results to full slingshot systems that could have occurred in the early Universe. We will present the characteristic properties of this radiation and provide estimations for the expected signal observable today.

Furthermore, we will discuss the phenomenological consequences of the D-brane slingshot. We will show that it can lead to detectable gravitational radiation, as well as to the emission of Kaluza–Klein gravitons that may serve as a dark matter candidate [190]. Moreover, similar to the idea proposed in [191], the collapse of a D-brane slingshot can result in the formation of a primordial black hole [192, 193, 194, 195, 196].

This chapter about the slingshot effect is structured as follows. In Section 5.1, we introduce our prototype model. Since our work is based on numerical studies and the initial configurations of the simulations are highly non-trivial, Section 5.2 is devoted to the setup of these initial conditions and to the numerical implementation. The results of the simulations are then presented in Section 5.3, followed by an analysis of the gravitational radiation produced by the slingshot effect in Section 5.4. Subsequently, we will discuss applications of the slingshot effect in other theories beyond magnetic monopole models. This includes confined quarks in QCD (Section 5.5), D-brane cosmology (Section 5.6), and vortex/string models (Section 5.7).

5.1 The Slingshot Model

We want to construct a prototype model that, first, contains a magnetic monopole solution and, second, supports domain walls separating the $U(1)$-Coulomb vacuum from a vacuum in which the $U(1)$ theory is Higgsed. It turns out that the theory of the Subsection 4.5.2 is the perfect choice. It only requires a small modification of the potential:

$$V(\phi,\psi) = \lambda_\phi \left(\mathrm{Tr}\big(\phi^\dagger\phi\big) - \frac{v_\phi^2}{2} \right)^2 + \lambda_\psi \left(\psi^\dagger\psi - v_\psi^2\right)^2 \psi^\dagger\psi + \beta\psi^\dagger\phi\psi\,, \tag{5.1}$$

where we replaced the quartic potential for ψ by a sextic potential.

Notice that the sextic structure of the potential for ψ is not renormalizable. However, this is not an issue in our context, since we are treating it as an effective potential derived from an underlying renormalizable theory (see the discussion about the Coleman-Weinberg potential in Section 4.2).

In Subsection 4.5.2, we already discussed the role of the β-term. Besides its role in ensuring stable strings, it provides an additional advantage for the slingshot mechanism, as it allows for accelerating domain walls. One can construct scenarios in which a vacuum energy persists in the Coulomb phase, leading to an acceleration of the wall towards that phase. In this way, we can effectively simulate the dynamics of expanding vacuum bubbles.

This model contains three types of topological defects. First, it supports magnetic monopoles, because the scalar field ϕ breaks the $SU(2)$ symmetry to $U(1)$.

Second, due to the disconnected vacuum manifold structure of the ψ field (for $\beta = 0$), the theory admits static domain wall solutions separating the $\psi = 0$ (Coulomb) phase from the $|\psi| = v_\psi$ (Higgsed) phase. Explicit domain wall solutions can be found by solving the Bogomol'nyi equation [30]. For example the solution can be of the form $\psi = (\xi, 0)^T$, with four non-trivial possibilities for ξ:

$$\xi_{(\pm v_\psi,0)}(z) = \frac{\pm v_\psi}{\sqrt{1+e^{m_{h,\psi} z}}}\,, \tag{5.2}$$

$$\xi_{(0,\pm v_\psi)}(z) = \frac{\pm v_\psi}{\sqrt{1+e^{-m_{h,\psi} z}}}\,. \tag{5.3}$$

This shows that the $U(1)$-invariant Coulomb phase and the $U(1)$-Higgsed phase can indeed coexist, separated by domain walls formed by the ψ field.

For $\beta \neq 0$, a potential difference arises between the two vacua. This causes a pressure that acts on the domain wall leading to an acceleration toward the phase with the higher potential energy. In this process, the vacuum energy is converted into kinetic energy of the accelerating wall. The magnitude of the potential difference, and hence the acceleration, is controlled by the parameter β. Such accelerating domain walls play an important role in first-order phase transitions, where bubbles of the Higgsed phase nucleate and expand until all of the space is filled with the broken phase. A substantial part of this chapter will focus on these scenarios.

Last but not least, there exists a third type of topological defect in this theory. For $|\psi| \neq 0$, the $U(1)$ symmetry is Higgsed, and the magnetic field becomes confined within Nielsen–Olesen magnetic flux tubes (cosmic strings) [11]. Consequently, in the Higgsed vacuum, free monopoles can no longer exist and each must be attached to such a string. This occurs either by connecting a monopole–anti-monopole pair or by attaching an individual monopole to the domain wall separating the Coulomb phase from the Higgsed phase. In this chapter, we will focus on the latter configuration. It is important to note that, because monopoles are part of the allowed spectrum of solutions, these cosmic strings are not stable. Through quantum pair production of monopole–anti-monopole pairs, a string can break into several segments [197]. Nevertheless, this process is exponentially suppressed.

5.2 Initial Configuration and Numerical Simulation

We want analyse the collision of magnetic monopoles, initially placed in the Coulomb vacuum, with domain walls separating the Coulomb vacuum from the Higgsed vacuum. There are two main goals of our simulations: first, to understand the dynamics of these processes, and second, to compute the resulting spectrum of gravitational radiation (see Section 5.4). Our strategy is as follows. Accurate calculations of the gravitational wave spectrum require both a high lattice resolution in the numerical simulations and carefully prepared initial conditions. For this, we used several tricks to optimise the results for a single monopole colliding with the wall. We will extrapolate the results for the gravitational waves originating from this process involving only one monopole to multiple monopoles colliding with the wall. For the understanding of the dynamics of multiple monopoles colliding with such a domain wall we also extend our analysis to more complex scenarios. We will study two monopoles colliding with the wall, and a prototype phase transition in which an expanding vacuum bubble interacts with monopoles. The construction of these initial configurations, along with the details of their numerical implementation, will be presented in the following.

5.2.1 One Slingshot

For precise measurements, it is important that the initial configuration does not deviate too strongly from the true solution. Therefore, we need an ansatz that captures the correct physical behaviour of the system. If a monopole is placed in a pure Coulomb vacuum, the magnetic field spreads radially outward decreasing as $1/r^2$. In contrast, in the Higgsed vacuum the magnetic field is confined, leading to a repelling behaviour along the wall that separates the Coulomb from the Higgsed phase[1]. To construct an analytic ansatz that incorporates this structure, we used the analytic equations describing a monopole–anti-monopole configuration with maximal twist [100]. For this ansatz, in the central plane between the two monopoles, the magnetic field lines go parallel to the surface, and the field flips sign across it. The resulting field-line structure resembles that of two monopoles with the same charge, except that the magnetic field direction in half of the volume is inverted. In Section 3.7.3, it was noticed that if this sign flip is compensated by an additional signum function, one can obtain an approximate ansatz for two monopoles of equal charge. The monopole–anti-monopole ansatz with arbitrary relative twist angle α is given in equations (3.23), (3.24), (3.25). For the maximal twist this reduces to

$$\hat{\phi}^a = \begin{pmatrix} \sin(\varphi)\sin\big(\theta+\bar{\theta}\big) \\ -\cos(\varphi)\sin\big(\theta+\bar{\theta}\big) \\ -\cos\big(\theta+\bar{\theta}\big) \end{pmatrix} . \tag{5.4}$$

where $\hat{\phi}^a$ is defined by $\hat{\phi}^a = \phi^a/\sqrt{\phi^b\phi^b}$. The monopole and anti-monopole are located on the z-axis at z_{M} and $z_{\bar{\mathrm{M}}}$, respectively. θ and $\bar{\theta}$ represent the polar angles (with respect to

---

[1] Notice that this effect is analogous to the Meissner effect of superconductors [198].

the z-axis) centred at the monopole and anti-monopole positions. The angle φ denotes the angle around the z-axis. As already discussed in Section 3.4, an approximate monopole–anti-monopole ansatz is then given by [100]

$$\begin{aligned}\phi^a =& \frac{1}{g}\frac{H(r_{\mathrm{M}})}{r_{\mathrm{M}}}\frac{H(r_{\bar{\mathrm{M}}})}{r_{\bar{\mathrm{M}}}}\hat{\phi}^a\,, & (5.5)\\ W^a_\mu =& -\frac{1}{g}(1-K(r_{\mathrm{M}}))(1-K(r_{\bar{\mathrm{M}}}))\,\varepsilon_{abc}\,\hat{\phi}^b\partial_\mu\hat{\phi}^c\,, & (5.6)\end{aligned}$$

where H and K are the profile functions for a single monopole. r_{M} and $r_{\bar{\mathrm{M}}}$ are the radii measured from the monopole and anti-monopole and are given by $r_{\mathrm{M}} = \sqrt{x^2+y^2+(z-z_{\mathrm{M}})^2}$ and $r_{\bar{\mathrm{M}}} = \sqrt{x^2+y^2+(z-z_{\bar{\mathrm{M}}})^2}$, respectively.

We place the domain wall separating the Coulomb and Higgs phases at the central plane between the monopole and the anti-monopole. In this setup, the monopole at $z = z_{\mathrm{M}} < 0$ lies in the Coulomb phase, while the anti-monopole at $z = z_{\bar{\mathrm{M}}} > 0$ is fully contained in the Higgsed phase. Since we wish to simulate only a single monopole entering from the Coulomb vacuum into the Higgsed vacuum, we remove the anti-monopole in the Higgsed phase by applying the following modification:

$$\begin{aligned}\phi^a(x,y,z>0) &\to \phi^a(x,y,z=0)\,, & (5.7)\\ W^a_\mu(x,y,z>0) &\to W^a_\mu(x,y,z=0)\frac{1}{1+e^{\varepsilon z}}\,. & (5.8)\end{aligned}$$

The suppression factor ε is chosen such that most of the gauge field is suppressed within the domain wall of thickness $m^{-1}_{v,\psi}$. This suggests $\varepsilon = m_{v,\psi}$.

With the monopole solution, the directions of the scalar fields are constrained, which must be taken into account when implementing the domain wall solution. As mentioned in Section 4.5.2, for the minimization of the potential we require that $\psi^\dagger T^a\psi$ is parallel to ϕ^a. One possible choice is given by

$$\begin{aligned}\psi^1 =& -\frac{\xi_{(0,+v_\psi)}}{\sqrt{2}}\frac{(\hat{\phi}^1 - i\hat{\phi}^2)}{\sqrt{1+\hat{\phi}^3}}\,,\\ \psi^2 =& \frac{\xi_{(0,+v_\psi)}}{\sqrt{2}}\sqrt{1+\hat{\phi}^3}\,. & (5.9)\end{aligned}$$

The magnetic field lines, the ϕ field vector, and the profile of the ψ field in the final configuration are shown in Figure 5.1. As a cross-check of how well this ansatz satisfies the field equations, we applied a numerical relaxation to it. For more details on the relaxation we refer to Appendix A. Remarkably, the resulting changes in the configuration turned out to be very small. Moreover, inserting the above ansatz into a numerical simulation showed that there are almost no initial fluctuations. Taken together, these observations demonstrate that our constructed ansatz provides an excellent approximation for our purposes.

For $\beta \neq 0$, the domain wall accelerates toward the monopole, naturally leading to a collision event. To observe stronger effects, we additionally Lorentz boost both the

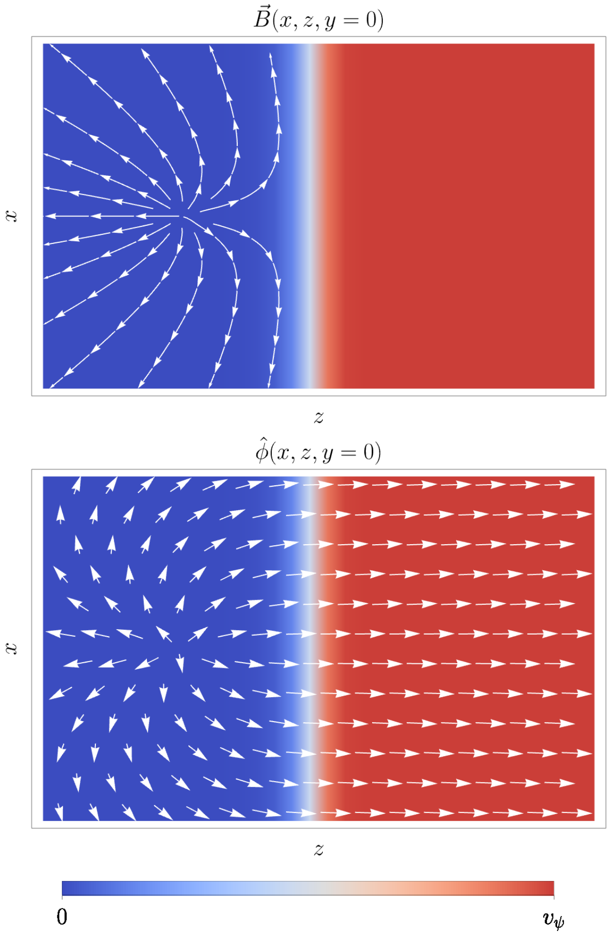
$\vec{B}(x,z,y=0)$

$\hat{\phi}(x,z,y=0)$

Figure 5.1: This figure schematically illustrates the initial configuration. The colour plot represents the profile of the ψ field. The blue region ($\psi = 0$) corresponds to the unbroken Coulomb phase, while the red region ($|\psi| = v_\psi$) corresponds to the Higgsed phase. In the upper plot, the field lines show the magnetic field of the monopole. In the lower panel, the vectors indicate the scalar field direction $\hat{\phi}$.

monopole and the domain wall. The monopole can be boosted by replacing $z - z_{\mathrm{M}}$ and $z - z_{\bar{\mathrm{M}}}$ with $\gamma_{\mathrm{M}}(z - u_{\mathrm{M}}t - z_{\mathrm{M}})$ and $\gamma_{\mathrm{M}}(z + u_{\mathrm{M}}t - z_{\bar{\mathrm{M}}})$, respectively, in equations (5.5) and (5.6), where u_{M} is the monopole velocity and γ_{M} is the corresponding Lorentz factor. A boost of the domain wall is implemented by replacing z with $\gamma_{\mathrm{DW}}(z - u_{\mathrm{DW}}t)$ in equation (5.9), where u_{DW} is the domain wall velocity and γ_{DW} its Lorentz factor. Accordingly, in equation (5.8), the suppression factor ε should be replaced by $\gamma_{\mathrm{DW}}\varepsilon$.

The above-described initial configuration was implemented into a numerical simulation to study the time evolution of the system. The simulation program was written in Python. The strong improvement in computational speed was achieved by making use of the axial symmetry of the system. This symmetry allows us to evaluate the field equations only in a single plane, which we will choose to be the $y = 0$ plane. For the time evolution of the equations of motion, we employed the second-order Crank–Nicolson method. As boundary conditions, we used absorbing boundaries for the fields ϕ^a and W^a_μ. For the ψ field, we imposed Dirichlet boundaries in the z-direction and since the domain wall is moving, we applied periodic boundaries in the x-direction[2]. All details about the programming language, axial symmetry method, the Crank–Nicolson method, and the boundary conditions can be found in Appendix A.

For the field equations, we fixed the gauge by choosing the Lorenz gauge, $\partial_\mu W^\mu_a = 0$. To satisfy this condition initially, we imposed $\partial_t W^a_t = \partial_i W^a_i$ as an initial condition. Analytically, the Lorenz gauge remains satisfied at all times. However, numerically it can become violated. Therefore, we kept track of the gauge condition throughout the time evolution to ensure it was maintained. In the axially symmetric cases, the condition was always preserved.

In the simulations we obtained great results for a lattice and time spacing of $0.25\, m_{v,\phi}^{-1}$ and $0.1\, m_{v,\phi}^{-1}$, respectively. The lattice size was $[-60\, m_{v,\phi}^{-1}, 60\, m_{v,\phi}^{-1}]$ in the x-direction and $[-180\, m_{v,\phi}^{-1}, 60\, m_{v,\phi}^{-1}]$ in the z-direction. The analysed time interval was given by $[0, 180\, m_{v,\phi}^{-1}]$.

To obtain a big picture of the dynamics, we varied all free parameters. However, we focused on the cases where $g = 1$ and $m_{v,\phi}/m_{h,\phi} = 1$, while varying the remaining free parameters within the intervals $m_{v,\psi} \in [0.1\, m_{v,\phi}, 0.7\, m_{v,\phi}]$, $m_{h,\psi} \in [0.1\, m_{v,\phi}, 1.0\, m_{v,\phi}]$, and $\beta \in [0.001\, m_{v,\phi}, 0.1\, m_{v,\phi}]$. The domain wall and the magnetic monopole were initially placed at $z = 0$ and $z_{\mathrm{M}} = -40\, m_{v,\phi}^{-1}$, respectively. The initial velocities of the magnetic monopole and the domain wall were varied within the interval $u_{\mathrm{M}}, u_{\mathrm{DW}} \in [0, 0.98]$. Notice that an initial Lorentz boost of the monopole is not required in order to ensure a collision with the domain wall, since the wall itself accelerates due to the β-term in the potential (5.1).

The monopole–anti-monopole ansatz given in equation (5.4) can be generalized to a configuration of multiple monopole–anti-monopole pairs placed along the z-axis. We simulated two untwisted pairs with a maximal relative twist between them. The orientation of the scalar field is then described by

$$\hat{\phi} = \begin{pmatrix} -\sin\big(\theta_1 - \bar{\theta}_1 + \theta_2 - \bar{\theta}_2\big)\sin\phi \\ \sin\big(\theta_1 - \bar{\theta}_1 + \theta_2 - \bar{\theta}_2\big)\cos\phi \\ -\cos\big(\theta_1 - \bar{\theta}_1 + \theta_2 - \bar{\theta}_2\big) \end{pmatrix} . \tag{5.10}$$

Here, θ_1 and $\bar{\theta}_1$ denote the polar angles around the monopoles of the first pair, while θ_2 and $\bar{\theta}_2$ are the corresponding polar angles for the second pair. As before, we can place the domain wall between the two pairs and remove the second pair. This gives an initial configuration describing a monopole and an anti-monopole entering the Higgsed phase subsequently.

---

[2] Notice that for maximal twist ($\alpha = \pi$), the imaginary component of ψ^1 is anti-symmetric in x-direction. This has to be taken into account for the periodic boundary conditions.

5.2.2 Two Slingshots

In the previous section, we found an ansatz for two monopoles entering the Higgsed phase subsequently along the z-axis. However, this setup produces only a single slingshot. We also aim to study interactions between different slingshots, since in the Universe multiple monopoles are expected to collide with vacuum bubbles.

To this end, we simulated a monopole–anti-monopole pair entering the Higgsed phase in parallel. For this, we used the monopole–anti-monopole ansatz (3.23), (3.24), (3.25) without twist ($\alpha = 0$). Instead of placing the domain wall perpendicular to the z-axis, we aligned it parallel to it. An analytic approximate configuration capturing the repelling behaviour of the magnetic field lines at the wall is not known. However, since the axis going through the monopoles is parallel to the wall, the magnetic field lines are approximately aligned correctly near to the wall. A subsequent numerical relaxation was applied to further improve the configuration and minimize energy emissions in the form of radiation during the simulation.

This numerically determined configuration, however, cannot be Lorentz boosted as easy as the analytic initial configuration in the previous section. Therefore, the monopole–anti-monopole pair was kept static initially, and only the domain wall was boosted. In addition, the domain wall naturally accelerates toward the monopoles due to the β-term.

In this scenario, the system no longer exhibits axial symmetry. Consequently, a full three-dimensional simulation was required, which results in a lower lattice resolution due to the limits of computational resources. Instead of the $0.25\, m_{v,\phi}^{-1}$ spacing used in axially symmetric cases, we used $1.0\, m_{v,\phi}^{-1}$. The full lattice was cubic with edge length $240\, m_{v,\phi}^{-1}$. While the resolution was lower than in the axially symmetric cases, it remained sufficient to capture the relevant phenomena qualitatively. To avoid numerical instabilities, we also included a small artificial friction term in the field equations.

Contrary to the previously described axially symmetric cases, the Lorenz gauge condition, $\partial_\mu W^\mu_a = 0$, was not maintained throughout the simulation. Therefore, we adopted the better behaving time gauge, $W^a_t = 0$, as gauge fixing condition in the equations of motion. This choice was straightforward to implement, because the static monopole–anti-monopole configuration already satisfies $W^a_t = 0$.

5.2.3 Many Slingshots

In addition to the constructed scenarios discussed above, we also simulated a full vacuum bubble that grows and collides with many monopoles. This provides a qualitative picture of how a first-order phase transition may evolve. The initial configuration for this setup is rather simple. The gauge fields W^a_μ were set to zero at the beginning. For the scalar field ϕ^a we introduced small random perturbations around $\phi^a = 0$. Since the system naturally minimizes the potential, the scalar field ϕ quickly falls into the minimum of the potential. In this process magnetic monopoles and anti-monopoles form dynamically. All of the initial potential energy of the system is converted into the creation of these monopoles, along with the emission of radiation. We included a small artificial damping term in the field equations, which suppresses this radiation. In a cosmological context, such damping could arise naturally through interactions with a surrounding plasma.

For the ψ field, we initially inserted a small vacuum domain wall bubble of radius $R = 3\, m_{v,\phi}^{-1}$:

$$\begin{aligned} \psi^1 &= \xi_{(0,\pm v_\psi)}(r - R)\,, \\ \psi^2 &= 0\,, \end{aligned} \tag{5.11}$$

where $\xi_{(0,\pm v_\psi)}$ is the domain wall solution given in equation (5.3). At the beginning of the simulation, we did not evolve the field equations for the ψ field. This kept the bubble configuration fixed, while the scalar field ϕ automatically oriented itself such that the β-term in the potential (5.1) was minimized. Once the magnetic monopoles had formed and the radiation had been sufficiently damped, we began solving the field equations for ψ as well. Because of the vacuum energy, the domain wall bubble started to expand and subsequently collided with the monopoles. The results of this setup will be discussed in Section 5.3.3.

As boundary conditions, we utilized periodic boundaries in all directions. Moreover, the Lorenz gauge was chosen as the gauge-fixing condition. The lattice size was set to $180\, m_{v,\phi}^{-1} \times 180\, m_{v,\phi}^{-1} \times 360\, m_{v,\phi}^{-1}$ with a lattice spacing of $1.0\, m_{v,\phi}^{-1}$.

5.3 Results from the Numerical Simulations

The results of the numerical simulations outlined above provide us with valuable insight into the dynamics of magnetic monopoles during first-order phase transitions. The corresponding observations are presented in the following.

5.3.1 One Slingshot

In the case of a single monopole moving towards the Higgsed phase, we observe that as the monopole approaches the wall, electromagnetic energy appears along it. This energy can be understood by two effects. First, the magnetic field is repelled at the wall. As the monopole comes closer, the magnetic field lines rearrange themselves and dam up at the wall, thereby increasing the density of the field lines and, thus, the magnetic energy localizes there. This adjustment occurs very rapidly, which in turn produces electromagnetic radiation. Furthermore, the collision of the monopole with the wall serves as an additional source of radiation. The resulting radiation propagates towards the Coulomb phase. However, since the wall moves at ultra-relativistic speeds, much of the radiation energy remains near the wall for a long time. Radiation is also emitted into the Higgsed phase, but there the photon is massive, and as a result this radiation is strongly damped and will dissipate.

After the collision of the monopole with the wall, a string is stretched into the Higgsed region. This is the only way a monopole can enter the Higgsed phase, since all the magnetic flux originating from the monopole becomes confined within a flux tube. The string

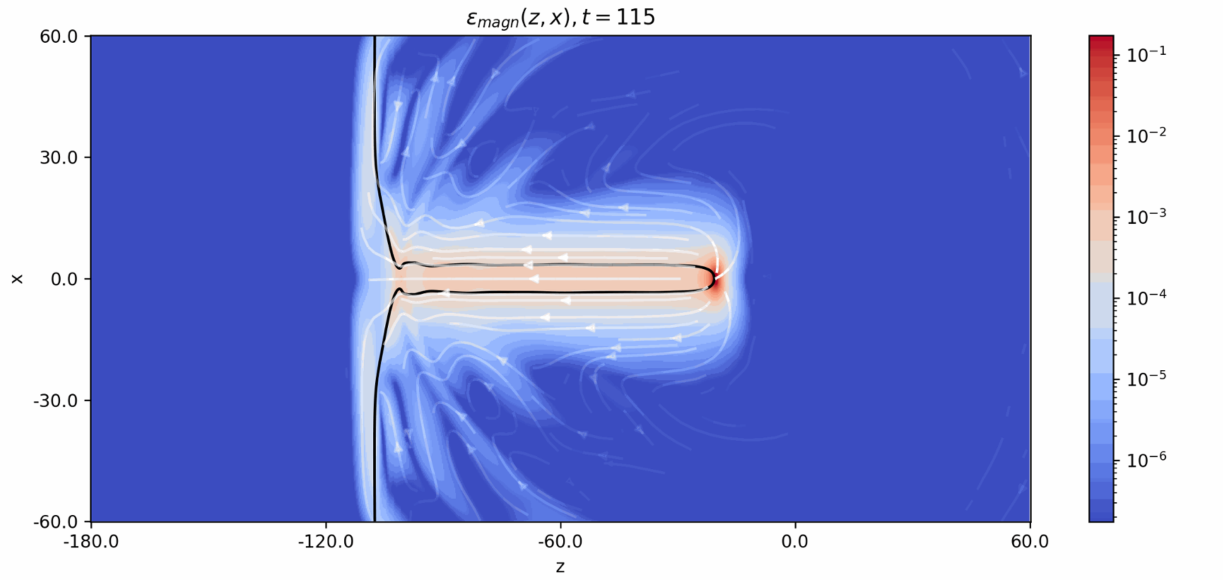

Figure 5.2: This figure shows a slingshot formed after the monopole collided with the ψ domain wall and entered the Higgsed phase. The colour plot illustrates the magnetic energy density in units of $m_{v,\phi}^4/g^2$, the field lines represent the magnetic field, and the black line indicates the contour with the ψ field profile being $|\psi| = 0.1\, m_{v,\phi}$. The coordinates are given in units of $m_{v,\phi}^{-1}$. For this figure we used the parameters $m_{h,\phi} = \sqrt{2\lambda_\phi}\, v_\phi = m_{v,\phi}$, $m_{v,\psi} = g v_\psi/\sqrt{2} = 0.15\, m_{v,\phi}$, $m_{h,\psi} = 2\sqrt{\lambda_\psi}\, v_\psi^2 = 0.6\, m_{v,\phi}$, and $\beta = 0.01\, m_{v_\phi}$. The initial velocities for the monopole and domain wall were $u_{\mathrm{M}} = 0.8$ and $u_{\mathrm{DW}} = -0.8$.

connects the monopole to the domain wall, where the magnetic flux is released into the Coulomb region. Hence, an observer in the Coulomb vacuum measuring the magnetic field would see a point-like magnetic source localized on the wall.

One time frame of the simulation can be found in Figure 5.2. There, the magnetic energy density and the magnetic field lines are illustrated. The full simulated time evolution can be found in the following video: `https://youtu.be/IPJAPjo3nSc`

If one modifies the potential for the field ψ such that the potential difference caused by the interaction term $-\beta\psi^\dagger\phi\psi$ is compensated, one can construct non-accelerating static domain walls. Here, the monopole would collide with the wall and also stretch a string. All the kinetic energy of the monopole then goes into some deformation of the domain wall and into the energy of the string. By neglecting the deformation of the wall, the maximal length of the string can be estimated to be

$$l_{\max} \sim (\gamma_{\mathrm{M}} - 1)\frac{m_{\mathrm{M}}}{\mu}\,, \tag{5.12}$$

where γ_{M} is the Lorentz factor of the monopole during collision, $\mu \sim m_{v,\psi}^2/g^2$ is the string tension, and $m_{\mathrm{M}} \sim m_{v,\phi}/g^2$ is the monopole mass.

After all of the monopole kinetic energy has been transferred into the energy of the string, the monopole changes its direction of motion and begins accelerating back towards the Coulomb phase. The energy stored in the string is then converted back into the kinetic energy of the monopole until it leaves the Higgsed region and moves freely away from the wall within the Coulomb phase. For this reason, we refer to this phenomenon as the *confinement slingshot effect*.

For an accelerating domain wall, the situation becomes more involved. In our simulations, we observed that the monopole decelerates when the string is stretching. Once the string reaches its maximal length, the monopole, the domain wall, and the string begin to move collectively toward the Coulomb vacuum. This behaviour occurs because additionally to the monopole that is accelerated by the string tension, there is the domain wall that is accelerated by the vacuum energy in the Coulomb phase. Notice that the equal velocity of the monopole and the domain wall is only an illusion. Both objects are strongly accelerated and quickly approach ultra-relativistic speeds. As a result, their velocities are only slightly below the speed of light, making the small difference between them difficult to resolve. These accelerations of the domain wall and the monopole can be estimated by

$$a_{\mathrm{DW}} \sim \frac{\delta}{\sigma_{\mathrm{DW}}} \sim \beta \frac{m_{v,\phi}}{g m_{h,\psi}}\,, \tag{5.13}$$

$$a_{\mathrm{M}} \sim \frac{\mu}{m_{\mathrm{M}}} \sim \frac{m_{v,\psi}^2}{m_{v,\phi}}\,, \tag{5.14}$$

with δ being the difference in the potential energy of the two different vacua. $\sigma_{\mathrm{DW}} \sim m_{h,\psi} v_{\psi}^2$ is the domain wall tension.

Several different outcomes are possible. If both $m_{v,\phi}$ and $m_{h,\psi}$ are large, the monopole may enter the Higgsed phase and stretch a string. However, if the acceleration of the wall is smaller than the acceleration of the monopole due to the string tension, the monopole can be pulled back into the Coulomb phase until the domain wall accelerates further and collides with it again. For sufficiently large masses, it may even occur that the monopole never enters the Higgsed phase at all but instead remains localized on the domain wall. Assuming the thin-wall and thin-string approximation, and neglecting any deformation of the wall due to the slingshot formation, the maximal string length can be estimated as

$$l_{\max} \sim \gamma_{\mathrm{c}} \frac{m_{\mathrm{M}}}{\mu}, \tag{5.15}$$

for ultra-relativistic collision velocities, where γ_{c} denotes the relative Lorentz factor.

Another natural question concerns the stability of the string. In principle, the energy stored in it could be sufficient for the string to split into a monopole–anti-monopole pair, leaving behind a shorter slingshot and a monopole–anti-monopole pair connected by a string. However, such processes can only occur through thermal or quantum effects. Although the collision of the monopole with the wall does generate small thermal fluctuations, they are far too weak to trigger a string breaking. Moreover, since our simulations capture only classical dynamics, quantum pair production cannot take place.

But a detachment of the string from the wall can occur when an anti-monopole enters the string at the string-wall junction. We simulated such a scenario by considering a

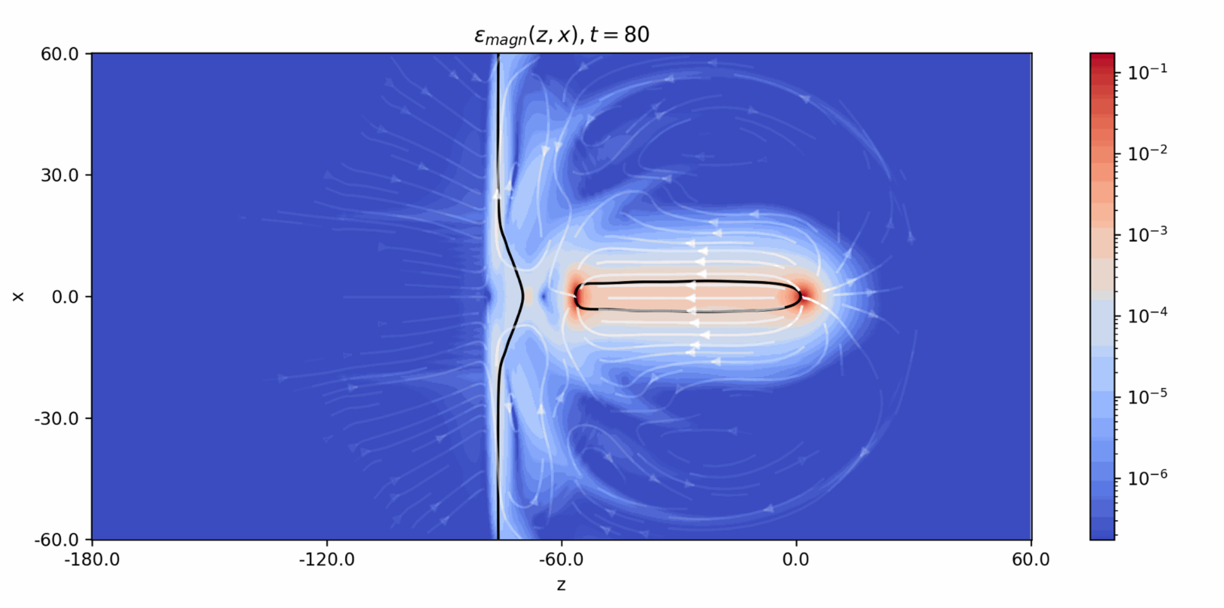

Figure 5.3: This figure shows a confined monopole–anti-monopole pair that forms after an anti-monopole enters the throat of the slingshot. The parameters are the same as those given in the caption of Figure 5.2.

monopole–anti-monopole pair colliding with the domain wall along the z-axis. When the first monopole enters, it stretches a string as explained in detail above. Once the anti-monopole enters the string throat, all the magnetic flux can be absorbed by it. As a result, the string detaches from the wall, leaving behind a monopole–anti-monopole pair connected by a string (see Figure 5.3). Subsequently, the two monopoles accelerate towards each other until they collide and annihilate [165], analogously to the dynamics described in Section 4.5.2. The animated time evolution of this slingshot process can be found in the following video: `https://youtu.be/IPJAPjo3nSc`

5.3.2 Two Slingshots

We saw that a detachment of the string from the wall can be achieved by introducing an additional anti-monopole that enters the throat of the string. Another possibility for the detachment can be obtained through interactions with a nearby (anti-)slingshot. To simulate this scenario, we considered a configuration in which, in addition to the monopole, an extra anti-monopole enters the Higgsed phase at a different location. Both monopoles enter the Higgsed phase simultaneously. The initial separation distance is given by $d = |z_{\bar{\mathrm{M}}} - z_{\mathrm{M}}|$, where z_{M} and $z_{\bar{\mathrm{M}}}$ denote the z-coordinates of the monopole and the anti-monopole, respectively.

We investigated different setups by varying the initial separation d between $20\, m_{v,\phi}^{-1}$ and $90\, m_{v,\phi}^{-1}$. This range was chosen for two reasons. For separations $d \lesssim 20\, m_{v,\phi}^{-1}$, the Coulomb attraction between the monopole–anti-monopole pair is so strong that the monopoles are already too close to each other when they collide with the domain wall, preventing the formation of two distinct slingshots. On the other hand, separations larger than $d \sim 90\, m_{v,\phi}^{-1}$ would require a larger lattice for the simulations, which was beyond our available computational power and memory. The animated results of the simulations are shown in the following video: `https://youtu.be/PnErf4-zUEg`

In addition to varying the initial separation distances, we also analysed different relative twists, α. Specifically, to gain a clearer understanding of the dynamics, we considered the cases $\alpha = 0$, $\alpha = \pi/2$, and $\alpha = \pi$. Finally, we rotated the monopole–anti-monopole pair such that the monopole enters the Higgsed phase before the anti-monopole, but at different locations on the domain wall.

By varying all these parameters, we obtained a clearer picture of how multiple slingshots interact with each other and of how the slingshot manifests itself in a full phase transition, which we will discuss later.

No Twist. If no relative twist, $\alpha = 0$, is present between the monopole and the anti-monopole, we observed that when the slingshots form, the strings bend away from each other (see Figure 5.4 (left)). Furthermore, a flux tube forms that is localized on the wall. Such flux tube formation was previously mentioned for quarks entering a confined region in [199]. This flux tube explains why the strings bend away from each other, because the magnetic field lines of the tube tend to straighten. For larger initial separation distances d, the flux tube on the wall becomes wider, weakening the bending effect. For very large d, the slingshots become completely isolated and behave like single fully separated slingshots, which were discussed in the previous section. In this case, the magnetic field in the Coulomb region resembles that of a widely separated monopole–anti-monopole pair.

Due to the magnetic flux tube on the wall, the attraction between the string-wall junctions is very strong. Within the investigated time interval, we observe for small initial distances d that the junctions approach each other until the slingshots detach from the domain wall, forming a monopole–anti-monopole pair connected by a single string. After the detachment, the string wishes to straighten, resulting in a strong acceleration toward the monopoles. If the string is sufficiently long, it can even oscillate between the monopoles multiple times.

Maximal Twist. If the monopole and anti-monopole are maximally twisted initially, the behaviour of the slingshots is entirely different. In this case, no flux tube forms on the wall and the magnetic field spreads further into the Coulomb region. Due to the absence of a flux tube, the strings do not bend but remain parallel to each other, as illustrated in Figure 5.4 (right). The string-wall junctions still attract each other via the Coulomb interaction, causing the slingshots to move towards each other. However, the strings remain parallel all the time. Once the slingshots approach sufficiently close, the strings annihilate, leaving behind a twisted monopole–anti-monopole pair connected by a very short string. This behaviour is in contrast to the untwisted case, where the strings bend and the monopoles are still far apart when the strings are detaching from the wall. Here in the twisted case, the strings stay parallel, and thus the monopoles are already very

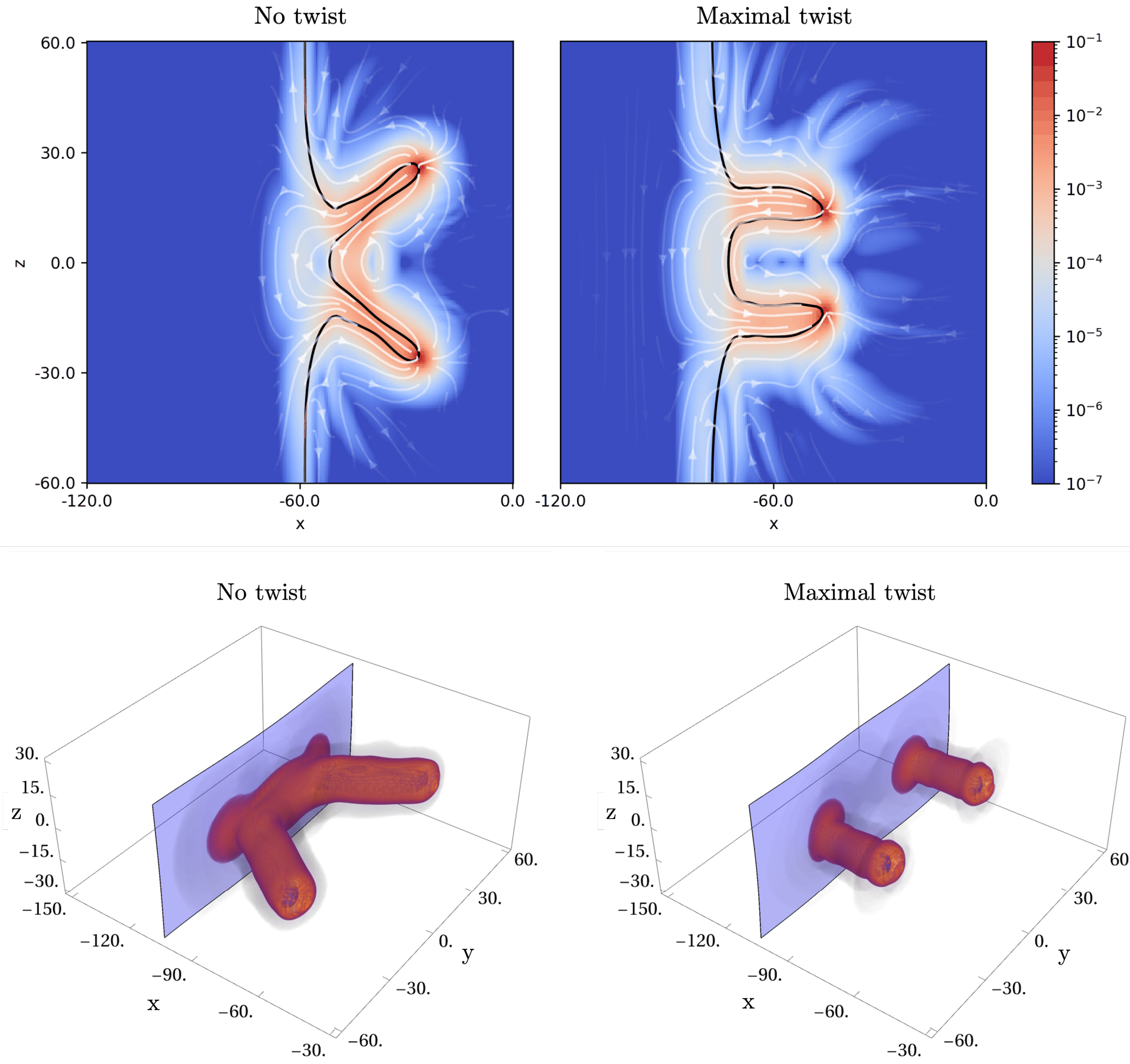

Figure 5.4: This figure shows monopole–anti-monopole pairs entering the Higgsed phase in parallel. The upper two plots illustrate the magnetic energy density in the $y = 0$ plane for two slingshots without relative twist (left) and with maximal twist (right). The black lines indicate the contour $|\psi| = 0.16\, m_{v,\phi}$, marking the location of the domain wall. For the upper plots, the initial separation between the monopoles was $d = 34\, m_{v,\phi}^{-1}$. In the lower plots, the initial separation is $d = 60\, m_{v,\phi}^{-1}$, with the left plot showing the untwisted case and the right plot the twisted case. The density plots illustrate the magnetic energy density for values greater than $5.0 \cdot 10^{-6}\, m_{v,\phi}^4/g^2$ (left) and $2.0 \cdot 10^{-5}\, m_{v,\phi}^4/g^2$ (right). The domain wall is represented by the contour $|\psi| = 0.2\, m_{v,\phi}$. For the simulations the following parameters were chosen: $m_{h,\phi} = m_{v,\phi}$, $m_{v,\psi} = 0.2\, m_{v,\phi}$, $m_{h,\psi} = 0.6\, m_{v,\phi}$, $\beta = 0.01\, m_{v,\phi}$.

close together when the detachment occurs.

Once the twisted monopole–anti-monopole pair connected by the string has formed, the monopoles collide. Before the annihilation we observe a single bounce. This feature is characteristic for maximally twisted monopoles and has already been reported in [165, 101]. In a perfectly symmetric setup, the monopoles would not annihilate at all and bounce multiple times until they form an unstable static sphaleron configuration [103]. Such a configuration was already discussed in Subsection 4.5.2.

In addition to the cases with zero twist, $\alpha = 0$, and maximal twist, $\alpha = \pi$, we also investigated intermediate twisting angles. In these scenarios, we observed a superposition of the two effects. A part of the magnetic field becomes confined in a flux tube on the wall, while another part spreads into the Coulomb region. As a result, the bending angle of the slingshots changes smoothly between the two extremes, showing maximal bending for $\alpha = 0$ and no bending for $\alpha = \pi$.

All simulations that we performed were for cases with rather small distances, d, between the slingshots. As mentioned earlier, for large separations, $d \gg 1/\Lambda$, we expect a Coulomb-like attraction, where Λ is the confinement scale which is of order $m_{v,\psi}$. Let us estimate the time it takes until two slingshots collide and annihilate. Here, we can distinguish two cases. If the distance between the slingshots is much smaller than the string length, L, the accelerated mass is given by a small piece of the string close to the string–wall junction, $m \sim \mu/\Lambda \sim \Lambda$. For $d \gg L$, the full string is accelerated, and thus the relevant mass is the full slingshot mass, $m \sim \mu L \sim \Lambda^2 L$. Assuming that only the magnetic field in the Coulomb phase contributes to the attraction, the time evolution of the separation distance between the slingshots is described by

$$m\ddot{x} \sim \frac{1}{x^2} \,. \tag{5.16}$$

The solutions of this equation provide an estimate for the lifetime of the two slingshots,

$$\tau \sim \begin{cases} \Lambda^{\frac{1}{2}}\, d^{\frac{3}{2}} & \text{for } d \ll L \,, \\ \Lambda\, L^{\frac{1}{2}}\, d^{\frac{3}{2}} & \text{for } d \gg L \,. \end{cases} \tag{5.17}$$

Note that we assumed that only the magnetic field in the Coulomb phase contributes to the attraction. The dynamics would change completely if, for example, a surrounding plasma is present or if the field lines are partially concentrated along the domain wall. However, since such effects depend strongly on the details of the model, like for example the abundance of slingshots, our above assumption is sufficient to obtain order-of-magnitude estimates.

5.3.3 Many Slingshots

The final scenario that we simulated was an expanding vacuum bubble colliding with magnetic monopoles. When they collide, the monopoles form many slingshots at different locations on the bubble's surface. The results are shown in Figure 5.5. The animated results can be found in the following video: `https://youtu.be/PnErf4-zUEg`

Again we observe phenomena similar to those discussed earlier. For instance, if two slingshots are sufficiently close, their strings bend strongly. When the string-wall junctions approach each other close enough, the slingshots detach from the wall and form a monopole–anti-monopole pair connected by a string. In addition to these already known effects, we also made further noteworthy observations.

It is a well-known fact that when two strings intersect, they can reconnect in different ways. This has interesting consequences for intersecting slingshots. In such a case, the strings can reconnect in a way that produces a monopole–anti-monopole pair, while leaving behind a string with both of its ends attached to the wall.

Another observation that we made was the formation of very long strings when two vacuum bubbles collide. To simulate this, we placed the vacuum bubble close to the boundary. Due to the periodic boundary conditions, the growing bubble reappears on the opposite side of the lattice. This setup allowed us to study domain wall collisions without explicitly implementing a second vacuum bubble. At the moment of the collision, we observed that very long strings can form, extending almost across the entire analysed volume. The reason for this effect can be understood as follows. Shortly before the walls collide, only few free monopoles and slingshots remain, since most of them have already formed confined monopole–anti-monopole pairs within the Higgsed phase of the vacuum bubble. When the walls collide, the few remaining monopoles and slingshots must still find partners. Because of the reduced density, these partners can be far apart, which naturally leads to the creation of very long strings. Later, through intersections with other confined monopole–anti-monopole pairs, these long strings can split into shorter segments.

Last but not least, we observed that collisions of monopoles with the wall, as well as the subsequent formation of slingshots, create strong deformations of the bubble wall. In addition, these monopoles act as a source of friction, effectively slowing down the bubble's expansion. Both the deformations and the friction effects are non-trivial for the resulting gravitational wave emission during bubble collisions [200]. Hence, the slingshot effect represents a relevant physical mechanism that must be taken into account in such analyses.

5.4 Gravitational Radiation

All the effects that we observed have important implications for gravitational wave physics. Among them are pure string loops that collapse, deformed domain wall bubbles that expand with constant acceleration and eventually collide, as well as confined monopole–anti-monopole pairs in which the monopoles are pulled together under strong acceleration. Each of these mechanisms is already a well-known source of gravitational waves. In this work, however, we found a new phenomenon, the slingshot effect, which provides an additional source of gravitational radiation in the early Universe, for instance during first-order phase transitions in GUTs.

In this section, we first analyse the gravitational radiation emitted by a single slingshot. Afterwards, we extrapolate these results to a full system of many slingshots. Our focus will be on deriving order-of-magnitude estimates for the characteristic gravitational wave

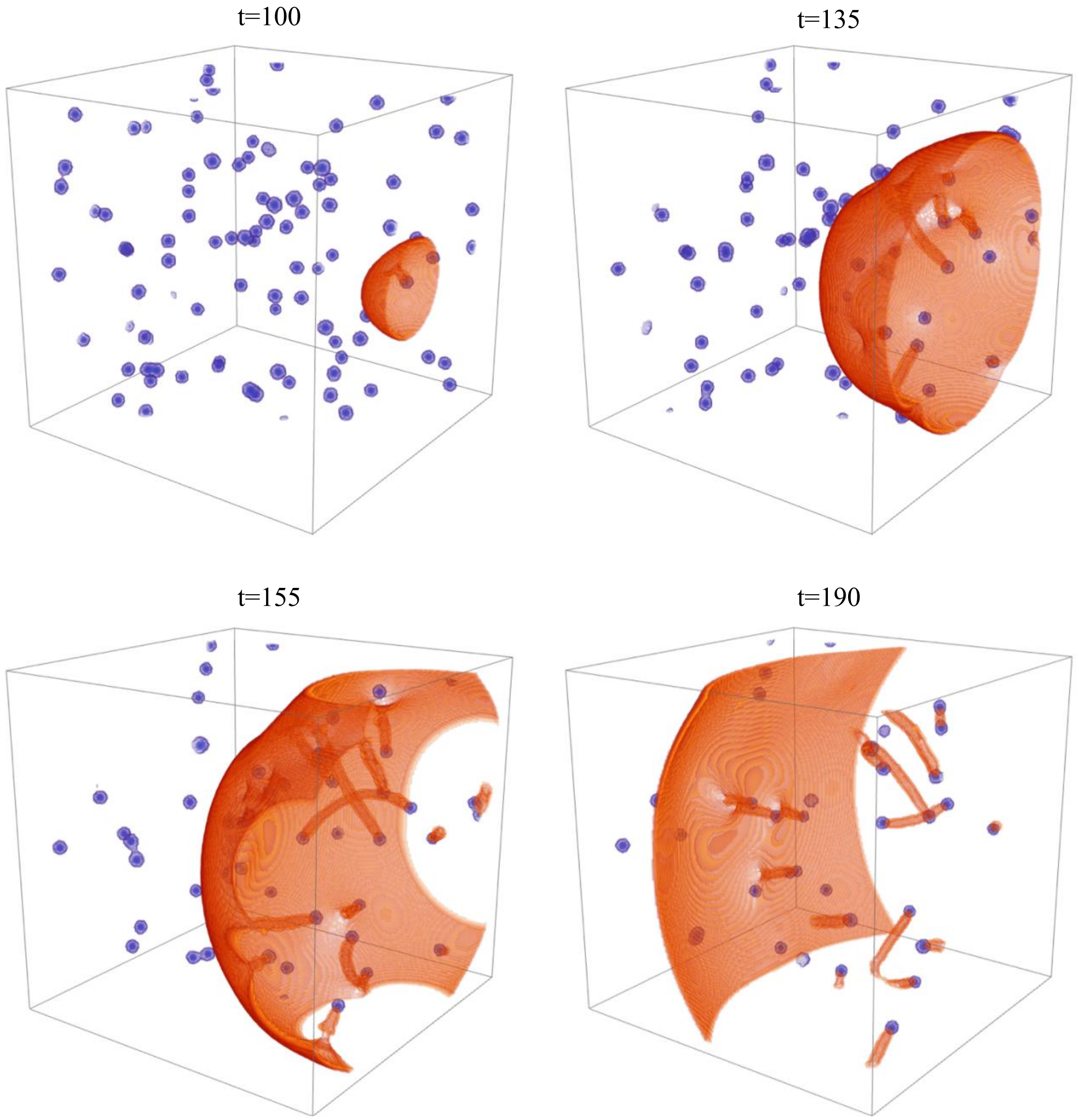

Figure 5.5: This figure shows the time evolution of an expanding vacuum bubble colliding with several magnetic monopoles, leading to the formation of multiple slingshots. The blue and red density plots illustrate the absolute values of the scalar fields, $|\phi|$ and $|\psi|$, respectively. Only a part of the full lattice is shown, corresponding to a box of size $(170\, m_{v,\phi}^{-1})^3$. The parameters chosen in the simulation are: $m_{h,\phi} = m_{v,\phi}$, $m_{v,\psi} = 0.15\, m_{v,\phi}$, $m_{h,\psi} = 0.6\, m_{v,\phi}$, $\beta = 0.2\, m_{v,\phi}$.

frequencies and the corresponding density parameters that would be expected today as remnants of the slingshot dynamics.

5.4.1 Spectrum for One Isolated Slingshot Event

For our study of the gravitational wave spectrum, we will neglect the back-reaction of the gravitational field on the slingshot dynamics. Since we assume that the mass scales of our theory are well below the Planck mass, the gravitational back-reaction is expected to produce only small corrections. These corrections could appear from the following effects. First, when the slingshot accelerates along with the domain wall, energy is radiated away in the form of gravitational waves, which slightly slows down the acceleration of the slingshot and modifies its dynamics. Second, the monopole in the Coulomb phase experiences a gravitational repulsion from the domain wall. As shown in [201, 202], planar infinite domain walls anti-gravitate. The gravitational force originating from the domain wall with tension σ_{DW} on a test mass m is $F \sim G\,\sigma_{\text{DW}}\,m$. For mass scales approaching the Planck mass, this force can compete with the string tension pushing the monopole away from the wall and may even prevent the monopole from entering the Higgsed phase. However, for scales well below the Planck mass, these effects are negligible.

Note also that, in addition to neglecting the gravitational back-reaction, we ignore the effects of a background plasma. Such a plasma could slow down the slingshot dynamics and thus reduce the emission of gravitational radiation.

With these assumptions, we can calculate the gravitational radiation spectrum from the energy-momentum tensor of the system. For this purpose, we use Weinberg's formula [176], which gives the radiated gravitational energy per unit frequency and solid angle[3]

$$\frac{\mathrm{d}E}{\mathrm{d}\Omega\,\mathrm{d}\omega} = \frac{G\,\omega^2}{2\pi^2}\Lambda_{ij,lm}(\hat{\boldsymbol{k}})T^{ij*}(\boldsymbol{k},\omega)T^{lm}(\boldsymbol{k},\omega)\,, \tag{5.18}$$

where ω is the frequency of the radiation, $\hat{\boldsymbol{k}}$ ($|\boldsymbol{k}| = \omega$) is the direction of radiation emission, and $\mathrm{d}\Omega$ is the differential solid angle. Notice that we have already used a rewritten version of this formula in Section 4.5.3. The Fourier transform of the energy-momentum tensor, $T_{\mu\nu}$, can be calculated with

$$T_{\mu\nu}(\boldsymbol{k},\omega) = \int_{I_t}\mathrm{d}t\int_{I_V}\mathrm{d}^3x\; e^{i\omega t - i\boldsymbol{k}\cdot\boldsymbol{x}}\; T_{\mu\nu}(\boldsymbol{x},t)\,, \tag{5.19}$$

where the investigated time interval and volume region are I_t and I_V, respectively. Within the analysed time interval of the full simulation, the duration during which the slingshot is present is $T \simeq 80\,m_{v,\phi}^{-1}$. As a volume, we chose a cubic box of size $V \simeq T^3$, which captures the relevant dynamics. In equation (5.18), $\Lambda_{ij,lm}$ is the projection operator that extracts the transverse-traceless part of the energy-momentum tensor. The operator is given by

$$\Lambda_{ij,lm}(\hat{\boldsymbol{k}}) \equiv P_{il}(\hat{\boldsymbol{k}})P_{jm}(\hat{\boldsymbol{k}}) - \frac{1}{2}P_{ij}(\hat{\boldsymbol{k}})P_{lm}(\hat{\boldsymbol{k}})\,, \tag{5.20}$$

where $P_{ij}(\hat{\boldsymbol{k}}) = \delta_{ij} - \hat{k}_i\hat{k}_j$ projects out the orthogonal direction of $\hat{\boldsymbol{k}}$.

---

[3] We follow the conventions from [203].

Notice that equation (5.18) is only valid if the energy-momentum tensor is divergence-free, $k_\mu T^{\mu\nu} = 0$, which is an assumption in the derivation of Weinberg's formula. As a check of the numerical data, we verified this condition and found it to be well satisfied.

The initial configuration used in the simulations does not solve the field equations exactly and therefore serves only as an approximate ansatz. This leads to fluctuations in the fields, which appear as noise in the gravitational wave spectrum. Additionally, the simulations are performed on a discretized lattice with finite spacing. Even with carefully chosen resolution and numerical methods, some numerical fluctuations are unavoidable.

To isolate the gravitational signal of the slingshot from the background, we calculated the gravitational spectrum for a monopole that is Lorentz-boosted with the same velocity in the direction away from the domain wall. Within the time interval under consideration, this monopole does not collide with the domain wall. Consequently, this spectrum contains only background contributions that are not of interest. We then used this background data to subtract it from the spectrum obtained in the simulation where the monopole collides with the wall and forms the slingshot.

In the analysis of the gravitational radiation, we kept the following parameters fixed: $m_{h,\phi} = m_{v,\phi}$, $m_{h,\psi} = 0.6\, m_{v,\phi}$, and $\beta = 0.01\, m_{v,\phi}$. We varied the photon mass for values $m_{v,\psi} \leq 0.7\, m_{v,\phi}$. For larger values of $m_{v,\psi}$, the Lorenz gauge was violated too strongly during the numerical simulation. In the following, we present an example with $m_{v,\psi} = 0.6\, m_{v,\phi}$, where the background noise contributes with less than 5% of the gravitational energy spectrum and is therefore negligibly small.

Integration over the solid angle yields the energy spectrum shown in Figure 5.6 (note that we set the gravitational constant to one, $G = 1$). We find that the scaling of the energy spectrum can be approximated by

$$\frac{\mathrm{d}E}{\mathrm{d}\omega} \propto \omega^{-1}\,. \tag{5.21}$$

This frequency dependence is very similar to that predicted for a confined magnetic monopole pair in the point-like approximation by Martin and Vilenkin [19] (for more details we refer to Section 4.5.3). This similarity is expected, since the acceleration of the monopole due to the string tension is the same as in the confined monopole pair. In [19], it was also noted that in the very high-frequency regime, the energy spectrum begins to decay exponentially. Unfortunately, the resolution of our lattice does not allow us to resolve this regime.

Weinberg's formula allowed us to calculate the direction of radiation emission. The result is illustrated in Figure 5.7. First, we observe that most of the radiation is emitted along the direction of acceleration. Second, a dependence between the emission angle θ and the frequency ω can be seen. This dependence is approximately given by

$$\theta \propto \omega^{-1/2}\,. \tag{5.22}$$

The same behaviour has also been calculated in the point-like approximation for a confined monopole–anti-monopole pair in [177]. However, there is a small difference. For the slingshot, the radiation is emitted mainly in the interval $\theta \in [0, \pi/2]$. In contrast, for two

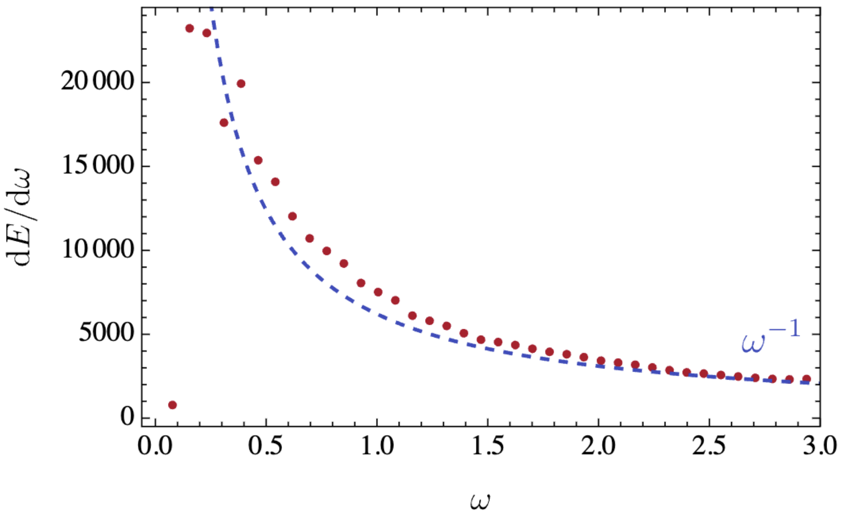

Figure 5.6: The red dots in this figure show the gravitational energy spectrum obtained from our numerical data. The blue dashed line illustrates an ω^{-1} behaviour for comparison with the numerical results. The frequency is given in units of $m_{v,\phi}$.

magnetic monopoles connected by a string, the same amount of radiation with the same scaling is additionally emitted in the interval $\theta \in [\pi/2, \pi]$, due to the second monopole.

Multiplying $\mathrm{d}E/\mathrm{d}\omega$ by $2\pi/T^2$ gives the instantaneous power P_{GW}. In Section 4.5.3, a scaling of $P_{\mathrm{GW}} \sim \mu^2/M_{\mathrm{P}}^2$ with $\mu \sim \Lambda^2$ was calculated, where $\Lambda \sim m_{v,\psi}$ is the scale of monopole confinement. From our numerical results, we observe that this scaling is in approximate agreement with the predicted behaviour.

Notice that in the simulations used to calculate the gravitational wave spectrum, we did not vary the parameters extensively. This was mainly due to numerical limitations. For instance, for sufficiently low $m_{v,\psi}$, we observed that the radiation from the collision of the monopole with the domain wall becomes comparable to the radiation emitted by the slingshot itself. A complete understanding of the gravitational radiation across different parameter regimes would require a detailed and precise study, which is beyond the scope of this work and left for future research. Nevertheless, we expect only small corrections to the results we obtained for the gravitational radiation emitted by the slingshot itself.

In summary, we have shown that the gravitational energy spectrum of the slingshot decays as ω^{-1}, and the emission angle depends on the frequency as $\theta \propto \omega^{-1/2}$. Therefore, the slingshot effect produces a characteristic gravitational radiation signal. To gain better intuition about the regimes in which these gravitational waves might be detectable, we use the results above to estimate the gravitational radiation density parameter.

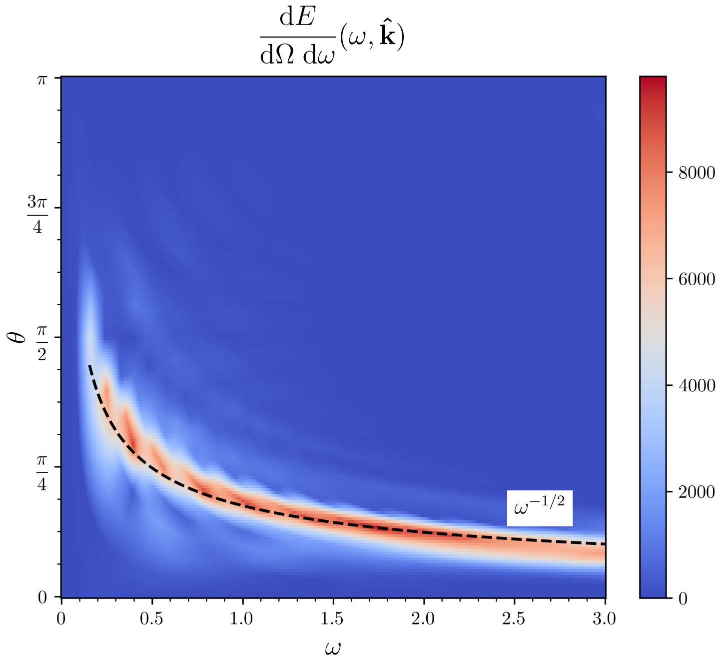

Figure 5.7: This density plot shows the radiated energy per unit frequency and solid angle as a function of the frequency ω and the radiation emission angle θ. The angle is the polar angle measured from the axis of motion with $\theta = 0$ corresponding to the direction of acceleration. The black dashed line indicates an $\omega^{-1/2}$ behaviour for comparison.

5.4.2 Estimation for the Gravitational Radiation Density Parameter

The gravitational radiation density parameter is given by $\Omega_{\mathrm{GW}} \equiv (1/\rho_{\mathrm{c}})\,\mathrm{d}\rho_{\mathrm{GW}}/\,\mathrm{d}(\ln f)$, where f is the frequency of the gravitational wave signal. In the slingshot example, this parameter measures the fraction between the energy density carried by gravitational waves from the slingshot, ρ_{GW}, and the critical energy density of the Universe, ρ_{c}. For a phase transition in which slingshots form, we expect the following density parameter, which accounts for the gravitational radiation emitted by the slingshots only:

$$\Omega_{\mathrm{GW}}^{\mathrm{peak}} \simeq P_{\mathrm{GW}}\, t_{\mathrm{sl}}\, n_{\mathrm{M}} \left(\frac{a(T_{\mathrm{sl}})}{a(T_0)}\right)^4 \frac{1}{\rho_{\mathrm{c}}}\,, \tag{5.23}$$

Here, $P_{\mathrm{GW}} \sim \Lambda^4/M_{\mathrm{p}}^2$ is the power emitted by a single slingshot, t is the duration of the slingshot, and n_{M} is the monopole density, which we assume to be approximately equal to the slingshot density since nearly every monopole stretches a string. The scale factors, a, account for the redshift due to the expansion of the Universe. Throughout these estimations, we assume that the Universe is radiation-dominated until all monopoles annihilate at $T \sim T_{\mathrm{sl}}$. Additionally, we will consider only scenarios in which all slingshots cease to exist once the entire Universe is filled with the Higgsed vacuum. We do not account for cases in which their intersections or annihilations could shorten their lifetime. Therefore, the duration of the slingshot can be estimated approximately by the horizon time, $t_{\rm sl} \sim M_{\rm P}/T_{\rm sl}^2$. This is justified, since the vacuum bubbles expand at relativistic speeds. Notice that we will focus only on the peak of the gravitational radiation density parameter. A detailed analysis of the full signal shape is left for future work. Furthermore, in our estimates we will neglect order-one factors.

Under these assumptions, the gravitational wave density parameter can be approximated as

$$\Omega_{\rm GW}^{\rm peak} \simeq \frac{\Lambda^4 n_{\rm M}}{T_{\rm sl}^6 M_{\rm P}}\,\Omega_{\rm rad}\,, \tag{5.24}$$

where we replaced the critical density of the Universe, $\rho_{\rm c}$, with the radiation density parameter, $\Omega_{\rm rad} = \rho_{\rm rad}/\rho_{\rm c} \sim T_0^4/\rho_{\rm c}$. The radiation frequency of the signal that would be observed today is

$$f \simeq \frac{1}{t_{\rm sl}}\frac{a(T_{\rm sl})}{a(T_0)} \simeq \frac{T_{\rm sl}T_0}{M_{\rm P}}\,. \tag{5.25}$$

In general, it is possible that the monopole confinement scale, Λ, does not coincide with the scale at which the slingshot occurs, $T_{\rm sl}$. The magnitude of any separation between these scales is highly model-dependent. At the end of this section, we will provide some qualitative discussion. For the purpose of keeping our estimations general, however, we treat these two scales as independent parameters.

These two parameters, Λ and $T_{\rm sl}$, together with the monopole density, $n_{\rm M}$, cannot be chosen arbitrarily in equation (5.24), because they must be consistent with observational constraints from our Universe. For instance, a phase with domain wall dominance could leave a too strong imprint on the cosmic microwave background. Avoiding such domain wall domination requires that the walls collapse at temperatures

$$T_{\rm sl} \gtrsim \left(\frac{\Lambda}{M_{\rm P}}\right)^{\frac{3}{2}} M_{\rm P}\,. \tag{5.26}$$

For the same reason, we also want to avoid a monopole domination phase. This requires

$$n_{\rm M} \lesssim \frac{T_{\rm sl}^4}{m_{\rm M}}\,, \tag{5.27}$$

where $m_{\rm M}$ is the monopole mass.

However, a stronger bound on the monopole density arises for a different reason. Above, we assumed that throughout the bubble expansion, the slingshots do not detach from the wall. As discussed in Section 5.3.2, two slingshots attract each other and eventually annihilate. To account for this effect, equation (5.24) is valid only if the slingshot lifetime due to their attraction is larger than the Hubble time used for the slingshot duration, $\tau \gtrsim t_{\rm sl}$. Since we are interested in the maximally possible values of $\Omega_{\rm GW}$, we consider the slingshot density to be as high as possible, which implies that the mean separation distance, $\langle d \rangle$, between the string-wall junctions is small compared to the slingshot length, L. From equation (5.17) with $\langle d \rangle \sim 1/\sqrt{n_\mathrm{M} t}$, it then follows that

$$n_\mathrm{M} \lesssim \frac{T_\mathrm{sl}^{\frac{14}{3}} \Lambda^{\frac{2}{3}}}{M_\mathrm{P}^{\frac{7}{3}}} \,. \tag{5.28}$$

Let us discuss some minimal examples for scenarios in which the slingshot effect can take place. The simplest case is a standard first-order phase transition with vacuum bubbles that expand, collide with monopoles, and form slingshots at the temperature scale $T \sim T_\mathrm{sl} \sim \Lambda$. In this setup, the resulting density parameter is given by

$$\Omega_\mathrm{GW}^\mathrm{peak} \lesssim \left(\frac{f}{T_0} \right)^{\frac{10}{3}} \Omega_\mathrm{rad} \,. \tag{5.29}$$

Another possibility is that the phase transition is delayed. This can, for example, occur through supercooling [204] or through domain walls that remain in a scaling regime with energy density $\rho_\mathrm{DW} \simeq \Lambda^3/t$ (for a review see [205]). In this case, the slingshot effect may take place at scales different from the confinement scale, i.e. $T_\mathrm{sl} < \Lambda$. Taking the caveats discussed above into account, this leads to a gravitational wave density parameter of

$$\Omega_\mathrm{GW}^\mathrm{peak} \lesssim \left(\frac{f}{T_0} \right)^{\frac{16}{9}} \Omega_\mathrm{rad} \,. \tag{5.30}$$

From equations (5.29) and (5.30) we can find that gravitational wave signals from the slingshot will not be in the sensitivity range of the next generation of gravitational wave experiments if we assume all the above mentioned constraints. In Figure 5.8 the bound (5.30) is illustrated as the red dashed line. More non-minimal scenarios that could lead to an even stronger signal within the reach of future experiments can be constructed, but we leave their exploration to future work. Taken together, the slingshot mechanism gives rise to gravitational radiation in the high-frequency regime. In this range, significant research is in progress to design new detection strategies [206, 207, 208].

Notice that all the above estimations are only first approximations. A more detailed and precise analysis is left for future work. Effects that should be taken into account include, for example, interactions with the surrounding plasma. This could slow down the slingshot attraction and thus weaken condition (5.28). If we only consider the constraint of avoiding monopole domination (5.27), we obtain a bound

$$\Omega_\mathrm{GW}^\mathrm{peak} \lesssim \left(\frac{f}{T_0} \right)^{\frac{2}{3}} \left(\frac{M_\mathrm{P}}{m_\mathrm{M}} \right) \Omega_\mathrm{rad} \,. \tag{5.31}$$

For $M \simeq 10^{16}\,\mathrm{GeV}$, a signal at $f \simeq 10^2\,\mathrm{Hz}$ can give a gravitational radiation density parameter of $\Omega_\mathrm{GW}^\mathrm{peak} \lesssim 10^{-8}$, which is within the reach of current gravitational wave experiments like aLIGO [209], Virgo [210], and KAGRA [211], but also future experiments

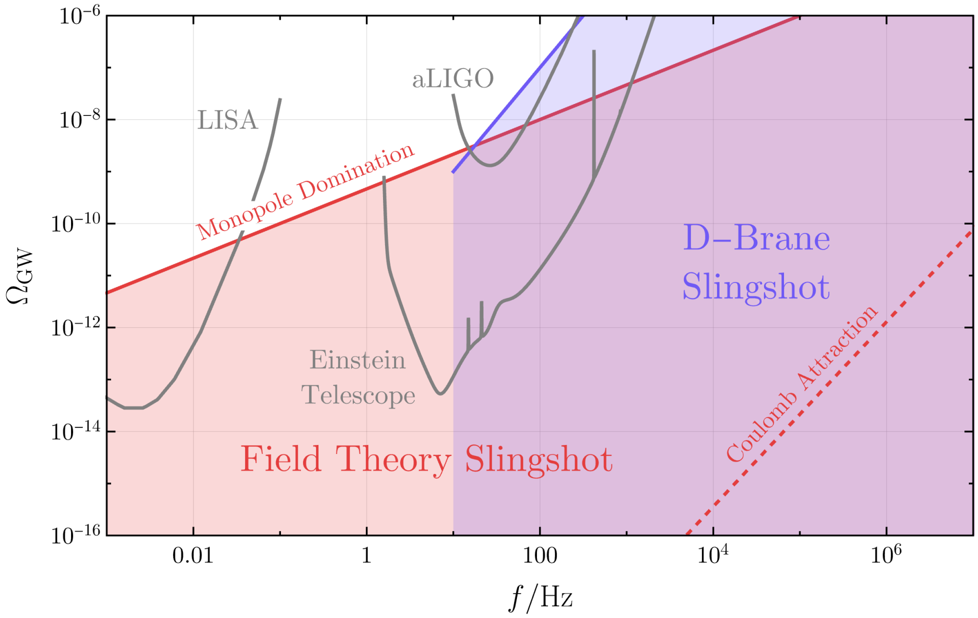

Figure 5.8: This figure indicates in which regime we may expect the peak of the gravitational radiation signals originating from the slingshot effect. The red region represents the magnetic monopole slingshot presented in this section. The solid red line shows the bound given in equation (5.31) for $M \sim 10^{16}\,\mathrm{GeV}$. The red dashed line shows the bound given in equation (5.30). The blue region illustrates the parameter regime in which the wrapped D-brane slingshot (which will be explained in Section 5.6) can emit signals. The blue line represents equation (5.47), which is bounded by equation (5.48). The sensitivity curves for LISA [212], aLIGO [209], and the Einstein Telescope [214] were taken from the open-access code provided in [216]. A Hubble constant of 68 km/s/Mpc was assumed to calculate the corresponding $\Omega_{\rm GW}$ values.

like LISA [212], Cosmic Explorer [213], and Einstein Telescope [214]. We illustrate the bound (5.31) as a solid red line in Figure 5.8. The full red region represents the regime in which the monopole slingshot can emit gravitational radiation, assuming the bound (5.31). Another possible increase of the upper bound for $\Omega_{\rm GW}^{\rm peak}$ could arise by allowing a short period of domain wall domination. With a careful choice of parameters, this may still be consistent with constraints from the cosmic microwave background [215]. This would weaken the condition (5.26).

Furthermore, besides the slingshot itself, there are additional sources of gravitational waves that arise after the slingshot effect has taken place. For instance, when the strings detach from the wall, they undergo a rapid acceleration towards the monopoles as the strings attempt to straighten. In addition, the confined monopoles themselves also emit gravitational waves. However, these further sources are beyond the scope of this thesis.

5.5 Slingshot in QCD

In 1974, Mandelstam [186] suggested that confined magnetic monopoles may give a model for quark confinement. And indeed, it turns out that the dynamics of a pair of confined magnetic monopoles behaves similarly to a pair of confined quarks due to their linear interaction potentials. Therefore, the slingshot effect may also exist in QCD-like gauge theories that allow for the coexistence of a confined and unconfined phase. An explicit realisation was first discussed in [160]. There, a scenario was considered in which the $SU(2)$ gauge theory is confined away from a domain wall, while on the wall it becomes unconfined. In a similar setup, the domain wall can be replaced by an unconfined vacuum layer of arbitrary thickness [158]. The Lagrangian density for such a model can be written as

$$\mathcal{L} = -\frac{1}{2}\,\mathrm{Tr}\left(G^{\mu\nu}G_{\mu\nu}\right) + \mathrm{Tr}\left(\left(D_\mu\phi\right)^\dagger\left(D^\mu\phi\right)\right) - V(\phi) + i\bar{Q}\gamma^\mu D_\mu Q - M_Q\bar{Q}Q\,, \tag{5.32}$$

with ϕ being the Higgs field transforming in the adjoint representation of the $SU(2)$ gauge group. The potential is given by

$$V(\phi) = \lambda\,\mathrm{Tr}\left(\phi^2\right)\left(\mathrm{Tr}\left(\phi^2\right) - \frac{v_\phi^2}{2}\right)^2 . \tag{5.33}$$

For simplicity, we consider only a single flavour of the quark Q with mass M_Q. The quark Q transforms in the fundamental representation of $SU(2)$, and we take it to be heavy, i.e. its mass lies above the confinement scale Λ of the theory.

Due to the sextic form of the potential, we have, similarly to the magnetic monopole slingshot model, two vacua with different properties. In the vacuum with $\phi = 0$, the $SU(2)$ gauge field is massless and the theory becomes confining below the confinement scale Λ. Hence, colour-electric flux can exist only in the form of flux tubes with tension $\mu \sim \Lambda^2$. These are the so-called QCD strings [217, 218]. In this confined phase, the model (5.32) does not support free quarks, which means that quarks are always confined, i.e. a string is attached to each of them. Such a string can either end on another (anti-)quark, forming a meson, or attach to the wall that separates the confined phase from a different, unconfined phase.

The unconfined phase corresponds to the second vacuum, for which $\phi = v_\phi$. In this case, the $SU(2)$ symmetry is broken to $U(1)$, and thus two of the gauge bosons acquire a mass $m_{v,\phi} = gv_\phi$, while the one associated with the residual $U(1)$ symmetry remains massless. Therefore, the effective low-energy theory is a $U(1)$ gauge theory and no confinement effects appear in this phase.

This theory has a classical solution for the domain wall, which has a shape similar to the domain wall given in equation (5.3). Notice that quantum effects can slightly deform the wall. However, these effects are negligible and do not change the overall behaviour of the wall. Furthermore, quantum corrections can induce a shift in the potential such that the two vacua become non-degenerate. This generates a pressure difference between the two phases and causes the wall to accelerate. If required, this can be compensated by an appropriate adjustment of the potential (5.33).

The slingshot effect in this model works as follows. When a quark enters the confining region, its entire colour-electric flux is squeezed into a QCD flux tube. As a result, the quark becomes connected to the wall by a QCD string. The resulting dynamics are directly analogous to those observed in our numerical simulations of the slingshot effect for magnetic monopoles. Therefore, in this QCD model, the role of the magnetic monopole is played by the quark, while the role of the cosmic string is taken over by the QCD string.

However, it should be noted that in the standard picture of QCD confinement the confinement scale, Λ, is much larger than the masses of the light Standard Model quarks. As a consequence, long strings cannot persist, since quark–anti-quark pair production quickly leads to hadronization [199]. Nevertheless, the situation changes for heavy quarks, where string breaking into smaller segments is exponentially suppressed. Moreover, since the QCD gauge coupling may have taken different values in the early Universe [219], the effective masses of the fields could also have been different such that the string breaking is unlikely. In such a case, the slingshot effect could have played a crucial role during the QCD confining phase transition.

5.6 Slingshot for D-Branes

Objects with the form of a slingshot can emerge naturally in D-brane physics, for example in D-brane inflationary scenarios [187, 188, 189], which can be realized in string theory. In this section we will focus on string theory in 10 dimensions. Six of the nine spatial dimensions are compactified, such that the only non-compact dimensions correspond to the $3 + 1$ space-time dimensions of "our world". A D-brane can have different dimensionalities. For instance, a D_0-brane is a point-like object, a D_1-brane has the form of a one-dimensional string, and a D_2-brane is a two-dimensional plane. The 10-dimensional tension of a D_p-brane is given by $\mathcal{T}_p \sim g_{\rm s}^{-1} M_{\rm s}^{p+1}$, where $M_{\rm s}$ denotes the string scale and $g_{\rm s}$ is the dimensionless string coupling, which we set to one in the following.

The slingshot in this theory can be realized in several different ways. The simplest configuration that reproduces the same dynamics as the magnetic monopole slingshot consists of a string-like D_1-brane connecting a point-like D_0-brane to a D_n-brane with $n \geq 2$. The slingshot can be oriented in different ways. It can be aligned parallel to our three non-compact spatial dimensions $x_{\parallel}$, or perpendicular to them, in which case it is stretched along the compact spatial dimensions $x_{\perp}$. More generally, it may be oriented at an arbitrary angle, with components along both directions.

D-branes aligned parallel to $x_{\parallel}$ have already been analysed in [220, 221]. Such objects can arise from brane collisions [222] at the end of brane inflation [187, 188, 189]. In this context, configurations analogous to monopole dumbbells, but of string-theoretic origin, can form. Their dynamics is expected to coincide with that of magnetic monopole dumbbells. The same correspondence applies to the slingshot dynamics.

The production of strings stretched along the $x_{\perp}$ coordinates has already been discussed in [188]. However, the slingshot effect was not considered there. The dynamics of the slingshot effect in the compact perpendicular coordinates is mainly controlled by the dynamics of the D-branes, which are parallel to the coordinates $x_{\parallel}$ but move along the $x_{\perp}$ coordinates.

The dynamics is similar for both the parallel slingshot and the perpendicular slingshot. However, their phenomenological consequences are different. Analogously to the magnetic monopole slingshot, the parallel D-brane slingshot emits gravitational radiation on our brane. The gravitational radiation from the perpendicular D-brane slingshot, however, is suppressed since the dynamics takes place entirely in the compact coordinates $x_{\perp}$. In general, we will assume that the slingshot can be oriented along both directions. The emitted gravitons can be both massless or massive. The massive gravitons are the so-called Kaluza–Klein (KK) gravitons, which are candidates for dark matter [190].

For the gravitational radiation from the magnetic monopole slingshot, the main restriction on the gravitational radiation density parameter was coming from avoiding domain wall dominance. However, the full D-brane tension, which corresponds to the brane we are living on, contributes to the vacuum energy that causes inflation and subsequently relaxes to today's vacuum. Therefore, the issue of wall dominance no longer arises. As we will see, this allows us to enter the regime in which the gravitational radiation may be detected by the next generation of gravitational wave experiments.

Before discussing gravitational radiation, some general properties of the D-brane slingshot should be mentioned. For simplicity, we focus on the slingshot effect stretched along one large extra dimension [223, 224, 190] of size $R_{\perp}$. In agreement with today's bounds on Newtonian gravity [225, 226], its largest allowed size is $R_{\perp} \sim 30\,\mu\mathrm{m}$. All other extra dimensions we assume to be compactified on scales smaller than $R_{\perp}$.

The tension of a stretched string is given by $\mu \sim M_{\mathrm{s}}^2$, where the string scale, M_{s}, is determined from the relation $M_{\mathrm{P}}^2 \sim M_{\mathrm{s}}^3 R_{\perp}$ [190]. This results in a slingshot mass of

$$M_{\mathrm{sl}} \sim \left(\frac{M_{\mathrm{P}}^2}{R_{\perp}}\right)^{\frac{2}{3}} L\,, \tag{5.34}$$

with L denoting the length of the slingshot, which we take to be of order $L \sim R_{\perp}$. The bound on the D_1-brane slingshot mass is given by

$$M_{\mathrm{sl}} \sim \left(\frac{M_{\mathrm{P}}^2}{R_{\perp}}\right)^{\frac{2}{3}} R_{\perp} \lesssim 10^{29}\,\mathrm{GeV}\,, \tag{5.35}$$

where we have inserted the experimental bound $R_{\perp} \lesssim 10^{-2}$ cm.

So far, we have discussed a string-like D_1-brane ending on a point-like D_0-brane. However, the D_1-brane can also be replaced by a higher-dimensional brane. In string theory with 10 dimensions, a brane can be wrapped around all 6 compact dimensions. We can consider a wrapped D_{1+5}-brane, which is wrapped around five small compact dimensions but acts effectively as a string-like object along the largest extra dimension. The wrapping effectively increases the string tension, which is given by

$$\mu \sim M_{\rm s}^{2+5} \prod_{j=1}^{5} 2\pi R_j \,, \tag{5.36}$$

Using the five small extra dimensions and the relation $M_{\rm P}^2 = g_{\rm s}^{-2}\, M_{\rm s}^8 V_6$, where V_6 is the total compactified volume, gives the effective string tension

$$\mu \simeq \frac{M_{\rm P}^2}{R_\perp M_{\rm s}} \,, \tag{5.37}$$

where $R_\perp$ is the size of the largest extra dimension. The current bound on the quantum gravity scale is $M_{\rm s} \sim$ TeV [190], which leads to the bound $M_{\rm sl} \lesssim 10^{35}$ GeV for the slingshot mass.

In the following, we first restrict our analysis to one large extra dimension of size $R_\perp$ and consider the D_1-slingshot. We discuss the emission of gravitational radiation in the form of massless gravitons as well as massive KK gravitons. Moreover, we briefly address the production of primordial black holes (PBHs) from a slingshot collapse. Finally, we consider all three aspects also for the wrapped D_{1+5}-slingshot.

5.6.1 Massless Gravitational Radiation in One Large Extra Dimension

For the emission of massless gravitons, for simplicity, we first assume that the slingshot effect takes place after inflation. Furthermore, we assume that the horizon size $M_{\rm P}/T_{\rm sl}^2$ at slingshot annihilation at temperature $T_{\rm sl}$ is set by the extra dimension size $R_\perp$. Notice that these are strong simplifying assumptions, which can of course be relaxed in a more detailed investigation. However, in this thesis only the main concepts will be introduced. Using these assumptions, the red-shifted frequency of today's gravitational wave signal is

$$f^{\rm peak} \simeq \frac{T_0}{\sqrt{M_{\rm P} R_\perp}} \,, \tag{5.38}$$

where we have also ignored factors that may arise from the number of degrees of freedom.

Using equation (5.23) and replacing the quantities by those of the D-brane slingshot results in the gravitational radiation density parameter

$$\Omega_{\rm GW}^{\rm peak} \simeq \epsilon_{\rm GW}\, \frac{N_{\rm sl} M_{\rm sl} H_{\rm sl}}{M_{\rm P}^2}\, \Omega_{\rm rad} \,, \tag{5.39}$$

where $H_{\rm sl} \sim 1/R_\perp$ is the Hubble parameter at slingshot time and $\epsilon_{\rm GW} \sim E_{\rm GW}/M_{\rm sl}$ is the conversion factor that quantifies how much of the slingshot energy is converted into gravitational radiation. The fraction describes the ratio between the energy in all slingshots per horizon, $N_{\rm sl}M_{\rm sl}$, and the total energy available within the horizon, $M_{\rm P}^2/H_{\rm sl}$, at slingshot time. Since we do not want a Universe dominated by slingshots, this fraction should not exceed one.

For the application of the above formula for $\Omega_{\mathrm{GW}}^{\mathrm{peak}}$, a few warnings need to be mentioned. First of all, the emission of massless gravitational radiation depends on the alignment of the slingshot. As mentioned earlier, a slingshot that is perfectly perpendicular to our world brane will not emit massless gravitational radiation. This can be understood intuitively from its geometry. We, living in the world with coordinates $x_{\parallel}$, see the slingshot only as a massive lump of mass M_{sl}. We are not able to observe the dynamics in the $x_{\perp}$ direction. Therefore, when the slingshot gets shorter, the string energy is converted into kinetic energy, but an observer living in $x_{\parallel}$ cannot see this. The massive lump remains unchanged (at least if we ignore other excitations of the slingshot). A similar argument applies to the massless gravitons. They are emitted only if the shape in the $x_{\parallel}$ coordinates changes. Since this is not the case for a perpendicular slingshot, the emission of massless radiation is suppressed. The situation, however, changes completely if there is an angle smaller than 90° between the slingshot and the brane. Therefore, for convenience, we take the slingshot to never be exactly perpendicular. We assume it has a significant contribution in both directions, $x_{\perp}$ and $x_{\parallel}$, such that the projection onto the corresponding coordinates is of order one.

An additional caveat concerns the emission of massive Kaluza–Klein gravitons. We assume that the energy spectrum scales with ω^{-1}, similarly to the magnetic monopole slingshot. However, the emission of KK gravitons, which is not present for the magnetic monopole slingshot, may lead to deviations from the ω^{-1} scaling. We do not take such an effect into account.

There is another difference between the magnetic monopole slingshot and the D-brane slingshot. Due to the long-range Coulomb magnetic attraction, the slingshot phase in the monopole case was strongly restricted. For the D-brane slingshot, however, only gravitational attraction has to be taken into account. The relevant time scales are therefore determined by gravitational merger effects, which can be neglected as long as there is no overabundance of slingshots in the Universe.

5.6.2 Emission of Kaluza–Klein Gravitons

Additionally to the massless gravitons, there can be massive gravitons emitted in the slingshot process. Such massive gravitons appear due to the compactification of $x_{\perp}$. These are the Kaluza–Klein gravitons, with masses $m_n = n/R_{\perp}$, where $n \geq 1$ is an integer. Through non-linear interactions, these KK gravitons can decay. Their lifetime is given by $\tau_n \sim M_{\mathrm{P}}^2/m_n^3$. This lifetime exceeds the current age of the Universe for masses below $100\,\mathrm{MeV}$. Hence, KK gravitons with masses $m_n \lesssim 100\,\mathrm{MeV}$ can serve as dark matter candidates [190].

The emitted KK gravitons have frequencies $\omega > m_n$. For massless gravitons, the emitted gravitational power is given by $\mathrm{d}P_{\mathrm{GW}}/\mathrm{d}\omega \sim \mu^2/(M_{\mathrm{P}}^2\,\omega)$ (for more details see the derivation in Section 4.5.3). We assume that the emission into a single KK channel does not exceed the energy emitted in the massless gravitational radiation channel and, for an order-of-magnitude estimate, we further assume that the spectrum exhibits the same frequency dependence.

Notice that the ω^{-1} scaling requires a perfectly straight string. However, in general it is quite natural for the slingshot to be curved. We will assume that the curvature occurs on length scales of order the slingshot length. This implies that only the lowest-frequency modes, $n < n_* \sim \mathcal{O}(1)$, radiate with a frequency scaling $\propto \omega^{-1}$. For $n > n_*$, the radiation is instead suppressed further [19]. With this scaling the total emitted energy in the nth KK graviton mode is

$$E_n \sim \frac{\mu^2}{M_{\mathrm{P}}^2} R_\perp \sum_{k=n}^{n_*} \frac{1}{k} \,. \tag{5.40}$$

This energy corresponds to the sum of the rest mass and the kinetic energy of the KK gravitons. Due to the expansion of the Universe, the kinetic contribution disappears, such that only the rest mass contribution remains. Thus, for each frequency mode, only a fraction m_n/ω contributes to the rest mass. Integrating over the spectrum then yields

$$E_n^{\mathrm{mass}} \sim N_{\mathrm{sl}} \frac{\mu^2}{M_{\mathrm{P}}^2} \frac{1}{m_n} \,. \tag{5.41}$$

This is the energy that can contribute to today's dark matter in the form of KK gravitons. Including the corresponding redshift factor then gives the density parameter

$$\Omega_n \sim \frac{1}{m_n R_\perp} \frac{T_{\mathrm{sl}}}{T_0} \Omega_{\mathrm{GW}}^{\mathrm{peak}} \,, \tag{5.42}$$

for the nth graviton mode. Here, $\Omega_{\mathrm{GW}}^{\mathrm{peak}}$ denotes the density parameter of the massless gravitational radiation given in equation (5.39).

All graviton modes with masses below $m_{\max} \sim 100\,\mathrm{MeV}$ can contribute to today's dark matter abundance. We therefore have to sum over all these graviton modes, which yields the total KK dark matter density parameter

$$\Omega_{\mathrm{KK}} \sim \Theta(m_{\max} R_\perp - 1) \sqrt{\frac{M_{\mathrm{P}}}{R_\perp}} \frac{1}{T_0} \ln\left(\min(m_{\max} R_\perp, n_*)\right) \Omega_{\mathrm{GW}}^{\mathrm{peak}} \,, \tag{5.43}$$

with Θ being the Heaviside step function.

For extra dimensions of size $R_\perp \gtrsim 10^{-13}\,\mathrm{cm}$, the lowest graviton mode already has a mass above 100 MeV. Therefore, for smaller sizes of the extra dimension, there are no KK gravitons that can serve as dark matter candidates. This condition is taken into account by the Heaviside step function Θ in equation (5.43).

As already mentioned for the massless gravitons, the emission of KK gravitons can modify the dynamics of the slingshot effect. Therefore, when applying equations (5.43) and (5.39), one should always verify that the total emitted energy is negligible compared to the total slingshot mass M_{sl}. Notice that, for the emitted energy, both the kinetic energy and the rest mass have to be taken into account, as given in equation (5.40). Since we are assuming $n_* \sim \mathcal{O}(1)$, the back-reaction can be always neglected.

The emission of KK gravitons imposes a strong bound on the gravitational wave density parameter $\Omega_{\mathrm{GW}}^{\mathrm{peak}}$, since their abundance must not exceed $\Omega_{\mathrm{KK}} \sim \mathcal{O}(1)$. We find that for frequencies $f < 10\,\mathrm{Hz}$ (corresponding to $R_\perp \gtrsim 10^{-13}\,\mathrm{cm}$), the gravitational radiation density parameter is strongly suppressed by this bound and therefore does not yield a signal within the reach of future gravitational wave experiments. For frequencies $f \gtrsim 10\,\mathrm{Hz}$, however, there is no Kaluza–Klein graviton dark matter contribution, and thus this bound does not affect $\Omega_{\mathrm{GW}}^{\mathrm{peak}}$.

5.6.3 Primordial Black Hole Production

Finally, the production of primordial black holes (PBHs) from a slingshot collapse should be briefly mentioned. The D_0-brane gains a significant amount of energy when it is pulled by the string toward our world brane. Upon colliding with the world brane, the Schwarzschild radius of the slingshot can exceed the string thickness, such that a black hole may form. This mechanism has already been discussed for confined quarks in [191].

The 5-dimensional gravitational radius for the rest mass of a slingshot of length $R_\perp$ (see equation (5.35)) is given by

$$R_5 \sim \left(M_{\mathrm{sl}} \frac{R_\perp}{M_{\mathrm{P}}^2} \right)^{\frac{1}{2}} \sim \frac{R_\perp^{\frac{2}{3}}}{M_{\mathrm{P}}^{\frac{1}{3}}} \sim \sqrt{\frac{R_\perp}{M_{\mathrm{s}}}} \sim \frac{M_{\mathrm{P}}}{M_{\mathrm{s}}^2} \,. \tag{5.44}$$

This relation shows that it is very likely that a PBH will form during the collision, since $R_5 \gg M_{\mathrm{s}}^{-1}$.

For the largest possible extra dimension size, $R_\perp \sim 10^{-2}\,\mathrm{cm}$, the PBH mass would be $\sim 10^5\,\mathrm{g}$. Using the extrapolated Hawking radiation emission rate would yield a lifetime of $\sim 10^7\,\mathrm{s}$. However, it has been shown that once the black hole's information load is taken into account, the memory burden effect can significantly extend the lifetime [227, 228, 229, 230, 231]. In the case of black holes with mass $\sim 10^5\,\mathrm{g}$, the memory burden effect could increase the lifetime to at least 10^{20} times the present age of the Universe. Therefore, PBHs produced through the slingshot effect can have masses that may be relevant for astrophysical Gamma-ray and neutrino observations [232, 233, 234, 235, 236].

The density parameter for the PBHs of mass $M_{\mathrm{BH}} = M_{\mathrm{sl}} = \mu R_\perp$ can be calculated to be [191]

$$\Omega_{\mathrm{PBH}} \sim \epsilon_{\mathrm{PBH}} \frac{\mu^{\frac{3}{2}}}{M_{\mathrm{BH}}^{\frac{1}{2}}\, T_0\, M_{\mathrm{P}}^{\frac{3}{2}}}\, \Omega_{\mathrm{rad}} \,, \tag{5.45}$$

where ϵ_{PBH} is the conversion factor of slingshots into black holes.

5.6.4 Phenomenology of the Wrapped D-Brane Slingshot

As mentioned earlier in this section, the D_1-string can be replaced with a wrapped D_{1+5}-brane. The resulting effective string tension is then given by equation (5.37). Using this tension results in a gravitational wave conversion factor of

$$\epsilon_{\rm GW}^{6d} \simeq \frac{\mu}{M_{\rm pl}^2} \simeq \frac{1}{M_{\rm s} R_\perp}\,, \tag{5.46}$$

which gives the gravitational radiation density parameter

$$\Omega_{\rm GW}^{\rm peak} \simeq \frac{N_{\rm sl}}{M_{\rm s}^2 R_\perp^2}\,\Omega_{\rm rad} \simeq 10^{-13}\,N_{\rm sl}\left(\frac{\rm TeV}{M_{\rm s}}\right)^2\left(\frac{f}{10\,{\rm Hz}}\right)^4\,. \tag{5.47}$$

To avoid an overabundance of slingshots, the number of slingshots per horizon should satisfy the bound

$$N_{\rm sl} \lesssim \frac{M_{\rm P}}{M_{\rm sl} H_{\rm sl}} \simeq M_{\rm s} R_\perp \simeq 10^4\,\frac{M_{\rm s}}{\rm TeV}\left(\frac{10\,{\rm Hz}}{f}\right)^2\,. \tag{5.48}$$

As an example, we can consider one slingshot per horizon. Furthermore, we take the values $M_{\rm s} \sim$ TeV and $f \sim 10\,{\rm Hz}$. For this frequency, no dark matter KK gravitons are produced and thus they do not impose an additional restriction on the density parameter. The resulting signal can be within reach of the next generation of gravitational wave experiments, such as the Cosmic Explorer [213] and the Einstein Telescope [214]. For $N_{\rm sl} \sim 10^4$, we can even obtain a signal that is in the reach of current gravitational wave detectors such as aLIGO [209], VIRGO [210], and KAGRA [211]. In Figure 5.8, we illustrate the regime (blue) in which the wrapped D-brane slingshot can emit a potentially observable gravitational radiation signal. For frequencies below 10 Hz, we do not expect a detectable gravitational wave signal due to dark matter bounds that arise because of the emission of a large number of KK gravitons. However, at these scales, corresponding to sizes $R_\perp \gtrsim 10^{-13}\,{\rm cm}$ for the largest extra dimension, we can obtain a significant contribution to the dark matter energy density from these massive KK gravitons. The corresponding density parameter is given by

$$\Omega_{\rm KK} \sim 10^{-1}\,N_{\rm sl}\left(\frac{10^{-9}\,{\rm cm}}{R_\perp}\right)^{\frac{5}{2}}\left(\frac{\rm TeV}{M_{\rm s}}\right)^2, \tag{5.49}$$

where we dropped logarithmic factors. Hence, for instance, for one slingshot per horizon, $M_{\rm s} \sim$ TeV, and $R_\perp \sim 10^{-9}\,{\rm cm}$, we obtain an abundance of KK gravitons, which could account for the entire dark matter energy density of the Universe today.

Last but not least, the collapse of the slingshot can lead to the production of a PBH. The corresponding density parameter is given by

$$\Omega_{\rm PBH} \simeq 10^{13}\,\epsilon_{\rm PBH}\,N_{\rm sl}\left(\frac{\rm TeV}{M_{\rm s}}\right)\left(\frac{10^{-13}\,{\rm cm}}{R_\perp}\right)^{\frac{3}{2}}\,. \tag{5.50}$$

For the previously mentioned example parameters, $M_\mathrm{s} \sim$ TeV and $R_\perp \sim 10^{-13}\,$cm, it is sufficient to have a conversion factor of about $\epsilon_\mathrm{PBH} \sim 10^{-14}$, i.e. only one out of 10^{14} slingshots has to end in a PBH that still exists today, to have the right present-day dark matter abundance. This small value of ϵ_PBH implies that most slingshots should not collapse into a PBH, but instead for instance be erased by a brane [23] or another annihilation mechanism.

Notice that all the above discussion about the D-brane slingshot relies on several strong assumptions. In particular, we assumed that the slingshots are simply present and then collapse. The question of how exactly these slingshots form remains open. Furthermore, we simplified their dynamics by assuming that they collapse only along the string direction. Bending of the strings could significantly modify the dynamics and potentially lead to different results.

5.7 Slingshot of Confined Vortices and Strings

So far, we have considered the slingshot only for point-like sources that are connected to walls by strings. However, the slingshot effect can also arise for objects with different co-dimensionalities. For example, a full string traversing from an unconfined region into a confined region can stretch an entire domain wall. The stretched object is a domain wall (partially) bounded by a string. Such configurations were already discussed in [139] and find applications in axionic models [31, 237, 238].

This phenomenon can be reduced to $2+1$ dimensions, where vortices can be confined by domain strings [239]. In this section, we modify the model of [239] by adapting the potential such that it supports two degenerate vacua, a confined vacuum and an unconfined vacuum. The model can then be straightforwardly extrapolated to a third spatial dimension. Therefore, analysing the vortex slingshot in $2+1$ dimensions provides insight into what happens in $3+1$ dimensions for the "string slingshot". Moreover, this setup can be viewed as a toy model for the magnetic monopole slingshot.[4]

The theory for the vortex slingshot effect requires two complex scalar fields, ϕ and χ. With ϕ we want to break a $U(1)$ gauge symmetry to Z_2. With χ we subsequently want to break the Z_2 symmetry. The Lagrangian supporting such an idea is given by

$$\mathcal{L} =(D_\mu\phi)^*(D^\mu\phi) + (D_\mu\chi)^*(D^\mu\chi) - \frac{1}{4}F_{\mu\nu}F^{\mu\nu} - V(\phi,\chi)\,, \tag{5.51}$$

where $F_{\mu\nu}$ is the field strength tensor for the $U(1)$ gauge field A_μ. The potential is given

---

[4] As already discussed in Chapter 3, to develop a good intuition for the topological structure of magnetic monopole systems, it is often useful to first consider a lower-dimensional analogue in which monopoles are replaced by vortices. Although vortex models are typically simpler, their dynamics often exhibit close similarities to those of monopoles (see, for example, the right-angle scattering of vortices and monopoles described in Section 3.6 and Section 3.7, respectively). When we started the project on the slingshot effect, we indeed first investigated the slingshot for vortices, since their dynamics were easier to simulate. Afterwards we extended the analysis to the magnetic monopole slingshot.

by

$$V(\phi,\chi) =\lambda_\phi(|\phi|^2 - v_\phi^2)^2 + \lambda_\chi(|\chi|^2 - v_\chi^2)^2|\chi|^2 + \beta\phi^*\chi^2 + c.c.\,. \tag{5.52}$$

The covariant derivatives are defined by

$$D_\mu\phi = \partial_\mu\phi - igA_\mu\phi\,, \tag{5.53}$$

$$D_\mu\chi = \partial_\mu\chi - i\frac{g}{2}A_\mu\chi\,. \tag{5.54}$$

Notice that the couplings to the gauge field are different for ϕ and χ. This is required due to the structure of the β interaction term and its gauge invariance. This theory is invariant under the $U(1)$ gauge transformation

$$\phi \mapsto e^{i\alpha}\phi\,, \qquad \chi \mapsto e^{i\frac{\alpha}{2}}\chi\,, \qquad A_\mu \mapsto A_\mu - \frac{1}{g}\partial_\mu\alpha\,. \tag{5.55}$$

When ϕ obtains a non-zero VEV, the $U(1)$ gauge symmetry is spontaneously broken to Z_2. In this phase, the Higgs boson mass is given by $m_{h,\phi} = 2\sqrt{\lambda_\phi}v_\phi$, while the gauge boson acquires a mass $m_{v,\phi} = \sqrt{2}\,gv_\phi$. Notice that, in contrast to the monopole model, there is no massless gauge boson. Therefore, no long-range gauge fluxes arise that could become confined when the Z_2 symmetry is further broken by a non-zero expectation value of χ.[5] In the confined phase, the Z_2 symmetry is Higgsed and the gauge boson mass receives an additional contribution given by $m_{v,\chi} = gv_\chi/\sqrt{2}$. The Higgs mass associated with the χ field is $m_{h,\chi} = 2\sqrt{\lambda_\chi}v_\chi$. The overall breaking pattern is given by

$$U(1) \xrightarrow{\langle\phi\rangle} Z_2 \xrightarrow{\langle\chi\rangle} 1\,. \tag{5.56}$$

Of course, here we assumed a hierarchy of the scales, $m_{h,\phi} > m_{h,\chi}$.

In the Z_2-symmetric phase, the $U(1)$ symmetry is broken and, correspondingly, Nielsen–Olesen vortices [11] with topological charge n can appear (more details on vortices are given in Section 2.2.3).

When the Z_2 symmetry is broken further by the χ field, these vortices become confined [239]. This is due to the β-term in the potential, which depends on the phase. The minimization of this term forces the phases of the two scalar fields to be

$$\theta_\phi = 2\theta_\chi\,. \tag{5.57}$$

However, this condition cannot hold everywhere if the ϕ field contains a vortex. Around a vortex, the phase of the ϕ field changes by 2π, whereas, due to equation (5.57), the phase of χ would change only by π. This would imply a discontinuity in the χ field. The phase jump is smoothed out by the formation of a domain wall, which we will refer to as a

---

[5] Due to the analogy with confinement, we will nevertheless sometimes use the term “confined”, even though in the standard literature confinement typically refers to the confinement of electric or magnetic flux.

domain string. This domain string solution arises from the breaking of the Z_2 symmetry. Consequently, the domain string is attached to the vortex.

Similarly to the cosmic string, which can pair up a monopole and an anti-monopole, the domain string can pair up two vortices. And similarly it is also possible for the domain string to connect a vortex with a domain wall separating the Z_2-symmetric phase from the Z_2-Higgsed phase. The domain wall separating the two phases has the same profile as the one encountered in the $SU(2)$ slingshot model for the ψ field:

$$\xi(x) = \frac{v_\chi}{\sqrt{1 + e^{m_{h,\chi}(x - x_{\mathrm{DW}})}}}\,, \tag{5.58}$$

where we fix the $U(1)$ direction of the wall by choosing $\xi = \mathrm{Re}\,\chi$.

For the simulation of the slingshot effect for vortices, the initial configuration is easier to construct. Since the gauge field is massive, there is no long-range field that requires special treatment at the domain wall. Therefore, we can simply choose the field orientations $\phi \sim \exp(in\theta)$ and $\chi \sim \exp(in\theta/2)$, with $\theta = \arctan(y/(x - x_{\mathrm{V}}))$ and x_{V} denoting the position of the vortex. The vortex in ϕ is implemented as the usual Nielsen–Olesen vortex described in Section 2.2.3, while the profile for the χ field is given by the domain wall (5.58).

The numerical methods are the same as in the monopole slingshot case. We again choose a lattice spacing of $0.25\,m_{v,\phi}^{-1}$ and a time step of $0.1\,m_{v,\phi}^{-1}$. The lattice size is $240\,m_{v,\phi}^{-1} \times 120\,m_{v,\phi}^{-1}$. We solve the equations of motion in Lorenz gauge and again use the Crank–Nicolson method for the time integration. The boundary conditions for the χ field are periodic in the y-direction and Dirichlet in the x-direction. For the ϕ and A_μ fields, we choose absorbing boundary conditions.

The parameters for the figures presented in this section are $m_{v,\phi} = m_{h,\phi} = 1$, $g = 1/\sqrt{2}$, $m_{v,\chi} = 0.3\,m_{v,\phi}$, $m_{h,\chi} = 0.8\,m_{v,\phi}$, and $\beta = -0.01\,m_{v,\phi}^{3/2}$. The initial separation between the vortex and the domain wall was chosen as $40\,m_{v,\phi}^{-1}$. Both the vortex and the domain wall were Lorentz-boosted towards each other with velocities 0.8.

The animated results of the simulations are shown in the following video:
`https://youtu.be/IPJAPjo3nSc?si`
Furthermore, Figures 5.9 and 5.10 show selected time frames of the scalar field structure obtained from the simulation.

In Figure 5.9, we observe that the vortex forms a domain string when it hits the domain wall and enters the Higgsed region. In contrast to the monopole slingshot, the domain string carries no flux, while the remaining dynamics is very similar. The effect of the β-term is also straightforward to see. While the ϕ field winds by 2π around the vortex, the χ field winds only by π and exhibits a jump along the domain string. This behaviour also explains why the domain string cannot detach from the domain wall. Detachment would require a full (or zero) winding in χ, which cannot be achieved with a single vortex in ϕ due to the condition (5.57).

To detach the domain string from the wall, we can introduce an additional anti-vortex that enters the throat of the domain string. Once the anti-vortex enters, the domain string detaches from the wall and a confined vortex–anti-vortex pair remains. This pair eventually

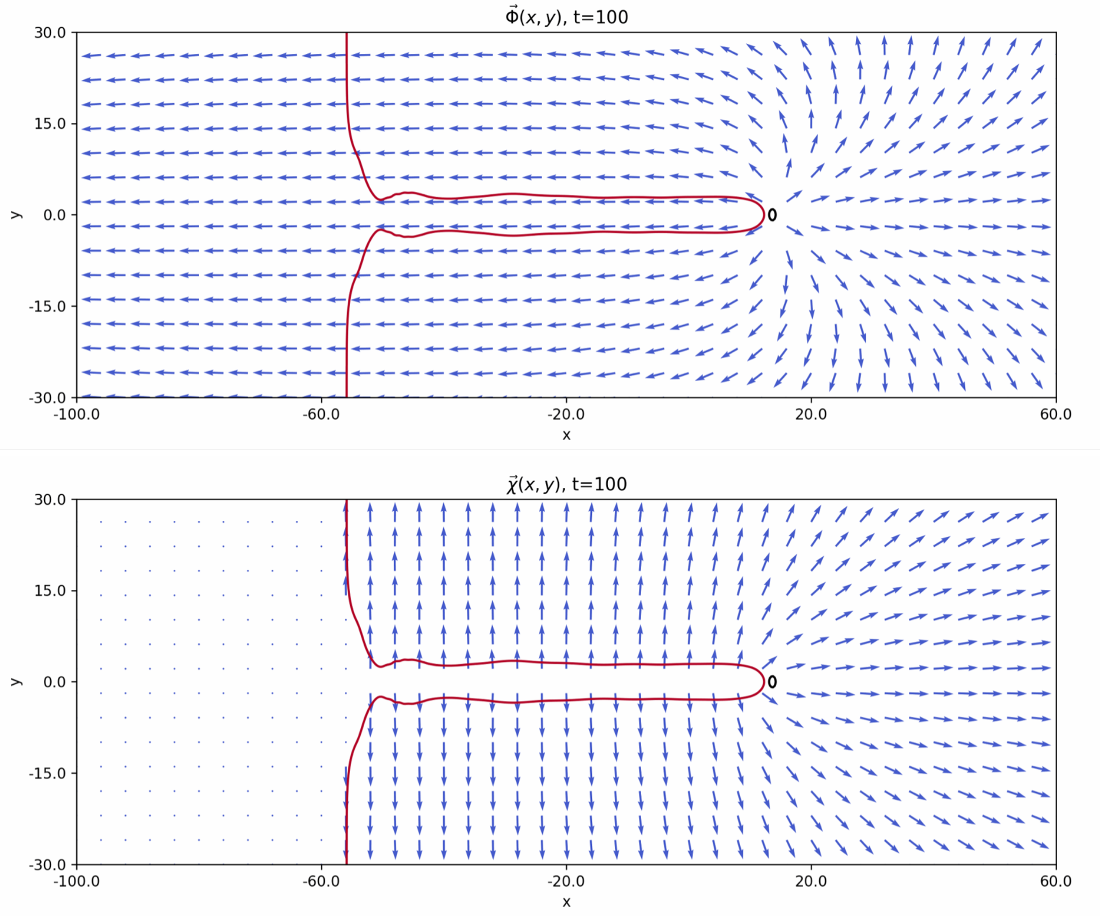

Figure 5.9: This figure shows the distribution of the phases of the scalar fields at time $t = 100\, m_{v,\phi}^{-1}$. The phase is illustrated in a vector plot using the parametrization $(\mathrm{Re}(\phi), \mathrm{Im}(\phi))^T$ (top) and $(\mathrm{Re}(\chi), \mathrm{Im}(\chi))^T$ (bottom). The profiles of the domain wall and the domain string are indicated by the red contour corresponding to $|\chi| = v_\chi/2$. The black circle marks the position of the vortex (contour $|\phi| = v_\phi/2$). All length scales are given in units of $m_{v,\phi}^{-1}$.

annihilates upon collision. However, due to the absence of a flux, there are two possible ways to detach the domain string. Besides forming a vortex–anti-vortex pair, we can also obtain a vortex–vortex pair. The latter carries winding number 2 in the ϕ field and winding number 1 in the χ field. The vortex–vortex pair forms a bound state. The string pulls the vortices together until they scatter at a right angle. Afterwards, they separate again, but the domain string pulls them back, leading to another right-angle scattering. This process repeats multiple times. Two time frames illustrating this behaviour are shown in Figure 5.10. The right-angle scattering of vortices was discussed in detail in Section 3.6.

As mentioned earlier, in the vortex slingshot case there is no confinement of a gauge flux, since the gauge field is already massive on both sides of the wall. However, there is a flux associated with the gradient of the Goldstone field. To see this more clearly, let us set

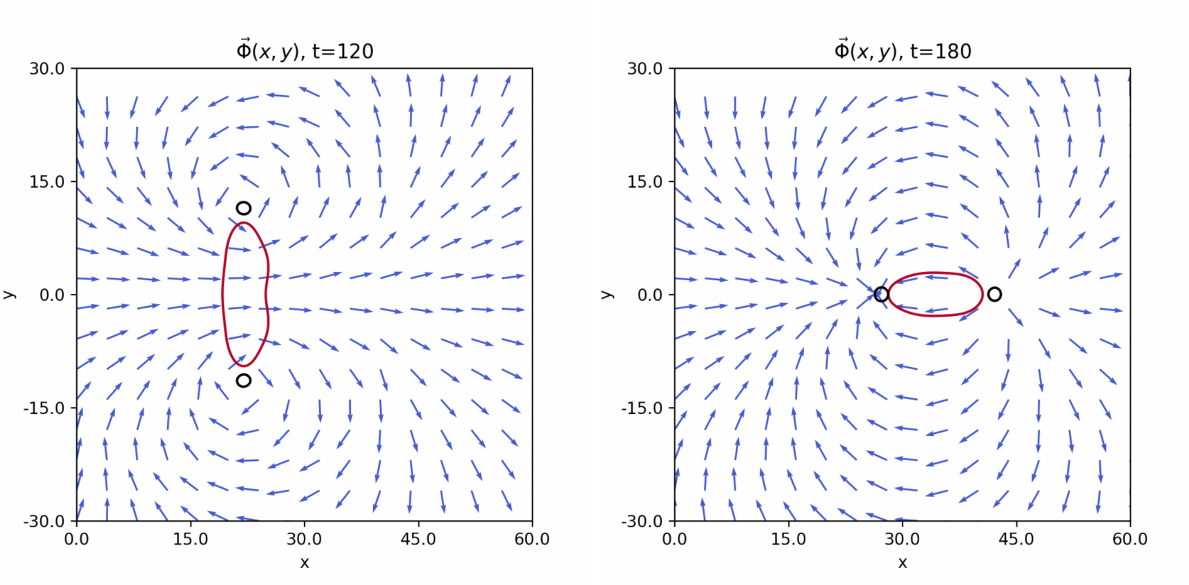

Figure 5.10: This figure shows the scalar field orientation at times $t = 120\, m_{v,\phi}^{-1}$ and $t = 180\, m_{v,\phi}^{-1}$ for a confined vortex–vortex pair that was formed after a single vortex slingshot detached from the domain wall when another vortex of the same charge entered the throat of the slingshot.

$\beta = 0$. In this case, the theory in (5.51), after the spontaneous breaking of the $U(1)$ gauge symmetry by the VEV of ϕ, still possesses a global $U(1)$ symmetry. When χ acquires a VEV, this global $U(1)$ symmetry is also spontaneously broken, giving rise to a massless Goldstone boson. This degree of freedom is responsible for the long-range (logarithmic) interactions between vortices in the χ-field. For $\beta \neq 0$, however, this Goldstone mode becomes confined within the domain string.

All the dynamics observed in $2+1$ dimensions can, of course, be extended to the $3+1$-dimensional case, where strings replace vortices. In that setting, a string can collide with a domain wall and stretch a full domain wall behind it. Similarly to the vortex–vortex pair, one can now obtain a string–string pair bounded by the χ-field. The resulting configuration has a cable-like structure.

Furthermore, by modifying the powers of the χ-field in the β-term, it is possible to confine more than two vortices/strings. For instance, one can form a bound state of three vortices/strings.

5.8 Conclusion and Outlook

In this chapter, we introduced the so-called *slingshot effect*. This effect occurs when a flux-carrying source enters a region in which the flux is confined. In the confined phase, the flux becomes concentrated into a string that connects the source to a wall separating the confined from the unconfined region. We observed that this effect is very general and can arise in several different models. While we mainly focused on magnetic monopoles that become confined in a region where the $U(1)$ symmetry, associated with the Coulomb magnetic field, is spontaneously broken, the effect also finds applications in QCD and in string theory. Moreover, as shown in the last section, it can be reduced to a $2+1$-dimensional model involving vortices.

As an example of the monopole slingshot, we considered an $SU(2)$ gauge theory with one adjoint scalar field ϕ, responsible for the symmetry breaking $SU(2) \to U(1)$, and a fundamental scalar field ψ, which subsequently breaks $U(1) \to 1$. Furthermore, we employed a sextic potential for ψ that allows confined and unconfined vacua to coexist. When the magnetic monopole collides with the domain wall, it stretches a string in the form of a Nielsen–Olesen flux tube. This string then pulls the monopole back into the unconfined region.

This slingshot effect may occur during first-order phase transitions in the early Universe. The motivation for this work originates from the Langacker–Pi mechanism [18], which exploits confining dynamics to reduce the monopole abundance and thereby solve the magnetic monopole problem. The slingshot model provides a framework in which such a reduction of the monopole number can be achieved through magnetic confinement.

Besides the magnetic monopole slingshot, we analysed the relevance of this effect in other scenarios that may have played a role in the early Universe.

First, a dual version of the slingshot effect can arise in QCD. In this case, quarks crossing the boundary between an unconfined and a confined region stretch colour-electric flux tubes (QCD strings). The dynamics we simulated for confined magnetic monopoles is expected to closely resemble the dynamics of confined vortices.

The slingshot effect also finds applications in D-brane physics. In particular, it can arise quite naturally in brane-inflationary scenarios [187, 188, 189]. In this context, the role of the monopole is played by a D_0-brane that is connected to "our world" brane by a string, or by a wrapped D-brane that effectively behaves as a string. Once again, the dynamics are similar to those observed for magnetic monopoles.

Taken all together, the slingshot effect may be relevant in many cosmological setups. We find that it is of phenomenological interest, in particular due to the emitted gravitational radiation. We found that both the monopole slingshot and the D-brane slingshot can produce signals within the sensitivity range of current gravitational wave experiments such as LIGO [209], Virgo [210], and KAGRA [211], as well as future experiments like the Einstein Telescope [214] and Cosmic Explorer [213]. In addition to gravitational radiation, the slingshot can also trigger the formation of primordial black holes via the mechanism proposed in [191]. If the memory burden effect [227, 228, 230] stabilizes these black holes, they could account for the present-day dark matter abundance [229, 240, 230, 231].

Chapter 6

Concluding Remarks and Outlook

This thesis provided an overview of several research topics in the field of topological defects. In particular, the focus was on the current status of magnetic monopole research. Thereby, this thesis concentrated on two main research directions: the dynamical properties of solitons and the applications of magnetic monopoles in high-energy physics.

My motivation for research on topological defects is that numerous experiments clearly demonstrate that our current understanding of the Universe, while robust, is still incomplete. The Standard Model of particle physics, although highly successful, is known to be missing key components and therefore requires extensions. There is, however, an overwhelming "sea" of possible extensions, which makes finding the correct one extremely challenging. To design targeted experiments, more theoretical work is needed to provide clear predictions that can be tested. Topological defects may be helpful in this context, since they are common by-products of SM extensions, even though the underlying theories themselves can differ significantly. Therefore, a promising strategy is to focus on topological defects as broader consequences of extensions to the SM.

As shown in detail in this thesis, topological defects can produce observable signals such as gravitational waves, making them attractive targets for future experiments. However, depending on their properties and abundance, topological defects can also create challenges. Studying these consequences provides an efficient way to narrow down the experimental search space and improve the chances of discovering new physics.

Following these principles, my research focuses on three main interests, which were presented throughout this thesis:

1. I aim to understand the structure and dynamics of topological defects. In Chapter 3, several steps towards a full understanding of the dynamical properties of vortices and magnetic monopoles were performed. New results such as the discovery of multi-bounce windows in vortex–anti-vortex collisions and the influence of resonances on BPS vortex dynamics were presented. Furthermore, several predictions from the 1980s and 1990s regarding the BPS dynamics of magnetic monopole collisions were confirmed using numerical simulations.

2. I aim to investigate the theories in which such defects can arise and study their specific properties and cosmological consequences within these frameworks. In Chapter 4, it was explained that magnetic monopoles are predicted by Grand Unified Theories. However, it was also shown that there may be an overproduction of magnetic monopoles. This motivated several ideas for solving the magnetic monopole problem. For example, magnetic monopoles could be erased by domain walls, as explained and numerically studied in Section 4.4, or magnetic monopoles can be connected by strings that pull them together until they collide and annihilate, as presented in Section 4.5. For the latter idea, we also studied a modification in Chapter 5, the so-called confinement slingshot effect, where monopoles become connected to a domain wall by a string when they collide with vacuum bubbles in first-order phase transitions.

3. I aim to provide guidance for experiments, for example by identifying frequency windows in which gravitational radiation originating from topological defects is expected. This can help for decisions about the design and construction of future experiments. In particular, for the slingshot effect presented in Chapter 5, we estimated the gravitational radiation density parameter for both the magnetic monopole slingshot and the D-brane slingshot. While we found that signals observable by current and future gravitational wave experiments may exist, we also observed that the signals from the slingshot effect, or more generally from magnetic monopoles connected by strings, are rather expected to lie in a high-frequency regime for which experiments currently do not exist. This provides motivation for further research on high-frequency gravitational wave experiments.

One of my goals with this thesis was to emphasize the importance of topological defects in a wide variety of theories. While one main focus was the cosmological magnetic monopole problem, magnetic monopoles and other solitons find applications in other areas of high-energy physics. As discussed briefly in Section 5.5, confined magnetic monopoles behave similarly to confined quarks. Therefore, studying the dynamics of confined monopoles may provide new insights towards understanding QCD confinement. Furthermore, as mentioned multiple times in Chapters 4 and 5, topological defects provide mechanisms for the production of primordial black holes, which are candidates for dark matter.

Additionally, I would like to mention an example that was not discussed in this thesis but was part of my PhD research. The non-trivial vacuum structure of QCD suggests an additional term in the SM Lagrangian, known as the θ-term. This term describes the so-called θ-vacua. Using quantum arguments, Witten argued in 1979 [241] that a magnetic monopole placed in a θ-vacuum acquires electric charge in addition to its magnetic charge. In an effective classical description of θ-vacua, we were able to provide the first classical effective demonstration of this effect using numerical tools [242]. Our work resulted in two important outcomes: first, it provides a direct confirmation of Witten's prediction, and second, it deepens our understanding of θ-vacuum physics. As a side result of this project, we also discovered that a magnetic monopole is polarizable. This means that when it is placed in a background electric field, it develops an electric dipole moment. This finding provides valuable new insights into the internal structure of the ’t Hooft–Polyakov magnetic monopole.

In this thesis several open questions were identified that require further investigation. In Chapter 3, it was shown that in vortex–anti-vortex collisions the vortices can be recreated if the collision velocity is sufficiently high. An open question is whether a similar phenomenon occurs for magnetic monopoles. Additionally, we provided an approximate ansatz for certain multi-monopole configurations that were useful for studying monopole collisions in numerical simulations. However, many configurations remain to be constructed in order to obtain a more complete understanding of the moduli space structure of magnetic monopoles.

In Chapter 4, it was demonstrated that a monopole–anti-monopole pair can become connected by a cosmic string. In extended theories, even confined monopole–monopole configurations may exist. However, such a configuration has not yet been found. Identifying such solutions could provide an interesting analogy to mesons and baryons arising from confinement in QCD. Furthermore, we introduced the erasure mechanism as a possible solution to the magnetic monopole problem. The central idea is that magnetic monopoles could be completely eliminated through collisions with domain walls. However, it remains unclear whether this process occurs efficiently in a realistic cosmological setting. In particular, an important question is whether all monopoles can be erased or whether a surviving fraction would still exceed cosmological bounds.

In Chapter 5, we presented the slingshot effect as a mechanism that may arise in theories that support the coexistence of confined and unconfined phases. We provided preliminary estimates of the resulting gravitational wave signals, which may lie within the sensitivity range of current or future gravitational wave experiments. For the magnetic monopole slingshot scenario, we imposed constraints derived from avoiding domain wall or monopole domination. It remains to be clarified whether relaxing these constraints is theoretically acceptable, or whether additional cosmological or phenomenological bounds must be taken into account.

These are only a few of the new questions that emerged during the projects presented in this thesis. While many questions were answered, even more new ones appeared. In the upcoming years, I wish to address many of them and contribute to a better understanding of topological defects, extensions of the Standard Model, and the fundamental nature of the Universe. This thesis is just the beginning …

Appendix A

Numerical Methods

The majority of the discussions in this thesis is based on numerical results. This appendix provides a brief overview of the numerical methods that have been applied. It should be noted that this appendix is not intended as an introduction to numerical methods, but rather as a short summary of the techniques used throughout this thesis and together with their implementation. Readers interested in further details are referred to standard textbooks [243, 244, 245], which have partially served as a basis for this appendix.

Performing numerical simulations requires several steps to obtain the final results. First, one needs suitable initial conditions. This initial ansatz does not have to solve the field equations exactly, but it should be sufficiently close. The farther away the initial configuration is from the true solution, the larger the numerical fluctuations and the less reliable the results become. Finding appropriate initial conditions is a non-trivial task, as discussed throughout the thesis. One important subtask is determining the profile functions of solitons. While the domain wall solution is often known analytically, the profile functions for vortices and magnetic monopoles (except for the BPS monopole) are not. Section A.2 presents the methods that can be used to obtain these profile functions.

The numerical computation of the time evolution is explained in Section A.4. When performing the time iteration on a lattice, one must keep in mind that the lattice represents a finite volume, which requires careful treatment at the boundaries. The choice of boundary conditions is crucial in all numerical simulations. Therefore, all possibilities we have used are discussed in Section A.5.

Initial conditions and the time evolution are the two main ingredients of numerical simulations. However, there are many additional subtleties that must be taken into account, several of which are also discussed in this appendix.

A.1 Discretized Derivatives

In the following, we use one representative function f to describe the methods. Everything can be straightforwardly generalized to the full field content of the theory, i.e. f can be replaced by the fields ϕ^a, W^a_μ, etc. To solve differential equations numerically, one needs to discretize time and space. We use the same lattice for each field of the theory. The differential equations are then solved by computing the field values $f(t_n, x_n, y_n, z_n)$, where x_n, y_n, and z_n denote the spatial lattice points and t_n are the discrete time steps at which the fields are evaluated. For simplicity, we will present the numerical methods mostly in one spatial dimension.

To calculate spatial derivatives, one needs at least two lattice points for first-order derivatives and at least three lattice points for second-order derivatives. The simplest way to compute them on the lattice is

$$f'(x) = \frac{f(x+\mathrm{d}x) - f(x-\mathrm{d}x)}{2\mathrm{d}x}\,, \tag{A.1}$$

$$f''(x) = \frac{f(x+\mathrm{d}x) + f(x-\mathrm{d}x) - 2f(x)}{\mathrm{d}x^2}\,, \tag{A.2}$$

where we assume the central difference approximation of the derivatives. Besides this central version, there are also forward and backward derivatives, which for first-order derivatives are given by $f'(x) = (f(x+\mathrm{d}x) - f(x))/\mathrm{d}x$ and $f'(x) = (f(x) - f(x-\mathrm{d}x))/\mathrm{d}x$, respectively. However, we do not apply them on the spatial lattice in order to avoid a breaking of symmetries.

To improve the precision, one can include more lattice points in the calculation of spatial derivatives. The first- and second-order derivatives can be computed more accurately by

$$f'(x) = -\frac{1}{12}f(x+2\mathrm{d}x) + \frac{2}{3}f(x+\mathrm{d}x) - \frac{2}{3}f(x-\mathrm{d}x) + \frac{1}{12}f(x-2\mathrm{d}x)\,, \tag{A.3}$$

$$f''(x) = -\frac{1}{12}f(x+2\mathrm{d}x) + \frac{4}{3}f(x+\mathrm{d}x) - \frac{5}{2}f(x) + \frac{4}{3}f(x-\mathrm{d}x) - \frac{1}{12}f(x-2\mathrm{d}x)\,. \tag{A.4}$$

Including additional lattice points with appropriate coefficients can further improve the accuracy. Tables of the finite difference coefficients are provided in [246].

A.2 Numerical Calculation of Profile Functions

To calculate profile functions of solitons numerically, one can use different methods. The most well-known is probably the shooting method, which we describe in Subsection A.2.2. In this thesis, however, we mainly used the relaxation method, which is discussed in the following subsection.

A.2.1 Relaxation Method

For the relaxation method, one already needs an ansatz. Such an ansatz can be obtained by making an educated guess that takes into account specific properties of the solutions.

For example, for the profile function of the vortex, we already know its approximate shape. For $H_n(r)$ in equation (2.32), we know that it satisfies the boundary values $H_n(r \to 0) = 0$ and $H_n(r \to \infty) = 1$. Furthermore, the function approaches 1 exponentially fast.

These properties are all captured by the hyperbolic tangent function. Therefore, we can take $H_n(r) = \tanh(r)$ as an ansatz.

For the magnetic monopole profile functions, there exists an analytic solution in the BPS limit, given in equations (2.86) and (2.87). This can be used as an ansatz for the relaxation method for solutions beyond the BPS limit, that is, for values $m_h \neq 0$.

The relaxation method used in this work is the Gauss–Seidel method. The following discussion is based on [100, 183, 12]. Consider the profile equations written as

$$E[f] = \partial_x^2 f + S[f] = 0\,, \tag{A.5}$$

where f denotes the profile function and $S[f]$ collects all terms in the differential equation except for the second-order derivative term. The second-order derivative can be discretized as

$$\partial_x^2 f = -\frac{2}{\delta^2} f(x) + \frac{\Delta}{\delta^2}\,, \tag{A.6}$$

where $\Delta = f(x+\delta) + f(x-\delta)$. Inserting this expression into (A.5) gives

$$f = \frac{\Delta}{2} + \frac{\delta^2}{2} S[f] = \frac{\delta^2}{2} E[f] + f\,. \tag{A.7}$$

For f to be a solution of the differential equation $E[f] = 0$, equation (A.7) must be satisfied. However, the exact solution is not known. As discussed at the beginning of this subsection, we therefore require an educated guess as a starting point. In this context, $E[f]$ quantifies how well a given function f satisfies the profile equation. The correct solution can then be approached numerically by applying the following iteration:

$$f^{(n+1)} = \frac{\delta^2}{2} E[f^{(n)}] + f^{(n)}\,. \tag{A.8}$$

This procedure updates the function $f^{(n)}$ by adding a correction proportional to the error. The exact solution is obtained once $E[f^{(n)}] = 0$. Of course infinitely many iterations would be required to reach the exact solution, so a stopping criterion is needed. A convenient choice is the total energy. During the iteration, the energy should approach a constant value. Once it is sufficiently close to its converged value, the iteration can be terminated.

To determine the profile functions, we applied a small modification to improve the precision. In equation (A.8), we replaced δ^2 by δ^4, which leads to smaller but more precise iteration updates. We first performed several iteration steps at low resolution to obtain an approximate shape. For the final refinement, we then increased the spatial resolution up to $\delta \sim 0.05$.

A.2.2 Shooting Method

For the shooting method, a full ansatz is not required. One only needs to know the solution at one point and its behaviour at another point. Let us consider, as an example, a second-order differential equation for a function $f(x)$ of the form

$$\partial_x^2 f = S[f, f']\,. \tag{A.9}$$

If we start at one point $f_0 = f(x_0)$, we can use the forward derivative to iterate from one lattice point to the next via

$$f_{n+1} = f_n + \mathrm{d}x\, f_n'\,, \tag{A.10}$$
$$f_{n+1}' = f_n' + \mathrm{d}t\, S[f_n, f_n']\,. \tag{A.11}$$

This method is called Euler integration. Usually, one value f_0 together with its derivative f_0' is sufficient to determine the full solution. However, the reliability of the result depends on the accuracy of the iteration method. The Euler integration presented here has rather low precision, which means that the solution at points far away from x_0 cannot be trusted. To improve the accuracy, one can use more advanced iteration schemes. These follow the same implementation principles as the time integration methods described in Section A.4. To determine the Feshbach resonance frequencies shown in Figure 3.3, we used the shooting method with the modified Runge–Kutta iteration scheme described in Subsection A.4.4.

Now we come to the actual shooting procedure. The previous paragraph assumes that at a single point, both the function value f_0 and its derivative f_0' are known. However, this is not necessarily the case. Very often, only the function value f_0 is known, while the derivative is not. In such cases, one has to guess the derivative. In general, this initial guess will not yield the desired result. However, from the resulting solution, one can find whether the chosen derivative was too large or too small. Typically, the asymptotic behaviour of the function is known, and this information can be used to iteratively adjust the derivative until the correct asymptotic behaviour is obtained for a specific choice of the derivative.

Of course, tuning the parameters by hand is tedious and time-consuming. However, this procedure can be automated by writing an algorithm. The shooting method is particularly easy to apply in problems where only a single parameter needs to be adjusted. For this reason, we used it to determine the Feshbach resonance frequencies shown in Figures 3.3. For problems involving more parameters, the shooting method can still be applied, but its implementation becomes less straightforward, as the algorithm required to tune multiple parameters is more involved.

Finally, we want to note that the results obtained from the shooting method can be further improved by applying a relaxation procedure afterwards. This is especially useful for function values far away from the initial point f_0.

A.2.3 Eigenvalue Method

As a final method for finding profile functions, we discuss the eigenvalue method. This method is very powerful, as it requires only the boundary values. However, it can only be applied to linear differential equations, i.e. equations in which every term is linear in the function f.

For the implementation of this method, we followed [108, 62]. The main ideas are briefly summarized in this subsection. As in the referenced works, we apply this method to determine the profile functions and frequencies of bound modes of vortices. It was used to obtain the functions shown in Figure 3.1 and the frequencies presented in Figure 3.2. The differential equations we consider are of the form

$$Df + Af + Cg = \omega^2 f\,, \tag{A.12}$$

$$Dg + Bg + Cf = \omega^2 g\,, \tag{A.13}$$

where A, B, and C collect all non-derivative terms, which may also be space-dependent, D contains the derivative terms, and ω denotes the frequency of the mode. For the radial profile functions of vortices, D is given by

$$D = -\frac{\mathrm{d}^2}{\mathrm{d}r^2} - \frac{1}{r}\frac{\mathrm{d}}{\mathrm{d}r}\,. \tag{A.14}$$

The differential equation system can be written as a matrix equation by

$$\begin{pmatrix} D+A & C \\ C & D+B \end{pmatrix} \begin{pmatrix} f \\ g \end{pmatrix} = \omega^2 \begin{pmatrix} f \\ g \end{pmatrix}. \tag{A.15}$$

We now expand the two-dimensional matrix equation to a $2N$-dimensional system, where N denotes the number of lattice points. This is done by treating the lattice values $f_n = f(r_n)$ and $g_n = g(r_n)$ as components of the vectors $\boldsymbol{f}$ and $\boldsymbol{g}$. In this representation, A, B, and C become diagonal $N \times N$ matrices. The matrix D is obtained by discretizing the first- and second-order derivatives (A.1), (A.2):

$$\begin{aligned} (Df)_n &= -\left(\frac{1}{\mathrm{d}r^2} + \frac{1}{2\mathrm{d}r\, r_n}\right) f_{n+1} + \frac{2}{\mathrm{d}r^2} f_n + \left(-\frac{1}{\mathrm{d}r^2} + \frac{1}{2\mathrm{d}r\, r_n}\right) f_{n-1} \\ &= L_n^+ f_{n+1} + L_n^0 f_n + L_n^- f_{n-1}\,. \end{aligned} \tag{A.16}$$

This can be written as a matrix equation by

$$\boldsymbol{Df} = \begin{pmatrix} L_1^0 & L_1^+ & & \\ L_2^- & L_2^0 & L_2^+ & \\ & L_3^- & L_3^0 & L_3^+ \\ & & L_4^- & \ddots \end{pmatrix} \begin{pmatrix} f_1 \\ f_2 \\ f_3 \\ \vdots \end{pmatrix}. \tag{A.17}$$

Using this rewriting, the full system of differential equations can be expressed as a $2N \times 2N$ matrix equation, $\boldsymbol{Mv} = \omega^2 \boldsymbol{v}$. This is an eigenvalue problem, meaning that the eigenvalues of $\boldsymbol{M}$ correspond to ω^2. Numerically, we determine the eigenvalues and eigenfunctions of $\boldsymbol{M}$ using the linear algebra tools provided by the Python package *SciPy* [247].

In this section, we have applied the eigenvalue method to a coupled system of differential equations involving two functions. Of course, the method can be straightforwardly reduced to a single function or extended to systems with more than two functions. The implementation remains essentially the same.

A.3 Relaxation Method for Static Soliton Configurations

In Subsection A.2.1, we have already explained how the relaxation method can be used to obtain solutions for the profile functions. Of course, this method can also be applied to higher-dimensional problems. For example, we used it to find toroidal higher-charged magnetic monopole solutions in Section 3.7.2 or the confined monopole–anti-monopole configuration in Section 4.5.2. The following explanations were taken from [100, 183, 12].

The static field equations can again be written as

$$E[f] = \partial_i^2 f + S[f] = 0\,, \tag{A.18}$$

where the Laplacian $\partial_i^2 f$ can be discretized by

$$\partial_i^2 f = -\frac{6}{\delta^2} f(x,y,z) + \frac{\Delta}{\delta^2}\,, \tag{A.19}$$

with

$$\begin{aligned} \Delta =& f(x+\delta,y,z) + f(x-\delta,y,z) + f(x,y+\delta,z) && \text{(A.20)}\\ &+ f(x,y-\delta,z) + f(x,y,z+\delta) + f(x,y,z-\delta)\,. && \text{(A.21)} \end{aligned}$$

Following the same idea as in Subsection A.2.1 gives the iteration rule

$$f^{(n+1)} = \frac{\delta^2}{6} E[f^{(n)}] + f^{(n)}\,. \tag{A.22}$$

In some cases, we applied this method to non-static or unstable configurations. In such situations, a modification of the relaxation procedure is required. For example, when constructing a static ansatz for a confined monopole–anti-monopole pair, one needs to enforce that the monopoles remain at fixed positions. The relaxation method typically minimizes the total energy. However, since the energy of a monopole–anti-monopole configuration decreases as the distance between them becomes smaller, the relaxation would not converge. Instead, the monopoles would approach each other, eventually overlap, and annihilate.

To fix the positions, we can constrain the scalar field structure $\hat{\phi}^a$. With this choice, the relaxation is applied only to $|\phi| = \sqrt{\phi^a\phi^a}$. This can be implemented by inserting $\phi^a = |\phi|\hat{\phi}^a$ into the scalar field equations and deriving the corresponding static equation for the profile $|\phi|$. By keeping $\hat{\phi}^a$, $\partial_i\hat{\phi}^a$, and $\partial_i^2\hat{\phi}^a$ fixed throughout the iteration procedure, the scalar field profile is relaxed while its orientation remains unchanged. For all other field components, the standard relaxation equations can be used.

Fixing the scalar field orientation forces the monopole zeros to remain at their initial positions. Of course, this method does not give the exact solution, since in general there can be a back-reaction on the scalar field orientation, which is not captured in this approach. However, for all applications considered in this thesis, the method was very precise. This can be cross-checked by inserting the obtained result into a numerical simulation.

A.4 Time Iteration Methods

In this section, we briefly present the methods that we used for the simulations in this thesis. For any simulation, the starting point is always the initial configuration. These initial configurations have to be chosen very carefully, as they set the foundation of the entire simulation. Since everything builds on the initial configuration, the time iteration must be sufficiently precise in order to reliably describe also the late-time evolution. This requires appropriate choices for the time integration methods. We discuss our choices in this section. For more detailed information, we refer to [243, 245].

A.4.1 Euler Integration

The simplest time integration method is the Euler integration. It is based on the forward derivative

$$\dot{f}_n = \frac{f_{n+1} - f_n}{\mathrm{d}t}\,, \tag{A.23}$$

$$\ddot{f}_n = \frac{\dot{f}_{n+1} - \dot{f}_n}{\mathrm{d}t}\,. \tag{A.24}$$

Using these definitions one can solve differential equations of the form

$$\partial_t^2 f = S[f, \dot{f}]\,, \tag{A.25}$$

by the iteration procedure

$$f_{n+1} = f_n + \mathrm{d}t\, \dot{f}_n\,, \tag{A.26}$$

$$\dot{f}_{n+1} = \dot{f}_n + \mathrm{d}t\, S[f_n, \dot{f}_n]\,. \tag{A.27}$$

This method works for simple simulations, such as the erasure of a static magnetic monopole by a slowly moving domain wall. However, for more relativistic velocities, the method breaks down. In general, its precision is rather low, and it is therefore not recommended for accurate measurements. Nevertheless, it provides the basis for the integration methods that we will present in the following three sections.

A.4.2 Crank–Nicolson Method

For all magnetic monopole simulations, we employed the Crank–Nicolson method with two iterations. The main reason for this choice is that it has already been shown in [99, 165] to work well in magnetic monopole simulations. Of course, it is possible that other methods, such as the Runge–Kutta method, which we briefly describe in Subsection A.4.4, could provide better results. This remains to be investigated in future work.

The following description of the Crank–Nicolson method is taken from [248, 12]. The field equations for which we used this method have the form

$$\partial_t^2 f = S[f, \dot{f}]\,. \tag{A.28}$$

We can split this second-order differential equation into two first-order differential equations by treating $\dot{f}$ as a separate field,

$$\partial_t \dot{f} = S[f, \dot{f}]\,, \tag{A.29}$$

$$\partial_t f = \dot{f}\,. \tag{A.30}$$

The initial iteration step of every time step is given by

$$\tilde{\dot{f}}^{(1)} = \mathrm{d}t\, S[f_0, \dot{f}_0] + \dot{f}_0\,, \tag{A.31}$$

$$\tilde{f}^{(1)} = \mathrm{d}t\, \dot{f}_0 + f_0\,, \tag{A.32}$$

with f_0 being the initial field. Before the next iteration is applied, one takes the average of f_0 and $\tilde{f}_0$,

$$\bar{\dot{f}}^{(1)} = \frac{\tilde{\dot{f}}^{(1)} + \dot{f}_0}{2}\,, \qquad \bar{f}^{(1)} = \frac{\tilde{f}^{(1)} + f_0}{2}\,. \tag{A.33}$$

The next iteration steps (still within the same time step) are given by

$$\tilde{\dot{f}}^{(n)} = \mathrm{d}t\, S[\bar{f}^{(n-1)}, \bar{\dot{f}}^{(n-1)}] + \dot{f}_0\,, \tag{A.34}$$

$$\tilde{f}^{(n)} = \mathrm{d}t\, \bar{\dot{f}}^{(n-1)} + f_0\,, \tag{A.35}$$

$$\bar{\dot{f}}^{(n)} = \frac{\tilde{\dot{f}}^{(n)} + \dot{f}_0}{2}\,, \qquad \bar{f}^{(n)} = \frac{\tilde{f}^{(n)} + f_0}{2}\,. \tag{A.36}$$

The step that closes the iteration is finally

$$\dot{f}_1 = \mathrm{d}t\, S[\bar{f}^{(n)}, \bar{\dot{f}}^{(n)}] + \dot{f}_0\,, \tag{A.37}$$

$$f_1 = \mathrm{d}t \bar{\dot{f}}^{(n)} + f_0\,. \tag{A.38}$$

At each time step, this full iteration procedure is applied. We used two iteration steps, meaning that we have the initial and the final step, along with one additional intermediate iteration. In [248], it was argued that more than two iterations do not further improve the accuracy of the simulation significantly.

We found that the Crank–Nicolson method is particularly precise for Lorentz-boosted magnetic monopole configurations. However, it also comes with some disadvantages. One is that, for two iterations, it requires computing the field equations three times, which slows down the computational speed by a factor of around three compared to the Euler method. Nevertheless, this is a reasonable price to pay for the improved precision of the simulations. Another disadvantage is that the Crank–Nicolson method does not conserve energy very well over long time scales. For the relatively short time intervals considered in the monopole simulations, the energy conservation was sufficient. However, for scenarios that require longer evolution times, such as the analysis of oscillons [249, 250], we found that the rather poor energy conservation leads to an artificially fast decay of the oscillons. For such setups, methods like leapfrog and Runge–Kutta, which we describe in the following, are more suitable choices.

A.4.3 Leapfrog Method

In this section, we describe the leapfrog integration method following the description given in [243]. First of all, this method can only be applied to field equations of the form

$$\partial_t^2 f = S[f]\,, \tag{A.39}$$

i.e. without $\dot{f}$-dependence in the equations of motion. The iteration scheme works as follows

$$\dot{f}_{n+1/2} = \dot{f}_{n-1/2} + \mathrm{d}t\, S[f_n]\,, \tag{A.40}$$

$$f_{n+1} = f_n + \mathrm{d}t\, \dot{f}_{n+1/2}\,. \tag{A.41}$$

This iteration means that the time derivative is never evaluated at the same time as the field values themselves, but rather at the midpoint times. Compared to the Euler integration, which has an accuracy of $\mathcal{O}(\mathrm{d}t)$, the accuracy here improves to $\mathcal{O}(\mathrm{d}t^2)$ [243].

This leapfrog iteration can be modified to the so-called *synchronized leapfrog*, also referred to as *Verlet integration*. This is the method we used to obtain the results in Figure 3.6. The idea is to eliminate the midpoints in the time derivative by averaging:

$$\dot{f}_{n+1} = \frac{1}{2}\left(\dot{f}_{n+1/2} + \dot{f}_{n+3/2}\right). \tag{A.42}$$

Then, to obtain the value f_{n+1}, one computes $\dot{f}_{n+1/2}$ not from $\dot{f}_{n-1/2}$, but instead from $\dot{f}_n$:

$$\dot{f}_{n+1/2} = \dot{f}_{n-1/2} + \mathrm{d}t\, S[f_n] = \dot{f}_n + \frac{1}{2}\mathrm{d}t\, S[f_n]\,. \tag{A.43}$$

The resulting iteration scheme is

$$f_{n+1} = f_n + \mathrm{d}t\, \dot{f}_n + \frac{1}{2}\mathrm{d}t^2\, S[f_n]\,, \tag{A.44}$$

$$\dot{f}_{n+1} = \dot{f}_n + \frac{1}{2}\mathrm{d}t\, \left(S[f_n] + S[f_{n+1}]\right). \tag{A.45}$$

A.4.4 Runge–Kutta Method

The last method we will discuss has a similar accuracy to the leapfrog algorithm but with the advantage that it can be applied to field equations of the form

$$\partial_t^2 f = S[f, \dot{f}]\,, \tag{A.46}$$

which means that the equations of motion may also depend on the first time derivative of the field f. In this section we follow the explanations of [243, 245]. The method described in the following is of second order, which implies that one has to perform two steps (i.e. evaluate $S[f, \dot{f}]$ twice) for obtaining a single time iteration. First, one computes intermediate values for the fields using the standard Euler integration

$$\bar{f} = f_n + \mathrm{d}t\, \dot{f}_n \,, \tag{A.47}$$

$$\bar{\dot{f}} = \dot{f}_n + \mathrm{d}t\, S[f_n, \dot{f}_n] \,. \tag{A.48}$$

The $n+1$ values can then be obtained by

$$f_{n+1} = f_n + \mathrm{d}t\, \dot{f}_n + \frac{1}{2}\mathrm{d}t^2\, S[f_n, \dot{f}_n] \,, \tag{A.49}$$

$$\dot{f}_{n+1} = \dot{f}_n + \frac{1}{2}\mathrm{d}t \left(S[f_n, \dot{f}_n] + S[\bar{f}, \bar{\dot{f}}] \right) . \tag{A.50}$$

The term *Runge–Kutta method* should be understood as a full class of numerical time integration methods. There are several different ways in which this procedure can be implemented. The scheme described above corresponds to the so-called *midpoint method*. For other implementations, the interested reader is referred to [245]. Furthermore, the method is of second order, i.e. one needs to evaluate $S[f, \dot{f}]$ twice, which is why it is commonly referred to as RK2. The accuracy can be increased by introducing additional intermediate steps. For instance, the fourth-order RK4 method requires evaluating $S[f, \dot{f}]$ four times and improves the accuracy to $\mathcal{O}(\mathrm{d}t^4)$ [243, 245].

In this thesis we used a slight modification of the RK2 method, which can be seen as a combination of the RK2 and the synchronized leapfrog algorithms. In the last step of the RK2 midpoint method we replace $S[\bar{f}, \bar{\dot{f}}]$ by $S[f_{n+1}, \bar{\dot{f}}]$. In the cases we analysed, this was found to slightly improve the precision.

It turns out that the Runge–Kutta method performs very well in conserving the energy. Therefore, it is a perfect choice for simulations over large time intervals. This includes, for instance, simulations of oscillons [249, 250], as well as simulations of excited solitons [83, 85, 86]. We made use of the above mentioned modified version of the RK2 method in the vortex simulations presented in Sections 3.3 and 3.6.

A.5 Boundary Conditions

An important aspect of numerical simulations is how the fields are treated at the boundary. Of course, one can choose sufficiently large lattices such that boundary effects do not play a role within the investigated time interval, and indeed this is the standard approach in simulations in one spatial dimension. In more than one dimension, however, computational resources typically do not allow for such large lattices, and therefore appropriate boundary conditions are required. There is no general perfect choice of boundary conditions, since every system is different and comes with its own constraints at the boundary. In this section, we briefly describe all boundary conditions used in the simulations of this thesis.

For simplicity, we restrict the discussion to one spatial dimension. However, all methods can be straightforwardly generalized to higher dimensions.

A.5.1 Dirichlet Boundaries

The boundaries that are easiest to implement are Dirichlet boundaries. They correspond to fixed boundaries, where the field values at the boundary lattice points are not updated during the time evolution. In other words, the boundary values are entirely determined by the initial conditions. Clearly, for describing dynamical situations, this is in general not an ideal choice, since the field values are time-dependent. However, Dirichlet boundaries can still work very well if most of the dynamics takes place sufficiently far away from them. We used them, for example, in the simulations of magnetic monopole collisions in Section 3.7.

Several issues can arise in the vicinity of Dirichlet boundaries. For instance, energetic radiation or localized objects such as solitons are typically reflected at the boundary. While the total energy of the system is conserved, the overall momentum can change. Moreover, particularly in simulations involving topological defects, the motion of these objects can be affected by the fact that the scalar field orientation is fixed at the boundary. For example, from the scalar field orientation at infinity, one can reconstruct the position of a vortex zero. However, when a vortex moves, its zero also moves accordingly, whereas the boundary information remains unchanged due to the fixed condition. As a result, the boundary becomes incompatible with the field configuration in the interior of the lattice. Nevertheless, Dirichlet boundaries remain a useful choice for sufficiently large lattices, where such boundary effects are rather small.

A.5.2 Periodic Boundaries

Another type of boundary that we used multiple times, when we wanted to avoid reflections or modifications of the motion, are periodic boundaries. The idea is that the space is smoothly connected everywhere, meaning that a lattice point on one side of the lattice is identified with a corresponding point on the opposite side. For N lattice points, the boundary condition can be implemented by $\phi(x_N) = \phi(x_1)$.[1] As a consequence, when a wave or a classical solution such as a soliton approaches the boundary, there is no back-reaction. Instead, it passes through the boundary and reappears on the opposite side of the lattice. These boundaries are particularly useful for simulations in which topological defects, such as cosmic strings, are created dynamically, as in Section 4.5.

Furthermore, in the simulations of the slingshot effect in Chapter 5, we utilized these boundaries for the ψ field along the directions parallel to the wall (i.e. in the x- and y-directions). In this context, periodic boundaries are especially useful, since the domain wall hits the boundary.

Nevertheless, periodic boundaries also have disadvantages, particularly in the case of domain walls, as observed in the slingshot simulations. The total mass of the wall depends on the lattice size. If the lattice is too small, one can observe a significant back-reaction on the domain wall when a monopole collides with it at high velocities. The momentum transfer can be large enough to push back the entire domain wall. Even if some push back is expected physically, with periodic boundaries this effect becomes dependent on the

---

[1] Note that, in some cases, periodic boundaries require an additional sign shift.

lattice size, which makes it unphysical. However, for sufficiently large lattices, this artifact becomes negligible and the resulting dynamics are more reliable.

A.5.3 Time-dependent Boundaries

Periodic boundaries were the ideal choice for the ψ domain wall in the slingshot simulations. In contrast, in the simulations of the erasure of magnetic monopoles through a domain wall (Section 4.4), we could not use periodic boundaries. The reason is that the domain wall is described by the same scalar field ϕ^a as the magnetic monopole. Periodic boundaries require the total winding number of the system to vanish, which prevents the implementation of a single magnetic monopole on a lattice with periodic boundaries.

For the erasure simulations, we instead employed time-dependent boundaries. The initial boosted configuration already requires a time-dependent ansatz, which can be used to approximately predict the position of the domain wall at later times. This allows us to adapt the boundary values at each time step using this ansatz. For a setup involving a single domain wall, this is an excellent choice. However, once interactions with other objects become relevant, this approach is no longer exact. Nevertheless, for sufficiently large lattices, the error sourced by the boundary remains negligible. Therefore, for the erasure simulations, this method was a very good option.

Note that these time-dependent boundaries behave similarly to Dirichlet boundaries, in the sense that they reflect energetic waves.

A.5.4 Absorbing Boundaries

Absorbing boundaries describe boundaries where energetic waves are, as the name says, absorbed by the boundary. This implies that radiation is not reflected back at it. Such boundaries are especially useful when one aims to avoid a back-reaction on the dynamics in the interior of the lattice. However, it should also be mentioned that absorbing boundaries are never perfect. There is always a small fraction of radiation that may be reflected. The goal is therefore to minimize this reflected contribution as much as possible. Within this thesis, we used two types of absorbing boundaries, the Sommerfeld radiation condition, and a method that combines natural boundaries with an adiabatic damping.

Sommerfeld Radiation Condition

For the Sommerfeld radiation condition, we rewrite all field equations in the form of a Klein–Gordon equation, $(\partial_x^2 + m^2)\phi(x,t) = 0$, where m denotes the effective mass of the field. Solutions to this equation are given by

$$\phi(x,t) = A\, e^{i(\omega t - kx)} + B\, e^{i(\omega t + kx)}\,, \tag{A.51}$$

where the first term describes waves propagating to the right, while the second term corresponds to waves propagating to the left. At the boundary, we require that waves can leave the lattice but do not enter it. Therefore, at the right boundary, right-moving waves are allowed, whereas left-moving ones are excluded. This corresponds to considering only solutions with $A \neq 0$ and $B = 0$. This condition leads to the relation

$$\dot{\phi} = -\frac{\omega}{k}\phi' \,. \tag{A.52}$$

This can be implemented in the time iteration through the boundary condition

$$\phi(t + \Delta t) = \phi(t) - \Delta t \, \frac{\omega}{k} \, \phi'(t) \,, \tag{A.53}$$

where for $\phi'(t)$ one can use the backward derivative.

The remaining question is how to choose ω/k. For massless fields, this is rather straightforward, since the dispersion relation is simply $\omega = k$. For massive fields with effective mass m, the situation is less clear. In that case, the dispersion relation reads $\omega^2 = k^2 + m^2$, and therefore $\omega/k = \sqrt{1 + m^2/k^2}$. The ratio thus obtains a dependence on k. However, this means that the condition is only valid for one specific k. Hence, for massive fields, the Sommerfeld radiation condition cannot absorb all waves equally well. In our simulations, we assumed that the wavelength is of order m_v^{-1} and therefore took $k \sim m_v$. By trial and error, we then tuned k to a value that yields reasonable absorption at the boundary.

We applied this boundary condition to the simulations with confined magnetic monopoles. This includes the simulations in Section 4.5 as well as those in Chapter 5.

Natural Boundaries with Adiabatic Damping

The second method we used consists of natural boundaries in combination with an adiabatic damping region. It turns out that this approach is very effective, in the sense that, if implemented correctly, it absorbs almost all energetic radiation regardless of the frequency. Moreover, in contrast to the Sommerfeld radiation condition, it is perfectly compatible with the initial conditions, i.e. during the initial stage of the simulation no artificial radiation is emitted from the boundaries, which is typically observed for Sommerfeld conditions applied to massive waves. However, the price to pay for this absorption method is that it requires a rather large lattice. Therefore, we used it only in two-dimensional problems, such as the vortex simulations in Sections 3.3 and 3.6.

A detailed explanation of natural boundaries can be found in [83, 251]. The idea is to consider the energy functional $E[f^a, \partial_i f^a]$, where f^a denotes the full field content of the theory. Due to energy conservation, its variation should vanish:

$$\begin{aligned} 0 = \delta E &= \int_V \mathrm{d}^3x \left(\frac{\partial E}{\partial f^a} \delta f^a + \frac{\partial E}{\partial(\partial_\mu f^a)} \delta(\partial_\mu f^a) \right) \\ &= \int_V \mathrm{d}^3x \left(\frac{\partial E}{\partial f^a} - \partial_\mu \left(\frac{\partial E}{\partial(\partial_\mu f^a)} \right) \right) \delta f^a + \int_{\partial V} \mathrm{d}S \left(n_i \frac{\partial E}{\partial(\partial_i f^a)} \right) \,, \end{aligned} \tag{A.54}$$

where, in the second line, we integrated by parts and imposed the constraint $\partial_t \left(\partial E / \partial_t f^a \right) = 0$. The first term in the second line vanishes due to the Euler–Lagrange equations. The second term is a boundary contribution, which we also require to vanish. This leads to the boundary conditions

$$n_i \frac{\partial E}{\partial(\partial_i f^a)} = 0 \,. \tag{A.55}$$

Applying this boundary condition to vortices resolves a problem that arises for Dirichlet boundaries. As discussed, for a single vortex the position of the vortex zero can be reconstructed from the field orientation at infinity. In the Dirichlet case, this property breaks down once the vortex moves, since the field orientation at the boundary is fixed. With the natural boundary conditions introduced above, this issue does not appear, because the field orientation at the boundary adjusts dynamically.

An advantage compared to the Sommerfeld radiation condition is that this boundary condition does not generate radiation at the initial stage. The boundaries are fully consistent with the field configuration, and therefore no artificial radiation is emitted from the boundaries at the initial time step.

Using the above condition does not prevent radiation from being reflected at the boundary. For this reason, an additional adiabatic damping can be applied. In this thesis, we used this damping method only in combination with natural boundaries. However, it can also be applied to all other boundary conditions discussed previously. An adiabatic damping can be implemented by modifying the field equations in a region close to the boundary. The idea is to add a term proportional to the time derivative of the field to the equations of motion, in the form [252]

$$\Theta(r - r_{\text{min}})\, \alpha\, (\partial_t f^a)\, e^{-\beta(r - r_{\text{min}})^2} \,, \tag{A.56}$$

where Θ denotes the Heaviside step function, α controls the strength of the damping, and r_{min} sets the radius beyond which the damping is applied. The parameter β determines how rapidly the damping increases with increasing radius r. The Gaussian profile is chosen to ensure that the damping does not become too strong too quickly, since a strong damping term effectively behaves like a Dirichlet boundary. The appropriate choice of parameters must be determined by trial and error.

For the vortex simulations in Sections 3.3 and 3.6, we chose the minimal radius as $r_{\text{min}} = 25$ for simulations with a 60^3 lattice, and $r_{\text{min}} = 35$ for those with an 80^3 lattice. For the damping parameters, we used $\alpha = 0.1$ and $\beta = 0.0035$.

A.6 Axial Symmetry

One major disadvantage of numerical calculations is that their precision is often limited by available computational resources. Therefore, techniques such as taking advantage of symmetries can be used to improve computational efficiency. In this thesis, we make use of such a technique for certain magnetic monopole configurations. Many of the head-on collision scenarios considered in this thesis possess an axial symmetry, which allows us to

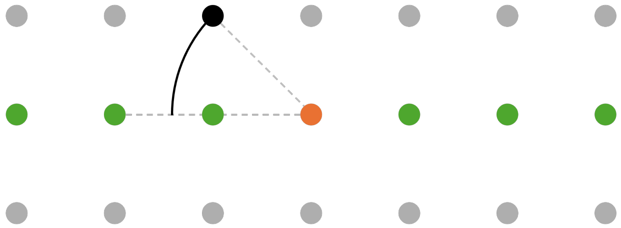

Figure A.1: This figure illustrates schematically why interpolation is required to calculate the field values at the lattice points of neighbouring planes using the axial symmetry. The lattice points of the central plane are shown in green, while those of the neighbouring planes are shown in grey. The orange point corresponds to a point on the axial symmetry axis.

solve the field equations on a single two-dimensional plane rather than in the full three-dimensional space. This approach was suggested in [253].

Before presenting the axial symmetry of magnetic monopole systems, let us briefly explain how the method works. The equations of motion contain second-order derivatives. To evaluate them, one needs at least three lattice points in each direction. This implies that, if we wish to compute the field equations solely in the x-z-plane, we still require at least three lattice points in the y-direction. In other words, we need the values on the two neighbouring planes with $y = \pm\Delta x$. These values can be obtained using the axial symmetry. Accordingly, the simulation proceeds as follows. First, the field equations are computed on the central plane using a chosen time integration method, for example one of the methods described in Section A.4. In a second step, axial symmetry is used to determine the values on the neighbouring planes. This then enables the computation of the field equations on the central plane in the subsequent time iteration step.

One subtlety should be mentioned here. We use the simplest implementation of a lattice, where each cell is cubic. As illustrated in Figure A.1, applying axial symmetry on a cubic lattice to determine the values at a lattice point on a neighbouring plane requires the field value at a point that lies between two lattice points of the central plane. To obtain this value, an interpolation method is needed. In our cases, we used Lagrange interpolation, as suggested in [253].

The axial symmetry method was first applied to magnetic monopole systems in [102], where an axial symmetry was identified for a system consisting of a single magnetic monopole and a domain wall. In [20], we extended the axial symmetry equations to configurations involving monopole–anti-monopole pairs. The scalar field ansatz for the monopole–anti-monopole configuration with maximal twist is given in equation (3.23). From this, we can read off the axial symmetry of the scalar field.

$$\begin{aligned}\phi^1 &= x f_1 + y f_2\,,\\ \phi^2 &= y f_1 - x f_2\,,\\ \phi^3 &= f_3\,,\end{aligned} \tag{A.57}$$

with f_i being functions that depend only on the axial radius, the z-coordinate, and time t. The ansatz for the gauge fields can be obtained by inserting the scalar field ansatz (A.57) into the condition $D_\mu\phi = 0$, which yields

$$\begin{aligned}
W_x^1 &= xyf_4 + y^2 f_5 + f_6\,, & W_y^1 &= y^2 f_4 - xyf_5 - f_7\,,\\
W_x^2 &= -x^2 f_4 - xyf_5 + f_7\,, & W_y^2 &= -xyf_4 + x^2 f_5 + f_6\,,\\
W_x^3 &= xf_8 + yf_9\,, & W_y^3 &= yf_8 - xf_9\,,\\[1ex]
W_z^1 &= xf_{10} + yf_{11}\,, & W_t^1 &= xf_{12} + yf_{13}\,,\\
W_z^2 &= -xf_{11} + yf_{10}\,, & W_t^2 &= -xf_{13} + yf_{12}\,,\\
W_z^3 &= 0\,, & W_t^3 &= 0\,. \qquad \text{(A.58)}
\end{aligned}$$

For the cases in which we consider magnetic monopole–anti-monopole pairs confined by a cosmic string, an additional field, described by ψ, is required. From equation (4.41), we obtain the following ansatz for ψ

$$\begin{aligned}
\psi^1 &= (x - iy)f_{14} + (y + ix)f_{15}\,,\\
\psi^2 &= f_{16}\,. \qquad \text{(A.59)}
\end{aligned}$$

The axial symmetry method is a useful way to significantly increase the computation speed in three-dimensional simulations. Instead of evaluating the equations of motion on N^3 lattice points, it is enough to compute them on only N^2 lattice points. Of course, some additional computation time is required to determine the values on the neighbouring planes of the central plane using the axial symmetry. However, the computational cost is small compared to the time that is saved.

A.7 Gauge Choices

For all simulations we performed, we chose either the time gauge, $W_t^a = 0$, or the Lorenz gauge, $\partial_\mu W_a^\mu = 0$. Both conditions require a careful treatment in the numerical calculations, which we briefly explain in this section. For this purpose, let us focus on the $SU(2)$ gauge theory described by the Lagrangian (2.56). However, the discussion can be applied to all gauge theories.

First of all, the choice of gauge often depends on the initial conditions. As an example, consider a single static magnetic monopole. The 't Hooft–Polyakov ansatz (2.67) satisfies both the time gauge and the Lorenz gauge conditions. Therefore, both gauges can be applied straightforwardly. Now let us instead consider a Lorentz-boosted magnetic monopole. Since the Lorenz gauge is Lorentz-invariant, it remains satisfied. The time gauge, however, is no longer fulfilled, because the Lorentz transformation generates a non-vanishing W_t^a component. In principle, one can use a gauge transformation to set this component back to zero, but this is rather non-trivial. For this reason, for boosted configurations the Lorenz gauge condition is the more convenient choice.

Let us first discuss how one implements the time gauge. Inserting $W_t^a = 0$ into the equations of motion yields three gauge field equations that are second-order in time, corresponding to the $\nu = i$ components of equation (2.64). The $\nu = 0$ component of equation (2.64), on the other hand, reduces to a first-order differential equation in time. This is the so-called Gauss constraint. If the initial conditions satisfy the Gauss constraint, it will remain satisfied at all times. For more details on this so-called Cauchy problem, we refer to [28]. However, one should keep in mind that in numerical simulations the Gauss constraint can be violated due to small numerical inaccuracies. Therefore, one has to ensure that it is satisfied at all times. Here we follow the approach of [184]. The Gauss constraint can be written as

$$\partial_t \partial_i W_i^a + g\varepsilon_{abc} W_i^b \partial_t W_i^c + g\varepsilon_{abc}\phi^b \partial_t \phi^c = 0\,. \tag{A.60}$$

We now implement the Gauss constraint into the simulation by treating $\partial_i W_i^a$ as an independent field Γ^a and enforcing the constraint by

$$\partial_t \Gamma^a = \partial_t \partial_i W_i^a - \eta\left(\partial_t \partial_i W_i^a + g\varepsilon_{abc} W_i^b \partial_t W_i^c + g\varepsilon_{abc}\phi^b \partial_t \phi^c\right)\,, \tag{A.61}$$

where η is a numerical parameter. In all equations of motion, we now replace $\partial_i W_i^a$ by Γ^a. Equation (A.61) then provides a way to correct $\partial_i W_i^a$ by adding a term proportional to the violation of the Gauss constraint. The numerical parameter η has to be chosen by trial and error.

The Lorenz gauge is easier to implement. Inserting the condition $\partial_\mu W_a^\mu = 0$ into the equations of motion does not directly reduce them to three second-order equations plus one Gauss constraint. To recover the Gauss constraint, one would need to replace $\partial_t W_t^a$ by $\partial_i W_i^a$ in the equations of motion for W_t^a. However, this is not the approach we take. Instead, we keep all four gauge field equations, which are second-order in time, and evolve all four components W_μ^a accordingly. To ensure that the Lorenz gauge is satisfied initially, we impose $\partial_t W_t^a = \partial_i W_i^a$ as an initial condition.

A.8 Measurements

By measuring physical quantities such as the energy density of the system, one can gain good intuition about the outcome of a given setup. In many cases in this thesis, we used simulations primarily to obtain qualitative results. However, in some cases we also performed more precise measurements of non-trivial quantities beyond the energy density. These include the positions of the zeros of topological defects, the mode frequencies, and the gravitational spectrum of confined magnetic monopoles. These three measurements will be briefly discussed in this section.

A.8.1 Soliton Zero Position Measurement

To determine the positions of solitons, one can follow different approaches. The most precise, but also more involved, method is the following. For simplicity, we consider a vortex as an example. The vortex is described by the scalar field components $\mathrm{Re}(\phi)$ and $\mathrm{Im}(\phi)$. The zeros are given by the points where both components vanish. These can be found by first determining the contour lines defined by $\mathrm{Re}(\phi) = 0$ and $\mathrm{Im}(\phi) = 0$, and then identifying their intersection points. In general, however, this procedure is not always straightforward to implement for numerical data. In cases where the solitons move along the coordinate axes, the method becomes much simpler. One can then choose the phase such that one of the two contour lines coincides with a coordinate axis. The problem reduces to finding the intersection of the remaining contour with this axis, which is typically easy to determine. We used this approach, for example, for the vortex position measurements in Section 3.3 and for the zero-position measurement of magnetic monopoles shown in Figure 3.38.

For the discussion of the zero behaviour in the non-planar tetrahedral scattering of three monopoles in Section 3.7.6, we did not determine the exact positions. Instead, we plotted the $\phi^1 = 0$, $\phi^2 = 0$, and $\phi^3 = 0$ contour surfaces using Mathematica and interpreted the results qualitatively by analysing the intersections of these three surfaces, which correspond to the zeros of the field.

In Section 3.6, we determined the vortex centres by computing the winding number for each grid cell of the lattice. This is done by evaluating the complex phase of ϕ at each lattice point and summing the phase differences around the four points that form a given grid cell. If the result is approximately $2\pi n$, the cell contains an n-vortex. Numerically, some careful treatment is required along lines where the phase jumps from 0 to 2π. Keeping this in mind, we wrote an efficient program based on this method to track the positions of the vortices.

A.8.2 Mode Frequency Measurement

In the vortex simulations of Sections 3.3 and 3.6, internal modes of the vortices were excited. These modes carry characteristic frequencies, which can be measured. They transfer energy between different energy components, such as potential and kinetic energy. While the total energy is conserved, individual contributions like the potential energy are not and therefore fluctuate. These fluctuations can be used to extract the mode frequencies.

There are two main approaches to do this. First, one can perform a Fourier analysis of the data to identify frequency peaks. However, this method only works reliably if the available time interval is sufficiently large. In the cases we analysed, such large intervals were not available, since the vortices move and reach the boundaries of the lattice too quickly.

The second approach is to determine the frequency directly by measuring the time difference between peaks of a given energy component. In our case, we always used the potential energy for measuring the frequency. The advantage of this method is that it allows to track the time dependence of the frequency. Since in Section 3.6 we were particularly interested in how the frequency depends on the arrangement of multiple vortices, this method was especially useful.

The measured results typically contain numerical noise. To reduce this noise, we applied a Gaussian filter to the data. This smooths the frequency curves and leads to cleaner results. The outcomes of the frequency measurements in multi-vortex collisions are shown as light-gray curves in Figures 3.24, 3.28, and 3.29.

A.8.3 Gravitational Radiation Spectrum

The basis for the gravitational radiation measurement in Sections 4.5.3 and 5.4 is given by the Weinberg formula in equation (5.18). In this section, we briefly discuss some details of the computation that are not included in the main text.

To calculate the spectrum, one requires the Fourier-transformed energy-momentum tensor. An important point is that our simulations were performed using the axial symmetry method described in Section A.6. Therefore, before applying the full three-dimensional spatial Fourier transform, one first has to reconstruct the complete three-dimensional energy-momentum tensor from the axially-symmetric data. This can be done straightforwardly by making use of the symmetry. We then perform the Fourier transform first in space and subsequently in time. The Fourier-transformed energy-momentum tensor can then be inserted into equation (5.18).

To obtain the radiated power as a function of the direction $\hat{\boldsymbol{k}}$ and the frequency ω, one has to ensure that the dispersion relation $\omega^2 = \boldsymbol{k}^2$ is satisfied. To this end, we first reduce the dimensionality by setting $k_y = 0$, which is justified by the axial symmetry. We then compute the gravitational energy per solid angle per frequency on a Fourier lattice spanned by ω, k_x, and k_z. Using the dispersion relation, this three-dimensional lattice can be reduced to a two-dimensional one. For this we use an interpolation method (NumPy `interp()` function) to express the gravitational energy in terms of k_x and k_z. Subsequently, we rewrite k_x and k_z in polar coordinates ω and θ by applying a second interpolation (SciPy `interpolate.interpn()` function). Here, θ corresponds to the direction of the emitted radiation.

A.9 Creating Defects Dynamically

Within this thesis we sometimes created topological defects dynamically. This method was used, for example, in Figures 4.10 and 4.12. Let us briefly describe how this can be achieved in numerical simulations. The key idea lies in the choice of the initial configuration. Let us consider, for instance, a quartic potential of an $SU(2)$-adjoint scalar field with the form $V(\phi) \sim (\phi^a\phi^a - v^2)^2$. As discussed several times, this potential has minima on a two-sphere defined by $\phi^a\phi^a = v^2$, while at $\phi^a = 0$ it has a local maximum.

To create defects dynamically, we start by setting the scalar field to zero everywhere. We then choose as an initial condition small random fluctuations around zero. Since the system tends to evolve towards the minima of the potential, the scalar field will naturally acquire a non-zero vacuum expectation value during the time evolution. This, in turn, leads to the formation of magnetic monopoles.

The available energy is given by $\mathrm{Vol} \cdot V(\phi^a = 0)$, and only a small fraction of it is converted into the energy required to create the magnetic monopoles. The remaining energy is stored in thermal fluctuations and radiation. To remove this extra energy, one can introduce an artificial friction term in the field equations of the form $\alpha(\partial_t\phi^a)$ (and similarly for the gauge field). This damps the fluctuations, such that only slowly moving magnetic monopoles remain.

To create magnetic monopoles connected by cosmic strings, one follows the same procedure also for the additional fields that are required to form the strings.

A.10 Numerical Checks

To ensure that the numerical simulations provide reliable results, one always has to perform checks. Even if not explicitly mentioned in the main text, we carried out such checks for all simulations.

When writing simulation codes, small typos can easily occur. Therefore, the implementation of the equations of motion should first be tested in scenarios that are fully understood. For example, before analysing non-trivial collisions of topological defects, such as magnetic monopoles with domain walls, one can consider a single static monopole and insert it into the simulation. Apart from very small numerical fluctuations, the configuration should remain unchanged. As a next step, one can implement a Lorentz-boosted monopole, which should propagate with constant velocity without emitting radiation. Once these tests are successful, one can proceed to more complicated configurations and study the interactions of different solitons.

An important check in all simulations is the conservation of the total energy. While small fluctuations are acceptable, larger deviations should be avoided. In this context, the choice of boundary conditions is crucial. For absorbing boundaries, a decrease in energy is expected since radiation can leave the system. However, for Dirichlet or periodic boundaries, the total energy should be conserved at all times. Significant changes in the energy can typically be traced back to the numerical time integration scheme or to insufficient lattice resolution.

This leads to another essential check, the dependence of the results on the lattice resolution. A simulation result cannot be trusted if it changes with the resolution of the lattice. Therefore, one has to verify that the outcome remains unchanged under changes of the lattice spacing. A straightforward approach is to halve the lattice spacing and check that the results remain the same. In cases where computational resources do not allow for this, one can instead double the lattice spacing and verify that the results are consistent even at lower resolution.

Another important check concerns the boundaries. In some cases, boundary effects can influence the outcome of the simulations. In Section A.5, we already discussed different types of boundary conditions and in which setups they can be applied. To assess the influence of the boundaries, the simplest test is to vary the size of the lattice. For larger lattices, the boundaries should become less relevant and artificial effects should decrease. If the results do not change with an increasing lattice size, one can (not in all cases) trust the chosen boundary conditions. In addition, it can be useful to change the boundary conditions completely to check whether the results depend on their specific choice.

The checks mentioned above are crucial and were performed for all simulations. In addition, one can carry out further tests. For example, one can change the time integration method, consider different gauge choices, or monitor additional physical quantities besides the energy, such as the electric charge. Many other checks are possible. Which of these checks are necessary and useful always depends on the specific problem that is considered. However, the main message of this section is that numerical results should not be trusted without performing a sufficient number of consistency checks beforehand.

A.11 Python as a Coding Language for Numerical Simulations

As a coding language for all simulations performed within this thesis, *Python* [254] has been used. Python on its own is typically not well suited for numerical calculations on large lattices, as its execution speed is relatively slow. However, in combination with appropriate packages, the performance can be significantly improved. In all simulations, we used the package *Numba* [255]. Numba translates the Python code into efficient machine code and thereby speeds up the computations. The Numba package can be easily implemented by

```
from numba import jit

@jit(nopython=True)
def function():
    ...
```

where the `@jit` decorator indicates that the entire function `function()` is compiled into machine code before execution. Notice that Numba is not compatible with all Python packages. For all computations, we used only the package *NumPy* [256] in combination with Numba.

In addition to the machine code translation, Numba provides an easy way to implement parallelisation. In particular for three-dimensional lattices, this further speeds up the computation significantly. We implemented the parallelisation as follows. Instead of evaluating the field equations on all lattice points on a single core, we split the lattice into n parts and distribute the computation across n cores. This does not lead to a full speed-up by a factor of n, since communication between the cores is still required at each time-iteration step. Nevertheless, a substantial performance improvement can be achieved. Depending on the lattice size and the available computational resources, we used up to 64 CPU cores.

Using Numba, the parallelisation can be implemented by

```
from numba import jit, prange

@jit(nopython=True, parallel=True)
def function():
    for i in prange(N):
        ...
```

where `prange` indicates that the code within the `for`-loop is parallelised. Each computation corresponding to the index `i` is performed on a separate core. If fewer cores than iterations

N are available, computations that cannot be assigned initially are carried out once a core becomes available.

Besides computational speed, memory is often an important issue in simulations. For computing the field values at a single moment in time, the available RAM on the machines we used was always sufficient. However, to study the time dependence, one needs to store field configurations at many time steps. First, not all time steps need to be stored to extract the relevant physical information. Therefore, we saved only a subset of all time steps. Second, it is not necessary to store the full lattice. Instead, one can restrict the output to regions where the relevant dynamics occur, which further reduces memory usage. Another important aspect is that it is generally not recommended to keep all data in the RAM. A significant amount of memory can be saved by writing data that is not needed for further computations directly to the disk. NumPy provides an elegant solution for this. Before starting the time evolution, we save the required “empty” data arrays directly on the hard disk by

```
np.save('path/data.npy', data_array)
```

where `data_array` is the array that collects the data we want to store. Whenever we want to access or modify the data, we load it by

```
data_array=np.load('path/data.npy', mmap_mode='r+')
```

The `mmap_mode='r+'` ensures that not the entire array is loaded into the RAM, but only the part that is required when modifications are made.

All the aspects discussed so far in this section make Python a very convenient choice for numerical simulations. Besides NumPy and Numba, the only other package we used in a few numerical computations was *SciPy* [247], for small linear algebra tasks such as those required in the eigenvalue method described in Subsection A.2.3, as well as for efficient interpolations.

All figures in this thesis were created using the package *Matplotlib* [257] in Python or using the program *Mathematica* [258].

A.12 List of Numerical Methods

The following two tables provide an overview of many of the numerical calculations we have performed, together with the methods used. The first table lists the numerical methods used for static or initial configurations. The second table lists the methods used for the simulations.

Numerical Methods for Static and Initial Configurations		
	Numerical Method	**Lattice Properties**
Profile functions for the Nielsen–Olesen vortex (Figure 2.2)	Relaxation in multiple steps	4000 lattice points, $\mathrm{d}r \sim 0.025$
Profile functions for the ’t Hooft–Polyakov magnetic monopole (Figure 2.3)	Relaxation in multiple steps	4000 lattice points, $\mathrm{d}r \sim 0.025\, m_v^{-1}$
Vortex mode profile functions and frequencies (Figures 3.1 and 3.2)	Eigenvalue method	10000 lattice points, $\mathrm{d}r = 0.008$.
Feshbach resonance frequencies (Figure 3.3)	Shooting method	5000 lattice points, $\mathrm{d}r = 0.01$
Toroidal higher-charged monopole solutions (Figures 3.34 and 3.35)	Relaxation method with fixed scalar field orientation	240^3 lattice points, $\mathrm{d}x = 0.25\, m_v^{-1}$
Confined monopole pair (initial configuration) in Figures 4.11 and 4.13	Relaxation method with fixed scalar field orientation	$480^2 \times 3$ lattice points (axial symmetry method used), $\mathrm{d}x = 0.25\, m_{v,\phi}^{-1}$
Two slingshots (initial configuration) in Figure 5.4	Relaxation method with fixed scalar field orientation	240^3 lattice points, $\mathrm{d}x = 1.0\, m_{v,\phi}^{-1}$

Numerical Methods for Simulations			
	Numerical Integration Method	**Boundary Conditions**	**Lattice Properties**
Vortex–anti-vortex collisions in Section 3.3	Modified RK2	Natural boundaries with adiabatic damping	1200^2 lattice points, 5000 time points, $\mathrm{d}x = 0.05$, $\mathrm{d}t = 0.02$
Monopole–anti-monopole collisions in Section 3.4	Crank–Nicolson method	Sommerfeld radiation condition	$480^2 \times 3$ lattice points (axial symmetry method used), 2000 time steps, $\mathrm{d}x = 0.25\, m_v^{-1}$, $\mathrm{d}t = 0.1\, m_v^{-1}$
Multi-vortex collision in Section 3.6	Modified RK2	Natural boundaries with adiabatic damping	1200^2 lattice points (for some cases 1600^2 lattice points), 4000 time steps, $\mathrm{d}x = 0.05$, $\mathrm{d}t = 0.025$
Multi-monopole collisions in Section 3.7	Crank–Nicolson method	Dirichlet boundaries	240^3 lattice points, 1000 time steps, $\mathrm{d}x = 0.25\, m_v^{-1}$, $\mathrm{d}t = 0.1\, m_v^{-1}$
Erasure of magnetic monopoles in Section 4.4	Crank–Nicolson method	Dirichlet boundaries in z-direction and time-dependent boundaries in x-direction	For monopole velocities < 0.8, $480^2 \times 3$ lattice points (axial symmetry method used), 1500 time steps, $\mathrm{d}x = \mathrm{d}z = 0.25\, m_v^{-1}$, $\mathrm{d}t = 0.1\, m_v^{-1}$; For monopole velocities ≥ 0.8, $480 \times 960 \times 3$ lattice points, 3000 time steps, $\mathrm{d}x = 0.25\, m_v^{-1}$, $\mathrm{d}z = 0.125\, m_v^{-1}$, $\mathrm{d}t = 0.05\, m_v^{-1}$
Systems of monopole necklaces and monopole dumbbells in Figures 4.10 and 4.12	Crank–Nicolson method	Periodic boundaries	150^3 lattice points, 1200 time steps, $\mathrm{d}x = 1.0\, m_{v,\phi}^{-1}$, $\mathrm{d}t = 0.3\, m_{v,\phi}^{-1}$

Confined monopole pair in Figures 4.11 and 4.13, and for the gravitational radiation calculation with result given in Figure 4.14	Crank–Nicolson method	Sommerfeld radiation condition	$480^2 \times 3$ lattice points (axial symmetry method used), 1000 time steps, $\mathrm{d}x = 0.25\, m_{v,\phi}^{-1}$, $\mathrm{d}t = 0.1\, m_{v,\phi}^{-1}$
Slingshot with axial symmetry in Figures 5.2 and 5.3, and for the gravitational radiation calculation with the results given in Figures 5.6 and 5.7	Crank–Nicolson method	Sommerfeld radiation condition for ϕ and W_μ; For ψ, periodic boundaries in x-direction and Dirichlet boundaries in z-direction	$480 \times 960 \times 3$ lattice points (axial symmetry method used), 1800 time steps, $\mathrm{d}x = 0.25\, m_{v,\phi}^{-1}$, $\mathrm{d}t = 0.1\, m_{v,\phi}^{-1}$
Two slingshots in Figure 5.4	Crank–Nicolson method	Sommerfeld radiation condition, Periodic boundaries in x-direction for ψ	240^3 lattice points, 600 time steps, $\mathrm{d}x = 1.0\, m_{v,\phi}^{-1}$, $\mathrm{d}t = 0.5\, m_{v,\phi}^{-1}$
Slingshot system in Figure 5.5	Crank–Nicolson method	Periodic boundaries	$180 \times 180 \times 360$ lattice points, 600 time steps, $\mathrm{d}x = 1.0\, m_{v,\phi}^{-1}$, $\mathrm{d}t = 0.4\, m_{v,\phi}^{-1}$
Vortex slingshot in Section 5.7	Crank–Nicolson method	Sommerfeld radiation condition for ϕ and A_μ; For χ, Dirichlet boundaries in x-direction and periodic boundaries in y-direction	960×480 lattice points, 2000 time steps, $\mathrm{d}x = 0.25\, m_{v,\phi}^{-1}$, $\mathrm{d}t = 0.1\, m_{v,\phi}^{-1}$

Appendix B

Homotopy Theory

In the literature, arguments for the existence of topological defects are often given by the use of homotopy theory. In this section, the most relevant concepts of homotopy theory will be briefly reviewed. Thereby we follow the books [24, 28].

Let us first define the vacuum manifold of a scalar field theory more precisely. Let ϕ_0 be one minimum of the potential and G the symmetry group of the theory. We then define

$$\mathcal{O}_{\phi_0} = \{\phi = g\phi_0 : g \in G\}\,, \tag{B.1}$$

as the *orbit* of ϕ_0. In other words, the orbit is the set of all ϕ that are related by a transformation in G.[1] The vacuum manifold is defined as the set of all field values that minimize the potential,

$$\mathcal{M} = \bigcup_{\phi_0 \text{ minimizes } V} \mathcal{O}_{\phi_0}\,. \tag{B.2}$$

As an example let us consider a complex scalar field theory with $U(1)$ symmetry and the potential $V_1(\phi) = \lambda(|\phi|^2 - v^2)^2$. One minimum of the potential is given by $\phi = v$ and its orbit is given by

$$\mathcal{O}_{\phi_0=v} = \{gv : g \in U(1)\} = \{e^{i\alpha}v : \alpha \in [0, 2\pi)\}\,. \tag{B.3}$$

The vacuum manifold is just the orbit itself, $\mathcal{M} = \mathcal{O}_v$, because this orbit already contains all minima of the potential. Note that this is not true in general. As an example, consider a complex scalar field theory with the potential $V_2(\phi) = \lambda(|\phi|^2 - v_1^2)^2(|\phi|^2 - v_2^2)^2$ with $v_1 \neq v_2$. There are two non-equal orbits, $\mathcal{O}_{v_1}$ and $\mathcal{O}_{v_2}$, and the vacuum manifold is given by their union, $\mathcal{M} = \mathcal{O}_{v_1} \cup \mathcal{O}_{v_2}$.

The group G can contain elements that have no effect on the elements of the orbit. These elements are collected in the *stabiliser subgroup*

$$H_{\phi_0} = \{h \in G : \phi_0 = h\phi_0\}\,. \tag{B.4}$$

---

[1] For convenience, we write g, but we actually mean the representation $T(g)$.

Furthermore, let us define the *(left) coset* by

$$gH_{\phi_0} = \{gh : h \in H_{\phi_0}\}\,, \tag{B.5}$$

and the *coset space* by

$$G/H_{\phi_0} = \{gH_{\phi_0} : g \in G\}\,. \tag{B.6}$$

We can now observe that there is a one-to-one correspondence between G/H_{ϕ_0} and $\mathcal{O}_{\phi_0}$, i.e. each coset gH_{ϕ_0} can be mapped to a point ϕ_0 of the orbit. In this way, group transformations can be related to actual scalar field values of the vacuum manifold. The coset space G/H_{ϕ_0} corresponds to one single orbit $\mathcal{O}_{\phi_0}$. If there are more inequivalent orbits, one can combine the corresponding coset spaces into one single coset space by

$$G/H = \bigsqcup_{\text{inequivalent orbits}} G/H_{\phi_0}\,, \tag{B.7}$$

where $\bigsqcup$ denotes the disjoint union[2]. In this case, there is a one-to-one correspondence between the vacuum manifold $\mathcal{M}$ and G/H.

As an example let us consider the potential $V_1(\phi)$, which we have already used above. The stabiliser subgroup of ϕ_0 is simply given by $H_{\phi_0} = \{\mathbb{1}\}$, the coset is $gH_{\phi_0} = \{e^{i\alpha} : \alpha \in [0, 2\pi)\}$, and the coset space is $G/H = G/H_{\phi_0} = \{\{e^{i\alpha}\} : \alpha \in [0, 2\pi)\}$.

As a second example let us consider the potential $V_2(\phi)$, which makes clear why the disjoint union is required. In this case, we have two stabiliser subgroups, given by $H_{v_1} = H_{v_2} = \{\mathbb{1}\}$. The cosets are $gH_{v_1} = gH_{v_2} = \{g\}$ and the coset spaces are given by $G/H_{v_1} = G/H_{v_2} = \{\{e^{i\alpha}\} : \alpha \in [0, 2\pi)\}$. The full coset space is then given by $G/H = \{\{e^{i\alpha}\}_1, \{e^{i\alpha}\}_2 : \alpha \in [0, 2\pi)\}$. Without the disjoint union, one would obtain $G/H_{v_1} \cup G/H_{v_2} = \{\{e^{i\alpha}\} : \alpha \in [0, 2\pi)\}$, which does not provide a one-to-one correspondence with the vacuum manifold.

Let us take as a third example an $SU(2)$ theory with a scalar field transforming in the adjoint representation. For the potential we take the quartic form $V(\phi) = \lambda(\mathrm{Tr}(\phi^2) - v^2)^2$. One minimum of this potential is for example $\phi = vT^3$. Then the orbit, which also corresponds to the vacuum manifold of the theory is

$$\mathcal{O}_{vT^3} = \{e^{i\alpha^a T^a}\, vT^3\, e^{-i\alpha^a T^a} : \alpha^a \in [0, 2\pi)\} = \mathcal{M}\,. \tag{B.8}$$

The stabiliser subgroup is $H_{vT^3} = \{e^{i\alpha T^3} : \alpha \in [0, 2\pi)\}$, the coset is $gH_{vT^3} = \{ge^{i\alpha T^3} : \alpha \in [0, 2\pi)\}$, where $g \in G$, and the coset space is

$$G/H = G/H_{vT^3} = \{\{e^{i\beta^a T^a} e^{i\alpha T^3} : \alpha \in [0, 2\pi)\} : \beta^1, \beta^2 \in [0, 2\pi), \beta^3 = 0\}\,, \tag{B.9}$$

which is isomorphic to a 2-sphere S_2.

---

[2] The disjoint union keeps the information from which set an element is coming from. For example $\{1, 2\} \sqcup \{1, 2, 3\} = \{1_1, 2_1, 1_2, 2_2, 3_2\}$, where the number in the subscript denotes its original set. With the usual union we would just get $\{1, 2, 3\}$.

Now that we have discussed how the vacuum manifold is related to a coset space, we can continue with homotopy theory. Two mappings $f : X \to Y$ and $g : X \to Y$ are called *homotopic* to each other if they can be continuously deformed into one another, i.e. if there exists a family of continuous mappings h_t with $t \in [0, 1]$ such that $h_0 = f$ and $h_1 = g$. The set of all mappings that are homotopic to each other is called a *homotopy class*.

Let us consider, as an example, two continuous mappings from a circle to a two-dimensional real space, $f_{1,2} : S_1 \to \mathbb{R}^2$. In this case, the two mappings f_1 and f_2 are always homotopic to each other, since one can continuously deform one into the other. Therefore, all continuous mappings from S_1 to $\mathbb{R}^2$, of which there are infinitely many, belong to a single homotopy class.

The situation changes if we exclude a point, for example the origin. In that case, the mappings are from S_1 to $\mathbb{R}^2 \setminus (0, 0)$. Now there exist mappings that are not homotopic to each other. For instance, a mapping that describes a circle enclosing the excluded point is not homotopic to one that does not enclose it. Since one can also wind multiple times around the excluded point, there are infinitely many mappings that are not homotopic to each other. This means that there are infinitely many homotopy classes, where each is characterised by a winding number n.

The group of all homotopy classes consisting of mappings from S_k to a space G is called the *homotopy group* $\pi_k(G)$.[3] For the above example with the excluded point, this gives $\pi_1(\mathbb{R}^2 \setminus (0, 0)) \cong \mathbb{Z}$. Another example is $\pi_0(Z_2) \cong Z_2$, which shows that there are two homotopically distinct ways to map a set of two points to another set of two points: either both points are mapped to the same point or to two different points in the target space. An example of a trivial homotopy group is $\pi_1(S_2) = 0$. This homotopy group describes mappings of circles to a 2-sphere. Since each such mapping can be continuously contracted to a single point, all mappings are homotopic to each other. To be precise, these mappings should be included in the homotopy group, since they form a single homotopy class. However, since these mappings are trivial, they are often ignored, which is why we write $\pi_1(S_2) = 0$.

There are two important rules, which we will use in the following without proving them:

$$\pi_n(G_1 \times G_2) = \pi_n(G_1) \times \pi_n(G_2)\,, \tag{B.10}$$

$$\pi_2(G/H) = \pi_1(H)\,, \tag{B.11}$$

where G is a compact and simply connected group. The first rule can be understood intuitively by considering a torus T_2. There are two non-trivial ways to map circles S_1 onto the torus. One can map them through the hole of the torus and another one around its central hole. Each of these mappings can again have multiple windings. Therefore, the first homotopy group is given by $\pi_1(T_2) \cong \mathbb{Z} \times \mathbb{Z}$. The second rule can be applied to the $SU(2)$ adjoint scalar field theory with a quartic potential. In this case, the stabiliser subgroup

---

[3] The group operation of homotopy groups is given by the concatenation of maps from k-spheres S_k to G. For instance, let us take two elements of the homotopy group $\pi_1(G)$, which describe two loops based at the same point x_0. Their concatenation consists of following one loop starting at x_0 until returning to x_0, and then subsequently following the second loop.

(unbroken subgroup) is $H = U(1)$, and thus $G/H = SU(2)/U(1)$. Applying rule (B.11) then gives $\pi_2(SU(2)/U(1)) = \pi_1(U(1)) \cong \mathbb{Z}$.

Finally, let us connect these observations to topological defects. As we already saw throughout this chapter, we always got topological defects when there were non-trivial mappings from the boundary of the space to the vacuum manifold. In the language of homotopy theory this means that we can get topological defects if there are non-trivial homotopy groups. For example, the topology of the theory allows a domain wall, vortex, or magnetic monopole solution if the homotopy group $\pi_0(G/H)$, $\pi_1(G/H)$, or $\pi_2(G/H)$ is non-trivial, respectively.

The example $\pi_0(Z_2) = Z_2$ corresponds to domain walls. As discussed, there are two homotopy classes. One class describes mappings where both points of Z_2 (i.e. the two boundaries of the one-dimensional space) are mapped to the same point in the vacuum manifold. This corresponds to the trivial solution, where the scalar field takes the same vacuum expectation value everywhere. The second homotopy class describes mappings where the two points are mapped to two different values in the vacuum manifold. This corresponds to the domain wall solutions. Similarly, one can consider vortices with $\pi_1(U(1)/1) \cong \pi_1(S_1) = \mathbb{Z}$ or monopoles with $\pi_2(SU(2)/U(1)) \cong \mathbb{Z}$. In these cases, there are infinitely many homotopy classes, characterised by a winding number n, which correspond to the infinitely many winding solutions of vortices or monopoles.

Last but not least we want to give one example which is relevant for the GUT symmetry breaking discussed in Chapter 4. It is the symmetry breaking $SU(5) \to SU(3) \times SU(2) \times U(1)$. The second homotopy group is given by

$$\begin{aligned}
\pi_2(G/H) &= \pi_2\left(\frac{SU(5)}{SU(3) \times SU(2) \times U(1)}\right) \\
&= \pi_1\left(SU(3) \times SU(2) \times U(1)\right) \\
&= \pi_1(SU(3)) \times \pi_1(SU(2)) \times \pi_1(U(1)) \\
&= \pi_1(U(1)) \cong \mathbb{Z}\,,
\end{aligned} \tag{B.12}$$

where in the second equality we applied rule (B.11) and in the third equality we applied rule (B.10). Notice that in the last line we used $\pi_1(SU(3)) = 0$ and $\pi_1(SU(2)) = 0$.

Notice that the symmetry breaking of $SU(5)$ more precisely results in the coset space $\left(SU(3) \times SU(2) \times U(1)\right)/Z_6$. This Z_6 identification is required, since there exist six combinations of $SU(3)$, $SU(2)$, and $U(1)$ transformation matrices that correspond to the same $SU(5)$ matrix. Consequently, rule (B.10) cannot be applied. Nevertheless, the presence of Z_6 does not affect the topology arising from the $U(1)$ factor, and therefore the final result remains unchanged

$$\pi_2\left(\frac{SU(5)}{\left(SU(3) \times SU(2) \times U(1)\right)/Z_6}\right) \cong \mathbb{Z}\,. \tag{B.13}$$

For all purposes considered in this thesis, the calculation (B.12) remains valid.

List of Figures

List of Videos

1. **Resonance phenomena in vortex-antivortex collisions**
   Referred to in Section 3.3, (`https://youtu.be/1o__huMd13o`)
   This video summarizes the results of vortex–anti-vortex collisions. Several animated multi-bounce scattering events are illustrated using the data from numerical simulations.

2. **From BPS geodesics to mode-driven dynamics in the scattering of multiple BPS vortices**
   Referred to in Section 3.6, (`https://youtu.be/o-0fQn-0wlE`)
   Several representative examples of collisions of excited vortices are shown in this video. These include the 2-vortex–1-vortex collision, the four-vortex square collision, the $1 + 2 + 1$ collinear collision, and the $2 + 2$ head-on collision.

3. **Scattering of Magnetic Monopoles**
   Referred to in Section 3.7, (`https://youtu.be/2DfE9ty727c`)
   In this video, the explanations on the moduli space of two magnetic monopoles of Subsection 3.7.1 are presented using illustrative animations. Moreover the numerical results of the simulations of magnetic monopole collisions are shown.

4. **Simulations of Magnetic Monopole Collisions**
   Referred to in Section 3.7, (`https://youtu.be/a2wOOo2AAHI`)
   This video summarizes the numerical results we obtained for the collision of multiple magnetic monopoles. The planar scattering of two, three, and four monopoles, as described in Subsection 3.7.5, is shown, as well as the non-planar scattering scenarios described in Subsection 3.7.6.

5. **Radiation Emission during the Erasure of Magnetic Monopoles**
   Referred to in Section 4.4, (`https://youtu.be/JZaXUYikQbo`)
   The animated numerical results for the erasure of a magnetic monopole through its collision with an $SU(2)$-invariant vacuum layer are shown in this video. This includes all cases discussed in Section 4.4.

6. **Confinement Slingshot and Gravitational Waves**
   Referred to in Chapter 5, (`https://youtu.be/IPJAPjo3nSc`)
   In this video, the confinement slingshot effect introduced in Chapter 5 is presented. A single magnetic monopole slingshot is shown, as well as a slingshot that detaches from the wall via an anti-monopole entering the slingshot throat. Furthermore, animations corresponding to the vortex slingshot described in Section 5.7 are included.

7. **Cosmological Implications of the Slingshot Effect**
   Referred to in Chapter 5, (`https://youtu.be/PnErf4-zUEg`)
   This video summarizes the numerical results described in Subsections 5.3.2 and 5.3.3. It illustrates the behaviour of magnetic monopoles during first-order phase transitions, where the monopoles enter a confining phase. Interactions between two slingshots are shown, and a full monopole system interacting with an expanding bubble is presented.

Bibliography

[1] Paul Adrien Maurice Dirac, "Quantised singularities in the electromagnetic field,," Proc. Roy. Soc. Lond. A **133**, 60–72 (1931).

[2] Gerard 't Hooft, "Magnetic Monopoles in Unified Gauge Theories," Nucl. Phys. B **79**, 276–284 (1974).

[3] Alexander M. Polyakov, "Particle Spectrum in Quantum Field Theory," JETP Lett. **20**, 194–195 (1974).

[4] N. S. Manton, "The Force Between 't Hooft-Polyakov Monopoles," Nucl. Phys. B **126**, 525–541 (1977).

[5] Nigel J. Hitchin, N. S. Manton, and M. K. Murray, "Symmetric monopoles," Nonlinearity **8**, 661–692 (1995), arXiv:dg-ga/9503016 .

[6] Conor J. Houghton and Paul M. Sutcliffe, "Tetrahedral and cubic monopoles," Commun. Math. Phys. **180**, 343–362 (1996), arXiv:hep-th/9601146 .

[7] Conor J. Houghton, Nicholas S. Manton, and Paul M. Sutcliffe, "Rational maps, monopoles and Skyrmions," Nucl. Phys. B **510**, 507–537 (1998), arXiv:hep-th/9705151 .

[8] N. S. Manton, "A Remark on the Scattering of BPS Monopoles," Phys. Lett. B **110**, 54–56 (1982).

[9] M. F. Atiyah and Nigel J. Hitchin, "Low-Energy Scattering of Nonabelian Monopoles," Phys. Lett. A **107**, 21–25 (1985).

[10] MICHAEL FRANCIS ATIYAH and NIGEL HITCHIN, *The Geometry and Dynamics of Magnetic Monopoles* (Princeton University Press, 1988).

[11] Holger Bech Nielsen and P. Olesen, "Vortex Line Models for Dual Strings," Nucl. Phys. B **61**, 45–61 (1973).

[12] Maximilian Bachmaier, Gia Dvali, Josef Seitz, and Juan Sebastián Valbuena-Bermúdez, "Simulations of magnetic monopole collisions," Phys. Rev. D **111**, 075014 (2025), arXiv:2502.01756 [hep-th] .

[13] H. Georgi and S. L. Glashow, "Unity of All Elementary Particle Forces," Phys. Rev. Lett. **32**, 438–441 (1974).

[14] T. W. B. Kibble, "Some Implications of a Cosmological Phase Transition," Phys. Rept. **67**, 183 (1980).

[15] Ya. B. Zeldovich and M. Yu. Khlopov, "On the Concentration of Relic Magnetic Monopoles in the Universe," Phys. Lett. B **79**, 239–241 (1978).

[16] John Preskill, "Cosmological Production of Superheavy Magnetic Monopoles," Phys. Rev. Lett. **43**, 1365 (1979).

[17] Alan H. Guth, "The Inflationary Universe: A Possible Solution to the Horizon and Flatness Problems," Phys. Rev. D **23**, 347–356 (1981).

[18] Paul Langacker and So-Young Pi, "Magnetic Monopoles in Grand Unified Theories," Phys. Rev. Lett. **45**, 1 (1980).

[19] Xavier Martin and Alexander Vilenkin, "Gravitational radiation from monopoles connected by strings," Phys. Rev. D **55**, 6054–6060 (1997), arXiv:gr-qc/9612008 .

[20] Maximilian Bachmaier, Gia Dvali, Juan Sebastián Valbuena-Bermúdez, and Michael Zantedeschi, "Confinement slingshot and gravitational waves," Phys. Rev. D **110**, 016001 (2024), arXiv:2309.14195 [hep-ph] .

[21] Maximilian Bachmaier, Gia Dvali, Juan Sebastián Valbuena-Bermúdez, and Michael Zantedeschi, "Cosmological Implications of the Slingshot Effect: Gravitational Waves, Primordial Black Holes and Dark Matter," (2026), arXiv:2603.18512 [hep-ph] .

[22] G. R. Dvali, Alejandra Melfo, and Goran Senjanovic, "Is There a monopole problem?" Phys. Rev. Lett. **75**, 4559–4562 (1995), arXiv:hep-ph/9507230 .

[23] G. R. Dvali, Hong Liu, and Tanmay Vachaspati, "Sweeping away the monopole problem," Phys. Rev. Lett. **80**, 2281–2284 (1998), arXiv:hep-ph/9710301 .

[24] Erick J. Weinberg, *Classical solutions in quantum field theory: Solitons and Instantons in High Energy Physics*, Cambridge Monographs on Mathematical Physics (Cambridge University Press, 2012).

[25] N. S. Manton and P. Sutcliffe, *Topological solitons*, Cambridge Monographs on Mathematical Physics (Cambridge University Press, 2004).

[26] Mikhail Shifman, *Advanced topics in quantum field theory.: A lecture course* (Cambridge Univ. Press, Cambridge, UK, 2012).

[27] A. Vilenkin and E. P. S. Shellard, *Cosmic Strings and Other Topological Defects* (Cambridge University Press, 2000).

[28] V. A. Rubakov, *Classical theory of gauge fields* (Princeton University Press, Princeton, New Jersey, 2002).

[29] R. Rajaraman, *Solitons and Instantons. An Introduction To Solitons and Instantons in Quantum Field Theory* (1982).

[30] E. B. Bogomolny, “Stability of Classical Solutions,” Sov. J. Nucl. Phys. **24**, 449 (1976).

[31] A. Vilenkin and A. E. Everett, “Cosmic Strings and Domain Walls in Models with Goldstone and PseudoGoldstone Bosons,” Phys. Rev. Lett. **48**, 1867–1870 (1982).

[32] Michael E. Peskin and Daniel V. Schroeder, *An Introduction to quantum field theory* (Addison-Wesley, Reading, USA, 1995).

[33] Matthew D. Schwartz, *Quantum Field Theory and the Standard Model* (Cambridge University Press, 2014).

[34] Laurence Jacobs and Claudio Rebbi, “Interaction Energy of Superconducting Vortices,” Phys. Rev. B **19**, 4486–4494 (1979).

[35] Jose J. Blanco-Pillado, Ken D. Olum, and Benjamin Shlaer, “Large parallel cosmic string simulations: New results on loop production,” Phys. Rev. D **83**, 083514 (2011), arXiv:1101.5173 [astro-ph.CO] .

[36] Jose J. Blanco-Pillado, Ken D. Olum, and Benjamin Shlaer, “The number of cosmic string loops,” Phys. Rev. D **89**, 023512 (2014), arXiv:1309.6637 [astro-ph.CO] .

[37] Jose J. Blanco-Pillado, Ken D. Olum, and Benjamin Shlaer, “Cosmic string loop shapes,” Phys. Rev. D **92**, 063528 (2015), arXiv:1508.02693 [astro-ph.CO] .

[38] Jose J. Blanco-Pillado and Ken D. Olum, “Stochastic gravitational wave background from smoothed cosmic string loops,” Phys. Rev. D **96**, 104046 (2017), arXiv:1709.02693 [astro-ph.CO] .

[39] Jose J. Blanco-Pillado, Ken D. Olum, and Xavier Siemens, “New limits on cosmic strings from gravitational wave observation,” Phys. Lett. B **778**, 392–396 (2018), arXiv:1709.02434 [astro-ph.CO] .

[40] Ayush Saurabh, Tanmay Vachaspati, and Levon Pogosian, “Decay of Cosmic Global String Loops,” Phys. Rev. D **101**, 083522 (2020), arXiv:2001.01030 [hep-ph] .

[41] Mark Hindmarsh, Joanes Lizarraga, Jon Urrestilla, David Daverio, and Martin Kunz, “Scaling from gauge and scalar radiation in Abelian Higgs string networks,” Phys. Rev. D **96**, 023525 (2017), arXiv:1703.06696 [astro-ph.CO] .

[42] Jorge Baeza-Ballesteros, Edmund J. Copeland, Daniel G. Figueroa, and Joanes Lizarraga, “Gravitational wave emission from a cosmic string loop: Global case,” Phys. Rev. D **110**, 043522 (2024), arXiv:2308.08456 [astro-ph.CO] .

[43] Jorge Baeza-Ballesteros, Edmund J. Copeland, Daniel G. Figueroa, and Joanes Lizarraga, “Particle and gravitational wave emission by local string loops: Lattice calculation,” Phys. Rev. D **112**, 043540 (2025), arXiv:2408.02364 [astro-ph.CO] .

[44] Asier Lopez-Eiguren, Jon Urrestilla, and Ana Achúcarro, "Measuring Global Monopole Velocities, one by one," JCAP **01**, 020 (2017), [Erratum: JCAP 06, E01 (2017)], arXiv:1611.09628 [hep-ph] .

[45] D. P. Bennett and S. H. Rhie, "Cosmological evolution of global monopoles and the origin of large scale structure," Phys. Rev. Lett. **65**, 1709–1712 (1990).

[46] Erick J. Weinberg and Alan H. Guth, "Nonexistence of Spherically Symmetric Monopoles with Multiple Magnetic Charge," Phys. Rev. D **14**, 1660 (1976).

[47] M. K. Prasad and Charles M. Sommerfield, "An Exact Classical Solution for the 't Hooft Monopole and the Julia-Zee Dyon," Phys. Rev. Lett. **35**, 760–762 (1975).

[48] P. Forgacs, N. Obadia, and S. Reuillon, "Numerical and asymptotic analysis of the 't Hooft-Polyakov magnetic monopole," Phys. Rev. D **71**, 035002 (2005), [Erratum: Phys.Rev.D 71, 119902 (2005)], arXiv:hep-th/0412057 .

[49] B. Julia and A. Zee, "Poles with Both Magnetic and Electric Charges in Nonabelian Gauge Theory," Phys. Rev. D **11**, 2227–2232 (1975).

[50] Y. Brihaye, B. Kleihaus, and D. H. Tchrakian, "Dyon - Skyrmion lumps," J. Math. Phys. **40**, 1136–1152 (1999), arXiv:hep-th/9805059 .

[51] A. Yu. Loginov, "A differential relation between the energy and electric charge of a dyon," Phys. Lett. B **822**, 136662 (2021), arXiv:2108.05121 [hep-th] .

[52] G. H. Derrick, "Comments on nonlinear wave equations as models for elementary particles," J. Math. Phys. **5**, 1252–1254 (1964).

[53] Jose J. Blanco-Pillado, Daniel Jiménez-Aguilar, and Jon Urrestilla, "Exciting the domain wall soliton," JCAP **01**, 027 (2021), arXiv:2006.13255 [hep-th] .

[54] Maximilian Bachmaier, Davide Chiego, and Gia Dvali, (to be published) (2026).

[55] M. A. Lohe, "Soliton Structures in $P(\phi)$ in Two-dimensions," Phys. Rev. D **20**, 3120 (1979).

[56] Miguel A. Alejo, Claudio Muñoz, and José M. Palacios, "On asymptotic stability of the sine-gordon kink in the energy space," Communications in Mathematical Physics **402**, 581–636 (2023).

[57] Aliakbar Moradi Marjaneh, Fabiano C. Simas, and D. Bazeia, "Collisions of kinks in deformed l. 160 φ4 and l. 160 φ6 models," Chaos Solitons and Fractals: the interdisciplinary journal of Nonlinear Science and Nonequilibrium and Complex Phenomena **164**, 112723 (2022), arXiv:2207.00835 [hep-th] .

[58] João G. F. Campos and Azadeh Mohammadi, "Wobbling double sine-Gordon kinks," JHEP **09**, 067 (2021), arXiv:2103.04908 [hep-th] .

[59] M. Bachmaier and A. Wereszczynski, “Resonance phenomena in vortex-antivortex collisions,” Phys. Lett. B **875**, 140324 (2026), arXiv:2510.17964 [hep-th] .

[60] A. Alonso Izquierdo, M. Bachmaier, and A. Wereszczynski, “From BPS geodesics to mode-driven dynamics in the scattering of multiple BPS vortices,” (2026), arXiv:2603.04495 [hep-th] .

[61] A. Alonso-Izquierdo, W. Garcia Fuertes, and J. Mateos Guilarte, “A note on BPS vortex bound states,” Phys. Lett. B **753**, 29–33 (2016), arXiv:1509.06632 [hep-th] .

[62] A. Alonso-Izquierdo and D. Miguelez-Caballero, “Dissecting normal modes of vibration on vortices in Ginzburg-Landau superconductors,” Phys. Rev. D **110**, 125026 (2024), arXiv:2410.08705 [hep-th] .

[63] Ta-Pei [0000-0002-1137-0969] Cheng and Ling-Fong [0000-0002-8035-3329] Li, *Gauge Theory of Elementary Particle Physics* (Oxford University Press, Oxford, UK, 1984).

[64] Jose J. Blanco-Pillado, Daniel Jiménez-Aguilar, Jose M. Queiruga, and Jon Urrestilla, “Internal excitations of global vortices,” JCAP **10**, 047 (2021), arXiv:2107.02215 [hep-th] .

[65] Herman Feshbach, “Unified theory of nuclear reactions,” Annals Phys. **5**, 357–390 (1958).

[66] Gyula Fodor and Istvan Racz, “What does a strongly excited ’t Hooft-Polyakov magnetic monopole do?” Phys. Rev. Lett. **92**, 151801 (2004), arXiv:hep-th/0311061 .

[67] Peter Forgacs and Mikhail S. Volkov, “Resonant excitations of the ’t Hooft-Polyakov monopole,” Phys. Rev. Lett. **92**, 151802 (2004), arXiv:hep-th/0311062 .

[68] Gyula Fodor and Istvan Racz, “Numerical investigation of highly excited magnetic monopoles in SU(2) Yang-Mills-Higgs theory,” Phys. Rev. D **77**, 025019 (2008), arXiv:hep-th/0609110 .

[69] Katie M Russell and Bernd J Schroers, “On resonances and bound states of the ’t Hooft-Polyakov monopole,” Phys. Rev. D **83**, 065004 (2011), arXiv:1012.3438 [hep-th] .

[70] Alberto García Martín-Caro, Jose Queiruga, and Andrzej Wereszczynski, “Feshbach resonances and dynamics of BPS solitons,” Phys. Rev. D **111**, 096002 (2025), arXiv:2501.02589 [hep-th] .

[71] Ryogo Hirota, “Exact solution of the sine-gordon equation for multiple collisions of solitons,” Journal of the Physical Society of Japan **33**, 1459–1463 (1972).

[72] T. Sugiyama, "Kink - Antikink Collisions in the Two-Dimensional Phi**4 Model," Prog. Theor. Phys. **61**, 1550–1563 (1979).

[73] M. Moshir, "Soliton - Anti-soliton Scattering and Capture in $\lambda\phi^4$ Theory," Nucl. Phys. B **185**, 318–332 (1981).

[74] David K. Campbell, Jonathan F. Schonfeld, and Charles A. Wingate, "Resonance structure in kink-antikink interactions in φ 4 theory ," Physica D **9**, 1 (1983).

[75] Panayotis G. Kevrekidis and Roy H. Goodman, "Four Decades of Kink Interactions in Nonlinear Klein-Gordon Models: A Crucial Typo, Recent Developments and the Challenges Ahead," (2019), arXiv:1909.03128 [nlin.PS] .

[76] N. S. Manton, K. Oles, T. Romanczukiewicz, and A. Wereszczynski, "Collective Coordinate Model of Kink-Antikink Collisions in ϕ4 Theory," Phys. Rev. Lett. **127**, 071601 (2021), arXiv:2106.05153 [hep-th] .

[77] Patrick Dorey, Anastasia Gorina, Ilya Perapechka, Tomasz Romańczukiewicz, and Yakov Shnir, "Resonance structures in kink-antikink collisions in a deformed sine-Gordon model," JHEP **09**, 145 (2021), arXiv:2106.09560 [hep-th] .

[78] Patrick Dorey, Kieran Mersh, Tomasz Romanczukiewicz, and Yasha Shnir, "Kink-antikink collisions in the ϕ^6 model," Phys. Rev. Lett. **107**, 091602 (2011), arXiv:1101.5951 [hep-th] .

[79] C. Adam, P. Dorey, A. Garcia Martin-Caro, M. Huidobro, K. Oles, T. Romanczukiewicz, Y. Shnir, and A. Wereszczynski, "Multikink scattering in the ϕ6 model revisited," Phys. Rev. D **106**, 125003 (2022), arXiv:2209.08849 [hep-th] .

[80] Vakhid A. Gani, Vadim Lensky, and Mariya A. Lizunova, "Kink excitation spectra in the (1+1)-dimensional φ^8 model," JHEP **08**, 147 (2015), arXiv:1506.02313 [hep-th] .

[81] Vakhid A. Gani, Aliakbar Moradi Marjaneh, and Kurosh Javidan, "Exotic final states in the φ^8 multi-kink collisions," Eur. Phys. J. C **81**, 1124 (2021), arXiv:2106.06399 [hep-th] .

[82] Lukáš Rafaj, Ondřej Nicolas Karpíšek, and Filip Blaschke, "Scattering of kinks in Frankensteinian potentials: Kinks as bubbles of exotic mass and phase transitions in oscillon production," (2026), arXiv:2603.04101 [hep-th] .

[83] Steffen Krusch, Morgan Rees, and Thomas Winyard, "Scattering of vortices with excited normal modes," Phys. Rev. D **110**, 056050 (2024), arXiv:2406.04164 [math-ph] .

[84] A. Alonso Izquierdo, N. S. Manton, J. Mateos Guilarte, and A. Wereszczynski, "Collective coordinate models for 2-vortex shape mode dynamics," Phys. Rev. D **110**, 085006 (2024), arXiv:2405.20249 [hep-th] .

[85] A. Alonso-Izquierdo, J. Mateos Guillarte, M. Rees, and A. Wereszczynski, “Spectral wall in collisions of excited Abelian Higgs vortices,” Phys. Rev. D **110**, 065004 (2024), arXiv:2406.05725 [hep-th] .

[86] A. Alonso-Izquierdo, N. S. Manton, J. Mateos Guilarte, M. Rees, and A. Wereszczynski, “Dynamics of excited BPS three-vortices,” Phys. Rev. D **111**, 105021 (2025), arXiv:2502.15087 [hep-th] .

[87] Eric Myers, Claudio Rebbi, and Richard Strilka, “A Study of the interaction and scattering of vortices in the Abelian Higgs (or Ginzburg-Landau) model,” Phys. Rev. D **45**, 1355–1364 (1992).

[88] D. Canillas Martínez, A. González-Parra, D. Miguélez-Caballero, and A. Wereszczynski, “Oscillons in the broken vacuum and global vortex annihilation,” (2026), arXiv:2603.28298 [hep-th] .

[89] Marcelo Gleiser and Joel Thorarinson, “A Phase transition in U(1) configuration space: Oscillons as remnants of vortex-antivortex annihilation,” Phys. Rev. D **76**, 041701 (2007), arXiv:hep-th/0701294 .

[90] F. Blaschke, T. Romańczukiewicz, K. Sławińska, and A. Wereszczyński, “Amplitude modulations and resonant decay of excited oscillons,” Phys. Rev. E **110**, 014203 (2024), arXiv:2403.00443 [hep-th] .

[91] D. Canillas Martínez, P. Dorey, T. Románczukiewicz, Paul M. Saffin, K. Slawinska, and A. Wereszczy´nski, “Oscillons and bubbles in Q-ball dynamics,” JHEP **12**, 154 (2025), arXiv:2509.03192 [hep-th] .

[92] J. P. Bradshaw, A. N. W. Hone, and S. Krusch, “Modelling fractal behaviour of wobbling kinks,” (in preparation) (2026).

[93] Naoya Kitajima and Shota Nakagawa, “Abelian-Higgs vortices in the oscillating axion background,” (2025), arXiv:2507.16720 [hep-ph] .

[94] T. Vachaspati and A. Achucarro, “Semilocal cosmic strings,” Phys. Rev. D **44**, 3067–3071 (1991).

[95] Mark Hindmarsh, “Existence and stability of semilocal strings,” Phys. Rev. Lett. **68**, 1263–1266 (1992).

[96] G. R. Dvali and Goran Senjanovic, “Semiglobal Alice strings,” Phys. Rev. D **51**, 7148–7151 (1995), arXiv:hep-ph/9407306 .

[97] G. R. Dvali and Goran Senjanovic, “Topologically stable electroweak flux tubes,” Phys. Rev. Lett. **71**, 2376–2379 (1993), arXiv:hep-ph/9305278 .

[98] Tanmay Vachaspati and George B. Field, “Electroweak string configurations with baryon number,” Phys. Rev. Lett. **73**, 373–376 (1994), arXiv:hep-ph/9401220 .

[99] Tanmay Vachaspati, “Monopole-Antimonopole Scattering,” Phys. Rev. D **93**, 045008 (2016), arXiv:1511.05095 [hep-th] .

[100] Ayush Saurabh and Tanmay Vachaspati, “Monopole-antimonopole Interaction Potential,” Phys. Rev. D **96**, 103536 (2017), arXiv:1705.03091 [hep-th] .

[101] Ayush Saurabh and Tanmay Vachaspati, “Monopole–antimonopole: interaction, scattering and creation,” Phil. Trans. Roy. Soc. Lond. A **377**, 20190143 (2019), arXiv:1904.02257 [hep-th] .

[102] Levon Pogosian and Tanmay Vachaspati, “Interaction of magnetic monopoles and domain walls,” Phys. Rev. D **62**, 105005 (2000), arXiv:hep-ph/9909543 .

[103] Frans R. Klinkhamer and N. S. Manton, “A Saddle Point Solution in the Weinberg-Salam Theory,” Phys. Rev. D **30**, 2212 (1984).

[104] Michael Zantedeschi, *On structure and primordial origin of black holes*, Ph.D. thesis, Munich U. (2022).

[105] P. J. Ruback, “Vortex String Motion in the Abelian Higgs Model,” Nucl. Phys. B **296**, 669–678 (1988).

[106] T. M. Samols, “Vortex scattering,” Commun. Math. Phys. **145**, 149–180 (1992).

[107] E. P. S. Shellard and P. J. Ruback, “Vortex Scattering in Two-dimensions,” Phys. Lett. B **209**, 262–270 (1988).

[108] A. Alonso-Izquierdo, W. Garcia Fuertes, N. S. Manton, and J. Mateos Guilarte, “Spectral flow of vortex shape modes over the BPS 2-vortex moduli space,” JHEP **01**, 020 (2024), arXiv:2310.17486 [hep-th] .

[109] K. Arthur and J. Burzlaff, “Existence theorems for pi / n vortex scattering,” Lett. Math. Phys. **36**, 311–318 (1996), arXiv:hep-th/9503010 .

[110] C. Adam, K. Oles, T. Romanczukiewicz, and A. Wereszczynski, “Spectral Walls in Soliton Collisions,” Phys. Rev. Lett. **122**, 241601 (2019), arXiv:1903.12100 [hep-th] .

[111] J. I. Rawlinson, “Coriolis terms in Skyrmion Quantization,” Nucl. Phys. B **949**, 114800 (2019), arXiv:1908.03414 [nucl-th] .

[112] D. Miguélez-Caballero, S. Navarro-Obregón, and A. Wereszczynski, “Moduli space metric of the excited vortex,” Phys. Rev. D **111**, 105008 (2025), arXiv:2503.15227 [hep-th] .

[113] A. Alonso-Izquierdo, J. J. Blanco-Pillado, D. Miguélez-Caballero, S. Navarro-Obregón, and J. Queiruga, "Excited Abelian-Higgs vortices: Decay rate and radiation emission," Phys. Rev. D **110**, 065009 (2024), arXiv:2405.06030 [hep-th] .

[114] D. Stuart, "Dynamics of Abelian Higgs vortices in the near Bogomolny regime," Commun. Math. Phys. **159**, 51–91 (1994).

[115] J. M. Speight, "Static intervortex forces," Phys. Rev. D **55**, 3830–3835 (1997), arXiv:hep-th/9603155 .

[116] Martin Speight and Thomas Winyard, "Short-range intervortex forces," Phys. Rev. D **112**, 055024 (2025).

[117] Minoru Eto, Toshiaki Fujimori, Muneto Nitta, Keisuke Ohashi, and Norisuke Sakai, "Dynamics of Non-Abelian Vortices," Phys. Rev. D **84**, 125030 (2011), arXiv:1105.1547 [hep-th] .

[118] George Theodorou, Bruno Barton-Singer, and Stavros Komineas, "Interaction and collision of skyrmions in chiral antiferromagnets," SciPost Phys. **18**, 037 (2025), arXiv:2305.13515 .

[119] N. S. Manton, "Unstable Manifolds and Soliton Dynamics," Phys. Rev. Lett. **60**, 1916 (1988).

[120] Gia Dvali, "Swift Memory Burden in Merging Black Holes: how information load affects black hole's classical dynamics," (2025), arXiv:2509.22540 [hep-th] .

[121] D. Stuart, "The Geodesic approximation for the Yang-Mills Higgs equations," Commun. Math. Phys. **166**, 149–190 (1994).

[122] G. W. Gibbons and N. S. Manton, "Classical and Quantum Dynamics of BPS Monopoles," Nucl. Phys. B **274**, 183–224 (1986).

[123] N. S. Manton and T. M. Samols, "Radiation From Monopole Scattering," Phys. Lett. B **215**, 559–563 (1988).

[124] David Tong, "TASI lectures on solitons: Instantons, monopoles, vortices and kinks," in *Theoretical Advanced Study Institute in Elementary Particle Physics: Many Dimensions of String Theory* (2005) arXiv:hep-th/0509216 .

[125] R. S. Ward, "A Yang-Mills Higgs Monopole of Charge 2," Commun. Math. Phys. **79**, 317–325 (1981).

[126] Peter Forgács, Zalán Horváth, and László Palla, "Non-linear superposition of monopoles," Nuclear Physics B **192**, 141–158 (1981).

[127] M. K. Prasad and P. Rossi, "Rigorous Construction of Exact Multi - Monopole Solutions," Phys. Rev. D **24**, 2182 (1981).

[128] H. W. Braden and V. Z. Enolski, “The charge 2 monopole via the ADHMN construction,” Adv. Theor. Math. Phys. **25**, 791–956 (2021), arXiv:1903.00694 [math-ph] .

[129] H. W. Braden and Linden Disney-Hogg, “Towards a classification of charge-3 monopoles with symmetry,” Lett. Math. Phys. **113**, 87 (2023), arXiv:2303.18189 [hep-th] .

[130] Paul M. Sutcliffe, “Monopole zeros,” Phys. Lett. B **376**, 103–110 (1996), arXiv:hep-th/9603065 .

[131] H. Georgi, Helen R. Quinn, and Steven Weinberg, “Hierarchy of Interactions in Unified Gauge Theories,” Phys. Rev. Lett. **33**, 451–454 (1974).

[132] A. Takenaka *et al.* (Super-Kamiokande), “Search for proton decay via $p \to e^+\pi^0$ and $p \to \mu^+\pi^0$ with an enlarged fiducial volume in Super-Kamiokande I-IV,” Phys. Rev. D **102**, 112011 (2020), arXiv:2010.16098 [hep-ex] .

[133] Goran Senjanović and Michael Zantedeschi, “Minimal SU(5) theory on the edge: The importance of being effective,” Phys. Rev. D **109**, 095009 (2024), arXiv:2402.19224 [hep-ph] .

[134] Steven Weinberg, “Gauge and Global Symmetries at High Temperature,” Phys. Rev. D **9**, 3357–3378 (1974).

[135] L. Dolan and R. Jackiw, “Symmetry Behavior at Finite Temperature,” Phys. Rev. D **9**, 3320–3341 (1974).

[136] D. A. Kirzhnits and Andrei D. Linde, “A Relativistic phase transition,” Zh. Eksp. Teor. Fiz. **67**, 1263–1275 (1974).

[137] T. W. B. Kibble, “Topology of Cosmic Domains and Strings,” J. Phys. A **9**, 1387–1398 (1976).

[138] V. Mukhanov, *Physical Foundations of Cosmology* (Cambridge University Press, Oxford, 2005).

[139] T. W. B. Kibble, George Lazarides, and Q. Shafi, “Walls Bounded by Strings,” Phys. Rev. D **26**, 435 (1982).

[140] John Preskill and Alexander Vilenkin, “Decay of metastable topological defects,” Phys. Rev. D **47**, 2324–2342 (1993), arXiv:hep-ph/9209210 .

[141] Ian Affleck, “Quantum Statistical Metastability,” Phys. Rev. Lett. **46**, 388 (1981).

[142] Sidney R. Coleman, “The Fate of the False Vacuum. 1. Semiclassical Theory,” Phys. Rev. D **15**, 2929–2936 (1977), [Erratum: Phys.Rev.D 16, 1248 (1977)].

[143] Andrei D. Linde, "Fate of the False Vacuum at Finite Temperature: Theory and Applications," Phys. Lett. B **100**, 37–40 (1981).

[144] Sidney R. Coleman and Erick J. Weinberg, "Radiative Corrections as the Origin of Spontaneous Symmetry Breaking," Phys. Rev. D **7**, 1888–1910 (1973).

[145] Erick J. Weinberg, *Radiative corrections as the origin of spontaneous symmetry breaking*, Ph.D. thesis, Harvard U. (1973), arXiv:hep-th/0507214 .

[146] Sidney R. Coleman, V. Glaser, and Andre Martin, "Action Minima Among Solutions to a Class of Euclidean Scalar Field Equations," Commun. Math. Phys. **58**, 211–221 (1978).

[147] Mark Hindmarsh, Asier Lopez-Eiguren, Riikka Seppä, and David J. Weir, "Numerical simulations of magnetic monopole evolution in an expanding universe," (2025), arXiv:2511.14204 [astro-ph.CO] .

[148] Blas Cabrera, "First Results from a Superconductive Detector for Moving Magnetic Monopoles," Phys. Rev. Lett. **48**, 1378–1380 (1982).

[149] Maximilian Bachmaier, Gia Dvali, and Juan Sebastián Valbuena-Bermúdez, "Radiation emission during the erasure of magnetic monopoles," Phys. Rev. D **108**, 103501 (2023), arXiv:2306.12958 [hep-th] .

[150] Levon Pogosian and Tanmay Vachaspati, "Domain walls in SU(5)," Phys. Rev. D **62**, 123506 (2000), arXiv:hep-ph/0007045 .

[151] Micah Brush, Levon Pogosian, and Tanmay Vachaspati, "Magnetic monopole—domain wall collisions," Phys. Rev. D **92**, 045008 (2015), arXiv:1505.08170 [hep-th] .

[152] Goran Senjanović and Michael Zantedeschi, "Minimal Pati-Salam theory: From cosmic defects to gravitational waves and colliders," Phys. Rev. D **112**, 055018 (2025), arXiv:2504.01893 [hep-ph] .

[153] Stephon Alexander, Robert H. Brandenberger, Richard Easther, and Andrew Sornborger, "On the interaction of monopoles and domain walls," (1999), arXiv:hep-ph/9903254 .

[154] Gia Dvali and Juan Sebastián Valbuena-Bermúdez, "Erasure of strings and vortices," Phys. Rev. D **107**, 035001 (2023), arXiv:2212.07535 [hep-th] .

[155] Juan Sebastian Valbuena-Bermúdez and Juan Sebastian Valbuena-Bermúdez, *The erasure of topological defects and the saturation phenomenon*, Ph.D. thesis, Munich U., LMU Munich: Faculty of Physics (2024).

[156] Alexander Evgenyevich Kudryavtsev, B. M. A. G. Piette, and W. J. Zakrzewski, "Skyrmions and domain walls in (2+1)-dimensions," Nonlinearity **11**, 783–795 (1998), arXiv:hep-th/9709187 .

[157] Alexander Evgenyevich Kudryavtsev, B. M. A. G. Piette, and W. J. Zakrzewski, "On the interactions of skyrmions with domain walls," Phys. Rev. D **61**, 025016 (2000), arXiv:hep-th/9907197 .

[158] G. Dvali, H. B. Nielsen, and N. Tetradis, "Localization of gauge fields and monopole tunnelling," Phys. Rev. D **77**, 085005 (2008), arXiv:0710.5051 [hep-th] .

[159] Jan Ambjorn and P. Olesen, "Antiscreening of Large Magnetic Fields by Vector Bosons," Phys. Lett. B **214**, 565–569 (1988).

[160] G. R. Dvali and Mikhail A. Shifman, "Domain walls in strongly coupled theories," Phys. Lett. B **396**, 64–69 (1997), [Erratum: Phys.Lett.B 407, 452 (1997)], arXiv:hep-th/9612128 .

[161] Gia Dvali and Alexander Vilenkin, "Solitonic D-branes and brane annihilation," Phys. Rev. D **67**, 046002 (2003), arXiv:hep-th/0209217 .

[162] Vachaspati and T. Vachaspati, "Traveling Waves on Domain Walls and Cosmic Strings," Phys. Lett. B **238**, 41–44 (1990).

[163] Tanmay Vachaspati, Allen E. Everett, and Alexander Vilenkin, "Radiation From Vacuum Strings and Domain Walls," Phys. Rev. D **30**, 2046 (1984).

[164] Gia Dvali, "Entropy Bound and Unitarity of Scattering Amplitudes," JHEP **03**, 126 (2021), arXiv:2003.05546 [hep-th] .

[165] Gia Dvali, Juan Sebastián Valbuena-Bermúdez, and Michael Zantedeschi, "Dynamics of confined monopoles and similarities with confined quarks," Phys. Rev. D **107**, 076003 (2023), arXiv:2210.14947 [hep-th] .

[166] R. Holman, T. W. B. Kibble, and Soo-Jong Rey, "How efficient is the Langacker-Pi mechanism of monopole annihilation?" Phys. Rev. Lett. **69**, 241–244 (1992), arXiv:hep-ph/9203209 .

[167] H. J. de Vega and F. A. Schaposnik, "Electrically Charged Vortices in Nonabelian Gauge Theories With Chern-simons Term," Phys. Rev. Lett. **56**, 2564 (1986).

[168] M. Hindmarsh and T. W. B. Kibble, "Beads on Strings," Phys. Rev. Lett. **55**, 2398 (1985).

[169] Mark Hindmarsh, Kari Rummukainen, and David J. Weir, "Numerical simulations of necklaces in SU(2) gauge-Higgs field theory," Phys. Rev. D **95**, 063520 (2017), arXiv:1611.08456 [astro-ph.CO] .

[170] Veniamin Berezinsky and Alexander Vilenkin, "Cosmic necklaces and ultrahigh-energy cosmic rays," Phys. Rev. Lett. **79**, 5202–5205 (1997), arXiv:astro-ph/9704257 .

[171] Jose J. Blanco-Pillado and Ken D. Olum, "Monopole annihilation in cosmic necklaces," JCAP **05**, 014 (2010), arXiv:0707.3460 [astro-ph] .

[172] M. Shifman and Alexei Yung, "Metastable strings in Abelian Higgs models embedded in nonAbelian theories: Calculating the decay rate," Phys. Rev. D **66**, 045012 (2002), arXiv:hep-th/0205025 .

[173] T. W. B. Kibble and Tanmay Vachaspati, "Monopoles on strings," J. Phys. G **42**, 094002 (2015), arXiv:1506.02022 [astro-ph.CO] .

[174] Tomohiro Matsuda, "Primordial black holes from monopoles connected by strings," Astropart. Phys. **30**, 333–337 (2009), arXiv:hep-ph/0509061 .

[175] Eugeny Babichev, V. Dokuchaev, and M. Kachelriess, "Gravitational radiation from rotating monopole-string systems," Phys. Rev. D **71**, 044028 (2005), arXiv:astro-ph/0411794 .

[176] Steven Weinberg, *Gravitation and Cosmology: Principles and Applications of the General Theory of Relativity* (John Wiley and Sons, New York, 1972).

[177] Louis Leblond, Benjamin Shlaer, and Xavier Siemens, "Gravitational Waves from Broken Cosmic Strings: The Bursts and the Beads," Phys. Rev. D **79**, 123519 (2009), arXiv:0903.4686 [astro-ph.CO] .

[178] J. J. Blanco-Pillado and Ken D. Olum, "Monopole - anti-monopole bound states as a source of ultrahigh-energy cosmic rays," Phys. Rev. D **60**, 083001 (1999), arXiv:astro-ph/9904315 .

[179] Tomohiro Matsuda, "Primordial black holes from cosmic necklaces," JHEP **04**, 017 (2006), arXiv:hep-ph/0509062 .

[180] Wilfried Buchmuller, Valerie Domcke, and Kai Schmitz, "Metastable cosmic strings," JCAP **11**, 020 (2023), arXiv:2307.04691 [hep-ph] .

[181] A. Vilenkin, "Cosmological Evolution of Monopoles Connected by Strings," Nucl. Phys. B **196**, 240–258 (1982).

[182] Yoichiro Nambu, "String-Like Configurations in the Weinberg-Salam Theory," Nucl. Phys. B **130**, 505 (1977).

[183] Teerthal Patel and Tanmay Vachaspati, "Structure of electroweak dumbbells," Phys. Rev. D **107**, 093010 (2023), arXiv:2302.04886 [hep-ph] .

[184] Teerthal Patel and Tanmay Vachaspati, "Annihilation of electroweak dumbbells," JHEP **02**, 164 (2024), arXiv:2311.00026 [hep-ph] .

[185] Yifung Ng, T. W. B. Kibble, and Tanmay Vachaspati, "Formation of Non-Abelian Monopoles Connected by Strings," Phys. Rev. D **78**, 046001 (2008), arXiv:0806.0155 [hep-th] .

[186] S. Mandelstam, "Vortices and Quark Confinement in Nonabelian Gauge Theories," Phys. Rept. **23**, 245–249 (1976).

[187] G. R. Dvali and S. H. Henry Tye, "Brane inflation," Phys. Lett. B **450**, 72–82 (1999), arXiv:hep-ph/9812483 .

[188] G. R. Dvali, "Infrared hierarchy, thermal brane inflation and superstrings as superheavy dark matter," Phys. Lett. B **459**, 489–496 (1999), arXiv:hep-ph/9905204 .

[189] G. R. Dvali, Q. Shafi, and S. Solganik, "D-brane inflation," in *4th European Meeting From the Planck Scale to the Electroweak Scale* (2001) arXiv:hep-th/0105203 .

[190] Nima Arkani-Hamed, Savas Dimopoulos, and G. R. Dvali, "The Hierarchy problem and new dimensions at a millimeter," Phys. Lett. B **429**, 263–272 (1998), arXiv:hep-ph/9803315 .

[191] Gia Dvali, Florian Kühnel, and Michael Zantedeschi, "Primordial black holes from confinement," Phys. Rev. D **104**, 123507 (2021), arXiv:2108.09471 [hep-ph] .

[192] Ya. B. Zel'dovich and I. D. Novikov, "The Hypothesis of Cores Retarded during Expansion and the Hot Cosmological Model," Sov. Astron. **10**, 602 (1967).

[193] Stephen Hawking, "Gravitationally collapsed objects of very low mass," Mon. Not. Roy. Astron. Soc. **152**, 75 (1971).

[194] Bernard J. Carr and S. W. Hawking, "Black holes in the early Universe," Mon. Not. Roy. Astron. Soc. **168**, 399–415 (1974).

[195] George F. Chapline, "Cosmological effects of primordial black holes," Nature **253**, 251–252 (1975).

[196] Bernard J. Carr, "The Primordial black hole mass spectrum," Astrophys. J. **201**, 1–19 (1975).

[197] Alexander Vilenkin, "Cosmic Strings and Domain Walls," Phys. Rept. **121**, 263–315 (1985).

[198] A.A. Abrikosov, "The magnetic properties of superconducting alloys," Journal of Physics and Chemistry of Solids **2**, 199–208 (1957).

[199] Iason Baldes, Yann Gouttenoire, and Filippo Sala, "String Fragmentation in Supercooled Confinement and Implications for Dark Matter," JHEP **04**, 278 (2021), arXiv:2007.08440 [hep-ph] .

[200] Ariel Megevand and Federico Agustin Membiela, "Gravitational waves from bubble walls," JCAP **10**, 073 (2021), arXiv:2108.05510 [astro-ph.CO] .

[201] A. Vilenkin, "Gravitational Field of Vacuum Domain Walls," Phys. Lett. B **133**, 177–179 (1983).

[202] J. Ipser and P. Sikivie, "The Gravitationally Repulsive Domain Wall," Phys. Rev. D **30**, 712 (1984).

[203] Michele Maggiore, *Gravitational Waves. Vol. 1: Theory and Experiments* (Oxford University Press, 2007).

[204] Prateek Agrawal, Gaurang Ramakant Kane, Vazha Loladze, and Mario Reig, "Supercooled confinement," JHEP **10**, 066 (2025), arXiv:2504.00199 [hep-ph] .

[205] Ken'ichi Saikawa, "A review of gravitational waves from cosmic domain walls," Universe **3**, 40 (2017), arXiv:1703.02576 [hep-ph] .

[206] Nancy Aggarwal *et al.*, "Challenges and opportunities of gravitational-wave searches at MHz to GHz frequencies," Living Rev. Rel. **24**, 4 (2021), arXiv:2011.12414 [gr-qc] .

[207] Gabriele Franciolini, Anshuman Maharana, and Francesco Muia, "Hunt for light primordial black hole dark matter with ultrahigh-frequency gravitational waves," Phys. Rev. D **106**, 103520 (2022), arXiv:2205.02153 [astro-ph.CO] .

[208] Claudio Gatti, Luca Visinelli, and Michael Zantedeschi, "Cavity detection of gravitational waves: Where do we stand?" Phys. Rev. D **110**, 023018 (2024), arXiv:2403.18610 [gr-qc] .

[209] Aaron Buikema *et al.* (aLIGO), "Sensitivity and performance of the Advanced LIGO detectors in the third observing run," Phys. Rev. D **102**, 062003 (2020), arXiv:2008.01301 [astro-ph.IM] .

[210] F. Acernese *et al.* (VIRGO), "Advanced Virgo: a second-generation interferometric gravitational wave detector," Class. Quant. Grav. **32**, 024001 (2015), arXiv:1408.3978 [gr-qc] .

[211] T. Akutsu *et al.* (KAGRA), "KAGRA: 2.5 Generation Interferometric Gravitational Wave Detector," Nature Astron. **3**, 35–40 (2019), arXiv:1811.08079 [gr-qc] .

[212] Pau Amaro-Seoane *et al.* (LISA), "Laser Interferometer Space Antenna," (2017), arXiv:1702.00786 [astro-ph.IM] .

[213] Benjamin P Abbott *et al.* (LIGO Scientific), "Exploring the Sensitivity of Next Generation Gravitational Wave Detectors," Class. Quant. Grav. **34**, 044001 (2017), arXiv:1607.08697 [astro-ph.IM] .

[214] B. Sathyaprakash *et al.*, "Scientific Objectives of Einstein Telescope," Class. Quant. Grav. **29**, 124013 (2012), [Erratum: Class.Quant.Grav. 30, 079501 (2013)], arXiv:1206.0331 [gr-qc] .

[215] Sungwoo Hong, Sung Mook Lee, and Qiuyue Liang, "Gravitational Wave with Domain Wall Dominance," (2025), arXiv:2504.02462 [astro-ph.CO] .

[216] Chiara M. F. Mingarelli, Stephen R. Taylor, B. S. Sathyaprakash, and Will M. Farr, "Understanding $\Omega_{\rm gw}(f)$ in Gravitational Wave Experiments," (2019), arXiv:1911.09745 [gr-qc] .

[217] Gerard 't Hooft, "A Planar Diagram Theory for Strong Interactions," Nucl. Phys. B **72**, 461 (1974).

[218] Gerard 't Hooft, "Quarks and Gauge Fields," Conf. Proc. C **7406241**, 58–67 (1974).

[219] G. R. Dvali, "Removing the cosmological bound on the axion scale," (1995), arXiv:hep-ph/9505253 .

[220] Gia Dvali and Alexander Vilenkin, "Formation and evolution of cosmic D strings," JCAP **03**, 010 (2004), arXiv:hep-th/0312007 .

[221] Edmund J. Copeland, Robert C. Myers, and Joseph Polchinski, "Cosmic F and D strings," JHEP **06**, 013 (2004), arXiv:hep-th/0312067 .

[222] Saswat Sarangi and S. H. Henry Tye, "Cosmic string production towards the end of brane inflation," Phys. Lett. B **536**, 185–192 (2002), arXiv:hep-th/0204074 .

[223] Nima Arkani-Hamed, Savas Dimopoulos, and G. R. Dvali, "Phenomenology, astrophysics and cosmology of theories with submillimeter dimensions and TeV scale quantum gravity," Phys. Rev. D **59**, 086004 (1999), arXiv:hep-ph/9807344 .

[224] Ignatios Antoniadis, Nima Arkani-Hamed, Savas Dimopoulos, and G. R. Dvali, "New dimensions at a millimeter to a Fermi and superstrings at a TeV," Phys. Lett. B **436**, 257–263 (1998), arXiv:hep-ph/9804398 .

[225] E. G. Adelberger, J. H. Gundlach, B. R. Heckel, S. Hoedl, and S. Schlamminger, "Torsion balance experiments: A low-energy frontier of particle physics," Prog. Part. Nucl. Phys. **62**, 102–134 (2009).

[226] Wen-Hai Tan, Shan-Qing Yang, Cheng-Gang Shao, Jia Li, An-Bin Du, Bi-Fu Zhan, Qing-Lan Wang, Peng-Shun Luo, Liang-Cheng Tu, and Jun Luo, "New Test of the Gravitational Inverse-Square Law at the Submillimeter Range with Dual Modulation and Compensation," Phys. Rev. Lett. **116**, 131101 (2016).

[227] Gia Dvali, "A Microscopic Model of Holography: Survival by the Burden of Memory," (2018), arXiv:1810.02336 [hep-th] .

[228] Gia Dvali, Lukas Eisemann, Marco Michel, and Sebastian Zell, "Black hole metamorphosis and stabilization by memory burden," Phys. Rev. D **102**, 103523 (2020), arXiv:2006.00011 [hep-th] .

[229] Ana Alexandre, Gia Dvali, and Emmanouil Koutsangelas, "New mass window for primordial black holes as dark matter from the memory burden effect," Phys. Rev. D **110**, 036004 (2024), arXiv:2402.14069 [hep-ph] .

[230] Gia Dvali, Juan Sebastián Valbuena-Bermúdez, and Michael Zantedeschi, "Memory burden effect in black holes and solitons: Implications for PBH," Phys. Rev. D **110**, 056029 (2024), arXiv:2405.13117 [hep-th] .

[231] Gia Dvali, Michael Zantedeschi, and Sebastian Zell, "Transitioning to Memory Burden: Detectable Small Primordial Black Holes as Dark Matter," (2025), arXiv:2503.21740 [hep-ph] .

[232] M. Ackermann *et al.* (Fermi-LAT), "The spectrum of isotropic diffuse gamma-ray emission between 100 MeV and 820 GeV," Astrophys. J. **799**, 86 (2015), arXiv:1410.3696 [astro-ph.HE] .

[233] Zhen Cao *et al.* (LHAASO), "Measurement of Ultra-High-Energy Diffuse Gamma-Ray Emission of the Galactic Plane from 10 TeV to 1 PeV with LHAASO-KM2A," Phys. Rev. Lett. **131**, 151001 (2023), arXiv:2305.05372 [astro-ph.HE] .

[234] M. G. Aartsen *et al.* (IceCube), "Differential limit on the extremely-high-energy cosmic neutrino flux in the presence of astrophysical background from nine years of IceCube data," Phys. Rev. D **98**, 062003 (2018), arXiv:1807.01820 [astro-ph.HE] .

[235] R. Abbasi *et al.* (IceCube), "The IceCube high-energy starting event sample: Description and flux characterization with 7.5 years of data," Phys. Rev. D **104**, 022002 (2021), arXiv:2011.03545 [astro-ph.HE] .

[236] S. Aiello *et al.* (KM3NeT), "Observation of an ultra-high-energy cosmic neutrino with KM3NeT," Nature **638**, 376–382 (2025), [Erratum: Nature 640, E3 (2025)].

[237] P. Sikivie, "Of Axions, Domain Walls and the Early Universe," Phys. Rev. Lett. **48**, 1156–1159 (1982).

[238] Gia Dvali, Lucy Komisel, and Anja Stuhlfauth, "Cosmic strings and domain walls of the QCD quark condensate with and without a hidden axion," Phys. Rev. D **112**, 096023 (2025), arXiv:2505.03542 [hep-ph] .

[239] G. R. Dvali, "Goldstone bosons versus domain walls bounded by cosmic strings," Phys. Lett. B **265**, 64–68 (1991).

[240] Valentin Thoss, Andreas Burkert, and Kazunori Kohri, "Breakdown of hawking evaporation opens new mass window for primordial black holes as dark matter candidate," Mon. Not. Roy. Astron. Soc. **532**, 451–459 (2024), arXiv:2402.17823 [astro-ph.CO] .

[241] Edward Witten, "Dyons of Charge e theta/2 pi," Phys. Lett. B **86**, 283–287 (1979).

[242] Maximilian Bachmaier, Gia Dvali, and Juan Sebastián Valbuena-Bermúdez, "Witten Effect in 3-Form Description of θ-vacua," (2025), arXiv:2510.05237 [hep-th] .

[243] Daniel G. Figueroa, Adrien Florio, Francisco Torrenti, and Wessel Valkenburg, "The art of simulating the early Universe – Part I: Integration techniques and canonical cases," JCAP **04**, 035 (2021), arXiv:2006.15122 [astro-ph.CO] .

[244] Saul A Teukolsky, Brian P Flannery, W Press, and W Vetterling, "Numerical recipes in c," SMR **693**, 59–70 (1992).

[245] Ernst Hairer, Gerhard Wanner, and Syvert P Nørsett, *Solving ordinary differential equations I: Nonstiff problems* (Springer, 1993).

[246] Bengt Fornberg, "Generation of finite difference formulas on arbitrarily spaced grids," Mathematics of computation **51**, 699–706 (1988).

[247] Pauli Virtanen, Ralf Gommers, Travis E Oliphant, Matt Haberland, Tyler Reddy, David Cournapeau, Evgeni Burovski, Pearu Peterson, Warren Weckesser, Jonathan Bright, *et al.*, "Scipy 1.0: fundamental algorithms for scientific computing in python," Nature methods **17**, 261–272 (2020).

[248] Saul A. Teukolsky, "On the stability of the iterated Crank-Nicholson method in numerical relativity," Phys. Rev. D **61**, 087501 (2000), arXiv:gr-qc/9909026 .

[249] Mark Hindmarsh and Petja Salmi, "Oscillons and domain walls," Phys. Rev. D **77**, 105025 (2008), arXiv:0712.0614 [hep-th] .

[250] Petja Salmi and Mark Hindmarsh, "Radiation and Relaxation of Oscillons," Phys. Rev. D **85**, 085033 (2012), arXiv:1201.1934 [hep-th] .

[251] Martin Speight, Thomas Winyard, and Egor Babaev, "Chiral p-wave superconductors have complex coherence and magnetic field penetration lengths," Physical Review B **100** (2019), 10.1103/physrevb.100.174514.

[252] Marcelo Gleiser and Andrew Sornborger, "Longlived localized field configurations in small lattices: Application to oscillons," Phys. Rev. E **62**, 1368–1374 (2000), arXiv:patt-sol/9909002 .

[253] Miguel Alcubierre, Steven Brandt, Bernd Bruegmann, Daniel Holz, Edward Seidel, Ryoji Takahashi, and Jonathan Thornburg, "Symmetry without symmetry: Numerical simulation of axisymmetric systems using Cartesian grids," Int. J. Mod. Phys. D **10**, 273–290 (2001), arXiv:gr-qc/9908012 .

[254] Python Software Foundation, "Python language reference, version 3.x," (2026), accessed: 2026-04-07.

[255] Siu Kwan Lam, Antoine Pitrou, and Stanley Seibert, "Numba: A llvm-based python jit compiler," in *Proceedings of the Second Workshop on the LLVM Compiler Infrastructure in HPC* (2015) pp. 1–6.

[256] Charles R Harris, K Jarrod Millman, Stéfan J Van Der Walt, Ralf Gommers, Pauli Virtanen, David Cournapeau, Eric Wieser, Julian Taylor, Sebastian Berg, Nathaniel J Smith, *et al.*, "Array programming with numpy," nature **585**, 357–362 (2020).

[257] John D Hunter, "Matplotlib: A 2d graphics environment," Computing in science & engineering **9**, 90–95 (2007).

[258] Wolfram Research, Inc., "Mathematica, version 14.0," (2024).